HIGH DAM SCOUR HOLE GEOMETRY PREDICTION FOR FULLY DEVELOPED JETS PLUNGING INTO SHALLOW POOLS ON BEDROCK

by

Adèle Bosman

Dissertation presented for the degree of
Doctor of Philosophy in Civil Engineering
in the Faculty of Engineering
at Stellenbosch University

Supervisor:

Prof GR Basson

March 2021

DECLARATION

I hereby declare that the entirety of the work contained within this dissertation is my own, original work, that I am the sole author thereof (save to the extent explicitly otherwise stated), that reproduction and publication thereof by Stellenbosch University will not infringe any third party rights and that I have not previously, in its entirety or in part, submitted it for obtaining any qualification.

Date: March 2021

ABSTRACT

High dam scour hole geometry prediction for plunging jets on bedrock

The safety of dams is often endangered by rock scour formation near the dam's foundation due to a high-velocity free falling jet from the spillway plunging into the plunge pool. The prediction of the scour hole geometry (ultimate depth and maximum extent) is essential in the hydraulic design of high head dams to ensure the stability of the dam.

Rock scour is a complex physical phenomenon that is normally predicted by analytical-empirical formulae and methods, which combine laboratory and prototype observations. The empirical formulae however, cannot describe all the hydrodynamic and geo-mechanic effects involved in rock scour. Despite extensive research since the 1950s, presently there is no universally agreed method to accurately predict the equilibrium scour hole dimensions caused by plunging jets at dams.

The main purpose of the research is to contribute to the knowledge on the prediction of the equilibrium scour hole geometry downstream of a high head dam. The rock scour process was investigated via physical and numerical models, as well as by evaluation of scour prediction methods from literature.

The physical model investigated the hydrodynamic effects of a plunging jet and the subsequent scour of a rectangular, open-ended jointed, movable rock bed. Equilibrium scour hole geometries for various fissured dimensions (simulated with tightly hand-packed rectangular concrete blocks), for a range of flow rates, dam heights, plunge pool depths, rock sizes, and joint structure orientation scenarios were experimentally established with 31 model tests. The experimental results indicated that greater scour occurs if the deposited rocks downstream of the scour hole are removed by floodwaters. For the first time the transient pressures at the joint opening due to a high-velocity plunging jet were measured for a movable bed with a complex joint structure. Additionally, the research studied the scour hole geometry formed by a low-frequency turbulent jet issuing from a rectangular horizontal canal and not discharging from a nozzle. The dynamic pressures at the water-rock interface and the velocity distribution of the wall jet in the plunge pool were recorded and evaluated. Non-dimensional formulae were developed using ordinary least squares regression analysis on the physical model results.

The experimental scour results from this study were compared to various analytical methods found in literature. The scour prediction methods yielded a wide range of scour depths for the same input conditions. No single analytical method is superior, but the equilibrium scour hole depth established in this study best agrees with that predicted by the Critical Pressure method, followed by the Erodibility Index Method and Mason and Arumugam's empirical formula.

A three-dimensional, multi-phase, transient numerical model, in combination with the developed scour depth regression formula, was used to simulate the equilibrium scour hole geometry. The numerical model was calibrated against the physical model results. The numerical simulation results were satisfactory and representative of the model pressures in the open-ended joints.

The proposed three-dimensional numerical model, in conjunction with the scour depth regression formula developed in this study, is capable of simulating the scour hole geometry, which includes both hydrodynamic and geo-mechanical rock scour aspects, if the diffusion of the jet through the air and plunge pool is modelled accurately. Further research is required to improve the numerical simulations to automatically calculate the deformation of a movable bed using the approach developed by this research.

OPSOMMING

Voorspelling van hoë dam uitskuurgatgeometrie deur ’n vryvallende waterstraal op bodemrots

Die veiligheid van damme word dikwels in gedrang gebring deur die rotsuitskuring naby die dam se fondament as gevolg van ’n hoë-snelheid vryvallende waterstraal vanaf die damoorloop tot in die plonspoel. Die voorspelling van die uitskuurgatgeometrie (maksimum diepte en dimensies) is belangrik vir die hidrouliese ontwerp van hoë damme om die stabiliteit van die dam te verseker.

Rotsuitskuring is ’n komplekse fisiese proses wat normaalweg voorspel word deur analitiese-empiriese formules en metodes, wat laboratorium- en prototipe-waarnemings kombineer. Die empiriese formules is nie in staat om al die hidrodinamiese en geo-meganiese effekte wat rotsuitkuring veroorsaak aan te spreek nie. Ondanks vele navorsing sedert die 1950s, is daar tans geen universele metode om die ewewig uitskuurgatdimensies deur ’n vryvallende waterstraal vanaf ’n damoorloop te voorspel nie.

Die hoofdoel van die navorsing is om ’n bydrae te lewer tot die beskikbare kennis om die ewewig uitskuurgatgeometrie stroomaf van ’n hoë dam te voorspel. Die rotsuitskuringproses is ondersoek deur fisiese en numeriese modelle, sowel as die evaluasie van rotsuitskuring voorspelling metodes ontwikkel in voorafgaande studies.

Die fisiese model het die hidrodinamiese eienskappe van ’n vryvallende waterstraal en die uitskuring van ’n reghoekige, oop-eindigende nate, beweegbare rotsbed ondersoek. Ewewig uitskuringsgatvorms vir verskillende naat dimensies (gemodelleer met reghoekige betonblokke styf teen mekaar gepak met die hand) is eksperimenteel bepaal met 31 modeltoetse vir ’n reeks vloeitempos, damhoogtes, plonspoeldieptes, rotsblokgroottes, en naat oriëntasies. Die eksperimentele resultate het aangedui dat ’n groter uitskurigsgat sal vorm indien die gedeponeerde stene stroomaf van die gat deur vloedwaters verwyder word. Die dinamiese druk ondervind by die opening van die nate as gevolg van die vryvallende waterstraal is gemeet vir ’n beweegbare bed met ’n komplekse naatstruktuur. Verder het die navorsing bygedra deur die uitskuurgatgeometrie gevorm deur ’n lae-frekwensie turbulente waterstraal vanaf ’n horisontale kanaal en nie vanaf ’n ronde spuitstuk nie te bestudeer. Die dinamiese druk by die water-rots-oppervlak en die snelheidsverspreiding van die grensstraal in die plonspoel is aangeteken en ondersoek. Dimensielose formules is ontwikkel met die hulp van liniêre regressie analise gebaseer op die fisiese model resultate.

Die eksperimentele uitskuurresultate van die studie is met verskillende analitiese metodes van voorafgaande studies vergelyk. Die uitskuurresultate van die voorafgaande studies het ’n verskeidenheid van dieptes vir dieselfde inset parameters gelewer. Geen enkele analitiese metode is by uitstek die beste nie, maar die uitskuringdiepte resultate van die huidige studie stem die beste ooreen met diè van die Kritiese Durk-metode, gevolg deur die Erodeerbaarheidsindeks-metode en die empiriese formule van Mason en Arumugam.

’n Drie-dimensionele, multi-fase, numeriese model vir onbestendige vloeitoestande, in kombinasie met die ontwikkelde regressieformule vir diepteuitskuring, is gebruik om die uitskuring van die ewewigsgat na te boots. Die numeriese model is gekalibreer teen die resultate van die fisiese model. Die numeriese simulasieresultate was bevredigend en verteenwoordigend van die dinamiese druk ondervind by die oop-eindigende rotsnate in die fisiese model.

Die voorgestelde drie-dimensionele numeriese model in kombinasie met die diepte-regressie-formule wat ontwikkel is in hierdie studie, is in staat om die uitskuurgatvorm te simuleer, wat beide die hidrodinamiese en geo-meganiese eienskappe van rotsuitskuring insluit, mits die diffusie van die waterstraal deur die lug en plonspoel akkuraat gemodeleer word. Verdere navorsing is nodig om die numeriese simulasies te verbeter deur die vervorming van die bed outomaties te bereken deur middel van ’n beweegbare bed volgens die benadering wat in hierdie navorsing ontwikkel is.

PREFACE

The research findings from this dissertation were presented to the professional and academic engineering community at a conference and at a short course, and were published in a specialist journal. The research findings were incorporated into the following journal paper and conference proceedings:

- Bosman A and Basson GR (2020). Physical model study of bedrock scour downstream of dams due to spillway plunging jets, *Journal of South African Institute of Civil Engineering,* 62(3), 36-52. ISSN 1021-2019.
- Bosman A and Basson GR (2019). Rock scour hole equilibrium geometry prediction for plunging jets at dams. *SANCOLD Annual Conference: Sustainable long-term dam infrastructure development and management*, Benoni, South Africa, 6-8 November.
- Bosman A (2015). Plunge pool hydraulics and scour. *Stellenbosch University Short Course: Design and Construction of Hydraulic Structures* 28 September – 1 October.

ACKNOWLEDGEMENTS

I would like to extend my sincere gratitude to the following people and entities' assistance, support, guidance and advice:

- My supervisor, Prof GR Basson, for his support and guidance.
- The capable and hardworking laboratory team, Johann Nieuwoudt and Iliyaaz Williams.
- I acknowledge PERI, Blackheath, for supplying the scaffolding required to construct the physical model. In particular, I want to express my gratitude to Mr S Davis, Mr R Mulder and their team for assistance with supplying the scaffolding.
- I acknowledge Horts Geosolutions for supplying the Z+F Imager 5006h three-dimensional laser scanner. I want to thank Mr F Stroh and Mr G van der Walt for their technical assistance with the laser scanner.
- I am grateful to Mr A Kunneke of the Forest and Wood Science Department of Stellenbosch University for his enthusiasm and support throughout the physical model testing.
- Thank you to Continental Cobbles, Kraaifontein, for supplying the cobblestones required to model the moving bedrock.
- I acknowledge Kaytech Western Cape for supplying the Bidim required for constructing the physical model.
- Thank you to QFINSOFT for supplying the ANSYS FLUENT software and providing software training. In particular I want to thank Mr E Smuts for his numerical modelling advice.
- I thank the Centre for High Performance Computing, South Africa, for providing computational resources and reducing the simulation time required for the investigations. I particularly want to thank Charles Crosby for his advice and guidance.
- Thank you to Mr DE Bosman and Mr NF Katzke for their technical and theoretical assistance, and for elucidated certain programming or statistical concept.
- I further extend my gratitude towards Dr JK Vonkeman for her patience and numerical modelling assistance.
- Thank you to my family, especially my parents, Johann and Amanda Vos, and my sister, Chantel Minnaar, for their emotional support.
- To my husband, Renè, my son Josiah, and my daughter Beatrin, thank you very much for your unconditional love, encouragement and patience.
- Most importantly, praise to Jesus Christ for guiding and motivating me to persevere.

TABLE OF CONTENTS

LIST OF FIGURES

LIST OF TABLES

NOMENCLATURE

Constants

g = 9.81 m/s^2

ρ_a = 1.225 kg/m^3

ρ_w = 998.2 kg/m^3

ν = 1 x 10^{-6} m^2/s

Surface tension, σ = 0.072 N/m

Variables

A_i	Jet impact area at certain depths below tailwater level ……..……..[m^2]
A_{exp}	Exposed area of rock block ……..……[m^2]
AP	Applied stream power ……[KW/m^2]
$A_{wall\ jet}$	Area of wall jet ……..….[m^2]
a	Acceleration of rock block ……..……...[m/s^2]
a, b, c, d	Regression coefficients ……[-]
B_g	Impinging jet core thickness due to gravity effects ……..……..[m]
B_i	Jet thickness at issuance ……..……..[m]
B_j	Jet thickness in the impingement conditions ……..[m]
B_{out}	Outer thickness of a rectangular jet in impingement conditions ……[m]
b	Distance from the jet centreline to the point where the mean velocity's maximum value is halved, weir or channel width …..……[m]
C_d	Drag coefficient of water particle ……[-]
C_I	Impulsion coefficient ……....[-]

C_p	Mean dynamic pressure coefficient ……[-]
C_p'	Fluctuating dynamic pressure coefficient ……[-]
C_r	Relative density coefficient ……[-]
C_s	FLUENT roughness constant ……[-]
C_{sp}	Mean stream power decay coefficient ……[-]
C_u	Courant number ……[-]
C_{up}	Net uplift pressure coefficient for DI method ……[-]
C_{uplift}	Net uplift pressure coefficient for QSI method ……[-]
c	Mean pressure wave celerity ……[m/s]
D_h	Hydraulic diameter ……[m]
D_i	Jet diameter at issuance for circular jet ……[m]
D_j	Diameter of jet core of a circular jet in impingement conditions ……[m]
D_{out}	Outer diameter of a circular jet in impingement conditions ……[m]
D_s	Scour hole depth ……[m]
D_ω	Cross-diffusion term ……[-]
d	Diameter of a sphere with the same volume as a water particle ……[m]
d_m	Average rock block size of bed material ……[m]
d_{50}	Median rock block size ……[m]
d_{90}, d_{95}	Rock block diameters representing the 90% and 95% percentile ……[m]
E_u	Euler number ……[-]
e_{block}	Protrusion height of the block ……[m]

F Force, reduction factor for fluctuating stream power component for rectangular jet ……[N,-]

$\vec{F}$ Additional body forces ……..…..[N]

F_{QSL} Quasi-steady uplift force ……[N]

Fr Froude number ……..……[-]

F_{sh} Shear and interlocking forces ……..……..[N]

F_u, F_o Forces under and over block ……..[N]

F_{uplift} Uplift force ……..…..[N]

F_1, F_2 Blending functions …..……[-]

G_b Submerged weight of rock block ……...[N]

H_L Total energy dissipation ……..……[m]

H_{max} Maximum fall height, maximum pressure head limit of transmitter ……..…[m]

H_{med} Medium fall height ……..…..[m]

H_{min} Minimum fall height, minimum pressure head limit of transmitter ……..…..[m]

H_{out} Dynamic pressure head ……..……[m]

H_w Fall height ……[m]

h_{up} Height that rock block is lifted ……[m]

h_v Velocity head ……..…[m]

H_0 Energy of jet upstream of the submerged hydraulic jump at the pool bottom [m]

h_1 Flow depth above weir ……[m]

I_{max} Maximum net impulsion ……[Ns]

I_{min}, I_{max} Minimum and maximum current output of pressure transmitter ……..…[mA]

$I_{\Delta t,pulse}$ Net impulse on the rock block ……..[Ns]

J_a	Joint alteration number ……[-]
J_c	Joint count number ……[-]
J_n	Joint set number ……[-]
J_r	Joint wall roughness number ……[-]
J_s	Relative ground structure number ……[-]
J_x, J_y, J_z	Average spacing of joint sets ……[m]
K	Erodibility index ……[-]
K_b	Block size number ……[-]
K_d	Discontinuity bond shear strength number ……[-]
K_s	Bed surface roughness ……[m]
K'	Parameter ranges from 0.2 for smooth to 0.4 for rough turbulent jets [-]
k	Intercept value constant ……[-]
L	Characteristic block length ……[m]
L_b	Jet breakup length ……[m]
L_f	Joint length ……[m]
L_j	Jet trajectory length ……[m]
L_s	Scour hole length ……[m]
M_a	Mach number ……[-]
MN	Movability number ……[-]
M_s	Mass strength number ……[-]
m	Rock block mass ……[kg]
$\dot{m}_{pq}$, $\dot{m}_{qp}$	Mass transfer between phase p and q, and phase q to p, respectively ……[kg]

n_d	Nozzle diameter ……..[m]
P	1% exceedance dynamic head, perimeter ……[m]
P_{crit}	Critical pressure head ……[m]
P_{jet}	Mean stream power of jet per unit area …… ……..…[W/m^2]
P'_{jet}	Fluctuating stream power of jet per unit area ……..…[W/m^2]
P_{max}	Total dynamic pressure ……..…..[Pa]
P_{pool}	Stream power of jet per unit area in the pool at a certain depth ……..…[W/m^2]
P_{rock}	Rock scour threshold……[-]
P_{SP}	Stream power per unit area ……..…[W/m^2]
P_s	Weir crest height, pseudo-static pressure ……..…[m; Pa]
P_{total}	Total stream power of jet per unit area ……..……..…[W/m^2]
P_u, P_{uplift}	Uplift pressure ……..……..[Pa]
p_e	Jet perimeter ……..……..…..[m]
Q	Discharge……..……..……...[m^3/s]
q	Specific discharge……..……..….[m^3/s/m]
q_{up}, q_{down}	Deflected unit discharge up- and downstream from impingement point .[m^3/s/m]
R	Transmitter resistance, hydraulic radius ……[Ω, m]
Re	Reynolds number ……..……..[-]
Re_p	Particle Reynolds number ……..[-]
$\vec{r}$	Resultant force vector ……..…[N]
S	Strain rate tensor, thickness for stable rock block according to the Block stability method ……..[s^{-1}, m]
S_f	Energy slope ……..[-]

S_q Mass source term for phase q ……[-]

S_t Strouhal number ……...[-]

T_u Initial turbulence ……..……[%]

T_{up} Travel period of pressure waves inside rock joints ……..[s]

t Deflector height ……..…..[m]

t_n Sampling duration to determine air concentration of falling jet ……..[s]

t_{up} Duration of block movement due to initial velocity ……..[s]

t_{void} Total void periods during sampling the air concentration of the falling jet ……[s]

t_0 Energy loss in duct ……..……[m]

U_f Volume flux through cell face based on normal velocity ……..…[$m^3/s/m^2$]

u Longitudinal velocity ……[m/s]

u' Instantaneous root mean square value of axial velocity fluctuations ……[m/s]

$\overline{u_i'u_j'}$ Reynolds stress tensor .....[m^2/s^2]

V Mesh cell volume ……..…[m^3]

V^* Shear velocity ……..…..[m/s]

V_{air} Minimum air inception velocity ……..…..……[m/s]

V_b Volume of rock block ……[m^3]

V_i Issuance jet velocity ……[m/s]

V_j Jet velocity at impingement with the plunge pool water surface ……..……[m/s]

V_{mean} Mean horizontal velocity of wall jet ……..……[m/s]

$\vec{V}_q$ Velocity vector of phase q ……..……[m/s]

V_{ss} Settling velocity of rock block ..……..[m/s]

$V_{Xi,max}$	Velocity of the wall jet X-distance from the impingement point ……...[m/s]
$V_{Zbottom}$	Initial flow velocity of the wall jet at impingement with pool bed ……[m/s]
$V_{\Delta t,pulse}$	Average velocity experienced by the rock block during time period Δt ……[m/s]
$\overrightarrow{v_i}$	Block-side unit normal vector ……..[-]
We	Weber number ……..……[-]
W_i, W_j	Jet width in the issuance and impingement conditions ……[m]
W_{out}	Outer width of a rectangular jet in the impingement conditions ……..……..[m]
W_s	Scour hole width ……..[m]
x	Horizontal distance in flow direction, dynamic pressure voltage reading ..[m, V]
x'	Horizontal streamwise coordinate for flip bucket jets ……[m]
x_b, y_b, z_b	Rock block dimensions in the different directions ……..……[m]
x_{sta}	Voltage reading of static tailwater depth ……..……[V]
x_{UM}, x_{LM}	Longitudinal location of the maximum upper and lower trajectory of a deflector jet ……..……[m]
$x_{1,2,3..}$	Independent variables ……..……[-]
Y	Total scour depth below tailwater level ……..……...[m]
y	Lateral distance, distance to the next cell surface ……..[m]
y_s	Scour depth below original pool bed level ……...[m]
y_{up}, y_{down}	Up- and downstream wall jet thickness ……....[m]
$y_{V_{max}}$	Flow depth to the maximum horizontal velocity in wall jet ……..…[m]
y_w	Plunge pool depth ……...[m]
Z_{core}	Distance required for the jet core to become diffused in plunge pool …….[m]
z	Vertical distance ……..[m]

α	Defelctor angle relative to the chute bottom ..……...……..[degrees]
α_i	Air concentration at impact with plunge pool water surface ……...……..[-]
α_{in}	Inner core diffusion angle in plunge pool ……..[degrees]
α_j	Virtual flip bucket jet take-off angle ……[degrees]
α_k, α_ω	Prandtl numbers for k and ω ……..[-]
α_{out}	Outer expansion angle in plunge pool ……..[degrees]
α_q	Volume fraction of phase q ……...……..[-]
α_r	Joint structure angle ……...……...[degree]
β	Air-water flow ratio …….....[-]
β_a	Total deflection angle of a ski jump …….....[degrees]
γ	Unit weight ……..……..……..……..[N/m^3]
δ	Jet impingement angle with bedrock, equivalent deflector angle of a ski jump ……[degrees]
δ_{in}	Core contraction in air ……..……..[m]
δ_{out}	Lateral outspread of jet in air ..……...[m]
ε	Turbulence dissipation rate of $k-\varepsilon$ model, spread of a circular jet …[J/kg/s, m]
ζ_1	Jet trajectory length in the plunge pool ……....[m]
θ_i	Angle of jet at issuance ……[degrees]
θ_j	Angle of jet at impingement with the plunge pool water surface ……[degrees]
μ, μ_t	Shear viscosity, turbulent viscosity ……..……..[Pa-s]
v_ς	Maximum velocity at the jet centreline at the jet length in the plunge pool …[m/s]

ξ	Lateral spread distance of a rectangular jet ……[m]
π_0	Dependent variable ……..[-]
ρ_i	Average density of mixture ……[kg/m^3]
ρ_r	Rock density ……[kg/m^3]
σ_{pmax}	Maximum standard deviation of the fluctuating pressures ……..……[Pa]
φ	Parameter ($K_\varphi T_u$), with a recommended value of 1.14 for circular jets and 1.24 for nappe flow, chute bottom angle relative to the horizontal ……[-; degrees]
ϕ	Kinetic energy velocity coefficient (generally assumed as 1) ……..……[-]
Ω	Uplift coefficient according to the Block stability method ……[-]
ω	Turbulence dissipation rate of SST $k-\omega$ model ……[J/kg/s]
Δt	Time interval ……..……...[s]
Δl	Mesh cell size ……...[m]

Subscripts

a	air
r	rock
w	water
m	Model
p	Prototype
i	Variable at issuance
j	Variable at impingement conditions
min	Minimum value of variable
med	Medium value of variable
max	Maximum value of variable

Abbreviations

1D	One-dimensional
2D	Two-dimensional
3D	Three-dimensional
ADV	Acoustic Doppler Velocimeter
AIC	Akaike Information Criterion
BSS	Block scour spectrum
BS3D	Block stability in three-dimensions
CFD	Computational Fluid Dynamics
CFM	Comprehensive Fracture Mechanics
CHPC	Centre for High Performance Computing
CPU	Central processing unit
CSIR	Council for Scientific and Industrial Research
CSM	Compressive Scour Model
DEM	Discrete Element Modelling
DI	Dynamic Impulsion Method
DNS	Direct Numerical Simulation
EIM	Erodibility Index Method
EQ	Regression analysis option equation
FSI	Fluid-structure interaction
GUI	Graphical user interface
LES	Large Eddy Simulation
OLS	Ordinary Least Squares

QSI	Quasi Steady Impulsion
RANS	Reynolds Average Navier-Stokes
RMS	Root mean square
RNG	Renormalisation Group
RSM	Reynolds Stress model
RQD	Rock Quality Designation
SANCOLD	South African National Commission on Large Dams
SPH	Smoothed Particle Hydrodynamics
SSR	Sum of squared residuals
SST	Shear Stress Transport
STDEV	Standard deviation
TNP	Thermal Needle Probe
TWD	Tailwater depth
TWL	Tailwater level
UCS	Unconfined Compressive Strength
UDF	User defined function
VOF	Volume of Fluids

1. INTRODUCTION

1.1. Background

Spillways or flood release structures at dams help prevent uncontrolled overtopping of the dam structure and guide excess water downstream of the dam in a controlled manner during floods. A high head dam, designed to spill with a free falling jet with consequent high velocity head impacting on the foundation (bedrock) downstream of a dam, requires significant energy dissipation to limit erosion of the foundation. Depending on the circumstances this energy dissipation could be performed by means of a hydraulic jump in a stilling basin and/or aeration and diffusion of the jet in a plunge pool (Bollaert, 2002). If the energy dissipation of the jet is underestimated, a scour hole will form downstream of the dam embankment if the erosive capacity of the jet is larger than the erosion resistance of the rock.

The foundation of the dam could be endangered if the scour hole geometry becomes extensively large. Increased seepage, loss of stability of the downstream river bank slopes and the raise in tailwater level due to the formation of a mound of eroded material are additional undesirable effects if the scour hole becomes extensive (Azamathulla et al., 2009). The precise assessment of the equilibrium scour hole geometry (ultimate depth and maximum extension) is of crucial concern in the hydraulic design of a high head dam to ensure that the foundation is not endangered by the scour hole during the lifetime of the dam (Van Aswegen et al., 2001).

At several dam sites worldwide, significant scouring downstream of dams has been reported. Plunge pool scouring has become an even greater concern since it is expected that future flood events would be more severe due to climate change (Mok et al., 2014).

An example illustrating the consequences of plunge pool erosion is the Kariba Dam on the Zambezi River, on the border between Zimbabwe and Zambia. The Kariba Dam is a hydroelectric dam which forms Lake Kariba, the largest artificial lake in the world. The spillway comprises of six 9.14 m high by 8.4 m wide submerged sluice gates located in the central part of the dam (Munodawafa & Mhlanga, 2014). The dam is founded on hard gneiss rock, which has experienced scouring over the years. Currently, the depth of the scour hole is approximately 80 m, which is unprecedented in dam history, since it is almost two-thirds of the total dam height (Bollaert et al., 2012a). Figure 1.1 depicts the development of the scour hole downstream of the Kariba Dam from 1962 to 2014.

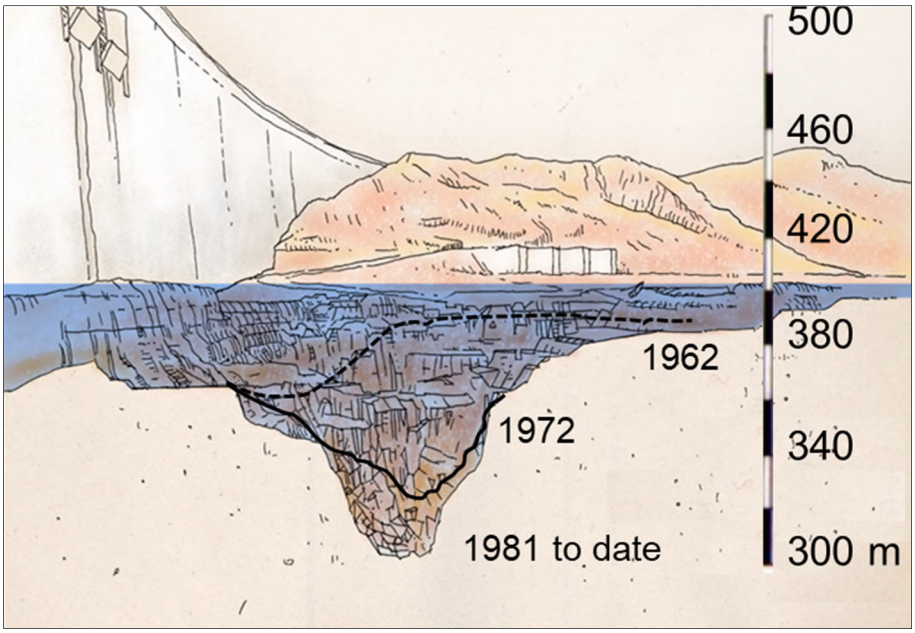

Figure 1.1: Kariba Dam: Plunge pool development (adapted from Bastier, 2018, and Munodawafa & Mhlanga, 2014)

Another example of plunge pool scouring is at the Wivenhoe Dam, situated on the Brisbane River, Australia. During January 2011, the Wivenhoe Dam experienced major flooding that caused significant erosion to the downstream plunge pool (Figure 1.2a). The floods caused a mound of eroded rock to be deposited downstream of the scour hole (Figure 1.2b). Some of the rock boulders were the size of a bus (Figure 1.2c), weighed up to 1200 tons and were lifted and transported 40 m downstream by the floodwaters (Bollaert et al., 2015). The scour hole depth after the January 2011 flood was one-third of the dam height of 33.87 m (full supply level to lip of spillway bucket) (Stratford et al., 2013).

Other examples of dams around the world that illustrate the severe consequences of scouring and show the need to develop adequate rock scour prediction methods include:

- Ricobayo Dam, Spain (Kieffer & Goodman, 2012)
- Bartlett Dam, Arizona (Annandale, 2006).
- Tarbela Dam, Pakistan (Annandale, 2006).
- Cahora Bassa Dam, Mozambique (Bollaert, 2002)
- Maguga Dam, Swaziland (Van Aswegen et al., 2001)
- Awoonga Dam, Australia (Bollaert & Lesleighter, 2014)
- Borumba Dam, Queensland, Australia (Bollaert & Lesleighter, 2014)
- Boondooma Dam, Queensland, Australia (Bollaert & Lesleighter, 2014)
- Burdekin Falls Dam, Australia (Bollaert & Lesleighter, 2014)
- Copeton Dam, Australia (Bollaert & Lesleighter, 2014)
- Julius Dam, Australia (Bollaert & Lesleighter, 2014)

(a) Dam in flood

(b) Downstream scouring

(c) Rock mound size scoured during flood

Figure 1.2: Wivenhoe Dam: January 2011 flood (Bollaert et al., 2015)

1.2. Problem statement

The energy of the jet is dissipated partly due to aeration along the jet trajectory in the air, partly by hydraulic diffusion in the plunge pool, and partly by the bedrock. Dynamic pressures are produced on the bottom of the plunge pool, acting on the water-rock interface, as well as inside the rock joints.

Fluctuating dynamic pressures can scour rock by brittle fracture, fatigue failure and block removal. In cases where large rock formations contain close-ended fissures the rock may scour by brittle fracture or fatigue failure, followed by block removal. In cases where the rock formation consists of rock blocks without close-ended fissures, the blocks may be removed by the actions of average and fluctuating dynamic pressures.

The number, duration and discharge of spilling events cause a scour hole to progressively form in the bedrock, until the equilibrium scour hole dimensions have been reached (Schleiss, 2002). No further block ejection will occur after the equilibrium condition has been reached, since the energy of the jet is sufficiently dissipated along the plunge pool and bedrock.

Most of the existing three-dimensional (3D) numerical models (normally based on the Saint-Venant equations) are capable of two-phase simulation (either water-and-rock or water-and-air). However, they cannot simulate fully three-dimensional models as they use layer-averaged approaches.

Additional knowledge of rock scour mechanisms is required to develop an understanding of the evolution of the scour hole to determine the equilibrium scour hole geometry (scour depth, length, width, and volume) using three-dimensional numerical models.

1.3. Thesis statement and research objectives

Understanding the scour behaviour of the rock downstream of a dam's spillway and determining the extent of the scour hole are of critical importance to ensure the overall safety of the dam and to guarantee the stability of its abutments. As such, the goal of the present research is to "**contribute towards better prediction of the equilibrium geometry of a scour hole in bedrock downstream of a high dam caused by a fully developed rectangular jet plunging into a shallow plunge pool**".

The main objective of this dissertation is therefore to contribute to the knowledge on the prediction of the equilibrium scour hole geometry downstream of high head dams. To realise the primary objective of investigating air-entrainment and hydrodynamic pressures in artificially simulated jointed rock due to high velocity aerated plunging jets, and to mitigate the three-dimensional modelling shortcomings, the following objectives were set:

- An experimental investigation (physical model) of a horizontal issuing jet that plunges into a plunge pool with a simulated fractured movable rock bed layered horizontally and at selected inclinations.
- An investigation of the dynamic pressures of the scour hole floor for different rock joint structure orientations. Other parameters to be observed in the experiments included trajectory of the plunging jet, jet aeration, plunge pool aeration and turbulence, velocity of the wall jets, equilibrium scour hole dimensions, and the time over which the rock was exposed to the action of the jet.
- The derivation of regression formulae based on the physical model results to predict the scour hole dimensions including equilibrium depth, length, width and volume.
- Development of a three-dimensional numerical model that is based on Navier-Stokes equations that include multi-phase flow to determine the rock scour hole dimensions. The model therefore simulated the experimentally measured results by including air entrainment, hydrodynamic parameters and sediment transport.

In summary, this study set out to develop a mathematical model (three-dimensional numerical modelling of hydrodynamic pressures and stream power in a plunge pool), and to evaluate the mechanical methods (scour estimation methods from literature) and physical methods (calibrate physical model results with the mathematical results) in order to determine the equilibrium scour hole geometry for different jointed rock bed materials.

1.4. Delineations and limitations

In this dissertation, the following delineations and limitations apply:

1. Only horizontally issuing *free falling* jets plunging into a pool with an unlined simulated fractured rock bottom were investigated.
2. Only a *single rectangular* plunging jet, and not that of multiple jets, or of circular jets was investigated.
3. The scour characteristics caused by a *fully developed* jet plunging into a *shallow* plunge pool was investigated.
4. The study did *not* investigate *spillway structures* that increase air entrainment, such as Roberts splitters.
5. Only *uniform open-end* rock joints and consequently uniform rock shapes (rectangular) were investigated.
6. Rock scour *without bed protection* was investigated.
7. Only the *equilibrium* scour hole and not the duration of the scour hole evolution was studied.
8. The *strength* of the model rock blocks used in the physical model was *not* simulated and did not fracture in smaller sizes during tests.

1.5. Significance of current study

The scour formation of rock is a complex phenomenon that includes three phases, namely air, water and rock. Over the years, rock scour formation has been assessed by empirical and semi-empirical formulae of which the Erodibility Index Method (EIM) developed by Annandale (2006) is well known. The EIM is based on 150 observations of scour holes, of which 137 observations were from auxiliary earth spillways and not for plunge pool scour (Monfette, 2004).

Bollaert (2002) studied rock scour by assessing dynamic pressures in joints. He developed the Comprehensive Scour Model (CSM), which is based on high velocity plunging jets impinging on one open-end and four closed-end joint geometries in a flat floor bottom. Bollaert (2002) studied the transient pressures in I-shaped and L-shaped rock joints. Further research

was required to assess the dynamic pressures in the joints of a three-dimensional rock joint of a movable rock bed, taking air entrainment into account. Thereafter, Manso (2006) studied the influence of the pool bottom geometry on the transient pressures inside a one-dimensional rock joint. The irregular bed shape used in the study by Manso (2006) was fixed. The exact influence on the turbulent pressures in the rock joints of a continuously changing movable bedrock due to the scour formation could not be accounted for. Federspiel (2011) used an embedded three-dimensional rock block in a plunge pool with a perfectly flat bottom in order to improve the representation of the bedrock. Duarte (2014) studied the influence of air entrainment of high velocity jets on the scour phenomenon in fractured rock. The current research endeavours to contribute to the knowledge and understanding air-water-rock interaction in predicting the equilibrium scour hole geometry. Thus, the dynamic pressures were analysed for a movable bedrock that could change continuously due to the scour formation with three-dimensional rock joints that are interconnected, and taking air entrainment into account of a free falling jet discharging from a horizontal spillway. Table 1.1 summarises the abovementioned rock scour research investigations, and indicates the studies' focus area.

Table 1.1: Research investigations conducted on rock scour with focus area

Bollaert (2002)	**Manso (2006)**	**Federspiel (2011)**	**Duarte (2014)**	**Current research**
Joint fracturing and block uplift	Pool geometry	Block response	Influence of air entrainment	Plunging jet and rock joint network
1D and 2D closed-end and open-end joints Flat bed	1D closed-end joint Fixed bed	3D block geometry Flat bed	3D block geometry Air entrainment Flat bed	3D block geometry Movable bed Joint angle Air entrainment
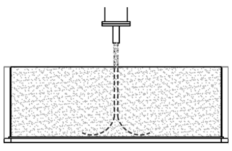	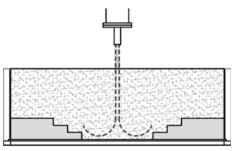	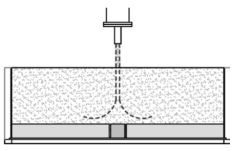	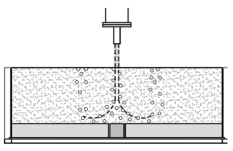	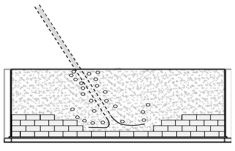

In the current study, the rock mass was represented by multiple blocks. These formed a network of joints, which is similar to a real case scenario. It is expected that the joint network will have an influence on the pressure wave reflections. The research also studied the scour hole geometry formed by a plunging jet issued from a horizontal canal, and compared this to

the previous research that studied rock scour due to high velocity jets discharged from a nozzle. The jet impinging angle with the plunge pool water surface ranged between 56° and 75°, corresponding to the natural angle of free falling water.

The intention of the current research is also to contribute towards the development of a numerical model to simulate the irregular scour shape by means of a three-dimensional model, to determine the equilibrium scour hole geometry shape in bedrock, and not just predict the maximum scour depth. As such, the proposed research, as described above, will contribute significantly towards improving the hydraulic design of high head spillways.

1.6. Methodology

The following methodology was followed to achieve the research objectives:

1. Undertake a literature review of rock scouring prediction methods (empirical and physically-based) and numerical modelling in the two-phase (water and air) approach.
2. Conduct rock scour laboratory tests by means of physical modelling and derive formulae representing the data at full prototype scale to enable prediction of scour hole dimensions with these formulae and to calibrate the numerical model.
3. Develop a three-dimensional numerical multi-phase model and calibrate it with the physical model data for application in the range of the physical model data.
4. Compare the proposed three-dimensional numerical model against the published rock scour methods in terms of scour hole geometry prediction in rock bed material.

1.7. Dissertation outline

The dissertation consists of four parts and a total of seven sections as shown in Figure 1.3.

The dissertation starts by explaining the rock scour formation process in Section 2, and goes on to cover the relevant literature regarding the commonly used scour prediction methods used to determine the ultimate depth of the scour hole in Section 3. Section 4 discusses the numerical approach used by existing numerical models, and presents the principles of the proposed numerical model for rock scour due to plunging jets.

The research design, methodology and results of the physical model are dealt with in Section 5, which also discusses the regression analysis and comparison with the published scour prediction methods.

Section 6 presents the development of the numerical model for fixed bed simulations, including the calibration of the numerical models. The results of the numerical models are compared

with the physical model results in the second part of Section 6. Section 5 and Section 6 form the core of the dissertation and describe the observed phenomena in detail.

Section 7 highlights the main conclusions on the rock scour prediction method and proposes future research.

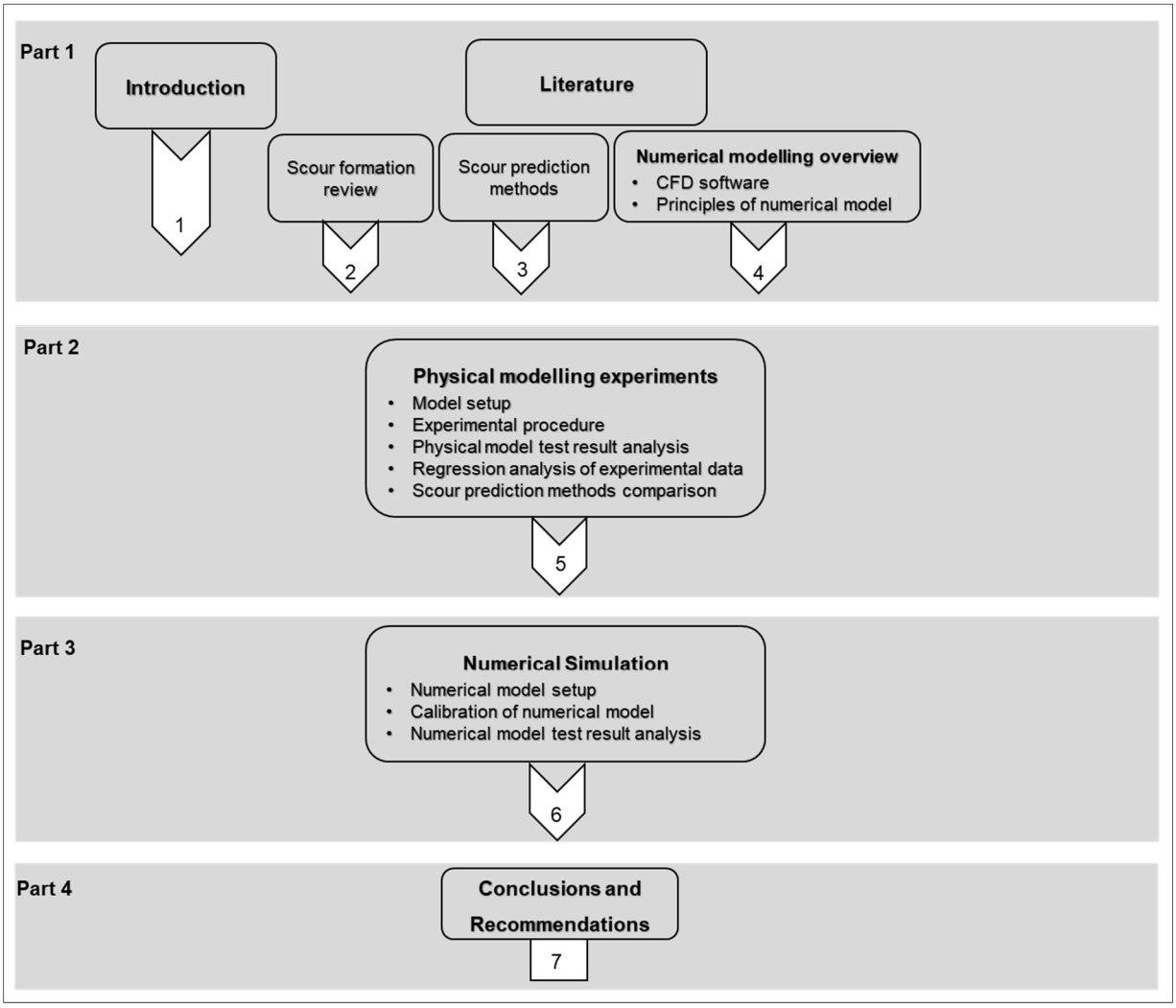

Figure 1.3: Dissertation outline

2. LITERATURE REVIEW OF SCOUR FORMATION

2.1. Background

Spillways release excessive flood discharges and are one of the primary safety structures of a dam. The design of many high head dams include a plunging jet impinging into a plunge pool and onto the underlying bedrock. A scour hole will form if the erosive capacity of the water exceeds the resistance potential of the rock. The foundation of the dam could be undermined if the scour hole dimensions becomes excessive. Thus, the estimation of the equilibrium scour hole dimensions is important to ensure the dam is not endangered by the scour hole during its lifetime.

Rock scour downstream of a dam is a complex physical process and a complete understanding of the air-water-rock phase interaction in the scouring process is required. Scouring downstream of a dam due to high velocity plunging jets is governed by three phase flow (Figure 2.1), namely the gas phase (air), the liquid phase (plunging jet and plunge pool) and the solid phase (bedrock). A theoretical background on each of these phases, as well as the interaction between the phases is presented in this section.

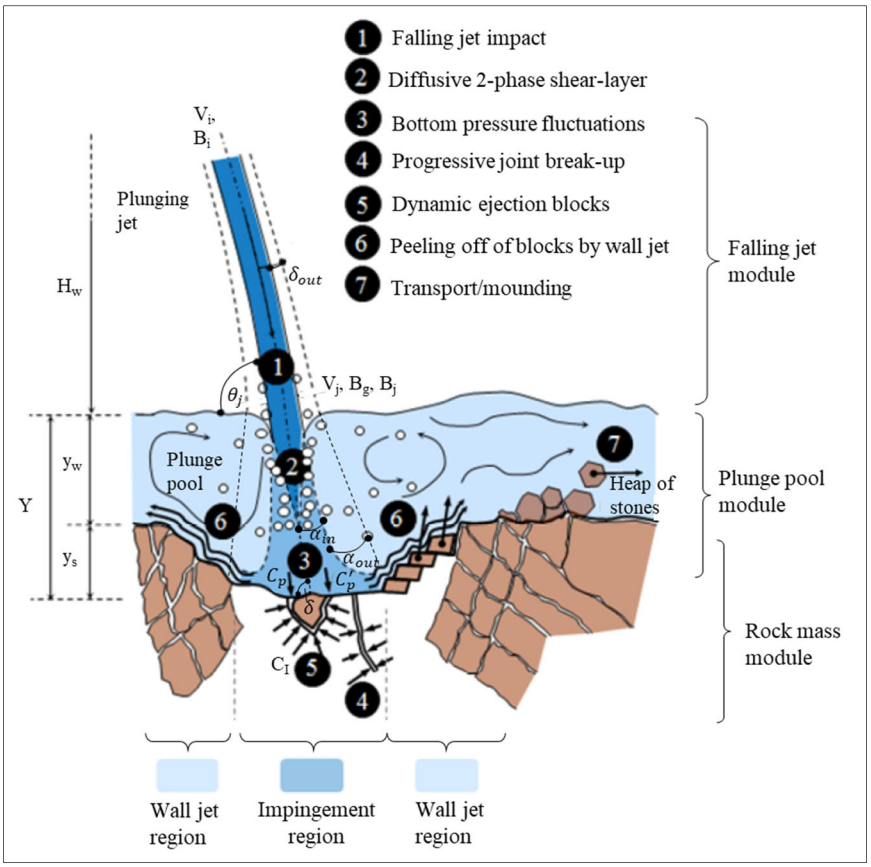

Figure 2.1: Impacting water jet stages in pool and on rock bed, and rock scouring mechanisms (adapted from Bollaert & Lesleighter, 2014)

2.2. Spillway types

Various types of spillways are used to issue excess flood water by means of plunging jets to the river downstream. The main spillway types that create plunging jets are discharge over ogee shaped arch dam crests, ski-jumps or flip-buckets, and pressurised, controlled and uncontrolled spillways.

A plunging jet can be either circular or rectangular depending on the issuance conditions, for example the spillway or sluice gate geometry (Hoffmans, 1998). A rectangular jet diffuses laterally as it falls through the air with a horseshoe shape footprint when impinging with the water surface of the plunge pool. Circular jets diffuse more radially and symmetrically. Bollaert and Schleiss (2003a) and Borghei and Zarnani (2008) found that the pressure fluctuations at the plunge pool floor are greater for rectangular jets than for circular jets. The reason is due to the non-symmetrical diffusion of a rectangular jet. However, when the cross-sectional average velocity for various jet geometries was considered, it was found that the cross-sectional effects were relatively small (Pagliara et al., 2004).

2.3. Plunging jet geometry

The geometric properties of a plunging jet are illustrated in Figure 2.2 and are discussed in this section.

The behaviour of the jet as it falls through the air for ski-jumps or free surface weirs is dependent on the fall height (H_w), and the jet's behaviour for pressure outlets is dependent on the net energy head ($H_w = H_b - t_0$). The behaviour of the jet falling through the air is also dependent on the issuance velocity (V_i) and discharge, air entrainment, initial turbulence intensity (T_u), issuance angle (θ_i), and cross-section (D_i for a circular jet and B_i the thickness of a rectangular jet) of the jet at issuance (Van Aswegen et al., 2001). The jet trajectory and energy at impingement with the plunge pool surface are reliant on the issuance velocity (V_i). As the jet falls through the air, the core contracts as the velocity increases due to gravity and the outer edge expands due to initial turbulence intensity (T_u) (Manso et al., 2008). The jet experiences additional diffusion when it plunges through the pool.

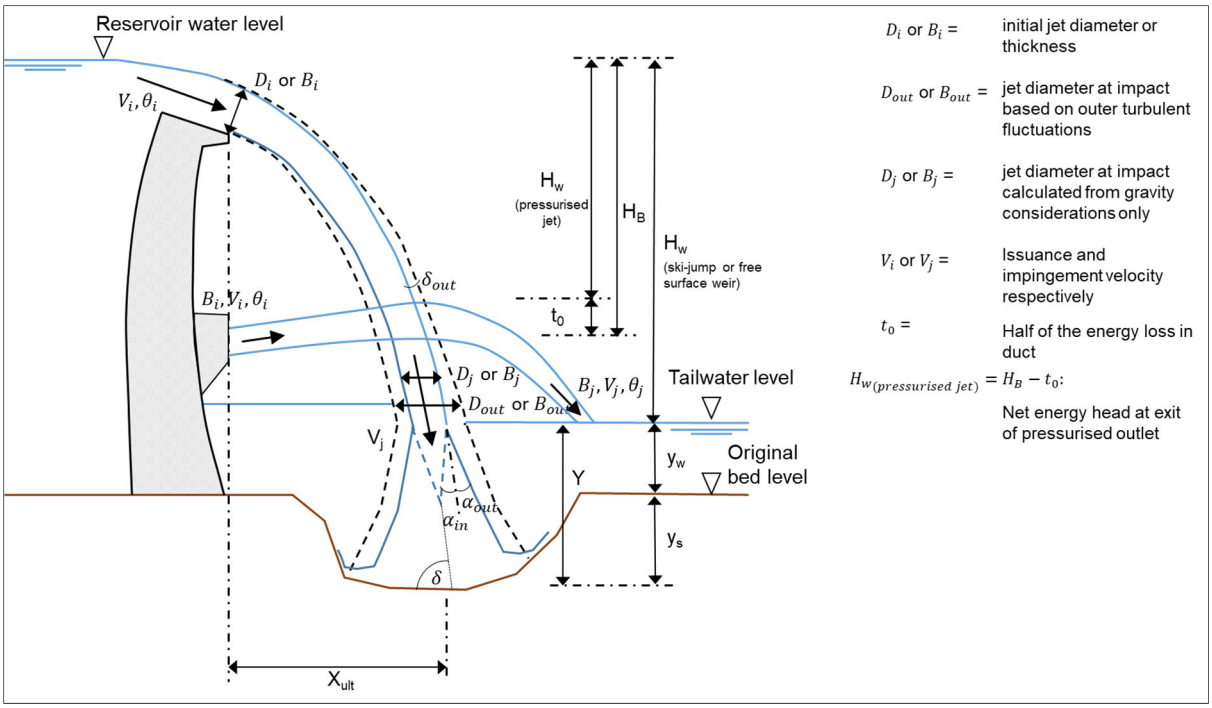

Figure 2.2: Plunging jet geometry

2.3.1. *Initial turbulence intensity*

The initial jet turbulence intensity (T_u) of the jet is the main parameter governing the deformation of the jet as it travels through the air (Ervine & Falvey, 1987). Thus, the initial turbulence intensity defines the rate the jet increases in lateral spread, distortion and the contraction of the core. Ervine (1998) and Zhu et al. (2000) proved that the turbulence intensity of the jet greatly influences the formation of jet surface disturbances, which effects air entrainment.

The initial turbulence intensity is defined by Equation 2.1 (Bollaert, 2002).

$$T_u = \frac{u'}{U} \qquad \textit{Equation 2.1}$$

where

T_u = initial turbulence (%)
u' = instantaneous root mean square (RMS) value of axial velocity fluctuations (m/s)
U = mean velocity (m/s)

The initial turbulence intensity (T_u) influences the root mean square values of the fluctuating pressures at the water-rock interface in the plunge pool that relates to the peak pressures experienced inside the rock joints (Bollaert, 2002).

Table 2.1 shows the initial turbulence values for typical spillway configurations. Ervine and Falvey (1987) determined the initial turbulence for turbulent jets to be between 5-8%, and for smooth jets to be between 1-2%. Annexure A summarises the hydraulic characteristics, such as initial turbulence intensity, for different spillway types.

Table 2.1: Initial turbulence for various spillway types (Manso et al., 2008)

Spillway Type	Initial Turbulence (T_u)
Free overfall or nappe flow	<3%
Orifice jets/bottom outlet/outflow under pressure	3% to 8%
Flip bucket/ski-jump jets	3% to 5%

Castillo (2007) proposed estimating the initial turbulence at issuance for a nappe flow case as follows:

$$T_u = \frac{q}{IC}^{0.43} \qquad \textit{Equation 2.2}$$

where q represents the unit discharge (m^3/s/m) and IC the initial conditions of flow at issuance, as determined by Equation 2.3.

$$IC = \frac{14.95g^{0.5}}{K^{1.22}C_d^{0.19}} \qquad \textit{Equation 2.3}$$

with the discharge coefficient C_d approximately 2.1 and coefficient K = 0.85. An initial turbulence value of 1.2% was proposed by Castillo et al. (2015) for prototype spillway nappe flow for unit discharges greater than 0.25 m^3/s/m.

2.3.2. *Jet trajectory*

Calculating the jet trajectory indicates the impingement location. The trajectory of a plunging jet issuing from a spillway is calculated with Equation 2.4 (Wahl et al., 2008). The edge of the spillway crest acts as the origin of the x-y coordinate system.

$$z = xtan\theta_i - \frac{x^2}{4h_v(cos\theta_i)^2} \qquad \textit{Equation 2.4}$$

where

z: vertical distance (m)

x: horizontal distance along jet trajectory (m)

θ_i: issuance angle from horizontal (degrees), positive if the jet is initially inclined upward and negative if the jet issues downward.

h_v: velocity head (m): $h_v = \frac{V_i^2}{2g}$

V_i: issuance jet velocity (m/s)

2.3.3. *Jet regions*

A jet plunging through the air can be categorised into an undeveloped jet region and developed jet region.

Plunging jets in the undeveloped region comprise a solid (compact) core of non-aerated water that is surrounded by a shell of aerated water as depicted in Figure 2.3 (Monfette, 2004). An undeveloped jet has a high rock scour potential, since the solid core of water that impinges on the rock preserves the erosive power of the water. As the jet travels through the air, the solid water core contracts in width (Lewis et al., 1999).

If the plunging jet travels a sufficient distance through the air and/or travels through a deep enough plunge pool, the core loses its coherence and breaks up completely, becoming a developed jet. A developed jet lacks a solid water core and comprises a conglomeration of individual water particles as illustrated by Figure 2.3. The erosive power of a developed jet is less than for an undeveloped jet, due to the absence of a solid water core (Lewis et al., 1999).

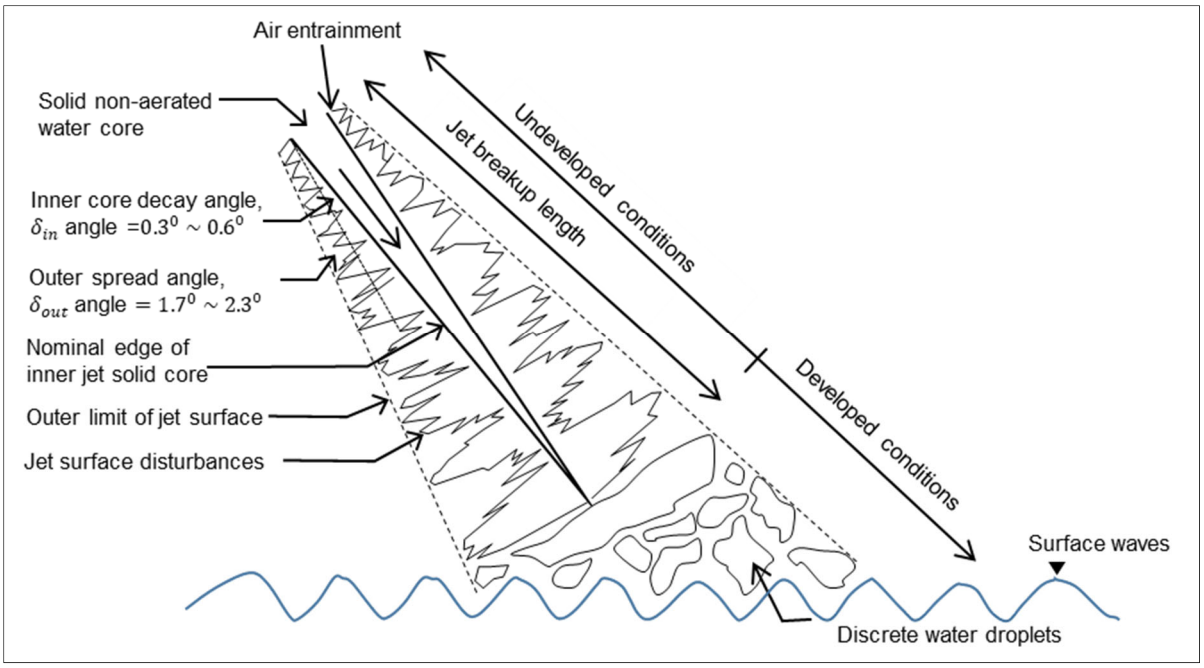

Figure 2.3: Falling jet regions (adapted from Monfette, 2004)

2.3.4. *Breakup length*

Comparing the jet trajectory and breakup length (L_b) determines the state of development of the plunging jet when it plunges into the pool. The state of the jet could be undeveloped or developed. If the breakup length is less than the trajectory length, the jet would be completely developed when impinging with the tailwater level. Thus, the breakup length could be defined as the length over which an undeveloped jet changes to a developed jet (Castillo et al., 2015).

The jet breakup length is dependent on the initial discharge, initial turbulence (T_u), initial jet geometry and air entrainment (Bollaert, 2002). A high initial turbulence would result in a shorter breakup length, due to the turbulent surface disturbances penetrating the jet core quicker. Noret et al. (2012) published the breakup length results of different researchers for various unit discharges (q). The results indicate that the jet breakup length increases with an increase in the unit discharge. The results also indicate that the jet breakup length of a rectangular nappe jet is less than that of a circular jet for the same unit discharge, proving that rectangular nappe jets are less compact than circular jets. Also, flip buckets, followed by deflectors, have a tremendous impact on the jet breakup by shortening the jet breakup length, which is very beneficial in the design.

Table 2.2 lists the relationships that describe the breakup lengths for rectangular nappe and circular jets derived by different researchers. The jet breakup length induced by deflectors and flip buckets are much shorter than for rectangular nappe jets and are also listed in Table 2.2.

Table 2.2: Breakup length equations

Jet geometry	Breakup length (L_b)	Turbulence intensity	Authors	Equation Number
Rectangular Nappe Jet	$L_b = 6q^{0.32}$	-	Horeni (1956)	*Equation 2.5*
	$L_b = \frac{0.85 B_i {Fr_i}^2}{(1.07 T_u {Fr_i}^2)^{0.82}}$ $Fr_i = \frac{V_i}{\sqrt{g B_i}}$ where B_i and Fr_i are the jet thickness and Froude number at issuance respectively, and T_u calculated using Equation 2.2.	$0 \leq T_u \leq 3\%$	Castillo (2007)	*Equation 2.6* *Equation 2.7*
Deflectors	$\frac{L_b}{B_i} = 74 Fr_i^{-1}(1+\tan\alpha)^{-0.5}(1+\sin\varphi)$ for $7 < \frac{L_b}{B_i} < 20$ where α is the deflector angle relative to the chute bottom, and φ the chute bottom angle relative to the horizontal.	-	Pfister & Hager (2009)	*Equation 2.8*
Flip buckets	$\frac{L_b}{B_i} = 76 Fr_i^{-1}(1+\tan\delta)^{-4}(1+\sin\varphi)$ $\tan\delta = (1-\cos\beta_a)/\sin\beta_a$ where δ is the equivalent deflector angle and β_a the total deflection angle.	-	Pfister et al. (2014)	*Equation 2.9* *Equation 2.10*
Circular Jet	$L_b = 60Q^{0.39}$	0.3%	Ervine et al. (1980), as cited by Annandale (2006)	*Equation 2.11*
	$L_b = 17.4Q^{0.31}$	3%	Ervine et al. (1980), as cited by Annandale (2006)	*Equation 2.12*
	$L_b = 4.1Q^{0.20}$	8%	Ervine et al. (1980), as cited by Annandale (2006)	*Equation 2.13*
	$L_b = 1.7\frac{We}{(10^{-4}Re)^{5/8}}$ with We the Weber number $\left(We = \frac{\rho {V_i}^2 D_i}{\sigma}\right)$ and the surface tension of water $\sigma \approx 0.073\ N/m$.	3%	Baron (1949), as cited by Annandale (2006)	*Equation 2.14*

Jet geometry	Breakup length (L_b)	Turbulence intensity	Authors	Equation Number
Circular Jet	with $\frac{L_b}{D_i {Fr_i}^2} = \frac{1.05}{C^{0.82}}$ $C = 1.14 T_u {Fr_i}^2$	-	Ervine et al. (1997)	*Equation 2.15* *Equation 2.16*
	$L_b = 50D_i \; to \; 100D_i$	3-8%	Ervine & Falvey (1987), as cited by Annandale (2006)	*Equation 2.17*

Q corresponds to the water discharge (m^3/s), where the unit discharge per width (m^3/s per meter) is given by q. The jet diameter at issuance is represented as D_i and Re is the Reynolds number.

2.3.5. *Plunging jet dimensions and velocity*

The jet entrains air as it falls through the air, resulting in the lateral spread (expansion) and distortion of the jet. Knowledge of the jet spread allows calculation of the jet footprint size at impingement with the bedrock surface where severe pressure and scour damage might occur (Bollaert, 2002).

Ervine and Falvey (1987) and Ervine et al. (1997) determined that the lateral spread of a circular jet (δ_{out}) and the jet trajectory length (X) are related to the turbulence intensity (T_u) as follows:

$$\frac{\delta_{out}}{X} = 0.38 T_u \qquad \textit{Equation 2.18}$$

where

δ_{out}: lateral outspread of jet (m)
X: distance along jet (m)
T_u: initial turbulence (Equation 2.1)

The typical outer spread of turbulent circular jets ($\frac{\delta_{out}}{X}$) is between 3% and 4%, which is equivalent to 1.7º to 2.3º (Bollaert, 2004). The angle of the decaying core is generally smaller than the lateral spread angle. The core contraction ($\frac{\delta_{in}}{X}$) is typically 15% to 20% of the outer spread, which is in the order of 0.5% to 1%, thus 0.3º to 0.6º (Ervine & Falvey, 1987) as illustrated in Figure 2.3.

The outer diameter (D_{out} for circular jets) and outer thickness (B_{out} for rectangular jets) of the jet at impact with the bedrock indicates the maximum area where severe scour and pressure

damage could occur at the water-rock interface as indicated in Figure 2.2. The outer diameter or thickness of the jet is determined by adding the lateral spread of the jet to the issuance jet diameter or thickness (D_i or B_i) (Bollaert, 2002).

According to Annandale (2006), by taking the outer jet spread (δ_{out}/X) into account, the outer diameter of a circular jet (D_{out}) could be calculated as:

$$D_{out} = D_i + 2\frac{\delta_{out}}{X}L_j \qquad \textit{Equation 2.19}$$

where D_i is the jet diameter at issuance (m) and L_j the trajectory length (m).

Ervine et al. (1997) proposed Equation 2.20 to calculate the outer diameter of a circular jet by making use of an estimate of the jet spread (ε) for issuance velocities $V_i \geq \frac{0.275}{Tu}$.

$$D_{out} = D_i\sqrt{\frac{V_i}{V_j}} + 2\varepsilon \qquad \textit{Equation 2.20}$$

$$\varepsilon(jet\ spread) = \frac{1.14T_uV_i^2}{g}\left[\sqrt{\frac{2L_j}{D_i{Fr_i}^2} + 1} - 1\right] \qquad \textit{Equation 2.21}$$

Bollaert (2002) proposed an equation to calculate the outer diameter of a circular jet by making use of the jet diameter at issuance (D_i) and the jet trajectory length (L_j), expressed as follows:

$$D_{out} = D_i + 2 \cdot (0.03\ to\ 0.04)L_j \qquad \textit{Equation 2.22}$$

Ervine et al. (1997) proved that the diameter (D_j) of a circular jet at impact with the tailwater level could be expressed as

$$D_j = D_i\sqrt{\frac{V_i}{V_j}} \qquad \textit{Equation 2.23}$$

where

D_i: jet issuance diameter (m)
V_i issuance velocity (m/s)
V_j: impact velocity with the tailwater level (m/s) (refer to Equation 2.29)

The core width for rectangular nappe jets (B_g) at impact with the water surface of the plunge pool could be determined with Equation 2.24 (Puertas & Dolz, 2005, and Castillo et al., 2015).

$$B_g = \frac{q}{\sqrt{2gH_w}} \qquad \textit{Equation 2.24}$$

where B_g is the core width of a rectangular jet (m), q the unit discharge (m²/s), and H_w the fall/drop height (m).

Castillo et al. (2015) proposed Equation 2.25 to calculate the thickness of a rectangular nappe jet (B_j) at impingement with the plunge pool water surface.

$$B_j = B_g + 2\xi = \frac{q}{\sqrt{2gH_w}} + 4\,\varphi\sqrt{B_i}\left(\sqrt{2H_w} - 2\sqrt{B_i}\right) \qquad \textit{Equation 2.25}$$

where B_i and B_g are the issuance depth and core thickness (m) at impact with the plunge pool respectively, ξ the lateral jet spread distance (m), q the unit discharge (m²/s), H_w the fall height (m), and $\varphi = K_\varphi T_u$. The experimental parameter K_φ is 1.14 for circular jets and 1.24 for nappe flow (Castillo & Carrillo, 2017).

The jet impinging thickness (B_j) of a deflector jet can be obtained by subtracting the maximum longitudinal location of the upper jet trajectory (x_{UM}) from the longitudinal location of the lower trajectory (x_{LM}). Pfister and Hager (2009) found that the issuance Froude number and deflector angle relative to the chute bottom (α) are the dominant parameters concerning the deflector jet locations. The longitudinal locations of the maximum upper and lower deflector jet trajectory are calculated with Equation 2.26 and Equation 2.27, respectively.

$$\frac{x_{UM}}{B_i} = 0.58 \times Fr_i^2(\tan\alpha)^{0.6} \cdot \left(\frac{t}{B_i}\right)^{0.2} \cdot (1+\sin\varphi)^{0.5} \qquad \textit{for } 0 < \frac{x_{UM}}{B_i} < 26 \qquad \textit{Equation 2.26}$$

$$\frac{x_{LM}}{B_i} = 0.45 \times Fr_i^2(\tan\alpha)^{0.6} \cdot \left(\frac{t}{B_i}\right)^{0.2} \cdot (1+\sin\varphi)^{0.5} \qquad \textit{for } 0 < \frac{x_{LM}}{B_i} < 22 \qquad \textit{Equation 2.27}$$

with t the deflector height (m) and φ the chute bottom angle relative to the horizontal (degrees).

The jet trajectory from a flip bucket can be considered to determine the impingement jet thickness (B_j). The maximum longitudinal location considered for flip bucket jet trajectories may be derived from Equation 2.28 according to the horizontal coordinate system.

$$\frac{x'}{x'_M} = \frac{2x'}{B_i Fr_i^2 \sin(2\alpha_j)} \qquad \textit{Equation 2.28}$$

where x' is the horizontal streamwise coordinate (m), x'_M is the maximum horizontal streamwise coordinate (m) and α_j is the virtual jet take-off angle (degrees).

The impact velocity of a plunging jet (V_j) is essential for quantifying the erosion potential of the jet. Ervine and Falvey (1987) theorised that air drag has a negligible effect upon the impact velocity of the solid core of a jet. The impact velocity (V_j) of a solid core of a plunging jet (undeveloped) at impingement with the tailwater level could be calculated as

$$V_j = \sqrt{{V_i}^2 + 2gH_w} \qquad \textit{Equation 2.29}$$

where V_i is the issuance jet velocity (m/s), and H_w is the fall height (Z in other literature) (m).

Lewis et al. (1999) determined that the impact velocity for a developed jet (core fully disintegrated) could be determined as follows:

$$V_j = \sqrt{{V_i}^2 + 2gH_w} - \sqrt{3C_d \left(\frac{\rho_a}{\rho_w}\right)\left(\frac{H_w}{d}\right){V_i}^2} \qquad \textit{Equation 2.30}$$

where

C_d: drag coefficient of a water particle (refer to Equation 2.31 and Figure 2.4)
ρ_a: density of air (1.29 kg/m^3)
ρ_w: water density (998.2 kg/m^3)
d: diameter of a sphere with the same volume as a water particle (m)

The particle drag coefficient (C_d) in Equation 2.30 is reliant on the Reynolds number (Re) of the water particle and is obtained from Figure 2.4. The Reynolds number is calculated with Equation 2.31 (Lewis et al., 1999).

$$Re = \frac{V_i d}{\nu} \qquad \textit{Equation 2.31}$$

where ν is the kinematic viscosity of water (1 x 10^{-6} m^2/s).

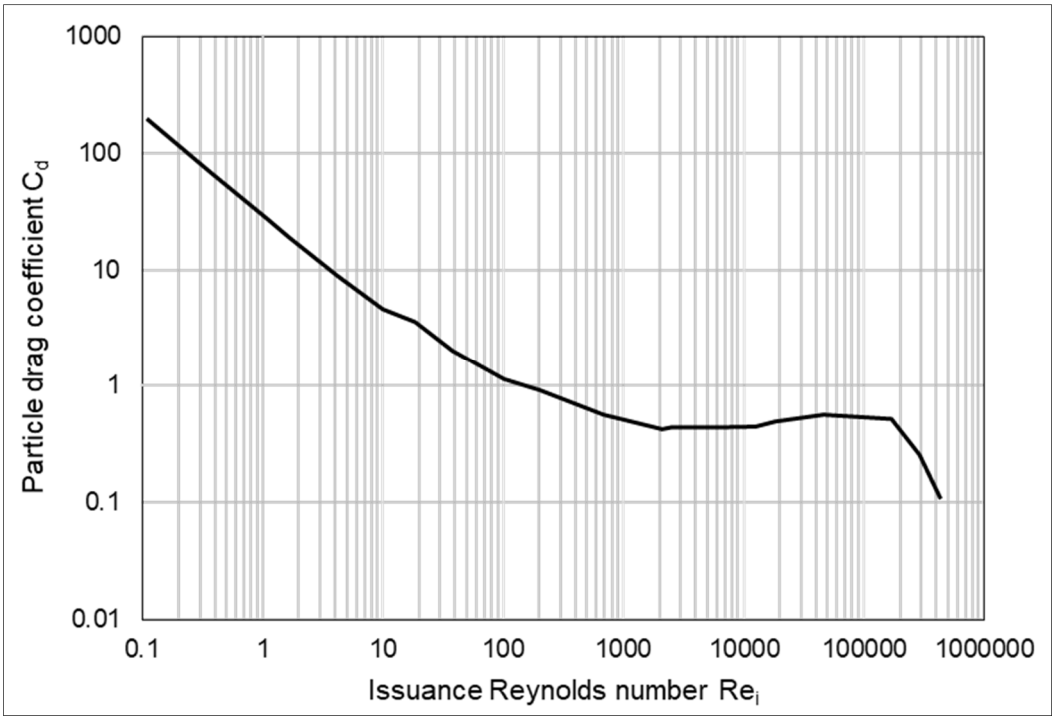

Figure 2.4: Coefficients of drag for spheres (Binder (1962) as cited in Lewis et al. (1999))

The submerged trajectory length in the plunge pool is dependent on the impingement angle (θ_j). The angle of the plunging jet to the horizontal plunge pool water level is calculated in degrees as follows (Wahl et al., 2008):

$$\theta_j = arctan\left[tan\theta_i - \frac{x}{2h_v(cos\theta_i)^2}\right](-1) \qquad \textit{Equation 2.32}$$

where

θ_i: issuance angle (degrees - positive if jet issues upwards, negative if downwards)

x: horizontal distance to point of impact (m)

h_v: velocity head (m): $h_v = \frac{V_i^2}{2g}$

V_i: issuance velocity (m/s)

g: gravitational acceleration (9.81 m/s^2)

Hoffmans (1998) suggested that the angle of a near-vertical jet at impact could be ignored, since the change in the scour hole geometry is marginal for impact angles between 60º - 90º. However, Kerman-Nejad et al. (2011) found that the fluctuating and mean pressures at the plunge pool floor are higher for greater jet impact angles, and that the maximum pressures occur when the impact angle is 90°.

2.4. Plunge pool geometry

2.4.1. *Jet diffusion in plunge pool*

The jet continues to break up in the plunge pool by means of diffusion until it impinges on the bedrock (Van Aswegen et al., 2001). Manso et al. (2008) studied the behaviour of the jet as it travels through the plunge pool. The jet impingement velocity (V_j), impact angle (θ_j) and turbulence when entering the plunge pool surface (Manso et al., 2008), as well as the plunge pool depth (Y) and geometry (Manso et al., 2009) determine the amount of energy that would be dissipated and how much of the jet core remains intact at impact with the bedrock. The higher the turbulence of the jet at impact with the tailwater level, the faster the jet core would diffuse and disintegrate (Manso et al., 2008).

The jet's scour potential reduces if the fluctuating pressures at the water-rock interface are limited by favourable plunge pool geometries (Bollaert et al., 2012b). The plunge pool acts as a water cushion by damping the scouring (Van Aswegen et al., 2001). Physical model tests have proved that the maximum scour hole depth is obtained with a low tailwater level and with continuous removal of the mound of eroded rock (Pagliara et al., 2006). Lencastre (quoted in Whittaker & Schleiss, 1984) observed that scouring would increase as the plunge pool depth increases up to a critical depth, whereafter the scouring would decrease as the plunge pool depth increases beyond this critical value. This phenomenon is attributed to the strength of current recirculating in the plunge pool (Bollaert, 2002).

The outer dimension of the jet expands progressively and the core of the jet contracts with a constant velocity profile as the jet travels through the plunge pool (Bollaert & Schleiss, 2003a). Ervine and Falvey (1987) studied the diffusion of circular jets in a plunge pool and found that the jet core contraction angle differs to the expansion angle of the outer jet boundary. The contraction angle of a jet travelling through a plunge pool is a function of the jet conditions, i.e. a laminar or a turbulent jet. Figure 2.5 illustrates the diffusion angle of circular jets in a plunge pool for highly turbulent jets with high air entrainment concentrations. The inner core diffusion angle (α_{in}) of highly turbulent plunging circular jets when travelling through a plunge pool is approximately 8º, whereas the outer expansion angle could increase to up to 15º (α_{out}).

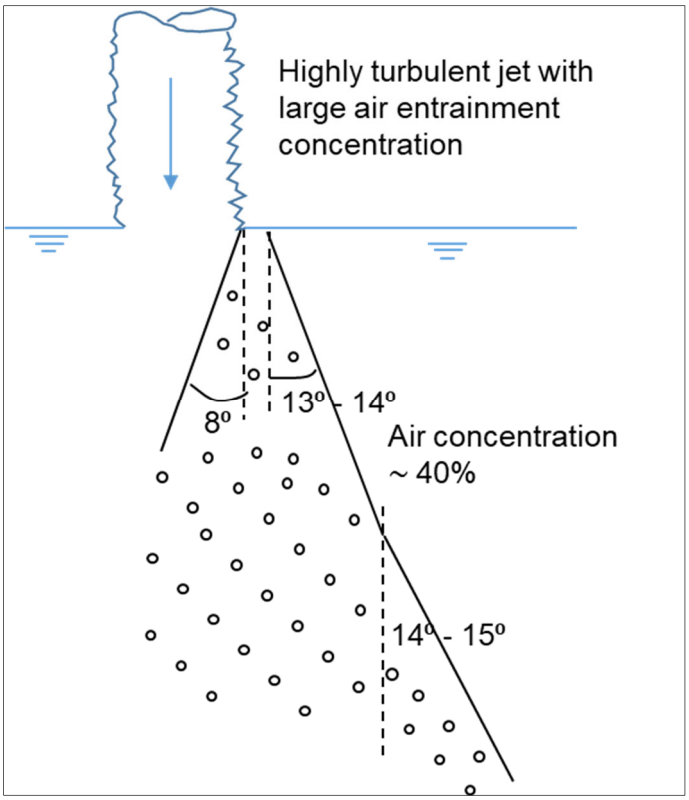

Figure 2.5: Diffusion of a highly turbulent circular jet in a plunge pool (adapted from Ervine & Falvey, 1987)

As discussed in Section 2.3.3, a jet plunging through the atmosphere can be classified either as an undeveloped (core intact) or developed jet. The character of the jet at impingement with the tailwater level largely determines how the energy of the jet will be dissipated in the plunge pool. When the plunge pool depth to jet diameter/thickness is less than five to six ($Y/D_j < 5{\sim}6$) the plunge pool is deemed to be shallow (Bollaert & Schleiss, 2003b). The jet directly impacts the pool bed and forms a hydraulic jump downstream of the impingement point. A hydraulic jump can also form upstream of the impingement point, depending on the jet impingement angle. Therefore, the reduction in the mean dynamic pressure coefficient is due to energy losses experienced as the jet falls through the atmosphere due to diffusion. Very little energy losses occur in a shallow plunge pool and the bedrock is directly exposed to the forces of the jet.

For Y/D_j ratios greater than 6, the plunge pool is deemed to be deep and the reduction in the mean dynamic pressure coefficient is due to the turbulence in the deep plunge pool (Bollaert & Schleiss, 2003b). The impact of the jet on the bedrock of a deep plunge pool would generate large, fluctuating pressures with low mean values at the water-rock interface compared to a jet plunging through a shallow pool (Bollaert, 2002).

2.4.2. *Quantifying dynamic pressures in plunge pool*

The dynamic pressures generated on the plunge pool bottom are a function of the plunging jet's turbulence intensity (T_u), the impact diameter D_j (circular jets) or thickness B_j (rectangular jets), the trajectory length (L_j) and the plunge pool depth (Y). The dynamic pressures comprise two components, namely the mean and fluctuating dynamic pressures. The total dynamic pressure (P_{max}) is expressed as (Annandale, 2006)

$$P_{max} = \left(C_p + C_p'\right)\gamma\phi\frac{V_j^2}{2g} \qquad \textit{Equation 2.33}$$

with C_p the mean dynamic pressure coefficient, C_p' the fluctuating dynamic pressure coefficient, and ϕ a kinetic energy velocity coefficient often assumed as 1.

The mean dynamic pressure coefficient C_p decreases with an increase in air content in the plunge pool. The maximum C_p-value attained for jets plunging through a deep pool is 0.8 ~ 0.9 instead of 1 due to aeration and jet spreading effects that cause energy losses (Bollaert & Schleiss, 2003a). Bollaert (2002) found that the mean dynamic pressures on the pool bottom become insignificant for Y/D_j ratios greater than 10, whereas Annandale (2006) found that the mean dynamic pressures become insignificant for $Y/D_j > 20$. The mean dynamic pressures become insignificant in deep plunge pools due to the fluctuating dynamic pressure coefficient obtaining a maximum value at approximately $Y/D_j = 5{\sim}6$ for intact jets, namely for a jet breakup ratio (L_j/L_b) less than 1.

A more significant decrease in C_p-values with Y/D_j can be observed for circular jets than for rectangular jets. A possible reason may be that diffusion occurs radially (every direction) for circular jets instead of laterally for rectangular jets (Bollaert, 2002).

Ervine et al. (1997) determined that the mean dynamic pressure coefficient C_p for circular jets is a function of Y/D_j expressed by Equation 2.34 and Equation 2.35.

For $Y/D_j \leq 4$ (shallow pool):

$$C_p = 0.85 \qquad \textit{Equation 2.34}$$

For $Y/D_j > 4$ to 6 (deep pool):

$$C_p = 38.4(1-\alpha_i)\cdot\left(\frac{D_j}{Y}\right)^2 \qquad \textit{Equation 2.35}$$

with α_i the air concentration at impact with the tailwater level defined by Equation 2.46 in Section 2.5.1.3.

Castillo et al. (2015) determined that the mean dynamic pressure coefficient (C_p) for rectangular jets is a function of the pool depth to jet thickness ratio (Y/B_j) and the fall height to jet breakup length ratio (H_w/L_b). Castillo et al. (2017) assumed that the jet becomes developed for a Y/B_j ratio greater than 5.5, as opposed to 4 for circular jets. The mean dynamic pressure coefficient (C_p) for rectangular nappe jets can be expressed as (Castillo et al., 2015):

For $Y \leq 5.5B_j$ (shallow pool):

If $H_w/L_b < 1$:

$$C_p = 1 - 0.0014e^{5.755(H_w/L_b)} \qquad \textit{Equation 2.36}$$

If $H_w/L_b \geq 1$:

$$C_p = 14.643e^{-3.244(H_w/L_b)} \qquad \textit{Equation 2.37}$$

For $Y > 5.5B_j$ (deep pool):

$$C_p = ae^{-b\left(\frac{Y}{B_j}\right)} \qquad \textit{Equation 2.38}$$

where a and b are constant parameters presented in Table 2.3.

Castillo et al. (2018) proposed updated formulae and parameters for determining the mean dynamic pressure coefficient for rectangular jets (C_p). However, the experimental data from the current study agreed better with the formulae and parameters presented previously by Castillo and Carrillo (2017) (listed above) compared to the new formulae and parameters presented in Castillo et al. (2018).

Table 2.3: C_p coefficient parameters for rectangular jets for $Y > 5.5B_j$ (Castillo et al., 2017)

H_w/L_b	a	b
≤ 0.85	2.5	0.20
0.9-1.00	1.70	0.18
1.00-1.10	1.35	0.18
1.10-1.20	1.05	0.18
1.20-1.30	0.88	0.18
1.30-1.40	0.39	0.15
1.40-1.60	0.24	0.14
≥ 1.60	0.14	0.12

The fluctuating component of the dynamic pressures in a plunge pool is affected by the initial turbulence (T_u), degree of jet breakup (H_w/L_b) and air content. Ervine et al. (1997) proved that the fluctuating dynamic pressure coefficient (C_p') for circular jets reaches a maximum for a jet breakup length ratio of 0.7 and reduces to approximately zero when the jet breakup length ratio is greater than 2.

Bollaert (2002) developed a third order polynomial regression function (Equation 2.39) to quantify the fluctuating dynamic pressure coefficient (C_p') of circular jets for $Y/D_j \leq 20$. For $Y/D_j > 20$, a C_p'-value of 0.05 is proposed. However, the assumption that the C_p'-value converges to 0.05 can lead to a condition where the applied stream power in the plunge pool never crosses the threshold stream power of the rock for dams with significant discharge. It is therefore rather recommended to assume the C_p'-value converges towards zero for $Y/D_j > 20$.

$$C_p' = a_1\left(\frac{Y}{D_j}\right)^3 + a_2\left(\frac{Y}{D_j}\right)^2 + a_3\left(\frac{Y}{D_j}\right) + a_4 \qquad \textit{Equation 2.39}$$

The relationship between the regression coefficients (a_1, a_2, a_3, a_4) and initial turbulence intensity (T_u) are listed in Table 2.4. Bollaert (2002) found that the fluctuating dynamic pressure coefficient for circular jets increases for greater turbulence intensities, and reaches a maximum when Y/D_j has a value of approximately 6.

Table 2.4: C_p' parameters for circular jets (Bollaert, 2002)

T_u (%)	a_1	a_2	a_3	a_4	Type of jet
< 1	0.0022	-0.0079	0.0716	0	Compact
1 to 3	0.00215	-0.0079	0.0716	0.050	Intermediate
3 to 5	0.00215	-0.0079	0.0716	0.100	Undulating
> 5	0.00215	-0.0079	0.0716	0.150	Very undulating

Castillo et al. (2015) determined that the fluctuating dynamic pressure coefficient (C_p') for rectangular jets is a function of the pool depth to jet thickness ratio (Y/B_j) and the fall height to jet breakup length ratio (H_w/L_b):

For $Y/B_j \leq 14$:

$$C_p' = a\left(\frac{Y}{B_j}\right)^3 + b\left(\frac{Y}{B_j}\right)^2 + c\left(\frac{Y}{B_j}\right) + d \qquad \textit{Equation 2.40}$$

For $Y/B_j > 14$:

$$C_p' = ae^{-b(Y/B_j)} \qquad \textit{Equation 2.41}$$

The relationship between the dimensionless parameters used in Equation 2.40 and Equation 2.35 and the breakup length ratio are presented in Table 2.5.

Table 2.5: C_p' parameters for rectangular jets (Castillo et al., 2015)

H_w/L_b	$0 \leq Y/B_j \leq 14$				$Y/B_j > 14$	
	a	b	c	d	a	b
≤ 0.8	0.00030	-0.01000	0.0815	0.08	1.50	0.21
0.8 – 1.0	0.00030	-0.01000	0.0790	0.13	1.80	0.21
1.0 – 1.3	-0.000005	-0.00220	0.0160	0.35	1.00	0.15
1.3 – 1.6	0.00003	-0.00180	0.0100	0.21	0.40	0.12
1.6 – 1.8	0.00005	-0.00195	0.0098	0.16	1.33	0.23
≥ 1.8	0.00005	-0.00190	0.0100	0.11	2.50	0.35

Castillo et al. (2018) also proposed updated parameters for determining the fluctuating dynamic pressure coefficient for rectangular jets ($C_p{}'$) compared to the parameters listed in Table 2.5. However, the experimental data from the current study agreed better with the parameters presented previously by Castillo et al. (2015) listed in Table 2.5 compared to the new parameters presented in Castillo et al. (2018).

Maleki and Fiorotto (2019) noted that the dimensionless dynamic pressures depend on the impingement angle of the jet with the bedrock (δ) surface and not the jet impact angle with the tailwater level (θ_j). Equation 2.42 gives the jet impingement angle with the bedrock surface.

$$\delta = cos^{-1}\left[\frac{3}{2}\frac{q_e}{q}\left(1-\frac{1}{3}\frac{q_e^2}{q^2}\right)\right] \qquad \textit{Equation 2.42}$$

where q_e is the jet unit discharge at impact with the tailwater level (m^3/s/m) and q is the jet unit discharge (m^3/s/m) calculated as follows:

$$q = 2bv_\varsigma/C \qquad \textit{Equation 2.43}$$

with b the distance from the jet centreline to the point where the mean velocity's maximum value is halved (m), v_ς is the maximum velocity at the jet centreline at the jet length in the plunge pool (m/s), and C is a constant (0.881).

2.5. Mechanisms of scour

2.5.1. *Jet scouring mechanisms*

The first scouring mechanism to consider is the plunging jet and how it impinges on the bedrock. The erosive capacity of the water is directly related to the amount of energy left when the jet impinges onto the bedrock after travelling through the air and plunge pool. No scouring of the bedrock would occur if the energy of the jet has been fully dissipated (Van Aswegen et al., 2001).

2.5.1.1 Discharge effects

Stratford et al. (2013) determined that the discharge affects the scour potential of a jet. An increase in discharge increases the stream power and scouring capacity of the jet (Annandale, 2006). Physical model studies conducted by Heng et al. (2012) proved that the width of the jet at impact with the plunge pool rock bottom decreases with an increase in the discharge. On the other hand, the scour hole width increased with a decrease in discharge for the same fall height due to the more developed jet.

2.5.1.2 Fall height effects

Ervine et al. (1997) found that an increase in the jet fall height (H_w) increases the jet velocity, which increases the vertical scour potential of the jet (depth of scour). Mason (1989) reasoned that the scour depth is independent of the fall height for fully developed jets, but dependent on the unit discharge (q) and air-water ratio (β) with apparent effects of the fall height (H_w) possibly due to variations of air entrainment with H_w. Castillo et al. (2015) proved that the mean and fluctuating dynamic pressure coefficients become very low for fully developed jets. Thus, for fully developed jets the fall height becomes less dominant in the scour process, as the individual water particles falling through the air experience resistance that significantly reduce the erosive capacity.

2.5.1.3 Aeration effects

Duarte (2014) found that air entrainment has a great influence on the rock scour process, since aeration affects hydrodynamic variables such as pressures and velocity profiles. Aeration is present in three locations, namely aeration of the jet as it travels through the air, plunge pool aeration when the jet impinges with the tailwater level and aeration in the rock joints (Bollaert, 2002) as depicted in Figure 2.6.

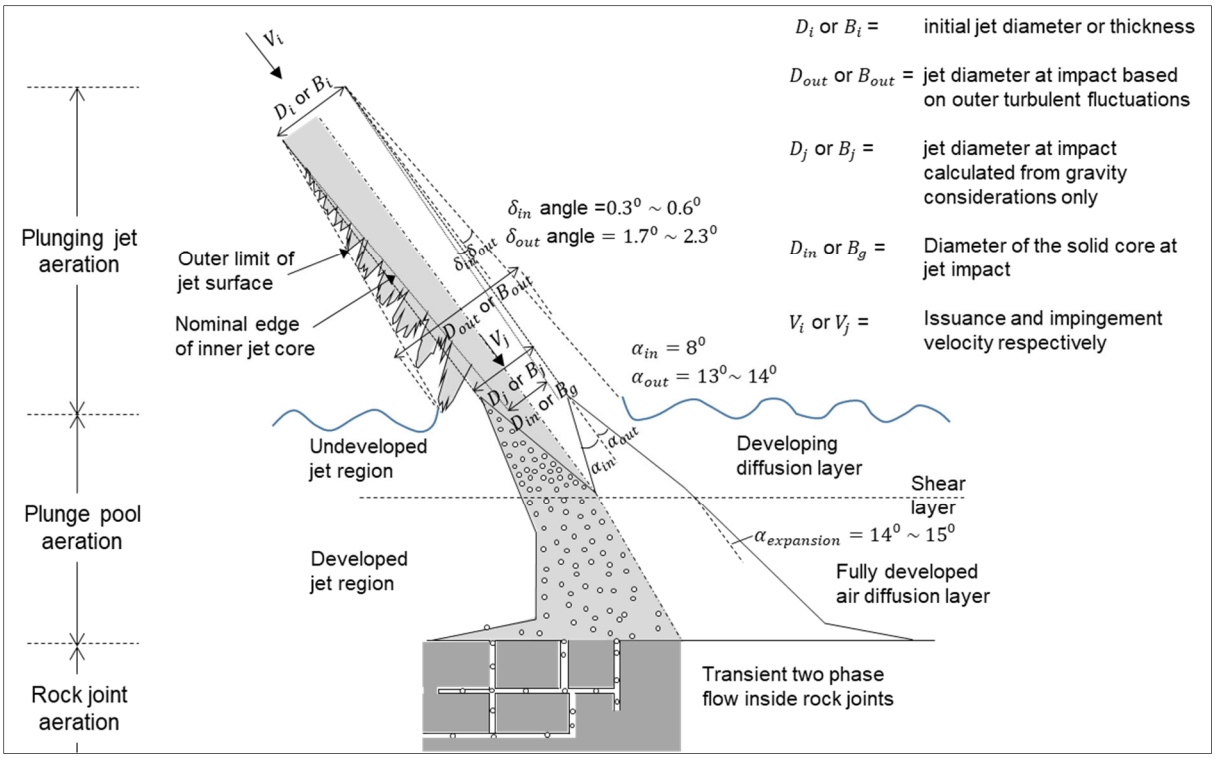

Figure 2.6: Jet, pool and rock air entrainment

As discussed in Section 2.3.3, a plunging jet consists of an expanding outer aerated shell and a decaying core as it travels through the air. According to Ervine et al. (1997), the footprint and magnitude of the jet's erosive capacity at impact with the rock bed are directly related to the percentage break up and air entrainment of the jet. Surface tension, internal turbulence and gravity govern the air entrainment rate of a plunging jet.

Some researchers found that the jet is never completely broken up or developed for the full fall height for most high dams (Annandale & George, 2011). Häusler (1983) suggested, due to the core of the jet remaining intact (undeveloped jet) for most cases, the aeration of the jet should be ignored or the width of the solid jet core at impact should be reduced if aeration is being accounted for. Monfett (2004) found that aeration of the jet has a negligible influence on the deceleration of the jet's velocity.

On the other hand, Van Aswegen et al. (2001), Melo (2002), Bollaert (2002), Pagliara et al. (2006), Annandale (2006), Toombes and Chanson (2007), and Johnson (1967, as referenced by Mason, 1989) found that aeration of the jet reduces the jet core, which dissipates the potential scour energy of the jet as it travels through the air and plunge pool, which in turn relates to a decreased of rock scour. Ervine et al. (1997) proved that the transient and mean pressures at the plunge pool floor decrease if the lateral spread and air entrainment of the jet increases.

Air entrainment of a plunging jet is important and should be included in rock scour calculations for the following reasons:

- Air entrainment of the plunging jet enhances plunge pool air entrainment (Bollaert, 2002).
- Air entrainment influences the jet geometry and impingement location with the plunge pool water surface and bedrock (Bollaert, 2002).
- An aerated jet has a lower momentum compared to a solid core jet, due to a lower density of the air-water mixture. Air also changes the elasticity bulk modulus of the water (Duarte, 2014).
- Air reduces the pressures experienced inside the joints and on the rock bed surface, except at the impingement centreline with the plunge pool rock bottom (Duarte, 2014).
- Entrained air in water reduces the pressure wave celerity of the water, which can then give rise to resonance in close-ended fissures. Such resonance can increase the potential for brittle fracture and change the rate of scour by fatigue failure (Bollaert, 2002).
- Air enhances the fluctuating pressures inside the rock joints that could break the rock bed into distinct blocks and generate uplift pressures (Manso et al., 2003).
- Pressure fluctuations are dampened by air due to the compressing and decompressing of the air (Duarte, 2014).
- The energy dissipation and pressure wave celerity, oscillation and amplification are influenced by air bubbles in the plunge pool and rock joints (Duarte, 2014).

A substantial amount of air is entrained as the jet plunges into the plunge pool. The total air entrained into the plunge pool is defined by the air-to-water flow ratio β (Equation 2.44) (Annandale, 2006):

$$\beta = \frac{q_a}{q_w} \qquad \textit{Equation 2.44}$$

where q_w is the water unit discharge ($m^3/s/m$) and q_a is the total unit air discharge entrained by the jet at impingement with the tailwater level ($m^3/s/m$). Currently, the best equation, however ambiguous, to calculate the air content in a plunging jet is presented by Ervine (1998):

$$q_a = 0.00002(V_j - 1)^3 + 0.0003(V_j - 1)^2 + 0.0074(V_j - 1) - 0.0058 \qquad \textit{Equation 2.45}$$

Equation 2.45 is only valid for a rectangular jet with a thickness greater than 30 mm and flow velocities between 1.5 m/s and 15 m/s, and has an approximate 30% accuracy.

Other equations found in literature to estimate the air-to-water ratio (β) are summarised in Table 2.6.

The concentration of air per cross-section (α_i) of the jet entering the plunge pool is determined by the associated void fraction (Equation 2.46) (Duarte, 2014).

$$\alpha_i = \frac{Q_a}{Q_a + Q_w} = \frac{\beta}{1 + \beta} \qquad \textit{Equation 2.46}$$

Bollaert (2002) determined that an air concentration of 15% to 35% would typically occur for jet velocities of 10 m/s, and air concentrations of 40% to 60% would occur for jet velocities of 30 m/s at impingement with the plunge pool water surface (Bollaert, 2002).

Whittaker and Schleiss (1984) suggested that the plunge pool depth could be reduced of what is required for solid jet if the jet is aerated. However, May and Willoughby (1991, cited in Bollaert, 2002) studied the aeration effect on the mean and fluctuating pressures for rectangular jets with 10% to 20% air ratios and found negligible influence by changing the air concentration.

Table 2.6: Air to water ratios (β) equations

Jet geometry	**β-ratio**	Author	***Equation number***
Rectangular jets	$\beta = 0.26\left(\frac{W_j}{p_e}\right)\cdot\left(\frac{L_j}{B_j}\right)^{0.446}$	McKeogh & Ervine (1981), as cited in Duarte (2014)	*Equation 2.47*
	$\beta = 0.13\left(1-\frac{V_{air}}{V_j}\right)\left(\frac{H_w}{B_j}\right)^{0.446}$	Ervine (1976), as cited in Bollaert & Schleiss, 2003a)	*Equation 2.48*
	$\beta = 2.9\times10^{-3}\left(\frac{L_j}{D_j}-0.52\right)\left(\frac{V_j-V_{air}}{\sqrt{gD_j}}\right)^{1.8}$ valid for $V_{air} < V_j < 4m/s$	(Brattberg & Chanson, 1998, as cited in Duarte, 2014)	*Equation 2.49*
	$\beta = 5.75\times10^{-3}\left(\frac{L_j}{D_j}-0.52\right)\left(\frac{V_j-V_{air}}{\sqrt{gD_j}}+6.6\right)$ valid for $4m/s < V_j < 8m/s$	(Brattberg & Chanson, 1998, as cited in Duarte, 2014)	*Equation 2.50*
Circular jets	$\beta = K'\sqrt{\frac{L}{D_j}}\cdot\left(1-\frac{V_{air}}{V_j}\right)$	(Ervine, 1976)	*Equation 2.51*
	$\beta = 0.04\cdot Fr_j^{0.28}\cdot\left(\frac{L_j}{D_j}\right)^{0.4}$ valid for vertical jets (90º)	(Biń, 1984)	*Equation 2.52*
	$\beta = 0.75R_e^{1.33}\left(\frac{\sqrt{W_e}}{R_e}\right)^{2.18}\left(\frac{v^2}{gH_w}\right)^{-0.447}\left(\frac{H_w}{n_d}\right)^{0.281}$	(Oyama et al. 1954, , as cited in Van Aswegen et al., 2001)	*Equation 2.53*

W_j: jet width in the impingement conditions (m)

p_e: jet perimeter (m)

V_{air}: minimum inception velocity (±1 m/s)

K': parameter ranges between 0.2 (smooth turbulent jet) and 0.4 (rough turbulent jet)

n_d: nozzle diameter (m)

2.5.2. *Rock scour mechanisms*

According to Annandale (2006), rock bed material could be categorised either as a physical or a chemical gel. Physical gels consist of individual elements touching each other, for example fractured rock. Rock that acts as a physical gel is more subject to scour failure and the removal of individual rock blocks from the bed matrix when turbulent flow with large fluctuating forces flows over the rock. Chemical gels are characterised as elements that are connected to each other by fixed bonds such as intact rock. These fixed bonds are of a chemical nature and therefore provide a higher scour resistance than those of physical gels. Chemical gels generally either fail in brittle fracture or fatigue failure.

Scouring of rock would occur when the erosive capacity of water exceeds the ability of the rock to resist it. Hydrostatic pressures are generated between the rock joints by the impacting jet and eddies are created by water flowing over the rock, resulting in fluctuating pressures (Annandale, 2006). The tugging and pulling action of the water causes progressive dislodgement and/or uplift of individual rock blocks (Annandale et al., 1996). Scouring of rock in turbulent flow is not a shear process, but results from turbulent pressure fluctuations.

Factors that affect the vulnerability of rock are lithology, the rock strength, and the spacing, orientation and condition of the joints (Bollaert et al., 2004). The rock failure mechanisms with their own timescale of occurrence, ranging from instantaneous to long term, include (Kieffer & Goodman, 2012, and George, 2015):

1. Brittle fracturing and fatigue failure (instantaneous and progressive) (Figure 2.7a)
2. Rock uplift and removal (pressures in joints and shear flow) (instantaneous) (refer to Figure 2.7b)
3. Peeling (instantaneous and progressive) (Figure 2.7c)
4. Abrasion (long term)

Fracturing of intact rock refers to the propagation of close-ended joints/fissures due to the dynamic action of the water jet (Peiqing & Aihua, 2007). The rate the hydrodynamic pressures are transmitted to the joint tip depends on the condition (open or tight ended) and orientation of the joints (Monfette, 2004). Rock can fail instantaneously (explosive manner) by brittle fracture or progressively over time by fatigue, depending on the magnitude of the applied hydraulic pressure (Bollaert, 2002, and George, 2015). Brittle and fatigue fracturing break the rock mass into distinct blocks and is the onset of rock block uplift (Bollaert, 2010a).

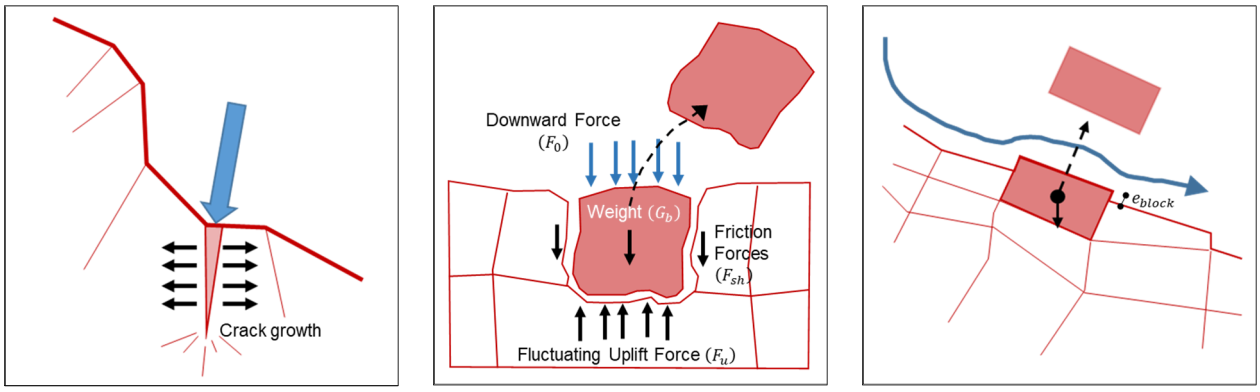

(a) Fracturing (b) Block uplift (c) Peeling of blocks

Figure 2.7: Rock scour mechanisms

Block uplift and removal is the main physical rock scour mechanism and refers to the plucking, dislodgement and displacement of rock blocks from the surrounding rock matrix due to hydraulic pressures induced by the plunging jet. The hydrodynamic pressures are transmitted through the joints to the underside of the rock blocks resulting in uplift forces (F_u) (Annandale et al., 1996). Figure 2.7b illustrates the uplift and resistance forces acting on and within the rock block. The resistant forces (downward forces) are the submerged weight of the block (G_b), the shear and interlocking forces between the block and the surrounding rock mass (F_{sh}) and hydraulic forces due to the plunging jet (F_0) (Peiqing & Aihua, 2007). The resistant forces decrease as the plunge pool depth decreases (Van Aswegen et al., 2001).

The removal of individual rock blocks from the rock mass is greatly dependent on the three-dimensional orientation of the fissures bounding the block, and causes different kinematic failure modes (George, 2015). The kinematic failure modes that could be produced when the transient uplift forces exceed the resistance forces, causing the block to dislodge and be swept away by the flow, include pure translational modes, for example lifting and sliding, pure rotational modes, being rotation about an edge or a corner, or a combination of translation and rotation, for example slumping or torsional sliding (Liu et al., 1998 and George, 2015). The type of removal that is most plausible is dependent on the size, dimensions and protrusion of the blocks compared to the surrounding rock mass, as well as the discharge characteristics of the jet. The three rock parameters define the significance of the static, quasi-steady and turbulent forces that would be able to lift the rock block (Bollaert, 2010c and Hickin, 2004).

Rock scour by means of peeling is a combination of brittle fracture or fatigue failure and quasi-steady uplift pressure forces. Peeling generally occurs for rock that consists of multiple thin, near horizontal layers, i.e. sedimentary rock (Van Schalkwyk et al., 1994). Peeling of rock is caused by flow turbulence and local flow deviations that are caused by the protrusion of the

block denoted as e_{block} in Figure 2.7c. The flow deviations generate lift and drag forces on the exposed rock faces resulting in displacement of the rock blocks (Bollaert, 2010c).

Abrasion implies the grinding away of a rock surface layer-by-layer due to repeated impacts from particles carried by the water. The rate at which abrasion occurs depends on the saltating particle size distribution, the saltating particle hardness compared to the surrounding rock experiencing abrasion, and the flow rate.

Abrasion is a lengthy process and is typically neglected when analysing rock scour (Bollaert, 2010b). The flow at engineering structures, such as dams, normally contains high energy with a high sediment transport capacity, but is generally sediment starved. In the particular case of plunging jets from dam spillways, the reservoir causes deposition of coarse incoming sediment and the jets contain few to no particles to impact the bedrock, which limits the abrasion rate (George, 2015). As the scour hole deepens, more energy is required to remove trapped ejected rock blocks in the scour hole. The trapped rock blocks would be eroded by a process called ball milling into smaller pieces. The rock blocks are ground against the sides of the scour hole and other rock blocks during the ball milling process, causing abrasion. When the rock pieces are small enough they will be transported out of the scour hole (Bollaert, 2005). Rock blocks can also be entrained from downstream and cause abrasion as observed at the stilling basin of Folsom Dam, American River, California (Annandale, 2006).

2.6. Rock scouring parameters

The correct parameters affecting rock scour need to be specified to ensure that physical and/or numerical models are representing the real-world processes (Annandale & George, 2011). The main hydraulic and geotechnical parameters effecting rock scour based on various literature sources are listed in Table 2.7.

Table 2.7: Parameters effecting rock scour

Group	Parameter	Symbol	Unit
Hydraulic loading parameters	• Flow velocities at issuance and impact with plunge pool	V_i, V_j	m/s
	• Jet discharge	Q	m^3/s
	• Jet turbulence intensity at issuance and impact	T_u	%
	• Jet geometry at issuance and impact	-	-
	• Plunge pool depth	y_w	m
	• Fall height	H_w	m
	• Jet breakup length	L_b	m
	• Jet thickness and width at issuance and impact with plunge pool	B_i, B_j	m
	• Jet trajectory length	L_j	m
	• Issuance and impinging angle	θ_i, θ_j	°
Geotechnical parameters	• Rock mass type (metamorphic, igneous and sedimentary)	-	-
	• Rock density	ρ_r	kg/m^3
	• Weight of rock block	G_b	N
	• Size of the rock blocks	x, y, z	m
	• Rock block settling velocity	V_{ss}	m/s
	• Rock mass structure	-	-
	• Rock layer thickness	H_{layer}	m
	• Uniaxial compressive strength of the rock	UCS	MPa
	• Rock quality designate	RQD	%
	• Uniaxial tensile strength (tensile properties of rock)	T	MPa
	• Young's modulus of elasticity	E_r	MPa
	• Rock joint set dip angle and dip direction	α_r	°
	• Joint set spacing	S_j	m
	• Joint set width	e_j	m
	• Joint set friction angle	φ_j	°
	• Joint set length	L_f	m
	• Number of joint sets	N_i	-
	• Fatigue failure properties and the rocks fracture toughness	-	-
	• Weathering of rock mass and joint fill material (Van Aswegen et al., 2001)	-	-
	• Cohesive strength of the rock – resistance to shear forces (Monfette, 2004)	-	-

2.7. Scour control measures

The main objectives of scour control measures are to safeguard the public and to protect infrastructure against scour. Rock scour can be minimized by reducing the erosive capacity of the jet, changing the properties of the flow boundaries in such a way to reduce the scour capacity of the water, or protecting or strengthening the plunge pool floor under hydraulic loading (Annandale, 2006). The following scour control measures could influence the scour extent:

- **Accommodating protection**
  This approach allows scour to occur unimpeded by arranging the surrounding infrastructure and property to prevent failure and ensure public safety (Annandale, 2006).
- **Limiting the spillway discharge:**
  This measure is mainly used for arch dams and free ogee crest spillways where the jet impacts relatively close to the dam foundation (Schleiss, 2016).
- **Forced splitting and aeration of jets:**
  Splitters, baffle blocks and/or deflectors at the end of a spillway split the jet to aerate the water, since the scour potential of a broken jet is less than a coherent jet for the same discharge as discussed in Section 2.5.1.3. The dynamic pressures generated at the plunge pool floor could also be reduced through chute widening (Guven, 2011).
- **Plunge pool boundary preforming and amendments:**
  The plunge pool could be pre-excavated based on the predicted natural scour hole extent. Pre-excavation of the plunge pool increases the dissipation volume (water cushion) that reduces the scour potential of the jet (Bollaert et al., 2012b). However, Whittaker and Schleiss (1984) cautioned that a water cushion is not the most effective scour control measure, unless the scour hole is very deep or used in conjunction with other control measures, i.e. aeration. The tailwater level could also be increased, thus increasing the dissipation volume (water cushion), by constructing a tail pond dam downstream of the jet impingement zone.
- **Enhancement of earth material**
  The enhancement of the earth material entails improving the naturally occurring material's scour resistance. Rock anchors and pre-stressed tendons could be used for strengthening (Annandale, 2006). If rock uplift is the main scour mechanism, earth material enhancement could be used. However, caution must be exercised when brittle and fatigue failure are present (Schleiss, 2016).

- **Hard protection:**
  Hardening of the pool bottom aims to resist the erosive power of the plunging jet. The pool bottom could be lined with concrete, riprap, or other lining systems to protect the underlining bedrock against scour. The thickness of a lining is limited by construction and economic considerations, thus anchors and pre-stressed tendons are required to ensure the stability of the lining in view of the high dynamic pressures (Annandale, 2006). A drainage system is imperative to protect the lining against uplift pressures during dewatering of the pool (Whittaker & Schleiss, 1984).

The scour control measures mentioned above could also be used in combination to optimise the design (Annandale, 2006).

2.8. Scour formation summary

In Section 2, the most commonly used terminology pertaining to rock scour was discussed, as many of the parameters describing rock scour properties are included in rock scour formulae.

The main focus of this section was to explain rock scour formation due to plunging jets. The hydrodynamics of a plunging jet through the air and plunge pool were first described, and thereafter various rock scour mechanisms. The overview of the jet and rock scour mechanisms are important to understand the rock scour prediction methods discussed in Section 3.

3. LITERATURE REVIEW OF SCOUR PREDICTION METHODS

3.1. General overview

Despite extensive research since the 1950s, at present there is no universally agreed upon method to predict the equilibrium scour depth due to plunging jets at dams accurately. The existing rock scour prediction methods due to the impingement of plunging high velocity jets are as follows (Bollaert & Schleiss, 2003a):

- physical models;
- empirical formulae based on laboratory and field observations; and
- analytical scour prediction method that combines laboratory and field observations with physics.

This section focuses on the more commonly used scour prediction methods to determine the ultimate depth of the scour hole.

3.2. Physical models

Scaled physical models are used to attempt to reproduce what the ultimate scour hole geometry would be in the prototype. The local topography and scour mechanism should be modelled correctly when using physical modelling to determine the scour hole extend (Van Aswegen et al., 2001).

Physical models could be limited to the physical resources available (i.e. size of laboratory and pump capacity), materials available to represent the rock mass and the structure (spillway and plunge pool) and scale effects due to forces, surface tension and viscosity that influence the motion of the water (Ghodsian et al., 2012). Ervine and Falvey (1987) proved that pressure fluctuations cannot be scaled between prototype and model, thus the model scale chosen and the model results must be carefully interpreted.

Surface tension, internal turbulence effects and gravity governs the air entrainment of a plunging jet. Thus, air entrainment is a combined Froude-Reynolds-Weber phenomenon (Webber, 1971). Refer to Annexure B for a detailed explanation of similarity laws. Additionally, the hydraulic loading on the rock bed follows the Strouhal similitude. A scaled physical model should correctly model the combined Froude-Reynolds-Weber phenomenon, which is impossible. However, the appropriate air entrainment could be simulated with a Froude scaled model when care is taken to represent the turbulence intensity of the prototype correctly. Furthermore, the physical model must be large enough in order to attain the onset velocity of air entrainment and that the surface tension effects are small. Prototype jets differ to that of

physical models, since the air entrainment of prototypes is greater than for a physical model, which produces lower mean dynamic pressure values at the plunge pool bottom of the prototype. The reason for lower mean dynamic pressures for prototypes is that a large amount of air is entrained into the diffusing layer of the jet at impact with the tailwater level, which modifies the theoretical pressure and velocity profiles (Bollaert, 2002).

Various authors recommend minimum Reynolds and Weber numbers to minimise the viscosity and surface tension effects for physical models based on Froude similarity.

Viscosity has a negligible influence if the Reynolds number is greater than a specific value, i.e. $R_e = Vd/\nu > 3 \times 10^4$ (Daggett and Keulegan (1974) as cited in Padmanabhan and Hecker (1984)), $R_e > 1 \times 10^4$ (Zielinksi and Villemonte (1968) as cited in Padmanabhan and Hecker (1984)), $R_e > 7.7 \times 10^4$ (Padmanabhan & Hecker, 1984), $R_e > 1.1 \times 10^5$ (Odgaard, 1986), $R_e > 10^5$ (Chanson, 2009 cited in Duarte, 2014, and Heller, 2011) in which V is the flow velocity (m/s), d the water depth (m) and ν the water kinematic viscosity (m^2/s).

Surface tension scale effects have been shown to be a minimum if the Weber number is greater than a specific value, i.e. $We = \rho d V^2/\sigma > 120$ (Jain *et al.* (1978) as cited in Padmanabhan and Hecker (1984)), $We > 120$ (Daggett and Keulegan (1974) as cited in (Kabiri-Samani and Borghei (2013)), $We > 600$ (Padmanabhan & Hecker, 1984), $We > 720$ (Odgaard, 1986), $We > 1000$ (Chanson, 2009 cited in Duarte, 2014, and Heller, 2011) where ρ and σ are the density (kg/m^3) and surface tension (N/m) of water, respectively.

Other major scaling effects that must also be taken into account are rock mass scaling, aeration scaling and time scaling (Bollaert, 2002). Rock mass scaling effects are difficult to incorporate into the design as it is difficult to simulate the rock foundation with a material that adequately represents the dynamic behaviour of the jointed prototype rock in a physical model (Whittaker & Schleiss, 1984). Therefore, most physical scour tests assume that the disintegration process of the rock mass has already taken place and make use of distinct blocks (cohesionless) to represent the prototype broken up rock. Thus, only the air entrainment and transportation of rock blocks are modelled (Bollaert & Schleiss, 2003a).

Some researchers suggest using non-cohesive particles in conjunction with cement mortar as a binder to represent the rock mass. However, using cement mortar as a binder could skew the data when doing long term testing as the characteristics of the material could change when submerged for long periods (Ghodsian et al., 2012). Using a binder could also increase the strength of the bed material, giving a false representation of the resistance of the rock to scour (Van Aswegen et al., 2001).

Bollaert and Schleiss (2005) determined that a physical model scale of approximately 1:10 is required to reproduce the pressures inside the joints accurately. Castillo et al. (2015) also found that aeration scale effects are negligible for model scales less than 1:10. Other authors suggest that for a model scale not exceeding 1:20 there are no scale effects on the plunging jet velocity and initial turbulence, plunge pool aeration and the dynamic pressures at the bedrock. However, model scales greater than 1:100 could cause incorrect aeration results (Boushaba et al., 2013). The compressibility of air also affects the behaviour of air entrainment in models, captured in the Mach number (M_a). For small model scales, air becomes less compressible (Heller, 2011).

Rouse (quoted in Bollaert, 2002) noted that erosion of a scour hole never ends with time, but that up to 90% of the ultimate scour depth is reached within a few days or weeks of discharge. Currently, there is no reliable method to express this time dependence (time scale effect) (Bollaert, 2002).

The geotechnical characteristics of the bedrock should be investigated for each case study to ensure that the prototype conditions are correctly represented in model studies. For example, the rock structure and type may vary laterally and with depth, affecting the rock scour resistance and increasing the difficulty to predict the equilibrium scour hole geometry. The Kariba Dam on the Zambezi River is an example where the uniaxial compressive strength (UCS) and joint type of the rock varied between the North and South banks in the downstream canal. The location of the maximum scour depth was consequently shifted to the north from the centre plane (Munodawafa & Mhlanga, 2014).

3.3. Empirical formulae

Rock scour in a plunge pool is often predicted by empirical formulae. Most of the empirical formulae are based on laboratory tests, with only a few based on prototype observations. Empirical formulae are simple to use, but have a major drawback in the lack of application ranges (Castillo & Carrillo, 2017). Empirical formulae are unable to describe all the physical processes involved in rock scour. Empirical formulae also neglect the role dynamic pressures have on the plunge pool floor and the transfer of pressures into the rock joints, as well as the influence aeration has on the dynamic pressures. Furthermore, empirical formulae cannot predict the resistance of the rock against progressive breakup correctly (Bollaert & Schleiss, 2003a).

Mason and Arumugam (1985) showed that significant differences in scouring results are obtained whether model or prototype conditions are used as input parameter in empirical

formulae. Empirical formulae are therefore greatly affected by scaling effects (Bollaert & Schleiss, 2003a).

The general empirical expression to calculate the scour depth is as follows (Mason & Arumugam, 1985):

$$Y = y_s + y_w = K \cdot \frac{q^a \cdot {H_w}^b \cdot y_w^c}{g^d \cdot d_m^e} \qquad \textit{Equation 3.1}$$

where y_s is the scour depth (m), y_w is the plunge pool depth (m), K is an experimental coefficient, q the unit discharge ($m^3/s/m$), H_w the effective head (m), g the gravitational acceleration (m/s^2), and d_m the mean rock cube size (m).

Various empirical formulae proposed by different authors are summarised in Table 3.1. Refer to Annexure C for lesser known empirical formulae found in the relevant literature.

Table 3.1: Empirical formulae

Formula (Empirical)	Author	Equation number
$y_s + y_w = 3.62 \frac{H_w^{0.225} q^{0.54}}{d_m{}^{0.42}}$	Veronese 1 (1937, as cited in Castillo & Carrillo, 2017)	*Equation 3.2*
$y_s + y_w = 1.32 H_w^{0.225} q^{0.54}$	Veronese 2 (1937, as cited in Wittler et al. *(1995)*)	*Equation 3.3*
$y_s + y_w = 1.9 H_w^{0.225} q^{0.54}$	Veronese 3 (1937, as cited in Noret et al. (2012))	*Equation 3.4*
$y_s + y_w = 1.9 H_w^{0.225} q^{0.54} \sin \theta_j$	Yildiz and Uzucek (1994, as cited in Alias et al. (2008)) – Modified Veronese	*Equation 3.5*
$y_s + y_w = 0.6\, q^{0.5}\, H_w^{0.25} \left(\frac{y_s}{d_m}\right)^{0.333}$	Jaeger (1939, as cited in Mason & Arumugam *(1985)*)	*Equation 3.6*
$y_s + y_w = 0.362 H_w^{0.5} q^{0.5}$	Damle (1966, as cited in Noret et al. (2012))	*Equation 3.7*
$y_s + y_w = 1.663 H^{0.2} q^{0.6}$	Chee and Kung (1974, as cited in Noret et al. (2012)	*Equation 3.8*
$y_s + y_w = 1.5 H_w^{0.1} q^{0.6}$	Martins (1975, as cited in Noret et al. (2012))	*Equation 3.9*
$y_s + y_w = \left(\frac{0.97}{\sqrt{d_{90}}} - \frac{1.35}{\sqrt{H_w}}\right) \frac{q \sin \theta_j}{1 - 0.175 \cot \theta_j} + 0.25 y_s$	Mirskaulava (1967, as cited in Mason & Arumugam *(1985)*)	*Equation 3.10*
$y_s + y_w = 3.39 \frac{q^{0.6} (1+\beta)^{0.3} y_w^{0.16}}{g^{0.3} d_m^{0.06}}$	Mason *(1989)*	*Equation 3.11*
$y_s + y_w = 3.27 \frac{q^{0.6} H_w^{0.05} y_w^{0.15}}{g^{0.3} d_m^{0.1}}$	Mason and Arumugam *(1985)*	*Equation 3.12*
$y_s + y_w = 0.78 \frac{H_w^{0.35} q^{0.7}}{d_{90}{}^{0.4}}$	Kotoulas (1967) (as cited in Whittaker & Schleiss, 1984)	*Equation 3.13*

In Table 3.1, d_{90} is the rock diameter (m) representing the 90% percentile, d_m the mean rock block size (m), β the air-water relationship, and θ_j is the impingement angle with plunge pool surface (degrees).

In conclusion, although empirical formulae are affected by major scale effects and ignore dynamic aspects, it is still useful to get a first-hand estimation of the equilibrium scour hole depth and to identify general scouring tendencies. The variety of available formulae makes it possible to establish a confidence interval of scour depths. Thus, empirical formulae are primarily used during preliminary design stages (Bollaert & Schleiss, 2003a).

3.4. Analytical methods

Scour prediction methods may utilise a combination of empirical formulae and laboratory and field observations. The two leading methods for assessing rock scour that allow for most of the rock scour mechanisms and the erosive capacity of the jet are the Erodibility Index Method (EIM) and the Comprehensive Scour Model (CSM). The EIM is discussed in Section 3.4.1 and the CSM in Section 3.4.2.

3.4.1. *Erodibility Index Method*

Annandale (2006) developed a semi-empirical, geo-mechanical classification method called the Erodibility Index Method (EIM) through studying rock scour formation of 150 spillways in South Africa and the United States of America. The EIM compares the erosive capacity of flowing water to the erosive resistance of the earth material represented by an erodibility index (K_h) (Annandale, 1995 and 2006). The hydraulic erodibility of rock could be characterised by the Kirsten index (Kirsten, 1982). According to the EIM, scour would occur when the erosive capacity of the water is greater than the erodibility threshold (Annandale, 1995) as seen in Figure 3.1.

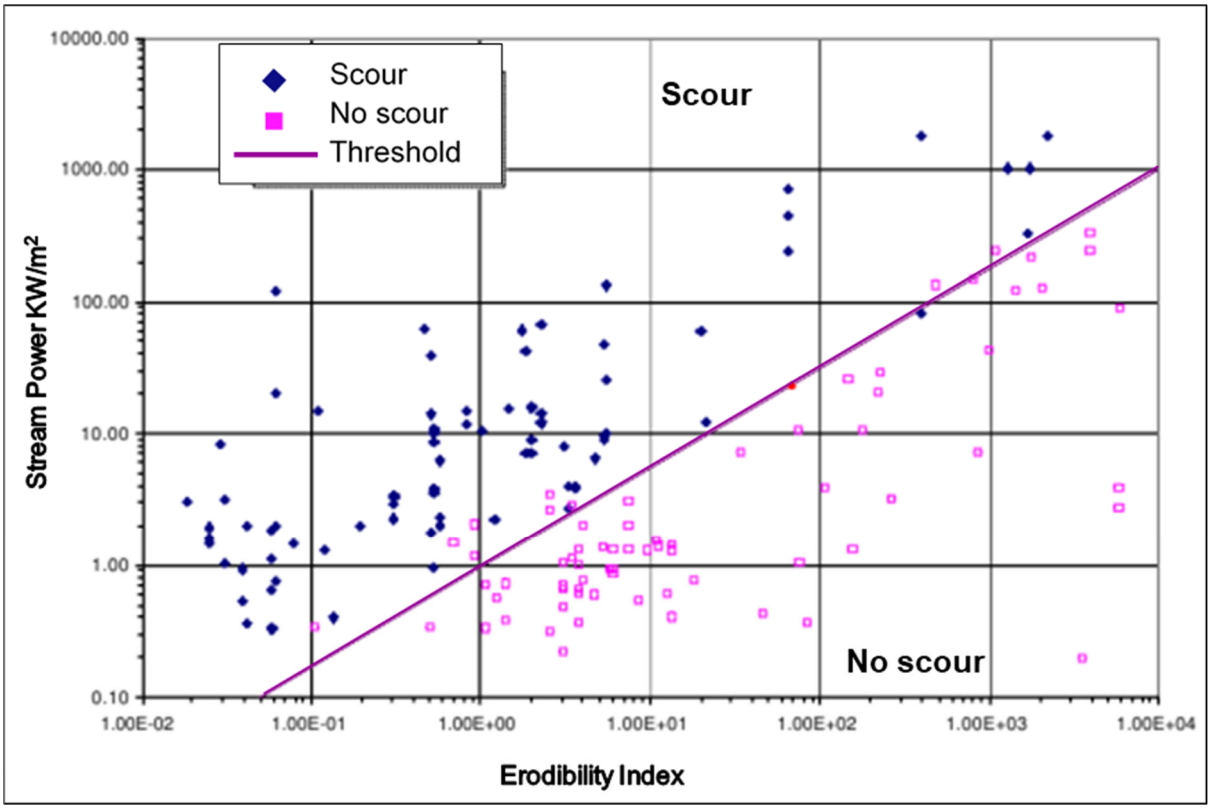

Figure 3.1: Erodibility threshold (Annandale, 1995 and 2006)

The erosive power of the water, or stream power, is characterised by the rate at which the energy of flowing water is dissipated. The energy dissipation rate of the jet is representative of the fluctuating pressures that are primarily responsible for rock dislodgement (Annandale, 1995). As the turbulence intensity of the jet increases, the rate of energy dissipation and the magnitude of the fluctuating pressures increases (Annandale, 1995 and 2006).

The erosive capacity of the jet is defined by stream power per unit area and varies with depth in the plunge pool. In general form, the stream power of a jet in a plunge pool can be calculated with Equation 3.14, taking diffusion of the jet in the plunge pool into account at different elevations (Annandale, 2006).

$$P_{pool} = \frac{\gamma Q H}{A_i} \qquad \textit{Equation 3.14}$$

where P_{pool} is the stream power per unit area in the pool at a certain depth (W/m^2), γQH is the stream power that stays the same of that at impact with the tailwater level (W), γ is the unit weight of water (N/m^3), Q is the total discharge (m^3/s), H_w is the fall height (m), and A_i is the jet footprint (impact area of the jet) at different elevations below the tailwater level (m^2). The area of the jet could be estimated using the jet expansion guidelines provided by Ervine and Falvey (1987) discussed in Sections 2.3.5 and 2.4.1 (refer to Figure 2.5).

Bollaert (2002) proved that the stream power in the plunge pool below the tailwater surface first increases and then decreases. In order to reflect this, the stream power makes use of mean and fluctuating stream power decay coefficients, and is similar to the approach when estimating the mean and fluctuating pressures detailed in Section 2.4.2. The variation in the total stream power per unit area as a function of dimensionless pool depth is the sum of the mean and fluctuating stream power components expressed as (Annandale, 2006):

$$P_{total}\left(\frac{Y}{D_j}\right) = P_{jet}\left(\frac{Y}{D_j}\right) + P'_{jet}\left(\frac{Y}{D_j}\right) \qquad \textit{Equation 3.15}$$

with $P_{jet}\left(\frac{Y}{D_j}\right)$ the mean stream power and $P'_{jet}\left(\frac{Y}{D_j}\right)$ the fluctuating stream power per unit area as a function of dimensionless pool depth Y/D_j.

Annandale (2006) and Castillo et al. (2017) proposed applying a reduction factor F (Figure 3.2) to the fluctuating stream power component, $P'_{jet}\left(\frac{Y}{D_j}\right)$, in Equation 3.15 for circular and rectangular jets depending on the breakup length ratio.

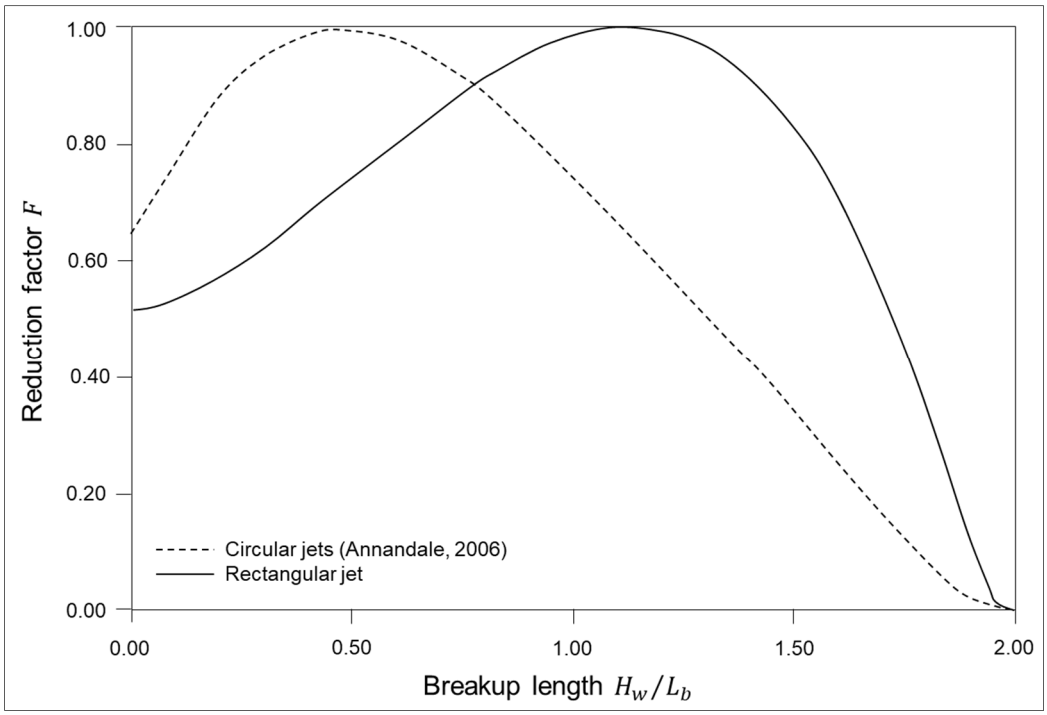

Figure 3.2: Reduction factor F of fluctuating dynamic pressure coefficient for rectangular jets (Castillo & Carrillo, 2017)

The variation in the mean stream power per unit area within the plunge pool is calculated as (Annandale, 2006):

$$P_{jet}\left(\frac{Y}{D_j}\right) = C_{sp}\left(\frac{Y}{D_j}\right)\frac{\gamma QH}{A} \approx C_p\left(\frac{Y}{D_j}\right)\frac{\gamma QH}{A} \qquad \textit{Equation 3.16}$$

where the mean stream power decay coefficient $C_{sp}(Y/D_j)$ is assumed to be equal to the average dynamic pressure coefficient $C_p(Y/D_j)$ as a function of Y/D_j, and $\frac{\gamma QH}{A}$ is the stream power per unit area at impact with the tailwater level (W/m^2).

The stream power's fluctuating portion per unit area (P'_{jet}) is calculated as (Annandale, 2006):

$$P'_{jet}\left(\frac{Y}{D_j}\right) = C'_p\left(\frac{Y}{D_j}\right)\frac{\gamma QH}{A} \qquad \textit{Equation 3.17}$$

where C'_p is the fluctuating pressure coefficient. The values for the mean and fluctuating dynamic pressure coefficients can be determined from Section 2.4.2.

The ability of the rock to resist scour is defined by the erodibility index K (see Equation 3.18), which takes several geological rock characteristics into account, such as the mass strength of the rock, block size and shape, the interparticle friction, and the joint orientation relative to the flow direction (Annandale, 1995). The parameters of Equation 3.18 can be determined from

standard lithology tables summarised in Annexure D or measured in the field. Table 3.2 summarises the formulae for determining the erodibility index parameters.

$$K = M_S \cdot K_b \cdot K_d \cdot J_S \qquad \textit{Equation 3.18}$$

in which K is the erodibility index, M_S is the mass strength number, K_b the block size number, K_d the discontinuity bond shear strength number, and J_S the relative ground structure number.

The EIM does not directly account for chemical processes that might affect the erosive resistance of the rock, but they can be taken into consideration by applying certain variables to the parameters (Mirtskhoulava, 1991).

Table 3.2: Erodibility index parameters (adapted from Annandale, 2006)

Rock characteristics	**Formulae**	**Parameter**
Mass strength number (M_s)	$M_s = C_r \cdot (0.78) \cdot (UCS)^{1.05}$ when $UCS \leq 10$ MPa $M_s = C_r \cdot (UCS)$ when $UCS > 10$ MPa $C_r = \frac{g\rho_r}{\gamma_r}$	UCS: Unconfined compressive strength C_r: Coefficient of relative density ρ_r: Rock density (kg/m^3) γ_r: Unit weight of rock ($27 \cdot 10^3$ N/m^3)
Block size number (K_b)	$K_b = \frac{RQD}{J_n}$ $RQD = (115 - 3.3J_c)$ $J_c = \left(\frac{3}{(J_x \cdot J_y \cdot J_z)^{0.33}}\right) + 3$	RQD values range between 5 and 100 J_n: Joint set number ranges between 1 and 5 J_c: joint count number J_x,J_y,J_z: Average spacing of joint sets (m)
Discontinuity bond shear strength (K_d)	$K_d = \frac{J_r}{J_a}$	J_r: Joint wall roughness number J_a: Joint alteration number

The mass strength number (M_s) represents the strength of perfectly intact earth material, without discontinuities or joints (Annandale, 1995). The mass strength number also represents the rock material's ability to resist break up and should be representative of the expected field conditions (Annandale, 1995). Weathering weakens the rock and affects the mass strength number and must therefore be accounted for (Annandale, 2006).

The block size number (K_b) represents the mean size of the rock blocks (Annandale, 1995, 2006). The block size number is determined by the number of discontinuities or joint sets (J_n) and the joint spacing is defined by the rock quality designation (RQD) (Annandale, 2006). Normally larger rock blocks are more difficult to erode and provide a greater erosive resistance than smaller rock blocks.

The interparticle strength between blocks (discontinuity shear) is based on the rock edge roughness, edge spacing, joint alteration and the fill material between the joints. The discontinuity bond shear strength number (K_d) is therefore directly proportional to the friction that develops between rock blocks. The shear strength between blocks would increase for smaller joint aperture and rougher surface edges. Thus, the block would be harder to erode corresponding to an increased discontinuity bond shear strength number. Joint walls are effectively in contact with each other for 1 mm joint spacing, whereas joint walls do not come into contact with each other upon shear for 5 mm and greater joint spacing (Kirsten, 1982).

The relative ground structure number (J_s) describes the erosion resistance of the rock due to the structure of the ground relative to the direction of the stream flow (Annandale, 2006). The shape and orientation of individual blocks, based on the joint set spacing, dip angles and dip directions are incorporated in the ground structure number (Annandale, 1995).

The orientation and shape of the rock blocks affect the ease with which the stream flow can penetrate the joints and dislodge the blocks. Joint structures dipped in the direction of the flow (dipping angle of the rock measured from the horizontal relative to the flow direction) are more likely to fail due to scour than if the joint structure dips against the flow direction. The well-known Ricobayo Dam case study highlights the role that the geological structure has on the erodibility of rock. The rock joint structure of the dam spillway is shown in Figure 3.3. On the downstream side of the spillway (Zone 1), the joint set dips in the direction of the flow, enabling sliding failure of large rock blocks. In Zone 2 (upstream side of spillway) the joint structure is dipped against the flow direction, making it more difficult to remove rock blocks from the bed.

The erodibility of the rock is also impacted by the shape of the rock that is represented by the ratio $r = \frac{z_b}{x_b}$, with x_b and z_b the length and thickness of the rock block. Equi-sided blocks would be more likely to fail due to scour and the removal of blocks compared to elongated rock blocks. Thus, larger r-ratios represent rock that is more resistant to scour (Annandale, 2006).

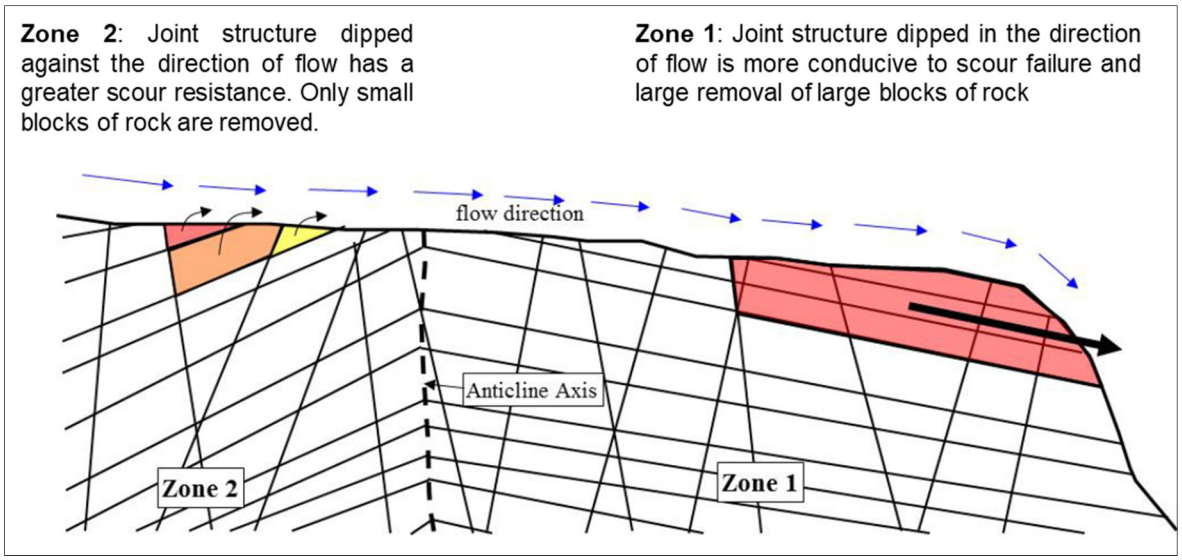

Figure 3.3: Ricobayo Dam cross-section showing rock joint structure (adapted from Annandale, 2006)

The scour threshold for the rock strength in terms of stream power per unit area (kW/m^2) is based on the erodibility index K (Annandale, 2006):

$$P_{rock} = 0.48(K)^{0.44} \text{ if } K \leq 0.1 \qquad \textit{Equation 3.19}$$

$$P_{rock} = K^{0.75} \text{ if } K > 0.1 \qquad \textit{Equation 3.20}$$

According to the EIM, the maximum scour depth is reached when the available stream power is equal to the resistive capacity of the rock ($P_{pool} \leq P_{rock}$) (Annandale, 2006).

3.4.2. *Comprehensive Scour Model*

The physically-based Comprehensive Scour Model (CSM) was developed to predict the ultimate scour depth and the evolution of the scour formation of any type of jointed rock. The model is based on near-prototype conditions in order to reproduce the dynamic pressure fluctuations at the plunge pool bottom and inside the rock joints correctly (Bollaert, 2002).

Bollaert (2002) used steel plates to model the rock mass and to represent one and two-dimensional configurations of open and close-ended rock joints. The model was developed for circular vertical jets.

The CSM is based on the assumption that rock scouring is governed by multi-phase interaction (air, water and rock) and that transient pressure effects in joints, such as oscillations and resonance, are one of the main physical processes for scour formation. The method also outlined that the presence of air in rock joints highly influences the pressure wave velocity (Bollaert & Schleiss, 2001).

The model considers the characteristics of the plunging jet (issuance velocity V_i and diameter D_i, and initial turbulence intensity T_u), diffusion and aeration of the jet through the air and in the plunge pool, the geo-mechanical properties of the rock mass, and the pressure fluctuations and hydrodynamic loading at the plunge pool floor and inside the rock joints (Bollaert, 2002). Therefore, the structure of the CSM consists of three modules, namely the falling jet, the plunge pool and the rock mass, as presented in Figure 2.1.

The falling jet and plunge pool modules define the hydrodynamic loading exerted by the jet onto the bedrock as discussed in Sections 2.3 and 2.4 respectively.

The rock mass module implements the rock scour mechanisms discussed in Section 2.5.2 (fracturing, rock removal and peeling) (Bollaert et al., 2015). The rock mass module has some limitations as the method simplifies the rock block geometry to a rectangular block. The rock mass module comprises of three separate detachment and transport methods describing rock failure, namely:

1. **Comprehensive Fracture Mechanics (CFM):** Determines the ultimate scour depth by expressing hydrodynamic fracturing (brittle or fatigue failure) of closed-ended rock joints (joint network has not completely formed yet) (Bollaert & Lesleighter, 2014).
2. **Dynamic Impulsion method (DI):** Expresses the ejection (dynamic uplift) of individual rock blocks due to sudden uplift pressures from the completely jointed rock (Bollaert et al., 2012b).
3. **Quasi-Steady Impulsion method (QSI):** Expresses the peeling off of thin layers of protruding rock blocks due to quasi-steady wall jet flows (Bollaert, 2012).

3.4.2.1 Comprehensive Fracture Mechanics method

The Comprehensive Fracture Mechanics (CFM) method assesses instantaneous or time-dependant joint propagation due to hydrodynamic fracturing of closed-end joints (Bollaert & Lesleighter, 2014). The CFM method can quantify the ultimate scour depth related to the considered flow event, as well as the time evolution of the scour development (Bollaert, 2011). Thus, the CFM method accounts for the time required for a fissure to propagate until a distinct rock block is created (Bollaert, 2010a).

The current study investigated the scour of completely jointed rock. Therefore, refer to Bollaert (2002), Bollaert (2004), Bollaert and Schleiss (2005), Bollaert et al. (2005), Bollaert and Lesleighter (2014), Bollaert et al. (2015) for a detailed explanation of the CFM method.

3.4.2.2 Dynamic Impulsion method

The Dynamic Impulsion (DI) method analyses sudden rock block ejection due to uplift pressures on individual rock blocks from the completely jointed rock bed. The net impulse or maximum dynamic impulsion underneath a rock block can be obtained by time integration of the net forces acting on and within the rock block (illustrated in Figure 2.7b in Section 2.5.2) (Bollaert, 2002):

$$I_{\Delta t,pulse} = \int_0^{\Delta t,pulse} (F_u - F_o - G_b - F_{sh})dt = mV_{\Delta t,pulse} \qquad \text{Equation 3.21}$$

where F_u and F_0 are the forces under and over the block (N) respectively, G_b is the submerged weight of the block (N) and F_{sh} represents the shear and interlocking forces on the block (N), m is the mass of the block (kg), $V_{\Delta t,pulse}$ is the average velocity (m/s) experienced by the rock block during time period Δt, $\Delta t, pulse$ is the time interval (s) of certain pressure pulse(s) and $I_{\Delta t,pulse}$ is the impulse on the rock block (Ns).

According to Bollaert and Schleiss (2005), the first step in the DI method is to define the maximum net impulsion as the product of a net force acting on the rock block and a period time. The corresponding pressure is non-dimensionalised by the incoming kinetic energy of the jet $V^2/2g$, resulting in the net uplift pressure coefficient (C_{up}). The time period is made non-dimensional by the travel period of pressure waves inside rock joints characterised as follows:

$$T_{up} = 2L_f/c \qquad \text{Equation 3.22}$$

with L_f the joint length ($L_f = x_b + 2z_b$), with x_b the width of the rock block (m) and z_b the height of the rock block (m), and the mean pressure wave celerity c assumed as 100 m/s by Bollaert (2002). The mean pressure wave celerity is a function of the air content in the water and can be lower that the assumed 100 m/s that results in a higher uplift pressure. The non-dimensional impulsion coefficient (C_I) can therefore be defined as follows:

$$C_I = C_{up} \cdot T_{up} = \frac{V_j^2 L_f}{g \cdot c} \qquad \text{Equation 3.23}$$

Bollaert (2002) proposed a second order polynomial function to calculate the dynamic impulsion coefficient (C_I) for impinging jets for ${}^{Y}/_{D_j}$ values less than 18:

$$C_I = 0.0035\left(\frac{Y}{D_j}\right)^2 - 0.119\left(\frac{Y}{D_j}\right) + 1.22 \qquad \textit{Equation 3.24}$$

with Y the total plunge pool depth $(y_w + y_s)$, and D_j the jet diameter at impact with the plunge pool free surface (m).

The maximum net impulsion (I_{max}) of fluctuating pressures on the pool bottom due to an impinging jet (excluding the weight and friction forces) is obtained as follows (Bollaert, 2002):

$$I_{max} = C_I A\gamma \frac{V_j^2 L_f}{gc} \qquad \textit{Equation 3.25}$$

The submerged weight of the rock block can be determined by using Equation 3.26 (Bollaert, 2002) .

$$G_b = (\gamma_r - \gamma)V_b \qquad \textit{Equation 3.26}$$

where V_b is the volume of the rock block (m^3).

The resistance offered by the weight of the rock block is the product of the submerged weight (G_b) and T_{up}.

Failure of the rock block is described by the displacement the block undergoes due to the net impulse during time period ∆t. The net uplift displacement h_{up} of a rock block, defined by Equation 3.27, is obtained by transformation of $V_{\Delta t,pulse}$ in Equation 3.21 (Annandale, 2006). As the block is ejected out of the bed matrix, the kinetic energy (velocity) applied to the block is transformed into potential energy.

$$h_{up} = \frac{{V_{\Delta t,pulse}}^2}{2g} \qquad \textit{Equation 3.27}$$

If the height that the block is lifted (h_{up}) during the time period (Δt), is high enough, the particle or rock block would be ejected out of the matrix and become mobilized. Tightly jointed rock, for example, would require a vertical displacement close to its height $(h_{up}/z_b > 1)$, while rock which is loosely jointed would require a lower value of h_{up}/z_b. Bollaert (2002) proposed criteria for determining whether a rock block would experience incipient motion as shown in Table 3.3.

Table 3.3: Incipient motion criteria for DI method (Bollaert, 2002)

Ratio	Rock block condition
$\frac{h_{up}}{z_b} \leq 0.1$	No movement
$0.1 < \frac{h_{up}}{z_b} < 0.5$	Vibration occurs
$0.5 < \frac{h_{up}}{z_b} < 1$	Vibration occurs and motion/removal likely to occur
$\frac{h_{up}}{z_b} \geq 1$	Block is removed from matrix

3.4.2.3 Quasi-Steady Impulsion method

The Quasi-Steady Impulsion (QSI) method (Bollaert, 2012) calculates the peeling of protruding rock blocks along thin layers in the wall jet region parallel to the plunge pool floor as illustrated in Figure 2.7c in Section 2.5.2. The quasi-steady high-velocity wall jets parallel to the pool floor create uplift forces on protruding rock blocks (Bollaert & Hofland, 2004). The wall jet would "pluck" or "peel" the rock block from the bed matrix when the quasi-steady uplift force (Equation 3.28) can overcome the submerged weight (Equation 3.26) of the protruding rock block (Pan et al., 2014).

$$F_{QSL} = C_{uplift} \cdot \gamma \cdot A_{exp} \cdot \frac{{V_{Xi,max}}^2}{2g} \qquad \textit{Equation 3.28}$$

where C_{uplift} is the net uplift pressure coefficient summarised in Annexure E, γ is the unit weight of water (N/m^3), A_{exp} is the exposed area of the rock block (m^2), and $V_{Xi,max}$ is the flow velocity (m/s)of the wall jet X-distance from the impingement point (Equation 3.31).

The plunging jet is deflected in both up- and downstream directions upon impact with the pool bottom as seen in Figure 3.4. The quotient of the discharge deflected up- and downstream depends on the jet impingement angle (δ) with the pool bottom set out in Table 3.4. As a starting point, the jet impingement angle (δ) with the pool bottom may be assumed equal to the impingement angle with the tailwater level (θ_j) (Bollaert, 2012).

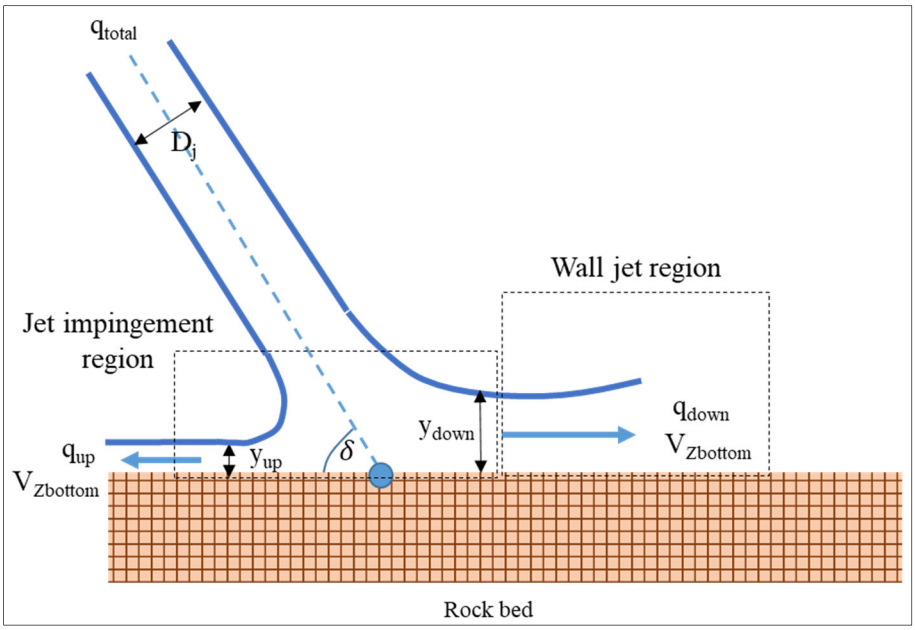

Figure 3.4: Deflection of a jet at pool bottom with wall jet regions (adapted from Bollaert, 2012)

Table 3.4: Discharge distribution of wall jets (Bollaert, 2012)

Jet angle (δ)	10°	20°	30°	40°	90°
q_{up}	1.5%	6.0%	7.0%	12.0%	50.0%
q_{down}	98.5%	94.0%	93.0%	88.0%	50.0%

The up- and downstream wall jet thicknesses y_{up} and y_{down} are theoretically determined with Equation 3.29 and Equation 3.30 respectively, with initial unit discharge q_{total} and jet diameter D_j impinging on the pool bed (Bollaert, 2012).

$$\frac{q_{up}}{q_{total}} = \frac{y_{up}}{D_j} = \frac{1}{2}(1 - cos\delta) \qquad \textit{Equation 3.29}$$

$$\frac{q_{down}}{q_{total}} = \frac{y_{down}}{D_j} = \frac{1}{2}(1 + cos\delta) \qquad \textit{Equation 3.30}$$

Once the jet deflects, the wall jet velocity at a horizontal distance X_i from the point of deflection can be characterised by its initial flow velocity ($V_{Zbottom}$) and initial thickness y_{up} or y_{down}. Initiating from the impingement point, the wall jets develop radially outwards following self-preserving velocity profiles given by Equation 3.31 (Beltaos and Rajaratnam, 1973, as cited in Bollaert, 2012). $V_{Xi,max}$ expresses the maximum cross-sectional jet velocity decay over the lateral distance X_i from the impingement point (Bollaert et al., 2015).

$$\frac{V_{Xi,max}}{V_{Zbottom}} = \frac{3.5}{\sqrt{\frac{X_i}{y_{down}}}} \qquad \textit{Equation 3.31}$$

The initial flow velocity of the wall jet at impingement $V_{Zbottom}$ depends on the jet's diffusion angle (α in Figure 2.2) and the development length through the plunge pool ($y_w + y_s$). $V_{Zbottom}$ changes continuously with the scour formation (Bollaert, 2012). Several researchers proposed relationships to determine the velocity decay through the plunge pool due to jet diffusion. The velocity decay through the plunge pool would increase for a greater jet diffusion angle (α).

Hartung and Hasuler (1973, as cited in Bollaert, 2012), proposed Equation 3.32 and Equation 3.33 to determine the velocity decay for circular and rectangular plunging jets, respectively.

$$\frac{V_{Zbottom}}{V_j} = \frac{Z_{core}}{Z} \qquad \text{for circular jets} \qquad \textit{Equation 3.32}$$

$$\frac{V_{Zbottom}}{V_j} = \sqrt{\frac{Z_{core}}{Z}} \qquad \text{for rectangular jets} \qquad \textit{Equation 3.33}$$

where Z is the depth below tailwater depth (m) and Z_{core} is the distance required for the jet core to become diffused in the plunge pool depth (m), generally taken as four times the jet diameter/thickness at impact (m).

Ervine and Falvey (1987) proposed Equation 3.34 to calculate the velocity decay of circular jets in the developed region.

$$V_{Zbottom} = \frac{4V_j D_j}{Z} \qquad \textit{Equation 3.34}$$

Beltoas and Rajaratnam (1974), as cited in Bollaert (2002), proposed Equation 3.35 to determine the velocity decay of circular jets.

$$\frac{V_{Zbottom}}{V_j} = 0.508\left(\frac{D_j}{Z}\right)^{0.5} \qquad \text{Equation 3.35}$$

Bohrer et al. (1998) studied the velocity decay of developed and undeveloped rectangular jets in plunge pools. According to Bohrer et al. (1998), the relationship for the velocity decay for developed rectangular jets (no core) is expressed as:

$$-\ln\left(\frac{V_{Zbottom}}{V_j}\right) = -0.638ln\left[\left(\frac{\rho_i}{\rho}\right)\left(\frac{{V_j}^2}{gZ}\right)\right] + 1.848 \qquad \textit{Equation 3.36}$$

with an application range of $-0.42 < ln\left[\left(\frac{\rho_i}{\rho}\right)\left(\frac{V_j{}^2}{gZ}\right)\right] < 2.05$, and minimum plunge pool depth $Y = \frac{\left[\left(\frac{\rho_i}{\rho}\right)\left(\frac{V_j{}^2}{g}\right)\right]}{18.1}$.

Equation 3.37 expresses the relationship for the velocity decay for undeveloped rectangular jets (core intact), with an application range $0.51 < \left(\frac{\rho_i}{\rho}\right)\left(\frac{V_j{}^2}{gZ}\right) < 5.76$ and minimum plunge pool depth $Y = \frac{\left[\left(\frac{\rho_i}{\rho}\right)\left(\frac{V_j{}^2}{g}\right)\right]}{12}$.

$$\frac{V_{Zbottom}}{V_j} = 0.0675\left[\left(\frac{\rho_i}{\rho}\right)\left(\frac{V_j{}^2}{gZ}\right)\right] + 0.1903 \qquad \textit{Equation 3.37}$$

where ρ_i is the average density of the mixture (kg/m^3), calculated as

$$\rho_i = (1-\beta)\rho \qquad \textit{Equation 3.38}$$

3.4.3. *Critical Pressure method*

In a similar manner as the DI method, the critical uplift pressure for scour initiation of a rock bed subjected to an impinging jet could be used to determine when a rock block would become dislodged from the bed matrix. This scour prediction method is named the Critical Pressure method in this current study. An equilibrium scour hole is obtained when the condition $P_{actual} < P_{critical}$ is met. The height a block should be lifted, defined in Table 3.3, for the particle to be displaced out of the bed matrix and become mobilized is quantified as (Annandale, 2006):

$$h_{up} = \left(2\frac{L_f}{c}\right)^2 \cdot \frac{1}{2g \cdot x_b^4 \cdot z_b^2 \cdot \rho_r^2} \cdot \left[P_u \cdot x_b^2 - G_b - F_{sh}\right]^2 \qquad \text{Equation 3.39}$$

with the critical net uplift pressure (P_u) underneath a rock block with open-ended joints calculated with Equation 3.40 (Bollaert, 2002).

$$P_u = \gamma C_I \frac{V_j^2}{2g} \qquad \text{Equation 3.40}$$

3.5. Alternative methods for predicting rock scour

3.5.1. *3D rock scour analytical methods*

The Block Scour Spectrum (BSS) is a three-dimensional analytical method for determining the erosive resistance of rock blocks subjected to an impinging jet. The BSS aims to determine

the erosive resistance of rock blocks, which depends on the rock mass and the orientation of the resultant force or loading applied to the rock block. Both gravity and hydrodynamic forces are considered in the BSS method. The BSS comprises kinematic, stability and spectrum analysis modules. The method can prioritise the rock blocks according to their scour resistance and thus identify potential locations where scour initiation is likely to occur, thus allowing the implementation of efficient scour control measures to be implemented. The BSS method assumes that block removal occurs along existing joints by separation or translational sliding (Kieffer & Goodman, 2012).

George (2015) researched three-dimensional rock scour in detail by incorporating the hydrodynamic characteristics of the plunging jet. The analytical method evaluates block stability in a pseudo-static manner by using block theory limit equilibrium and kinematic constraint formulae. To assess rock block stability, the magnitude, duration and distribution of the hydraulic forces applied to the block should be accounted for. The erodibility analysis is done by incorporating the applied hydrodynamic loads into the active resultant force vector ($\vec{r}$). The active forces acting on a rock block are mainly the pseudo-static pressures applied normal to the block faces and the submerged weight of the rock block. When assuming a uniform pressure distribution over the block faces, the active resultant force vector ($\vec{r}$) can be expressed as:

$$\vec{r} = \sum_{i}^{n} P_{si} \cdot A_i \cdot \vec{v_i} + \overrightarrow{G_b} = \sum_{i}^{n} \frac{1}{2} \cdot \rho \cdot u^2 \cdot C_{pi} \cdot A_i \cdot \vec{v_i} + \overrightarrow{G_b} \qquad \textit{Equation 3.41}$$

where P_{si} is the pseudo-static pressure (Pa) on the i^{th} block face, A_i is the area (m^2) of the i^{th} block face, ρ is the water density (kg/m^3), u is the flow velocity (m/s), C_{pi} is the mean dynamic pressure coefficient on the i^{th} block face, n is the total number of block faces, $\vec{v_i}$ is the block-side unit normal vector and $\overrightarrow{G_b}$ is the submerged weight (N) of the rock block due to gravity. Additional forces, such as shear forces, could be incorporated by adding their respective vector quantities to Equation 3.41.

3.5.2. *Block stability in 3D*

Block stability in three-dimensions (BS3D) is an incremental-iterative algorithm and code that could be used to analyse all failure modes of rock blocks due to water forces and pressure loadings (Asadollahi et al., 2011). The algorithm considers the stability of single rock blocks in plunge pools, similar to the DI method. However, the BS3D method has a number of advantages over the DI method, such as the capability to analyse all failure modes (Rashidian & Asadollahi, 2012).

According to the BS3D method, the net impulse could be determined with Equation 3.42 (Asadollahi & Tonon, 2010), which is similar to Equation 3.21 of the DI method.

$$F_{\Delta t} = F \cdot \Delta t = m \cdot V_{\Delta t} = m \cdot a \cdot \Delta t \qquad \textit{Equation 3.42}$$

where $F_{\Delta t}$ is the net impulse on the block (N.s), F is the unbalance force due to maximum dynamic pressure fluctuations (N), Δt is the maximum duration (s), m is the block mass (kg), $V_{\Delta t}$ is the initial velocity (m/s), and a is the acceleration of the block due to the unbalanced force (m/s^2).

The maximum upward displacement (h_{up}) is determined with Equation 3.43 (Asadollahi & Tonon, 2010), similar to Equation 3.27 for the DI method.

$$h_{up} = V_{\Delta t} \cdot t_{up} - g \cdot \frac{t_{up}^2}{2} \qquad \text{Equation 3.43}$$

where h_{up} is the maximum upward displacement of the block (m) and t_{up} is the duration of the block movement due to the initial velocity (s).

According to the BS3D method, rock failure occurs when the maximum upward block displacement is greater than a quarter of the block height ($\frac{h_{up}}{z_b} \geq 0.25$) (Asadollahi et al., 2011).

3.5.3. *Block stability*

Maleki and Fiorotto (2019) developed a block stability method that uses the peak fluctuating pressure coefficient at impingement to predict stability of a rock block. The method calculates the rock block stability thickness, based only on the fluctuating dynamic pressures and neglecting the mean dynamic pressures. The thickness S (vertical dimension) of a stable rock block is obtained as follows (Maleki & Fiorotto, 2019):

$$S = \frac{n\Omega\sigma_{pmax}}{(\gamma_r - \gamma)/\gamma\, L^2} \qquad \textit{Equation 3.44}$$

where $n = 6$ according to Castillo et al. (2015), Ω is the uplift coefficient defined byEquation 3.45, σ_{pmax} is the maximum value of the standard deviation of the fluctuating pressures ($C'_{p\,max}\gamma\frac{V_j^2}{2g}$) (Pa), and L is the characteristic block length (m).

$$\Omega = 0.35\left(1 - e^{(-L'/0.89)}\right) \qquad \textit{Equation 3.45}$$

with L' being the dimensionless length calculated as L/b. The distance (m) from the jet axis to the point where the average velocity halves its maximum value (b) is calculated as:

$$b\,(\zeta_1)/D_j = 0.228 + 0.0833\,(\zeta_1)/D_j + 0.0015\big((\zeta_1)/D_j\big)^2 \qquad \textit{Equation 3.46}$$

where ζ_1 is the jet trajectory length (m) in the plunge pool.

Maleki and Fiorotto (2019) neglect the downward force (F_0) on the rock block in the stability computation, since the bottom fluctuating pressures are amplified inside the rock joints. However, for stability, the submerged weight of the rock block should be at least equal to the uplift force created by the plunging jet. The following derivation of block stability assumes that the gravitational force should be equal to the buoyancy force on the block (Equation 3.47), which differs to Maleki and Fiorotto's (2019) approach:

$$F_{nett} = [L^2 \cdot S \cdot \gamma_r] - [L^2 \cdot S \cdot \gamma] \qquad \textit{Equation 3.47}$$

The uplift force is equal to the product of the amplified pressures inside the rock joints and the lower base area of the rock block:

$$F_{uplift} = n\Omega\sigma_{pmax}L^2 \qquad \textit{Equation 3.48}$$

From Equation 3.47 and Equation 3.48:

$$L^2S(\gamma_r - \gamma) = n\Omega\sigma_{pmax}L^2 \qquad \textit{Equation 3.49}$$

Thus, the stability block thickness is derived as:

$$S = \frac{n\Omega\sigma_{pmax}}{(\gamma_r - \gamma)} \qquad \textit{Equation 3.50}$$

Thus, the stable rock block thickness (vertical axis) is only dependent on the difference in unit pressure over and under the rock block.

3.5.4. *Statistical pattern recognition*

Statistical pattern recognition techniques were developed to determine the scour depth in plunge pools. According to Rashidian and Asadollahi (2012), the approach used in the statistical recognition techniques overestimate the scour depth by 34%, but the method is significantly simpler to use in comparison with the DI and BS3D methods. The statistical pattern recognition method estimates the scour depth with Equation 3.51 (Rashidian & Asadollahi, 2012).

$$y_s = \frac{-B + \sqrt{B^2 - 4C}}{2} \qquad \textit{Equation 3.51}$$

where

$$B = 0.57\frac{{V_j}^2 \gamma D_j}{2g\gamma_r a} - 8.02D_j - 0.89y_w \quad \text{Equation 3.52}$$

$$C = -1.07\frac{{V_j}^2 \gamma D_j}{2g\gamma_r} \quad \text{Equation 3.53}$$

with γ_r being the unit weight of rock (N/m^3), and a the size of rock blocks (m).

3.6. Limitations of current scour prediction methods

Some methods, such as the EIM, are limited, since they provide a generalised evaluation of rock scour and do not explicitly account for all scour mechanisms, such as block removal, brittle fracture and fatigue failure (Kieffer & Goodman, 2012, and George, 2015). As the methods consider rock joint orientation in a two-dimensional context, they cannot capture rock block removal in a three-dimensional fractured rock mass (George, 2015).

The current scour prediction methods can only predict the scour depth at the centreline of the jet (excluding the QSI method) and cannot provide information on the equilibrium scour hole shape (depth, length, width and scour volume).

Pells et al. (2015) argued that to determine the extent of the scour of unlined dam spillways in rock, a gradation that indicates regions of erosion (Figure 3.5) should be used rather than a threshold line. The erosion regions presented by Pells (2016) compared well with the independent data set presented by Van Schalkwyk et al. (1995). Wibowo et al. (2005) conducted a logistic analysis of Annandale's scour threshold and developed an equation providing the probability of scour with the stream power and erodibility index known (Equation 3.54). When using Equation 3.54 developed by Wibowo et al. (2005), one can demonstrate that the threshold line representing 0.001% probability of scour (negligible scour) lies along the upper boundary of the "Hoofsaaklik Geen Erosie" region of Van Schalkwyk et al. (1995) and Pells' (2016) green region, and the threshold line representing 50% probability of scour corresponds to Annandale's scour threshold, which lies almost exactly on the lower boundary of the "Hoofsaaklik Erensitge Erosie" region of Van Schalkwyk et al.'s (1995) data. Thus, using the concept of stream power and the Erodibility index (Kirsten index) by three independent researchers using different databases essentially reach the same conclusion.

$$P(E) = \frac{1}{1 + e^{\left(-1(-1.859 - 7.029\log(K) + 9.798\log(AP))\right)}} \quad \text{Equation 3.54}$$

where $P(E)$ is the probability of Erosion (%), K is the erodibility index, and AP is the applied stream power (KW/m^2).

Based on the abovementioned limitations, the current research focusses on developing a method for predicting the scour hole shape in a three-dimensional movable rock mass, comprising multiple blocks while under three-dimensional flow conditions and with various joint structure orientations.

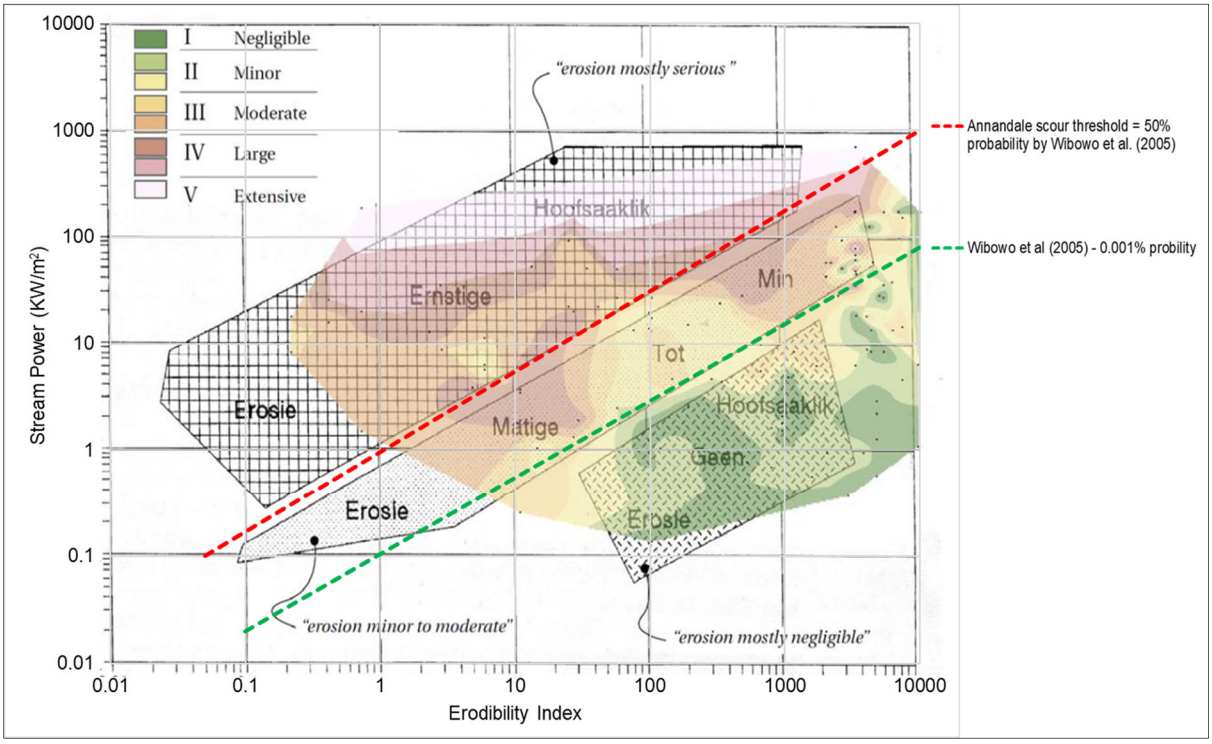

Figure 3.5: Erosion extent region contours (Pells et al., 2015) compared to Van Schalkwyk et al. (1995) data (black lines) and Wibowo et al.'s (2015) logistic regression equation

3.7. Scour prediction summary

Currently, there is no universally agreed upon method to predict the equilibrium scour depth due to plunging jets at dams accurately, since each method has its limitations. The existing methods used to predict rock scour due to a plunging jet are physical models, empirical formulae, semi-empirical methods and numerical simulations (discussed in Section 4).

Empirical formulae developed by different authors used to predict the equilibrium rock scour depth are limited to the test ranges and differences between the formulas. Semi-empirical methods consider the erosive potential of the rock bed, as well as the erosive capacity dissipation of the jet through the air and plunge pool. However, the hydrodynamic behaviour of rectangular jets through the air and plunge pool have not been studied in sufficient depth.

4. LITERATURE REVIEW OF NUMERICAL MODELLING OF BEDROCK SCOURING

4.1. Background

Several Computational Fluid Dynamics (CFD) software packages are available on the market for the numerical simulation of fluid flow and turbulence at dam spillways. The aim of this section is to provide an overview of the currently available numerical model packages as a background to the current study and to select the appropriate software for application in the current study. The overview is not complete, but indicates the development and general approach used in numerical simulations in rock scour.

4.2. CFD software currently available on the market

4.2.1. *FLUENT model*

FLUENT is a computer program that is a product of ANSYS's fluid analysis software range. FLUENT uses the finite volume method to model fluid flow and the transfer of heat in complex geometries. The program can simulate laminar and turbulent flow in three-dimensional geometries. User-Defined Functions (UDF) are a special feature in FLUENT that allows the user to customise certain aspect, such as boundary conditions, material properties and transport formulas.

In the literature, the studies that used FLUENT to simulate the flow at dam spillways are Karim and Ali (2000), Boroomand et al. (2007), Avila and Pitt (2008), Dey and Eldho (2009), and Dasgupta et al. (2011).

Dasgupta et al. (2011) simulated the plunge pool scour hole at Kariba Dam on the Zambezi River, Zimbabwe. FLUENT was used to simulate three-dimensional computational fluid dynamics, coupled with two-dimensional universal distinct element code (UDEC) to simulate the rock mass. Even though rock scour was simulated in two-dimensions, the approach shows promise in developing numerical methods to analyse rock scour in three-dimensions.

4.2.2. *FLOW-3D*

FLOW-3D provides an accurate and fast CFD solution for solving transient, free surface problems. FLOW-3D investigates the dynamic behaviour of fluids and gases by means of the finite volume method. The program focusses on free surface and multi-phase problems. FLOW-3D has the ability to prescribe specific properties for different non-cohesive sediment types. The sediment model of the program is primarily empirical in nature and based on

experimental data. The program makes use of the median diameter d_{50} of the material with the maximum particle size being 35 mm for version 11.1 (Castillo & Carrillo, 2016). The program cannot account for specific particle shapes.

Researchers that used FLOW-3D to simulate spillways hydraulics are Castillo and Carrillo (2014, 2016 and 2017), Savage and Johnson (2001), Avila and Pitt (2008), Chanel and Doering (2007), Kamanbedast and Aghamajidi (2013), and Epely-Chauvin et al. (2014).

4.2.3. *Smoothed Particle Hydrodynamics (SPH)*

Smoothed Particle Hydrodynamics (SPH) is a two- and three-dimensional meshless computation method that models free surface incompressible flow. SPH is able to simulate flows where there is complex moving boundaries. Researchers that have used SPH for modelling fluid dynamics or sediment erosion include De Padova et al. (2013), Ferrari (2010) and Zubeldia et al. (2016).

4.2.4. *Delft3D*

Delft3D is a three-dimensional numerical model that simulates the hydrodynamics, sediment morphology and transport, and water quality typically for estuarine and coastal environments. For example, the program can simulate unsteady flow and sediment transport that results from tidal forces. The sigma coordinate approach or Z-layer approach is used to define the vertical grid. Thus, Delft3D is more appropriate to be used for far-source problems and not for near-source problems, like rock scour due to a plunging jet.

4.2.5. *Rocky*

Rocky is a three-dimensional Discrete Element Modelling (DEM) software that simulates the flow behaviour of bulk particles through a system. Rocky is able to simulate the settling and compaction of various particles shapes (spherical, faceted, cylindrical, polygon, polyhedron and briquette) and sizes.

Rocky is fully coupled with FLUENT (two-way coupling). The coupled DEM-CFD approach makes numerical modelling of granular-fluid systems possible, such as the scouring of the bedrock of a plunge pool. However, Rocky has not been used in rock scour research due to the long time required to run and investigate simulations.

4.3. General background of some numerical modelling principles

Numerical modelling of fluids or Computational Fluid Dynamics (CFD), allows for the simulation or representation of the prototype processes. CFD models iteratively solve the Navier Stokes and partial differential continuity equations to obtain a numerical description of the flow field. The fluid flow is described within a computational grid that is defined by boundary conditions and turbulence models.

4.3.1. *Computational mesh*

In CFD, a computational mesh should be established that is capable of simulating the prototype with an optimum balance between computational time, stability, accuracy and grid independence. A good quality mesh is defined by low skewness (< 0.8), a high orthogonal quality (> 0.2), a low aspect ratio (< 90), and low smoothness (< 2.5) (ANSYS, 2015).

The different cell shapes available in FLUENT are as follows:

- A hexahedron mesh is generally used for simple model geometries, as this mesh provides a higher quality mesh for fewer cells when compared to a tetrahedron mesh.
- A tetrahedron mesh is used for more complex model geometries.
- A hybrid mesh uses the accuracy and efficiency of both the hexahedron and tetrahedron meshes.

For the simulation of the interaction of fluid, air and solids, a fairly dense mesh is required at the water-rock interface and also along the trajectory of a water jet falling through the air and impacting in the plunge pool. The dense mesh is required to resolve the boundary layer where air entrainment occurs. However, the mesh cell size should not be smaller than the wall boundary roughness height (ANSYS, 2015). Thus, the distance from a wall boundary to the centroid of the wall-adjacent cell should be greater than the bed roughness height (K_s), as explained in Section 4.3.2.

The permissible time step size for a stable transient model is constrained by the mesh size. Thus, a denser mesh requires a reduced time step size, increasing the computational time. The Courant number (C_u) is a spatial-time condition required for convergence that is calculated with Equation 4.1 for a three-dimensional domain (ANSYS, 2015).

$$C_u = \frac{\bar{V}\Delta t}{\Delta l_{min}} = \frac{V_x \Delta t}{\Delta l_x} + \frac{V_y \Delta t}{\Delta l_y} + \frac{V_z \Delta t}{\Delta l_z} \qquad \textit{Equation 4.1}$$

where $\bar{V}$ is the flow velocity (m/s) defined by the x-, y- and z-axis components, Δt is the time step (s), and Δl is the mesh cell size (m). The Courant number must be less than 1 for explicit solvers, compared to implicit solvers that are less sensitive to numerical instability and can tolerate larger Courant values (Versteeg & Malalasekera, 2007)

4.3.2. *Boundary conditions*

The boundary conditions define the fluid domain limits. The boundaries directly impact the quality of the results and must therefore be correctly described. The most commonly used boundary conditions are the inflow inlet and pressure outlet boundary, wall boundaries, and symmetry conditions.

Non-slip wall boundary conditions are more accurate compared to slip conditions where viscous effects are negligible or if the mesh cell size is larger than the thickness of the boundary layer. In FLUENT, the roughness height (K_s) and roughness constant (C_s) must be specified to model the roughness effects on the hydrodynamics of the fluid, for example, for the bedrock surface (ANSYS, 2015).

The default roughness height (K_s) is zero, corresponding to smooth walls. Thus, for roughness to affect the fluid, a non-zero roughness height must be specified. For a uniform sand-grain roughness bed, the roughness height can be approximated as the Chèzy roughness value, K_s. The median diameter (d_{50}) could be used to approximate the roughness height for a non-uniform sand-grain bed (ANSYS, 2015). The median particle size, d_{50}, is defined by Equation 4.2 (Pabst & Gregorova, 2007) with V_b the volume of the rock block (m^3).

$$d_{50} = \left(\frac{6}{\pi} V_b\right)^{1/3} \qquad \textit{Equation 4.2}$$

An equivalent sand-grain roughness height (refer to Figure 4.1) could be expressed as the perpendicular distance from the triangular cavities between the scoured rock bed to the pseudo-bottom. The pseudo-bottom is formed by the external edges of the scoured rock bed.

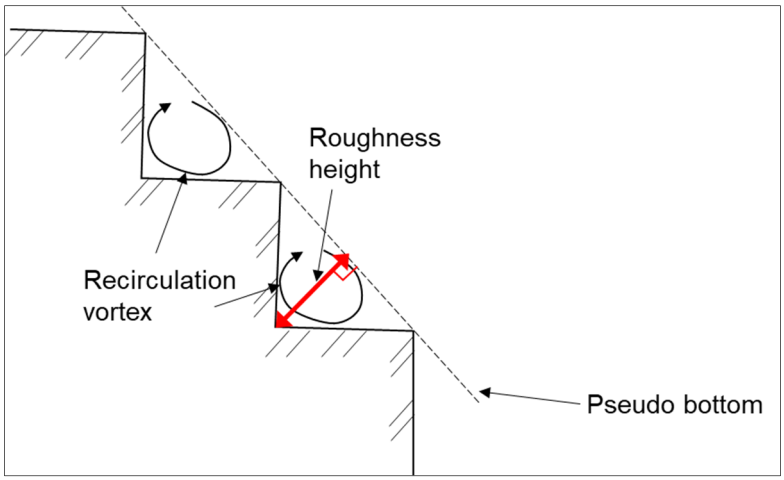

Figure 4.1: Perpendicular distance from rock cavity to pseudo-bottom

The default roughness constant (C_s) is 0.5 to reproduce Nikuradse's resistance data for pipes with uniform tightly-packed sand-grain roughness. Experiment evidence showed that for non-uniform beds a higher roughness constant (C_s = 0.5 up to 1) is more appropriate (ANSYS, 2015).

How the free surface interface of the multi-phase simulation is traced should also be considered. The free surface of the fluid is generally modelled by the multi-phase Volume of Fluid (VOF) method. The VOF model used by FLUENT solves the internal flow field and calculates the free surface profile simultaneously, thus modelling the flow formulae for both water and air and tracing the interface between the two phases (ANSYS, 2015). The VOF technique used by FLUENT is advantageous, since the interaction between the water and air is important to modelling the behaviour of the jet falling and dissipating through the air and plunge pool.

4.3.3. *Turbulence models*

Turbulence defines the fluctuating velocity and pressure components of flow with high Reynold numbers. Owing to the turbulent nature of, for example, plunging jets, a suitable turbulence model should be selected to solve the Navier-Stokes equations. There are several turbulence models since no single model is suited for solving all problems. However, each turbulence model has its own advantages and limitations. The turbulence models are briefly discussed in an overview:

- The Direct Numerical Simulation (DNS) model solves the full unsteady Navier-Stokes equations and can therefore model even the smallest meaningful eddy. The DNS model is the most accurate turbulence model. The DNS model is therefore generally

used for small Reynolds Number flow simulations, but is also described as uneconomical.

- The Large Eddy Simulations (LES) model solves the filtered Navier-Stokes equations. The model solves large eddies explicitly while smaller eddies are accounted for by sub-grids. The LES model is very accurate, but has a high computational cost.
- The Reynolds Averaged Navier-Stokes Simulation (RANS) model approximates time-averaged values of the velocities and pressures to describe the mean flow field. The RANS model consists out of various sub-models:
    - The $k-\varepsilon$ model is simple to use, economical, stable and reasonably accurate. However, the model predicts the separation of flows with less accuracy. Thus, none of the $k-\varepsilon$ models are recommended for severe pressure gradients and boundary layer separation simulations. The $k-\varepsilon$ model also fails to differentiate between, for example, the spreading rate of a circular and rectangular jet (Morgans et al., 1999). The different $k-\varepsilon$ RANS models are:
        - The standard $k-\varepsilon$ model is robust but is only applicable for fully turbulent flows. The model fails to accurately simulate highly swirled flows and eddy formations.
        - The Renormalisation Group (RNG) $k-\varepsilon$ model has improved accuracy for streamline curvature and transitional flow, and converges twice as fast than the standard $k-\varepsilon$ model (Karim & Ali, 2000).
        - The Realisable $k-\varepsilon$ model performs better than the other $k-\varepsilon$ models for complex flow separation simulations (Vonkeman, 2019)
    - The $k-\omega$ model
        - The standard $k-\omega$ model is based on the $k-\varepsilon$ model but replaces the dissipation rate (ε) with the specific dissipation rate (ω). The model performs better than the $k-\varepsilon$ models for complex boundary layer flows under high pressure gradients and flow separation.
        - The Shear Stress Transport (SST) $k-\omega$ model is a hybrid between the standard $k-\varepsilon$ and $k-\omega$ models. Illustrated in Figure 4.2, the SST $k-\omega$ turbulence model uses the standard $k-\omega$ model in the boundary layer (near wall region), and gradually changes to the $k-\varepsilon$ model in the freestream region. The SST $k-\omega$ turbulence model was developed by Menter (1994) and simulates flow separation and free shear flows more accurately compared to the other turbulence models. The $k-\omega$ model outperforms the $k-\varepsilon$ model for boundary layer flow. The $k-\omega$ model is overly sensitive to the free stream value, whereas the $k-\varepsilon$ is

not. The SST $k-\omega$ is therefore a good compromise between the $k-\varepsilon$ and $k-\omega$ models (ANSYS, 2015).

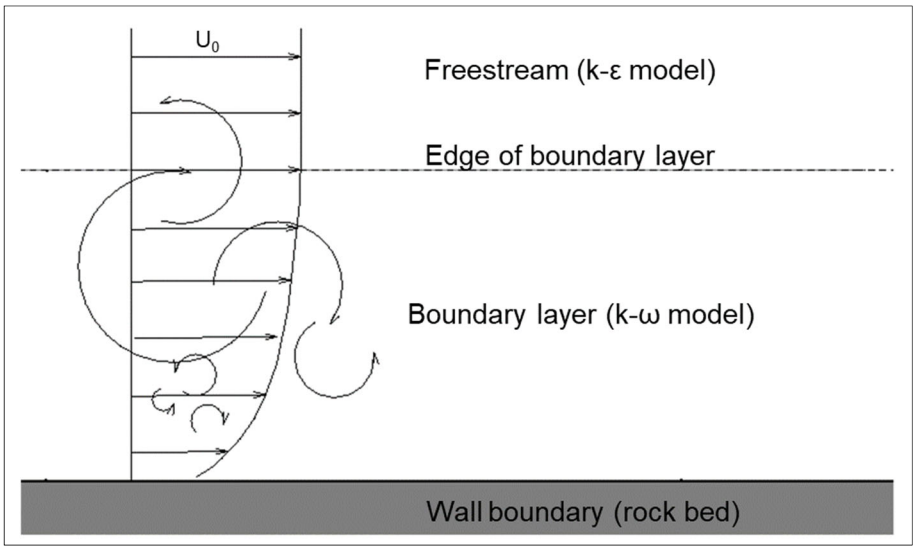

Figure 4.2: Turbulence model: SST k-ω

- The Reynolds Stress model (RSM) is suitable for flows with strong streamline curvature, circulation and separation. The RSM is more accurate, but requires two to three times more computational effort and time compared to the $k-\varepsilon$ and $k-\omega$ models (Vonkeman, 2019).

Many numerical studies have evaluated the applicability of the different turbulence models to simulate plunging jets. Evidently, the best turbulence model used to simulate rock scour due to a plunging jet is the SST $k-\omega$ model.

4.3.4. *Transient flow modelling*

According to ANSYS (2015), the PISO scheme for pressure-velocity coupling provides faster convergence for transient flow simulations than the SIMPLE scheme. However, some studies have successfully used the SIMPLE scheme in combination with the $k-\varepsilon$ turbulence model to simulate scour by a plunging jet (Neyshabouri et al., 2003).

The PRESTO! and Body Force Weighted pressure spatial discretisation schemes are recommended for natural convection problems where gravity is a dominant force. The Body Force Weighted scheme is applicable when body forces are large, i.e. for highly swirling flows. The PRESTO! scheme should rather be used for circulating flows with steep pressure gradients present (ANSYS, 2015). Therefore, the PRESTO! Spatial discretisation scheme should be used for simulating plunging jets.

4.4. Principles of proposed numerical model for falling jets

4.4.1. *Background*

For the current study, FLUENT was used to compose a model enabling the calculation of the equilibrium scour hole that forms due to a plunging jet impinging on rock downstream of a dam. The basics of fluid hydrodynamics theory incorporated in FLUENT, with respect to the Navier-Stokes equations, are discussed in this section, as well as giving insight into the theory used to model the internal turbulence phenomena.

4.4.2. *Computational Fluid Dynamic modelling (ANSYS, 2015)*

4.4.2.1 Governing Equations

The fundamental equations on which FLUENT is based to model the flow field are summarised in this section.

In developing the three-dimensional numerical model, the Volume of Fluid (VOF) multi-phase approach was followed in order to simulate water-air mixtures. The interfaces between the phases are tracked by solving the continuity equation for the volume fraction of one of the phases. The continuity equation for phase q yields:

$$\frac{\partial \alpha_q}{\partial t} + \nabla \cdot \left(\alpha_q \vec{V}_q\right) = \frac{1}{\rho_q}\left(\sum_{p=1}^{n}\left(\dot{m}_{pq} - \dot{m}_{qp}\right) + S_{\alpha_q}\right) \qquad \textit{Equation 4.3}$$

where α_q is the volume fraction of the q^{th} phase, $\vec{V}_q$ denotes the velocity of phase q, ρ_q is the density of phase q, $\dot{m}_{pq}$ characterises the mass transfer between phase p and q, and $\dot{m}_{qp}$ the mass transfer from phase q to p, and S_q the mass source term for phase q being zero. A constant density (ρ_q) was assumed. The mass transfer between phase p and q was neglected, thus $\dot{m}_{pq} = -\dot{m}_{qp} = 0$.

The volume fraction of the primary phase (α_q) is calculated based on the following constraint:

$$\sum_{q=1}^{n} \alpha_q = 1 \qquad \textit{Equation 4.4}$$

The volume fraction equation for the secondary phase is solved through explicit time discretisation by using Equation 4.5.

$$\frac{\alpha_q^{n+1}\rho_q^{n+1} - \alpha_q^n \rho_q^n}{\Delta t} V + \sum_f \left(\rho_q U_f^n \alpha_{q,f}^n\right) = \frac{1}{\rho_q}\left[\sum_{p=1}^{n}\left(\dot{m}_{pq} - \dot{m}_{qp}\right) + S_{\alpha_q}\right] V \qquad \textit{Equation 4.5}$$

where

$n+1$: index of current time step

n: previous time step index

$\alpha_{q,f}$: face value of the volume fraction of phase q, computed from the second-order upwind scheme

V: cell volume

U_f: volume flux through the face, based on normal velocity

The VOF model solves a single momentum equation throughout the domain, with the resulting velocity field being shared among the phases. The momentum equation (Equation 4.6) is dependent on the volume fraction of all the phases through properties ρ and μ:

$$\frac{\partial\left(\rho\vec{V}\right)}{\partial t} + \nabla\cdot\left(\rho\vec{V}\vec{V}\right) = -\nabla p + \nabla\cdot\left[\mu\left(\nabla\vec{V} + \nabla\vec{V}^T\right)\right] + \rho\vec{g} + \vec{F} \qquad \textit{Equation 4.6}$$

where $\vec{V}$ denotes the velocity, ρ is the pressure shared by all phases, μ is the shear viscosity, $\vec{g}$ is gravitational acceleration, and $\vec{F}$ is additional body forces.

4.4.2.2 Turbulence Model

The shear stress transport (SST) $k-\omega$ turbulence model was used in this research study to model the turbulence. The SST $k-\omega$ is a two-empirical equation model based on transport equations for the turbulence kinetic energy (k) and its specific dissipation rate (ω), obtained from Equation 4.7 and Equation 4.8 respectively.

$$\frac{\partial}{\partial t}(\rho k) + \nabla\cdot\left(\rho k\vec{V}\right) = \nabla\cdot(\Gamma_k\nabla k) + \tilde{G}_k - Y_k + S_k \qquad \textit{Equation 4.7}$$

$$\frac{\partial}{\partial t}(\rho\omega) + \nabla\cdot\left(\rho\omega\vec{V}\right) = \nabla\cdot(\Gamma_\omega\nabla\omega) + G_\omega - Y_\omega + D_\omega + S_\omega \qquad \textit{Equation 4.8}$$

where Γ_k and Γ_ω is the effective diffusivity of k and ω respectively, defined as

$$\Gamma_k = \mu + \frac{\mu_t}{\sigma_k} \qquad \textit{Equation 4.9}$$

$$\Gamma_\omega = \mu + \frac{\mu_t}{\sigma_\omega} \qquad \textit{Equation 4.10}$$

with the turbulent viscosity μ_t obtained with Equation 4.11.

$$\mu_t = \frac{\rho k}{\omega} \frac{1}{max\left[\frac{1}{\alpha^*}, \frac{SF_2}{\alpha_1 \omega}\right]} \quad \textit{Equation 4.11}$$

with S being the strain rate magnitude (Equation 4.27) and α^* is defined by Equation 4.12.

$$\alpha^* = \alpha_\infty^* \left(\frac{\alpha_0^* + R_{e_t}/R_k}{1 + R_{e_t}/R_k}\right) \quad \textit{Equation 4.12}$$

with

$$R_{e_t} = \frac{\rho k}{\mu \omega} \quad \textit{Equation 4.13}$$

$$R_k = 6 \quad \textit{Equation 4.14}$$

$$\alpha_0^* = \frac{\beta_i}{3} \quad \textit{Equation 4.15}$$

$$\beta_i = 0.072 \quad \textit{Equation 4.16}$$

σ_k and σ_ω in Equation 4.9 and Equation 4.10 represent the Prandtl numbers for k and ω respectively defined as:

$$\sigma_k = \frac{1}{F_1/\sigma_{k,1} + (1 - F_1)/\sigma_{k,2}} \quad \textit{Equation 4.17}$$

$$\sigma_\omega = \frac{1}{F_1/\sigma_{\omega,1} + (1 - F_1)/\sigma_{\omega,2}} \quad \textit{Equation 4.18}$$

F_1 and F_2 denotes the blending functions and are given by:

$$F_1 = tanh(\emptyset_1^4) \quad \textit{Equation 4.19}$$

$$\emptyset_1 = min\left[max\left(\frac{\sqrt{k}}{0.09\omega y}, \frac{500\mu}{\rho y^2 \omega}\right), \frac{4\rho k}{\sigma_{\omega,2} D_\omega^+ y^2}\right] \quad \textit{Equation 4.20}$$

$$D_\omega^+ = max\left[2\rho \frac{1}{\sigma_{\omega,2}} \frac{1}{\omega} \frac{\partial k}{\partial x_j} \frac{\partial \omega}{\partial x_j}, 10^{-10}\right] \quad \textit{Equation 4.21}$$

$$F_2 = tanh(\emptyset_2^2) \quad \textit{Equation 4.22}$$

$$\emptyset_2 = max\left(2\frac{\sqrt{k}}{0.09\omega y}, \frac{500\mu}{\rho y^2 \omega}\right) \quad \textit{Equation 4.23}$$

where D_ω^+ is the positive fraction of the cross-diffusion term and y is the distance to the next surface.

The generation of turbulence kinetic energy (k) owing to the mean velocity gradients is represented by $\tilde{G}_k$ in Equation 4.7 and is computed as follows:

$$\tilde{G}_k = min(G_k, 10\rho\beta^* k\omega) \qquad \textit{Equation 4.24}$$

with G_k defined as

$$G_k = -\rho\overline{u_i' u_j'}\frac{\partial u_j}{\partial x_i} \qquad \textit{Equation 4.25}$$

where $\overline{u_i' u_j'}$ is the specific Reynolds stress tensor and u_j is the local time-averaged flow velocity component. The turbulence generation can be simplified by using Boussinesq's hypothesis as follows:

$$G_k = \mu_t S^2 \qquad \textit{Equation 4.26}$$

where S is the mixture's mean rate-of-strain tensor, and is given as

$$S \equiv \sqrt{2S_{ij}S_{ij}} \qquad \textit{Equation 4.27}$$

The term G_ω in Equation 4.8 represents the generation of specific dissipation rate (ω) and is given by

$$G_\omega = \frac{\alpha}{v_t}\tilde{G}_k \qquad \textit{Equation 4.28}$$

The coefficient α is

$$\alpha = \frac{\alpha_\infty}{\alpha^*}\left(\frac{\alpha_0 + R_{e_t}/R_\omega}{1 + R_{e_t}/R_\omega}\right) \qquad \textit{Equation 4.29}$$

with R_ω=2.95, and α^* and R_{e_t} as defined by Equation 4.12 and Equation 4.13, respectively. The coefficient α_∞ is defined as follows for the SST $k-\omega$ model:

$$\alpha_\infty = F_1\alpha_{\infty,1} + (1 - F_1)\alpha_{\infty,2} \qquad \textit{Equation 4.30}$$

where

$$\alpha_{\infty,1} = \frac{\beta_{i,1}}{\beta_\infty^*} - \frac{\kappa^2}{\sigma_{w,1}\sqrt{\beta_\infty^*}} \qquad \textit{Equation 4.31}$$

$$\alpha_{\infty,2} = \frac{\beta_{i,2}}{\beta_\infty^*} - \frac{\kappa^2}{\sigma_{w,2}\sqrt{\beta_\infty^*}} \qquad \textit{Equation 4.32}$$

with κ = 0.41.

Y_k and Y_ω in Equation 4.7 and Equation 4.8 represent the dissipation of the k and ω because of turbulence, and are calculated respectively:

$$Y_k = \rho\beta^* k\omega \qquad \textit{Equation 4.33}$$

$$Y_\omega = \rho\beta_i \omega^2 \qquad \textit{Equation 4.34}$$

The β_i-coefficient is defined as

$$\beta_i = F_1\beta_{i,1} + (1 - F_1)\beta_{i,2} \qquad \textit{Equation 4.35}$$

with F_1 calculated from Equation 4.19.

The cross-diffusion term presented by D_ω in Equation 4.8, which blends the $k-\varepsilon$ and $k-\omega$ turbulence models, is defined as

$$D_\omega = 2(1 - F_1)\rho \frac{1}{\omega\sigma_{\omega,2}} \frac{\partial k}{\partial x_j} \frac{\partial \omega}{\partial x_j} \qquad \textit{Equation 4.36}$$

S_k and S_ω represent user-defined source terms for the turbulent kinetic energy (k) and specific energy rate (ω) in Equation 4.7 and Equation 4.8 respectively, with the default value equal to zero.

In this current research, the following model constants were used:

$\sigma_{k,1} = 1.176,$	$\sigma_{\omega,1} = 2.0\,,$	$\sigma_{k,2} = 1.0,$	$\sigma_{\omega,2} = 1.168,$	$\alpha_1 = 0.31,$
$\beta_{i,1} = 0.075,$	$\beta_{i,2} = 0.0828,$	$\alpha_\infty^* = 1,$	$\alpha_\infty = 0.52,$	$\alpha_0 = \frac{1}{9},$
$\beta_\infty^* = 0.09,$	$R_\beta = 8,$	$R_k = 6,$	$R_\omega = 2.95$	

4.5. Summary

Section 4 gives an overview of numerical modelling of fluid flow and flow of bulk particles by reviewing some of the existing numerical models that deal with hydrodynamic and discrete particle transport simulations. Generally, the hydrodynamics and particle transport are not coupled in the numerical models. A numerical model incorporating the hydrodynamic and geo-mechanical effects of rock scour would be beneficial for analysing scour downstream of a dam spillway. A three-dimensional numerical model that is able to predict rock scouring processes due to an impinging jet would therefore be beneficial in contributing to previous rock scour research. This section also address the Navier-Stokes formulae and the SST $k-\omega$ turbulent model.

5. PHYSICAL MODEL INVESTIGATIONS OF SCOURING OF FISSURED BEDROCK DUE TO PLUNGING JETS

5.1. Background

The main objective of the current research was to gain a greater understanding of the scouring process in bedrock due to spillway discharge downstream of a high head dam. Physical model tests are commonly used to investigate the depth and extent of local scour. Physical model tests were conducted in a laboratory to assess the equilibrium scour hole geometry downstream of a high head dam. The primary objective of the laboratory tests was to collect measurements of various scouring parameters in a controlled environment. The laboratory test results were compared to the predictions of other authors' equations. A dimensionless regression analysis was performed to compose equations based on the experimental data to aid in the prediction of the scour hole geometry. Subsequently, the collected physical model data was used to calibrate the three-dimensional numerical model of rock scouring presented in Section 6. A thorough understanding of all the parameters of the reproduced scouring phenomena was required that could be transferred to various prototype conditions. Details regarding the experimental set up and procedure, as well as the results are presented in this section.

5.2. Model scale

Bollaert and Schleiss (2005) determined that the pressures inside the rock joints are accurately reproduced in a physical model with an approximate scale of 1:10. Whereas Boushaba et al. (2013) found that the scale effect on the plunging jet velocity, initial turbulence, plunge pool aeration and the dynamic pressures at the bedrock surface are negligible for a physical model scale not exceeding 1:20. Physical model scales exceeding 1:100 could cause incorrect aeration results. Therefore, an undistorted model scale not exceeding 1:20 is recommended for the experimental results from this study. Additionally, with the available laboratory height, a 1:20 model scale is able to replicate realistic prototype spillway heights (i.e. 60 m up to 100 m).

The objective of the physical model was to reproduce near-prototype jet conditions (air entrainment, flow velocity and turbulence) by minimising scale effects related to rock scour modelling. The generated scour mechanics at the plunge pool bottom and inside the joint network would thus be representative of the prototype scour mechanics' spectra (Duarte, 2014).

A free surface gradient was present in the issuance canal. Gravitational and inertial forces dominated the motion of the fluid in the model, thus Froude's law was the criterion. Cognisance was given to possible scale effects due to viscosity (Reynolds number) and surface tension (Weber number) by meeting the minimum Reynolds and Weber numbers for Froude based models.

Table 5.1 summarises the scale effects for the lowest discharge tested (M: 0.392 $m^3/s/m$) at the point of issuance (spillway crest), and point of impingement with the pool bottom. The flow velocity of the wall jet inside the plunge pool was measured during the experimental tests and the depth of the wall jet was determined with Equation 3.30 (y_{down}). The similarity law equations listed in Annexure B were used. The Reynolds and Weber numbers for the lowest discharge tested satisfy the critical criteria to minimise scale effect as specified in Section 3.2. Thus the physical model layout would ensure that the minimum recommended Reynolds and Weber numbers of 3 x 10^4 and 120 respectively based on Froude similarity, would be obtained to circumvent potential scale effects.

Vibrations, captured by the Strouhal number (S_t), and pressures, in the form of the Euler number (E_u), have similitude by default due to their relation to the Froude number (Heller, 2011).

Table 5.1: Scale effect information for lowest discharge for model scale

Location	Discharge	Flow depth	Model values			
	Model ($m^3/s/m$)	Model (m)	Velocity (m/s)	Froude	Reynolds	Weber
Values at spillway crest	0.392	0.19	2.063	1.5	3.5E+05	11 079
Values inside plunge pool (wall jet)		0.331	0.477	0.3	1.4E+05	1 032

5.3. Physical model set up

The physical model emulating rock scour downstream of a dam was constructed in the Hydraulics Laboratory of the Civil Engineering Department of Stellenbosch University. The experimental set up is presented in Figure 5.1 with model dimensions in mm. Figure 5.2 shows photographs of the laboratory model set up. Additional photographs of the model and detailed model schematics are shown in Annexure F.

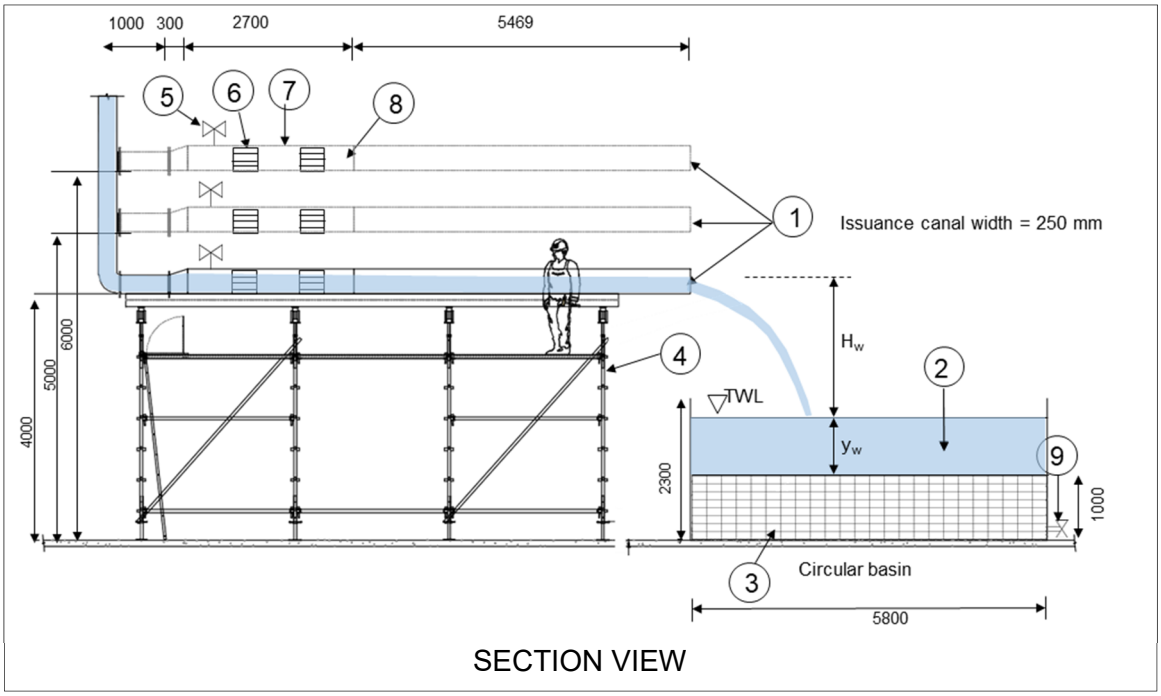

Figure 5.1: Model set up with (1) issuance canal; (2) plunge pool; (3) uniform rock blocks; (4) scaffolding; (5) air valve; (6) flow straighteners; (7) pressure box; (8) adjustable sluice gate and (9) butterfly valves

Figure 5.2: Photographs of experimental set up for lowest spillway height

The physical model consisted of the following items:

- An elevated rectangular horizontal issuance canal 0.25 m wide, 0.4 m deep and 9.5 m long. The canal was supported by scaffolding, and transported the pumped water from the laboratory's reservoir to the downstream rock bed. The issuance canal was equipped with a pressure box with flow straighteners at its upstream side. The pressure box created a smooth inflow and reduced the turbulence caused by the upstream 90º pipe bend and pump fluctuations. Additionally, the issuance canal was constructed with sufficient length to ensure fully developed uniform flow with low internal turbulence to appropriately simulate air entrainment for uncontrolled spillways. The invert level of the canal was adjustable to three fixed levels, namely 4 m, 5 m and 6 m relative to the

laboratory floor. These invert levels respectively corresponded to a 60 m, 80 m and 100 m fall height relative to the rock bed surface for the prototype for a 1:20 scale.

- A 5.8 m diameter corrugated dam represented the plunge pool. The dam was 2.3 m high, which made allowance for freeboard. The bedrock depth required for the available fall heights was determined from preliminary scour depth calculations. The plunge pool depth was determined considering the deepest scour depth and freeboard required, and subtracting it from the dam height. The plunge pool depths that were tested were 0.5 m and 1 m, replicating realistic prototype pool depths of 10 m and 20 m respectively for a 1:20 scale. Three outflow butterfly valves on the side of the dam were used to control the plunge pool depth.
- The size of the reservoir selected was based on preliminary scour prediction calculations for the shortest and longest jet trajectories with a shallow plunge pool depth to ensure that the walls of the reservoir do not affect the flow patterns and scour.
- Concrete paver blocks (cobblestones) tightly hand-packed to a height of 1.15 m relative to the laboratory floor represented the movable erodible pool bottom, emulating a uniform three-dimensional open-ended rock joint network, assuming that the rocks in the plunge pool have already been dislodged. The two rock sizes tested were rectangular concrete blocks with $x \times y \times z$ dimensions 0.1 m x 0.1 m x 0.075 m (prototype: 2.0 m x 2.0 m x 1.5 m), and 0.1 m x 0.1 m x 0.05 m (prototype: 2.0 m x 2.0 m x 1.0 m). Gravity cannot be scaled, therefore a similar prototype rock density of typically 2650 kg/m^3 should be used in physical models. The density of the concrete blocks used was 2388.1 kg/m^3 for the smaller blocks and 2355.4 kg/m^3 for the larger blocks. The density of the rock is required to determine the submerged weight of the rock block (G_b), which contributes to the resistant forces on the rock block used in rock scour prediction methods and the regression analysis. The angle of repose of the concrete blocks used was 38° for the smaller blocks and 39° for the larger block.

  It would be very expensive and time-intensive to manufacture model rock with the same tabular shape and density as that of typical prototype rock. Instead, cobblestones road blocks were used by applying the settling velocity criterion. The settling velocity was recommended as representative of the transportability of rock blocks in water, since it accounts for size, shape and density of the model rocks. A settling tank was used in the laboratory to determine that the median settling velocity of 1.12 m/s (prototype: V_{SS} = 4.99 m/s) for the 0.1 m x 0.1 m x 0.075 m rock block and 0.94 m/s (prototype: V_{SS} = 4.19 m/s) for the 0.1 m x 0.1 m x 0.05 m rock block.

The cobblestones used in the experimental tests had smooth and flat side and bottom surfaces and a slightly convex and undulated top surface as seen in Figure 5.7. The convex tops of the blocks were always placed to face upward for each layer. The vertical joints in both the x- and y-directions were randomly staggered with that of the adjacent and bottom layers. The joint structure orientation relative to the inflow jet tested are illustrated in Figure 5.3

5.4. Laboratory testing procedures

The concrete paver blocks were tightly hand packed to emulate a uniform three-dimensional open-ended horizontal and vertical rock joint network. The vertical joints were randomly staggered to emulate a typical prototype. The surface of the packed rock bed was levelled prior to each experimental test. The correct tailwater level was obtained by filling the plunge pool with water at low flow rates to not disturb the packed pool bottom before commencing with the actual test.

After the mentioned preliminary steps, the flow from the pipe system was activated and adjusted to obtain the preferred flow rate for the specific test. The actual test began as soon as the correct flow rate was reached and the tailwater level was lowered to the desired level. The flow rate and tailwater level were kept constant throughout the test. During each of the experimental tests, the scouring of rock by the free falling rectangular jet issuing from the spillway canal was monitored until scouring in the plunge pool stopped and equilibrium conditions were reached (after approximately 6 hours of testing), called Case A.

The plunge pool was drained after the equilibrium scour hole was reached. Care was taken to drain the pool at a slow flow rate to not alter the scour hole pattern before measurements commenced. The topography of the bed profile of the equilibrium scour hole was then surveyed using the Z+F Imager 5006h laser scanner.

The pressure transmitters were placed at several locations in the scour hole by assuming symmetry as seen in Figure 5.8. The test was repeated following the above mentioned procedure with the pressure transmitters in place. The pressures were recorded as soon as the flow stabilised. During this test, the flow velocity was also measured at the pressure transmitter locations using the ADV instrument for the tests with the 0.5 m plunge pool depth.

The same test was then repeated but instead of leaving the scoured blocks from the pool, the deposited rocks downstream of the scour hole were continuously removed until equilibrium conditions were reached again (called Case B) after approximately 16 to 28 hours. Thereafter the so formed equilibrium bed profile was surveyed again.

The issuance canal could be adjusted to three different fixed heights above the movable rock bed (not the laboratory floor), as shown for the different test conditions in Table 5.2. Plunging jets were evaluated for three different flow rates. The maximum flow rate corresponds to 80 m^3/s/m for the prototype, emulating a typical pressurised spillway. The middle flow rate corresponds to 45 m^3/s/m for an uncontrolled spillway prototype. The minimum flow rate (prototype: 35 m^3/s/m) was chosen based on the limitations of the model set up. Two plunge pool depths and two rock sizes were tested as summarised in Table 5.2. The scour hole geometry for different joint structure orientations was also studied. The three joint structure angles under investigation are presented in Table 5.2 and illustrated in Figure 5.3.

The above-mentioned test procedure was followed for all 31 tests. Refer to Annexure G.1 for the complete testing schedule with experimental measurements. Repeatability was tested by repeating 10% of the tests to ensure that no major discrepancies occur between experimental tests with the same flow conditions. The repeated tests showed a maximum deviation of 15% for the scour depth.

Table 5.2: Physical model target test conditions

Item	**Model value**	**Prototype value**
Elevation, H	3 m	60 m
	4 m	80 m
($H_w + y_w$ shown in Figure 5.1)	5 m	100 m
Unit discharge, q	0.894 m^3/s/m	80 m^3/s/m
(b_{model} = 0.25 m)	0.513 m^3/s/m	45 m^3/s/m
	0.391 m^3/s/m	35 m^3/s/m
Plunge pool depth, TWD	0.5 m	10 m
	1 m	20 m
Rock size	0.1 m x 0.1 m x 0.075 m	2.0 m x 2.0 m x 1.5 m
$x \times y \times z$ (length, width, thickness)	0.1 m x 0.1 m x 0.05 m	2.0 m x 2.0 m x 1.0 m
Rock joint angle	horizontal (0º)	
	45º against flow direction	
	45º in the flow direction (135º)	

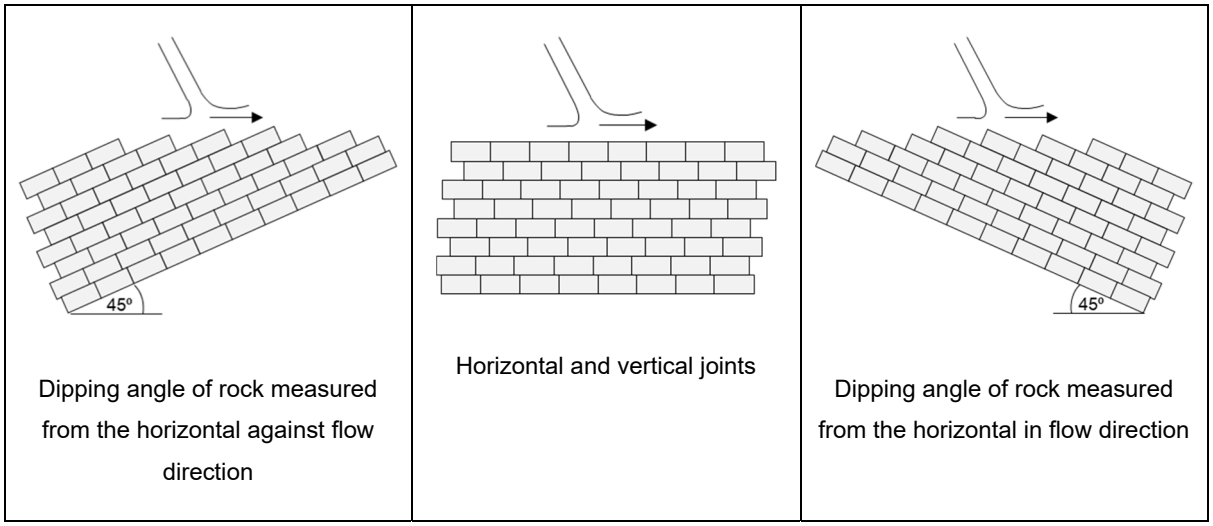

Dipping angle of rock measured from the horizontal against flow direction	Horizontal and vertical joints	Dipping angle of rock measured from the horizontal in flow direction

Figure 5.3: Joint structure orientation angles under investigation

5.5. Measuring equipment

5.5.1. *Discharge*

A Flowmetrix SAFMAG DN300 electromagnetic flowmeter was used to measure the flow. The flowmeter has an accuracy of ±0.5% and a reading repeatability of ±0.1%. A manual valve was located downstream of the flowmeter to adjust the flow rate to the required flow needed for the specific model test as seen in Figure 5.4.

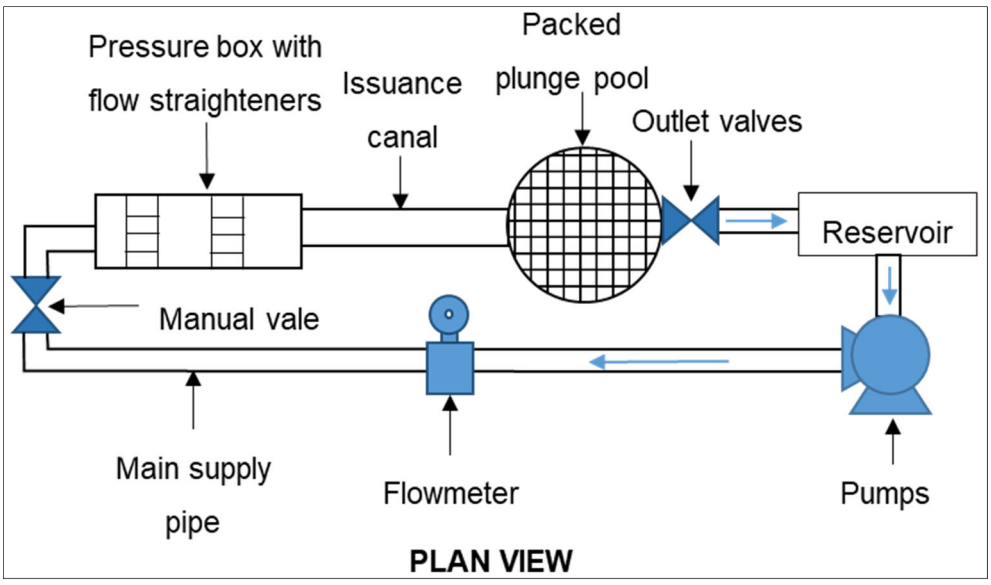

Figure 5.4: Schematic layout of experimental set up

5.5.2. *Water level*

A measuring needle was utilised to measure the water level in the issuance canal upstream of the drawdown zone, as well as inside the plunge pool for every test.

5.5.3. *Jet trajectory*

The three-dimensional coordinates of the trajectory of the falling jet between the issuance canal and the plunge pool were surveyed with a total station.

5.5.4. *Air concentration*

The air concentration in the plunging jet was measured to determine whether the plunging jet is fully developed or whether a core is still present (undeveloped jet) when entering the plunge pool.

An intrusive conductive needle probe was utilised to measure the air concentration and bubble velocity of the plunging jet along its trajectory in the air. The diameter of the needle is 0.1 mm. The air probe measures the electric conductivity of water and air by means of a high frequency amplifier that excites the probe tip, which returns a voltage signal to a data logger. Thermal Needle Probe (TNP) was used to log the data. The air probe and TNP unit are shown in Figure 5.5.

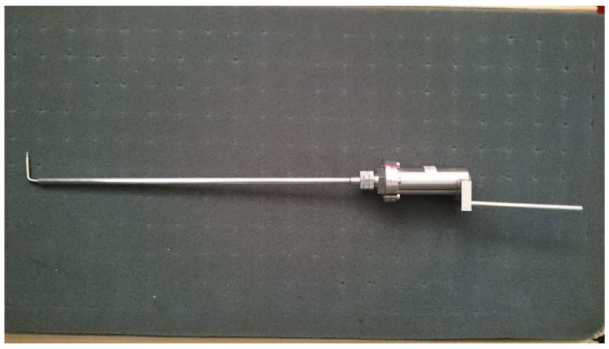

(a)

(b)

Figure 5.5: (a) Conductive needle probe; and (b) tip of conductive needle probe;

The acquisition logger registers the probe's output voltage within a specific conductivity range, with the upper threshold representing the liquid phase, and air the lower threshold. A steep drop in conductivity corresponds to an air bubble popped by the probe tip. The voltage signal is theoretically rectangular, however, the response from the probe is not rectangular, due to the wetting/drying time of the tip, size of the tip, and the measuring responds time (Chanson & Carosi, 2007).

The air concentration at the centreline of the plunging jet was measured at two locations, namely:

- point of issuance (end of spillway); and
- just above the tailwater level (jet impinging into the plunge pool).

The tip of the probe was orientated in the direction of the jet flow, ensuring best bubble penetration. A sampling period of 1 minute was selected for all the air concentration tests. Previous studies showed that a sampling duration of 15 s is sufficient for the conductive needle probe to obtain a representative set of data, but recommend that a sampling duration longer than 30 s should be used (Calitz, 2015). The probe has a 10 kHz signal acquisition frequency.

VoidWizard software was used to analyse the raw data logged by the TNP device. The software generates reports depicting the conductivity, void fractions, and number of bubbles over the selected sampling duration. The raw data is simplified into a binary format, resulting in either the liquid or the air phase. The binary data was averaged over a duration of 0.05 s. The average air concentration (%) is calculated by dividing the sum of the total void periods by the sampling duration as per Equation 5.1 (Calitz, 2015).

$$(Air\ (\%))_n = \frac{(\sum t_{void})_n}{t_n} \qquad \textit{Equation 5.1}$$

5.5.5. *Pressure sensors*

The pressure profile along the exposed scour hole surface was determined by measuring the dynamic flow pressures inside the rock joints at certain strategic points. This was done in order to analyse the uplift potential of rock blocks along the equilibrium scour hole surface.

Ten WIKA S-10 pressure transmitters were used, of which four transmitters have a linear working range of -1 to +5 m, and six a working range of ±1 m. Figure 5.6 depicts these pressure transmitters. All the pressure transmitters have an output range of 4 mA to 20 mA or DC 10 V to 30 V, an accuracy of ±0.2% and a reading reliability of ±0.1%. A sampling time of 5 minutes at a maximum frequency of 100 Hz were used, yielding a total of 30 000 readings per transmitter for each test.

5 m transmitter

1 m transmitter

Figure 5.6: WIKA S-10 pressure transmitters used

The transmitters were connected to cobblestones by 5 mm diameter plastic tubes. Bollaert (2002) established that the pressures inside the joints are defined by the pressures experienced at the joint entrance, namely at the water-rock interface. Therefore, the plastic tubes were installed flush with the slot-opening cut into the side of the cobblestones to measure the pressures experienced in the rock joints at the exposed surface of the scour hole (joint entrance) as illustrated in Figure 5.7. The cobblestones containing the pressure transmitters were painted blue for easy identification.

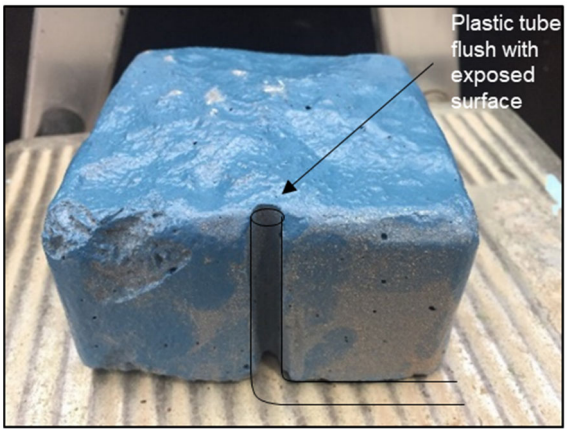

Slot cut into cobblestone for pressure transmitter pipe

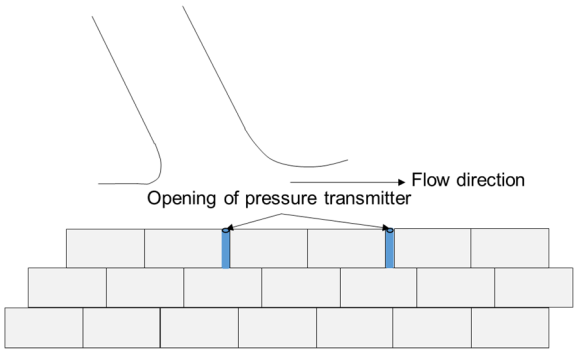

Cross-section showing an example of the location of pressure transmitter pipe

Figure 5.7: Pressure transmitter pipe location example showing measuring of pressures on the upper face of the upper level

The pressure transmitters were installed in the model bed after the formation of the equilibrium scour hole (Case A). A photograph illustrating a typical installation of the pressure transmitters symmetrically placed along the equilibrium scour hole surface is shown in Figure 5.8. The

locations of the pressure transmitters were surveyed with a total station. Special care was taken to prevent entrapped air inside the plastic tubes so as not to have any effect on the accuracy of the pressure transmitter signal.

Figure 5.8: Example of pressure sensor locations

The voltage output of the sensors at 100 Hz was recorded with a 10-channel analogue to digital data logger, namely PicoLog. The pressure transmitters measure the pressures in milli-ampere, which is converted to voltage by a 120 Ω resistor. The dynamic pressures were determined by subtracting the relative pressure experienced at the static tailwater depth from the total pressures recorded. Figure 5.9 shows an example of the pressure voltage recordings of the total, static and dynamic pressures. Figure 5.9 indicates that the dynamic pressure behaviour at the joint entrance is highly transient and cyclic.

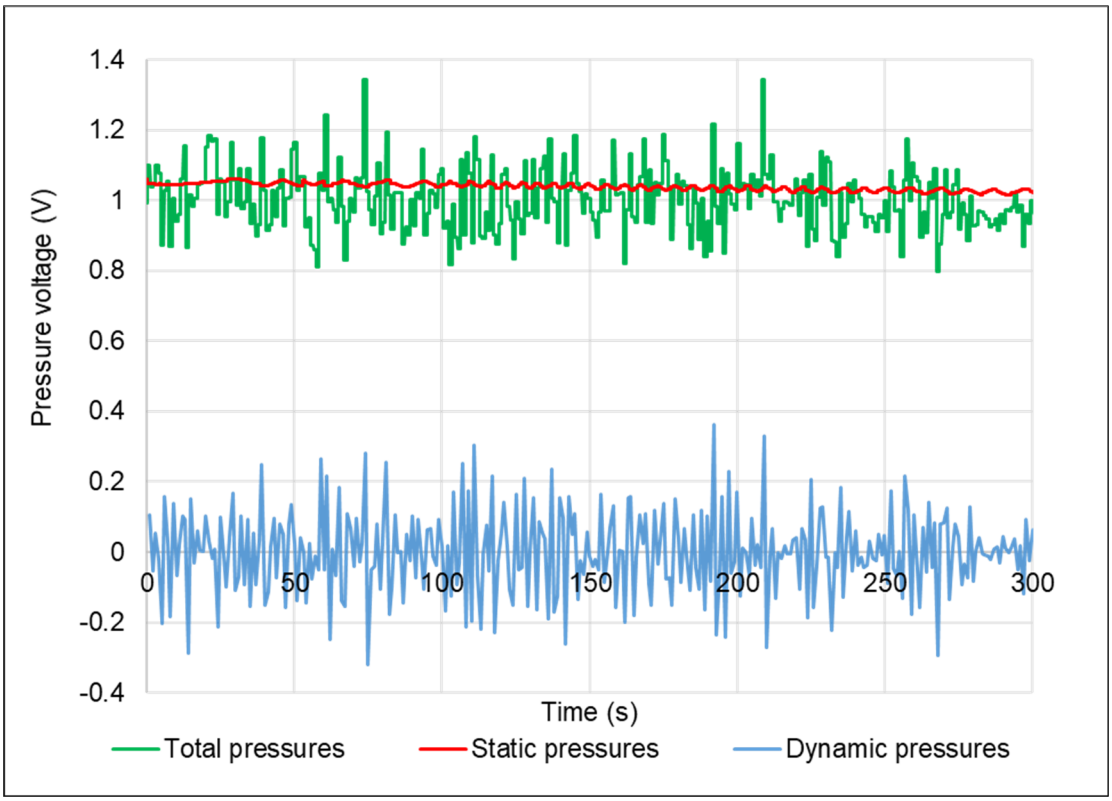

Figure 5.9: Example of pressure voltage recordings (Q_{min}, H_{med}, TWD_{min})

The dynamic pressure head was calculated by converting the voltage readings using Equation 5.2.

$$H_{out} = \frac{H_{max} - H_{min}}{I_{max} - I_{min}} \cdot \frac{1000}{R} [x - x_{sta}] \qquad \textit{Equation 5.2}$$

where:

H_{out}: dynamic pressure head (m)
H_{max}: maximum pressure head limit of transmitter (+1 m or +5 m)
H_{min}: minimum pressure head limit of transmitter (-1 m)
I_{max}: maximum current output of transmitter (20 mA)
I_{min}: minimum current output of transmitter (4 mA)
R: transmitter resistance (120 Ω)
x: measured dynamic pressure voltage reading (V)
x_{sta}: voltage reading of static tailwater depth (V)

Lopardo (1988, as cited in Castillo et al., 2018) recommended the use of the 1% exceedance pressure or 99 percentile pressure as the upper limit for design purposes, and was also used in this study as the relevant pressure parameter. Figure 5.10 shows an example of an exceedance graph with the dynamic pressure head recordings and the 99 and 99.9 percentile

values plotted, and the standard deviation shown. Figure 5.11 shows the distribution of the dynamic pressure head values on the plunge pool floor at the deepest point as an accumulative curve for one of the experimental tests.

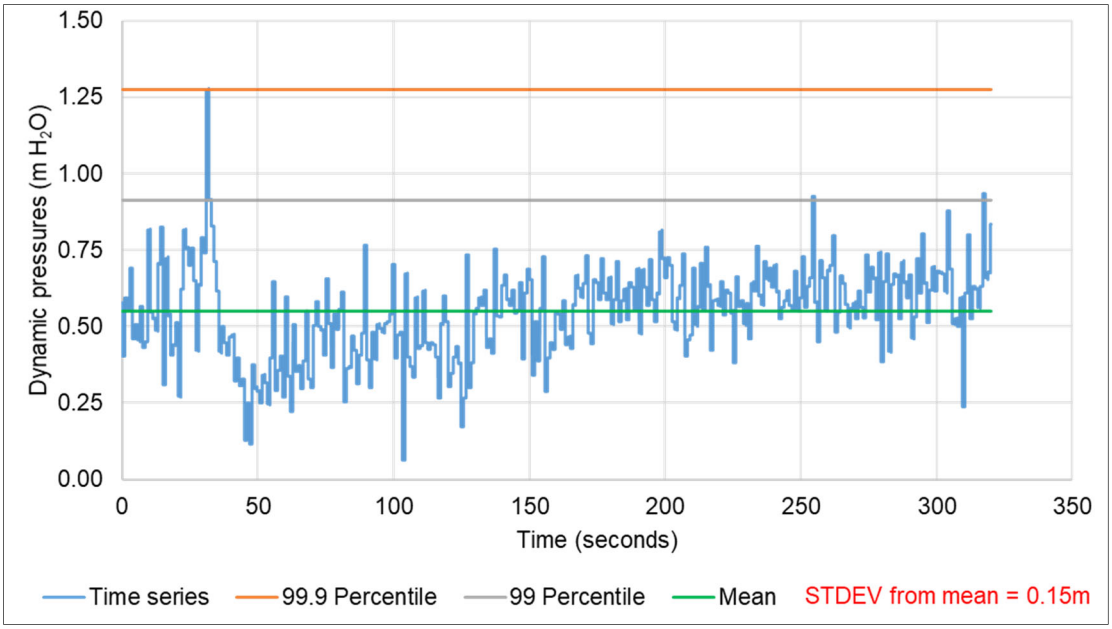

Figure 5.10: Exceedance graph of pressure recordings (Q_{max}, H_{max}, TWD_{max})

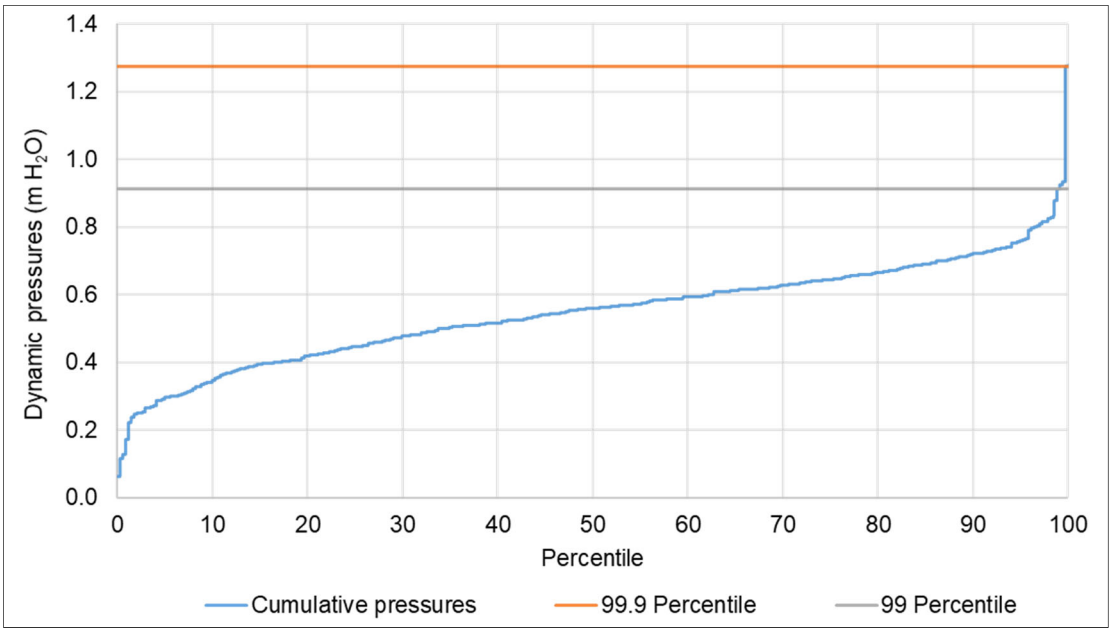

Figure 5.11: Distribution of recorded dynamic pressures on the plunge pool floor (Q_{max}, H_{max}, TWD_{max})

5.5.6. *Flow velocity*

The three-dimensional flow velocity field was measured along the bottom of the equilibrium scour hole in order to calculate the velocity of the wall jet flow. A Vectrino probe (Acoustic Doppler Velocimeter – ADV) was used for flow velocity data acquisition. Figure 5.12 shows the probe head. The tip of the ADV probe was orientated such that the red marker was orientated in the direction of the flow.

A sampling period of 1.5 minutes was selected for all the flow velocity tests at each location. The ADV has a frequency (sampling rate) of 100 Hz, a water velocity range of 0.01 m/s to 2.4 m/s, and an accuracy of 0.5% of the measured velocity value.

The probe measures the flow velocity 50 mm from the probe head. The velocity was measured 50 mm above the pressure transmitter locations, however, only for the tests conducted with the 0.5 m tailwater depth, since the probe length that could be submerged was 0.9 m.

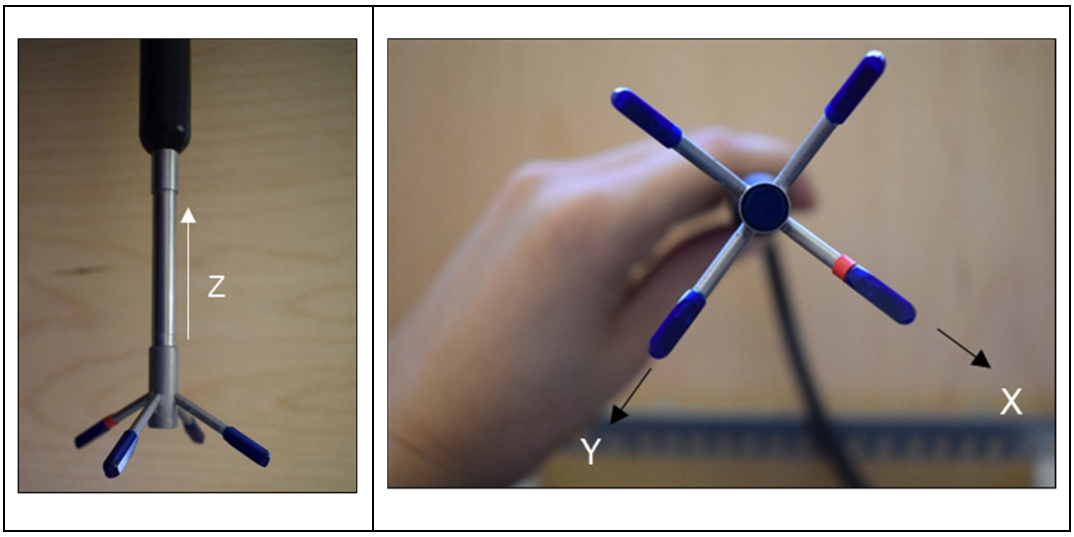

Figure 5.12: ADV probe head for velocity measurements

5.5.7. *Scour profile surveys*

The topography of the equilibrium scour hole bed profile was surveyed using a three-dimensional laser scanner, Z+F Imager 5006h, at a high resolution of 10 000 pixel/360º. The scanning time for the laser to survey the bed profile was 3:22 minutes.

5.5.8. *Location of points*

A Leica Total Station Positioning System 1205 recorded the location of points of interest (jet trajectory profile and location of pressure transmitters). The total station has a measuring accuracy of 5 mm.

5.6. Experimental test limitations

The experimental tests presented in this study consisted of simulating the rock scour due to a high velocity, fully developed jet plunging into shallow plunge pools. The experimental tests were run for different flow rates, fall heights and tailwater depths. The maximum flow rate, 80 $m^3/s/m$ for the prototype (0.896 $m^3/s/m$ for the model), emulating a typical pressurised spillway, constituted the limiting factor in the experimental set up. The suction head of the pump connected to the spillway and the laboratory roof level limited the maximum model height to a maximum of 6 m from the laboratory floor (prototype: 120 m).

The flow velocity and direction components in the plunge pool were only recorded for the tests with the 0.5 m plunge pool depth. The reason being that the ADV probe length that could be submerged was only 0.9 m.

5.7. Physical model test results and analysis

5.7.1. *Jet trajectory*

The jet trajectory, as well as the longitudinal and lateral jet spreading at impingement with the plunge pool water surface were assessed.

Figure 5.13 shows a schematic plot of the jet trajectory surveyed by the total station for the medium flow rate (M: 0.13 m^3/s, P: 45 $m^3/s/m$), medium high fall height (M: 4 m, P: 80 m), and deepest plunge pool depth (M: 1 m, P: 20 m). The theoretical jet trajectory was calculated with Equation 2.4 with the issuance angle (θ_i) equal to zero. In general, the theoretical jet trajectory corresponds well with the experimental jet trajectory as seen in Figure 6.7 in Section 6.5.7. Furthermore, if the experimental trajectory trendline is extrapolated, it intersects with the location where the maximum scour was measured for Case B (scour with deposition rocks removed) located 2.57 m (model) or 51.5 m (prototype) downstream of the spillway. All the tests followed a similar trend.

Figure 5.14 and Figure 5.15 show the lateral and longitudinal spreading of the jet respectively for the minimum discharge (M: 0.1 m^3/s, P: 35 $m^3/s/m$), maximum fall height (M: 5 m, P: 100 m) and deepest plunge pool depth (M: 1 m, P: 20 m). The photographs indicate that the theoretical jet width, W_{out}, (Figure 5.14) and thickness, B_{out}, (Figure 5.15) based on the outer turbulent fluctuations at impingement with the plunge pool water surface for the model (with some distortion in the photographs) are less than what were observed. Annexure G.1 presents the recorded jet dimensions at impingement with the plunge pool water surface for each experimental test.

The theoretical jet width, W_{out} (Figure 5.14), and the theoretical jet thickness, B_{out} (Figure 5.15), based on the outer turbulent fluctuations at impingement with the plunge pool water surface were calculated using Equation 2.19 and Equation 2.25. Equation 2.25 was used to determine the outer dimensions of the rectangular jet, since no other equation has been derived in literature to determine the outer dimensions (B_{out}) of a plunging rectangular jet. The predicted impinging jet thickness and width determined by Equation 2.25 is therefore less than that determined by Equation 2.19, since Equation 2.25 calculates B_j and not B_{out}. Equation 2.16, derived for circular jets, assumes the initial turbulence as 4% according to Table 2.1 in Section 2.3.1 for ski-jumps. The theoretical outspread of the jet δ_{out} required to calculate the jet thickness, was calculated using Equation 2.18. The theoretical jet spread angle for the medium flow rate, middle fall height and deepest plunge pool depth was calculated as 1.39º, whereas 1.92º was measured in the laboratory - a 27% difference. The measured longitudinal outspreading angle for all the tests ranged between 0.43º (for lowest discharge) up to 5.07º (for greatest discharge), in contrast to the narrower range of 1.7º to 2.3º recommended in literature (refer to Section 2.3.5).

The experimental jet spread results indicated that the lateral spreading angle (0.61º to 7.8º) is greater than the longitudinal spreading angle (0.43º to 5.07º) for rectangular jets. The jet impinging angle (θ_j) at the plunge pool water surface ranged between 56º and 75º, with the average being 65º. The experimental jet impinging angle is compared to the theoretical impinging angle calculated with Equation 2.4 in Table G.2 in Annexure G.1.

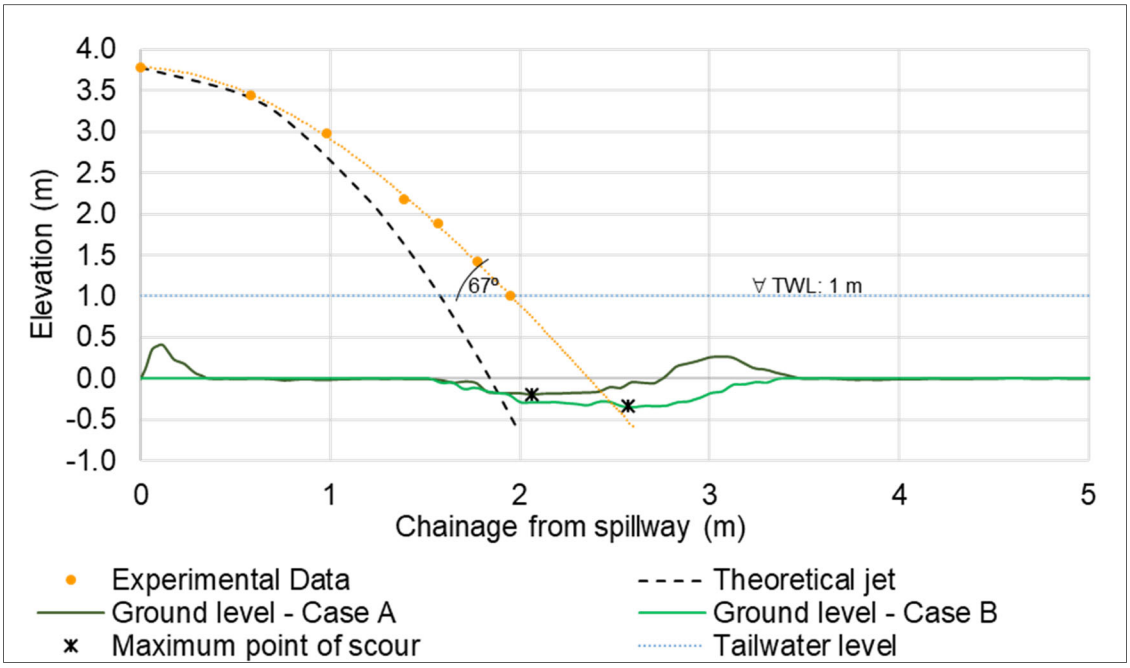

Figure 5.13: Jet trajectory for Q_{med}, H_{med}, TWD_{max} as model scale

Figure 5.14: Recorded lateral jet spreading near tailwater level for Q_{min}, H_{max}, TWD_{max} compared with theoretically calculated spreading after Annandale (2006) and Castillo (2007)

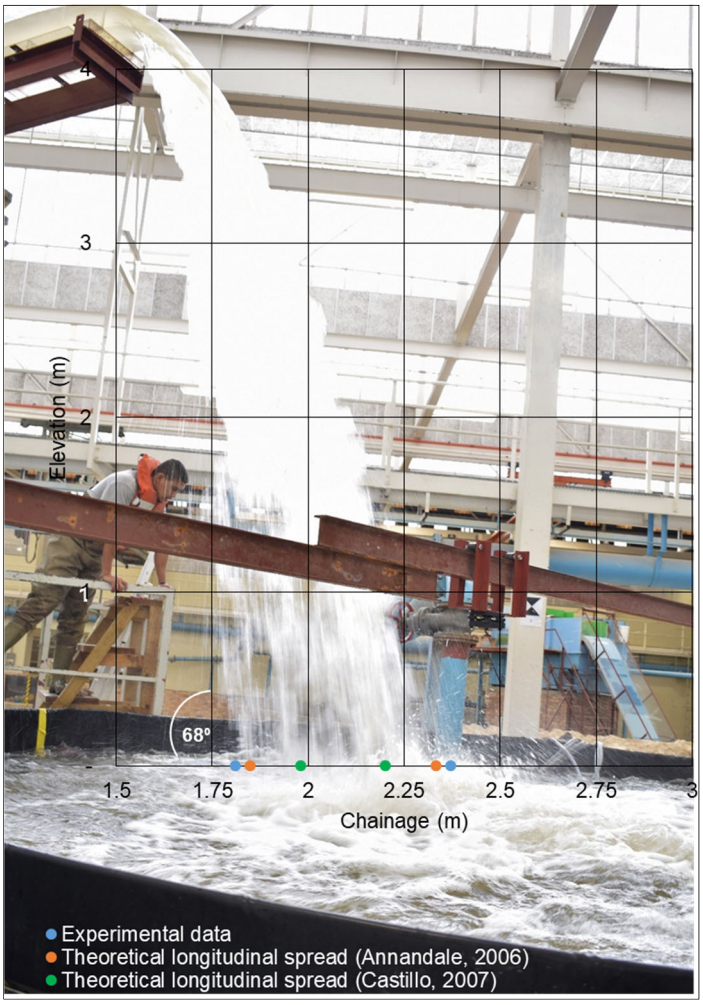

Figure 5.15: Recorded longitudinal jet spreading near tailwater level for Q_{min}, H_{max}, TWD_{max} compared with theoretically calculated spreading after Annandale (2006) and Castillo (2007)

5.7.2. *Visual observations of the scour process*

Figure 5.16 shows the bed deformation process for the horizontal and vertical aligned joint structures. Special attention was given to the scour development process during the laboratory tests. It was observed that the rock blocks were first lifted from the bed and put in suspension at the location where the jet impinges onto the rock bed. The suspended rock blocks were deposited downstream of the jet impinging zone, forming a pile of rocks seen in Figure 5.16b. It was observed that the flow velocities and pressures inside the scour hole decrease as the scour depth increases. Consequently, the uplift pressure in the jet impinging zone would reduce as the scour hole becomes deeper and eventually may fall below the critical uplift pressure value, obtaining the equilibrium scour hole. Comparing Case A and B, the velocity field inside the scour hole was affected by the presence (Case A scenarios) or absence (Case B scenarios) of the deposited rock downstream of the scour hole (Figure 5.16c).

From visual inspection it was observed that the scour volume (depth, length and width) was much greater for the Case B scenario (scour with deposited rocks removed), than for Case A (scour and deposition).

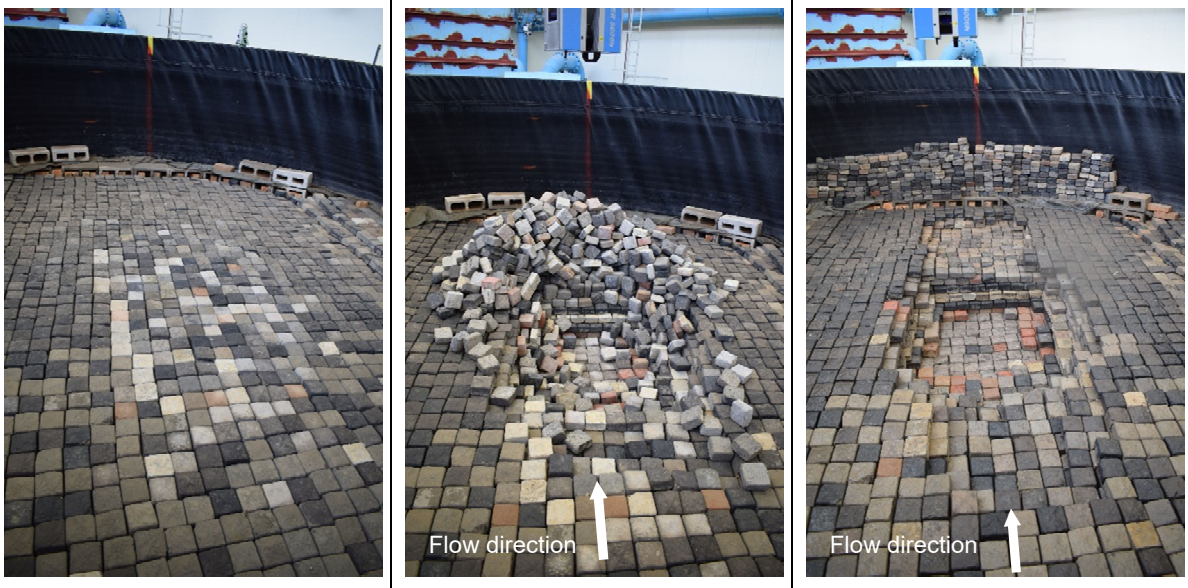

(a) Bed level prior to test

(b) Bed level after Case A (scour and deposition)

(c) Bed level after Case B (scour with deposition rocks removed)

Figure 5.16: Bed deformation process for Q_{max}, H_{min}, TWD_{max}

As an example, Figure 5.17 depicts the contour maps and three-dimensional surface mapping of the surveyed equilibrium scour holes of the model for Case A and Case B respectively for the maximum discharge (M: 0.894 $m^3/s/m$, P: $80m^3/s/m$), highest fall height (M: 5m, P: 100 m) and deepest plunge pool depth (M: 1 m, P: 20 m). The contour maps show that the scour hole

depth, length, width, and volume increase when the deposited rocks downstream of the hole are removed, and the horizontal distance to the onset of scour decrease.

The scour hole topography data gathered from the laser survey were plotted using SURFER, a three-dimensional surface mapping software. The upstream and downstream spikes shown in the three-dimensional surface maps indicate the reservoir walls and blocks, which do not affect the plunge pool formation or the plotting of the hole and deposited rocks. Annexure G.2 records the bed deformation contour maps in plan and the three-dimensional surface mapping for each experimental test.

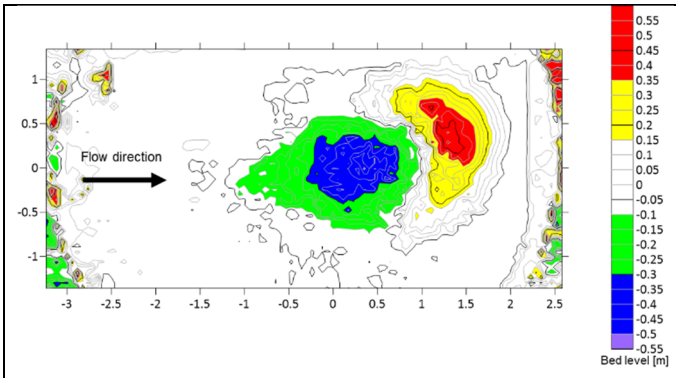

Contour map for Case A (scour and deposition)

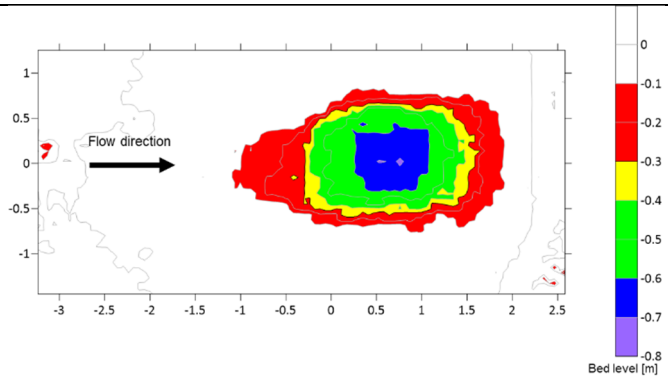

Contour map for Case B (scour with deposited rocks removed)

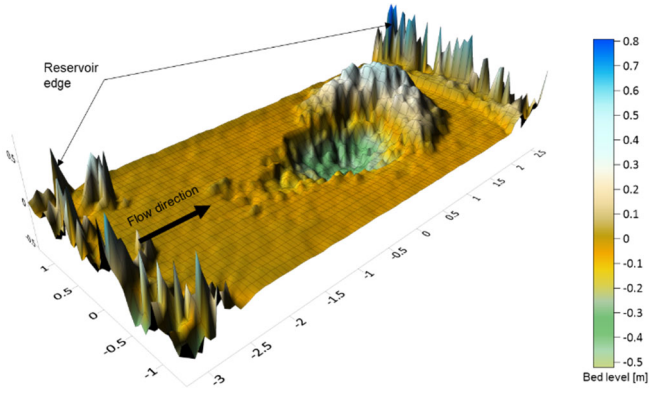

3D bed surface mapping of Case A (scour and deposition)

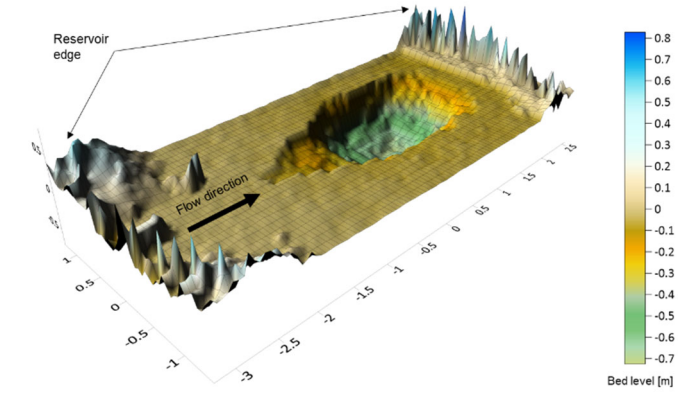

3D bed surface mapping of Case B (scour with deposited rocks removed)

Figure 5.17: Equilibrium bed levels for the Q_{max}, H_{max}, TWD_{max} for Case A and B

The scour hole geometry for the maximum discharge (80 $m^3/s/m$), the maximum fall height (100 m) and deepest plunge pool depth (20 m) are compared for Case A (deposited rocks intact) and Case B (deposited rocks continuously removed) for prototype and model values in Table 5.3. The experimental tests indicated that greater scour would occur if the deposited rocks downstream of the scour hole are removed by floodwaters, corresponding to Pagliara et al.'s (2006) finding. Thus, a dynamic scour limit is reached if the deposited rocks are not

removed, whereas a static scour limit is reached if the deposited rocks are continuously removed. Annexure G.1 presents the recorded scour results for all the experimental tests.

Table 5.3: Summary of result comparison between Case A and B for Q_{max}, H_{max}, TWD_{max}

Hole geometry	**Symbol**	**Case A**		**Case B**	
		P	**M**	**P**	**M**
Maximum scour depth	D_s (m)	8.71	0.436	12.85	0.642
Scour length	L_s (m)	42.93	2.147	63.84	3.192
Scour width	W_s (m)	26.15	1.307	29.47	1.473
Scour volume	V_s (m^3)	3391.4	0.424	8864.3	1.108
Length-width ratio	Ratio (L/(W/2))	3.28		4.33	
Time exposure	T_s (hours)	24.6	5.5	120.7	27

P = Prototype

M = Model

The length-width ratio is greater than one, implying that the outline of the scour hole tends relatively to an oval plan shape, with the major axis in the longitudinal direction.

The time over which the rock was exposed to the action of the jet with the associated scour volume for Case A and B for each tests is recorded in Annexure G.1.

5.7.3. *Scour hole depth and extent*

As mentioned in Section 5.4, a total of 31 experimental tests were performed to obtain the equilibrium scour hole for different discharges, dam heights, tailwater levels, bedrock sizes, and joint angle scenarios. Table G.1 in Annexure G.1 shows the test results for all the tests in terms of scour depth, length, width, and volume, as well as the length-width ratio. Although various tests were performed, only the results of selected tests are presented, since all the tests followed similar trends.

Both longitudinal and lateral bed profiles for the various tests were plotted in a Cartesian coordinate system using the plunge pool bottom surface as the vertical datum and the centre of the spillway as the horizontal datum. Figure 5.18 illustrates the coordinate system adopted for the experimental tests. In order to describe how the scour hole varies in the flow direction for the different tests, the longitudinal bed profiles are plotted along the x-axis passing through

the centre of the scour hole. The abscissa of the longitudinal bed profile depicts the longitudinal distance (x) from the spillway and the ordinate represents the bed surface elevation relative to the plunge pool bottom (Z). The lateral bed profiles are plotted along the y-axis describing the transversal change in the scour hole. The abscissa represents the lateral distance (y) from the issuance centreline and the ordinate the bed surface elevation relative to the plunge pool bottom (Z).

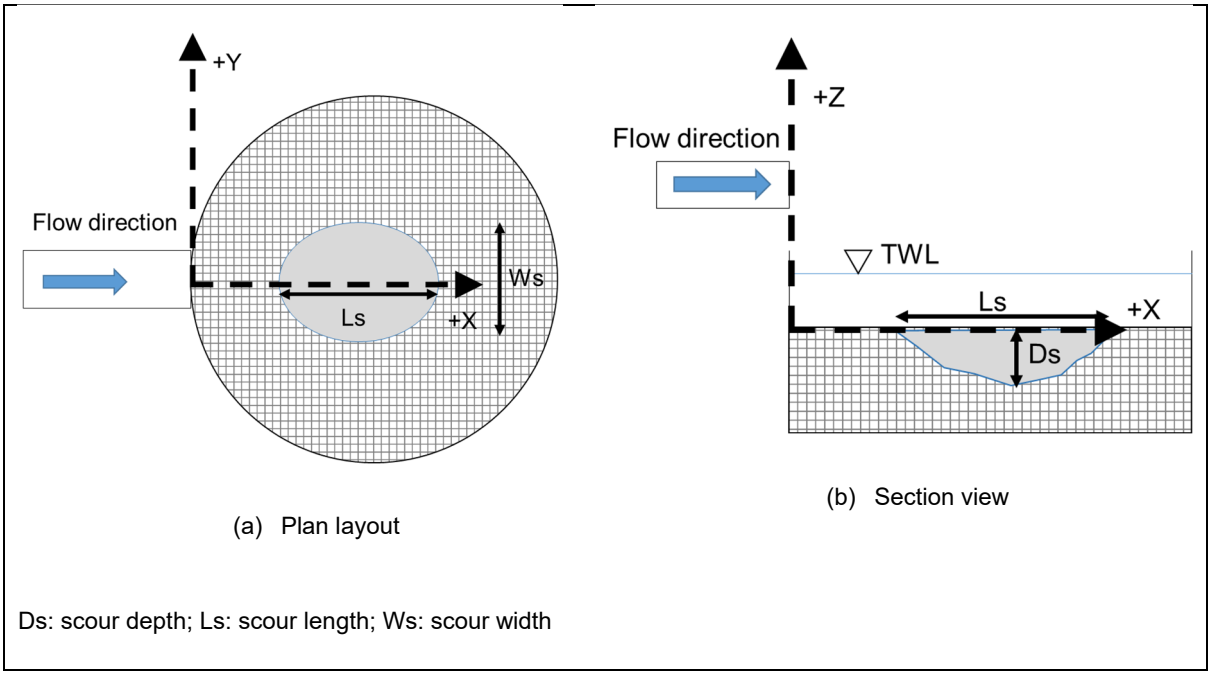

Figure 5.18: Cartesian coordinate system used in the recording of scour hole parameters in the physical model

5.7.3.1 Scour hole bed profile variation with flow rate

The longitudinal and lateral cross-sections for different discharges are plotted on the same graph in order to investigate any bed profile changes due to flow variation. Figure 5.19 depicts the model bed profiles at the deepest scour location for various flow rates for the highest fall height (H_{max} = 5 m for model or 100 m for prototype) and deepest tailwater depth (TWD_{max} = 1.0 m for model or 20 m for prototype) for Case A and Case B.

The results presented in Figure 5.19 indicate that the scour depth becomes deeper, the width becomes wider and the length increases as the discharge increases. The longitudinal cross-sections indicate that the point of maximum scour, as well as the horizontal distance from the spillway to start of the scour hole, is located further downstream from the spillway for higher discharges. The reason for this phenomenon is that the jet's point of impingement moves further downstream from the spillway due to the long jet trajectory as the discharge increases.

Figure 5.19 also indicates that the scour volume increases when the deposited rocks downstream of the scour hole are removed (Case B) compared to Case A (scour and deposition).

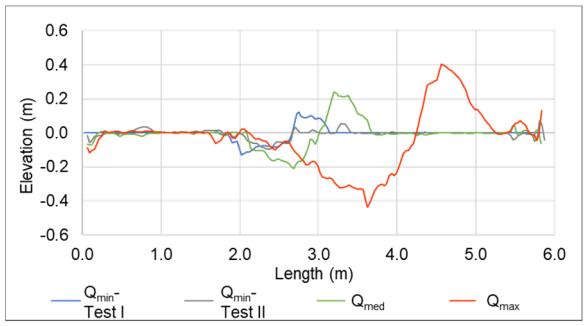

Longitudinal cross-section: Case A

Distance from spillway

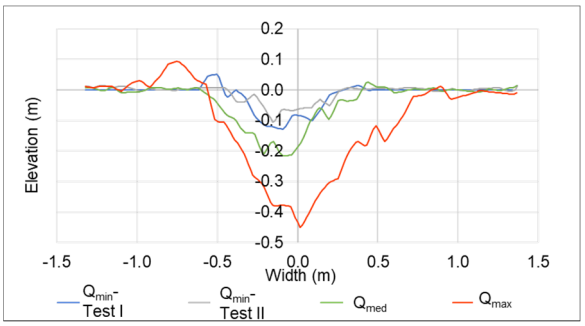

Lateral cross-section: Case A

Distance from issuance centreline

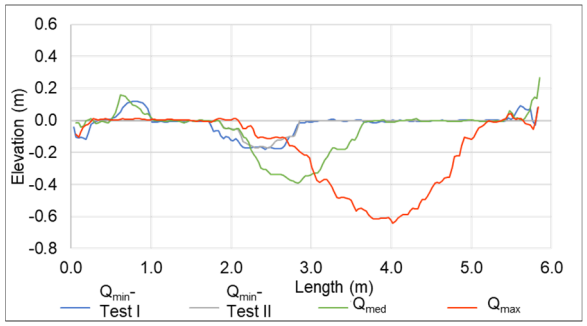

Longitudinal cross-section: Case B

Distance from spillway

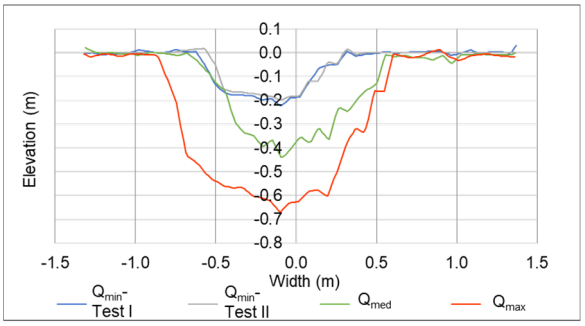

Lateral cross-section: Case B

Distance from issuance centreline

Figure 5.19: Observed longitudinal and lateral equilibrium cross-section variation with flow rate (H_{max}, TWD_{max})

Figure 5.20 indicates the effect the discharge had on the scour hole geometry for all the physical model tests performed. The experimental test results indicate that the shape of the scour hole is greatly dependent on the spillway discharge, since the scour hole geometry increases with an increase in the discharge as seen in Figure 5.20.

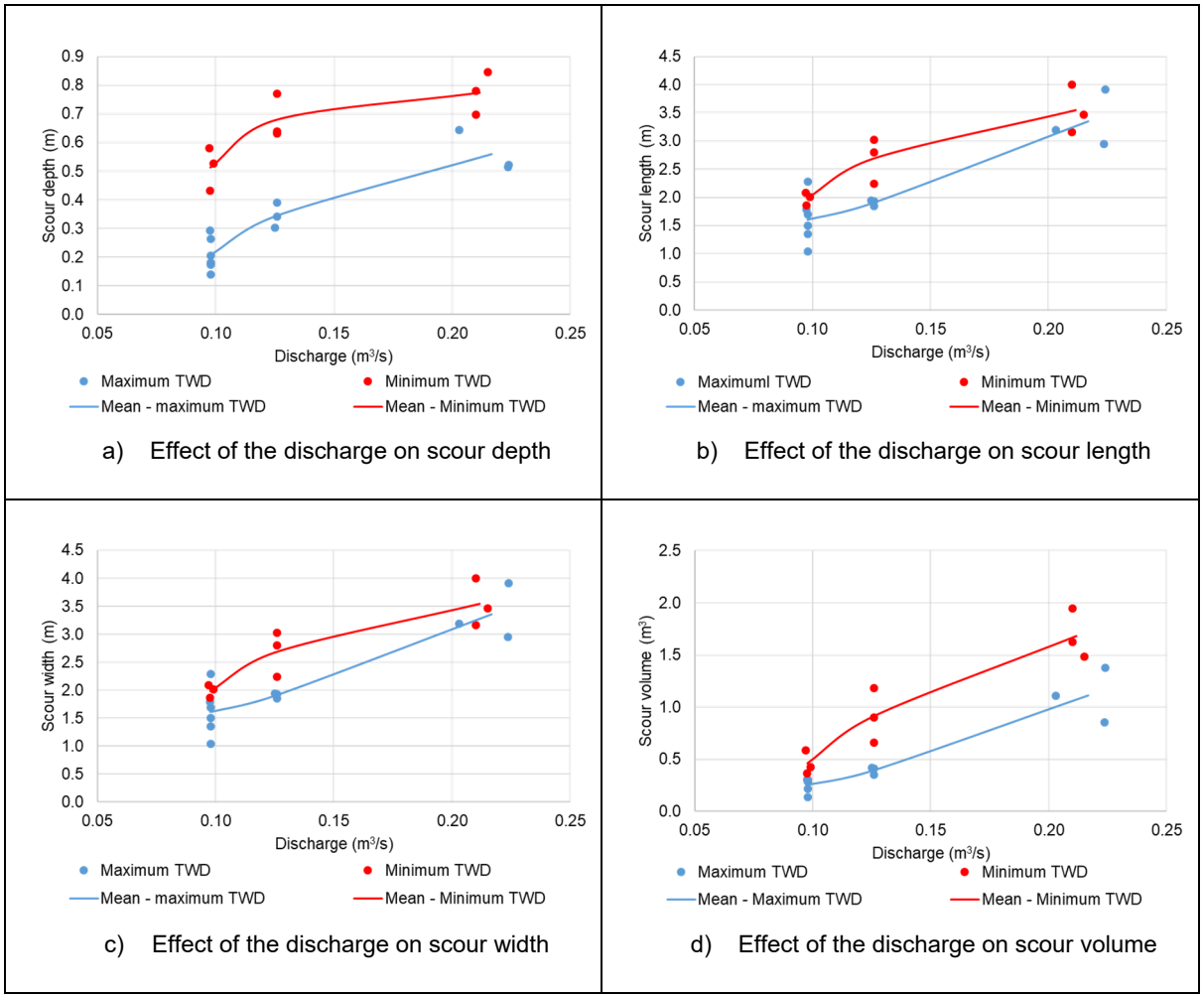

Figure 5.20: Effect of the discharge on the scour hole geometry for the experimental tests

5.7.3.2 Scour hole bed profile variation with fall height

The effect of the fall height on the bed profile was analysed by plotting the bed profiles for the different fall heights on the same graph, keeping the discharge and tailwater depth constant. Figure 5.21 compares the longitudinal and lateral bed profiles at the deepest scour hole location for the various fall height tests investigated in this experimental study for the maximum discharge and tailwater depth. Figure 5.21 indicates that the scour depth for the three different fall heights were of similar magnitude.

Figure 5.22 indicates the effect the fall height had on the scour hole geometry for all the experimental tests performed. Figure 5.22 shows that no prominent relationship occurred between the fall height and the scour hole geometries. Castillo et al. (2015) investigated the mean and fluctuating dynamic pressure coefficients for differing jet breakup length ratios. The mean and fluctuating dynamic pressure coefficients approach zero for fully developed jets. The current research exclusively tested the performance of fully developed jets, therefore the experimental results confirm that the fall height becomes less dominant in the scour process.

In conclusion, the scour hole shape is not dependent on the fall height when the jet has already become fully developed before impingement with the tailwater level.

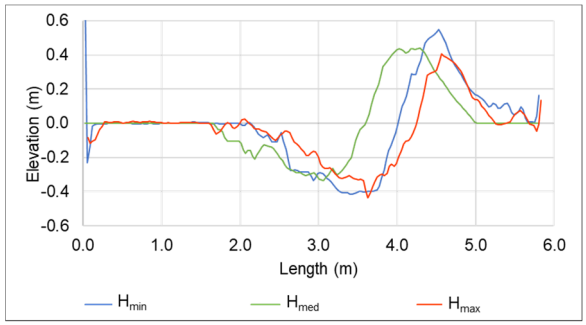

Longitudinal cross-section: Case A

Distance from spillway

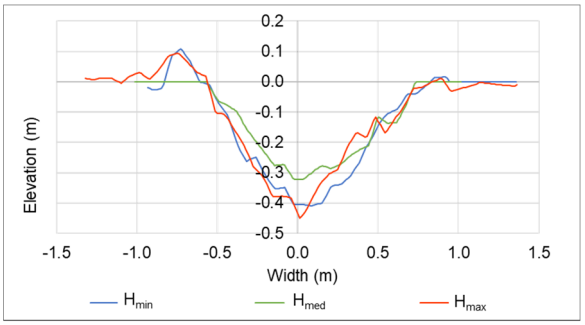

Lateral cross-section: Case A

Distance from issuance centreline

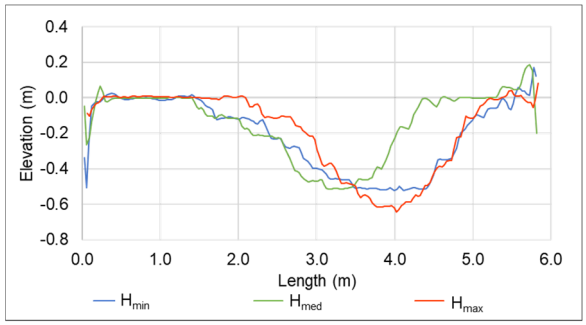

Longitudinal cross-section: Case B

Distance from spillway

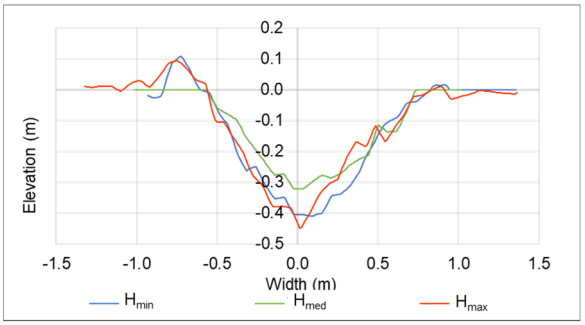

Lateral cross-section: Case B

Distance from issuance centreline

Figure 5.21: Observed model longitudinal and lateral equilibrium cross-section variation with fall height (Q_{max}, TWD_{max})

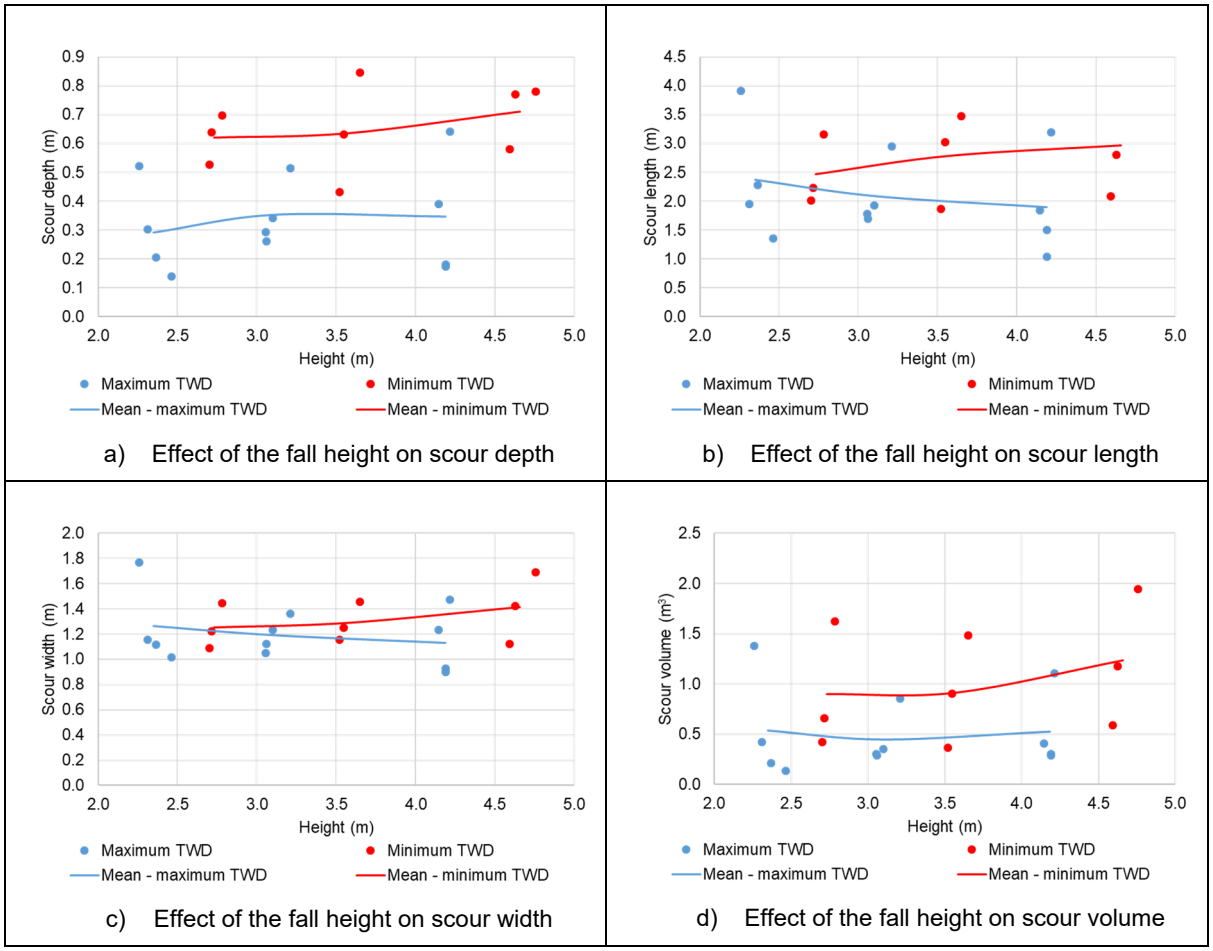

Figure 5.22: Effect of the fall height on the scour hole geometry for the experimental tests

5.7.3.3 Scour hole bed profile variation with plunge pool depth

In order to obtain an indication of the influence of plunge pool depth on the scour geometry, the longitudinal and lateral bed profiles for the two plunge pool depths for the medium discharge and maximum fall height are shown in Figure 5.23 for Case A and B. Figure 5.23 indicates that the plunge pool acts as a water cushion, reducing the scour potential of the jet, since the scouring volume (depth, length, and width) decreases with an increase in the plunge pool depth. The results for both Case A and B correspond well with the findings from Van Aswegen et al. (2001) and Bollaert et al. (2012b) detailed in Section 2.4.1.

On Figure 5.20 and Figure 5.22 the scour hole dimensions for the deeper plunge pool depth (blue curves) plot below that of the shallower plunge pool depth (red curves). Thus, the results shown on Figure 5.20 and Figure 5.22 also prove that the scour hole geometry (depth, length, width, and volume) increase with a decrease in the plunge pool depth for all the experimental tests performed.

In conclusion, the scour results presented in Figure 5.23 depict that the scour hole geometry is dependent on the plunge pool depth.

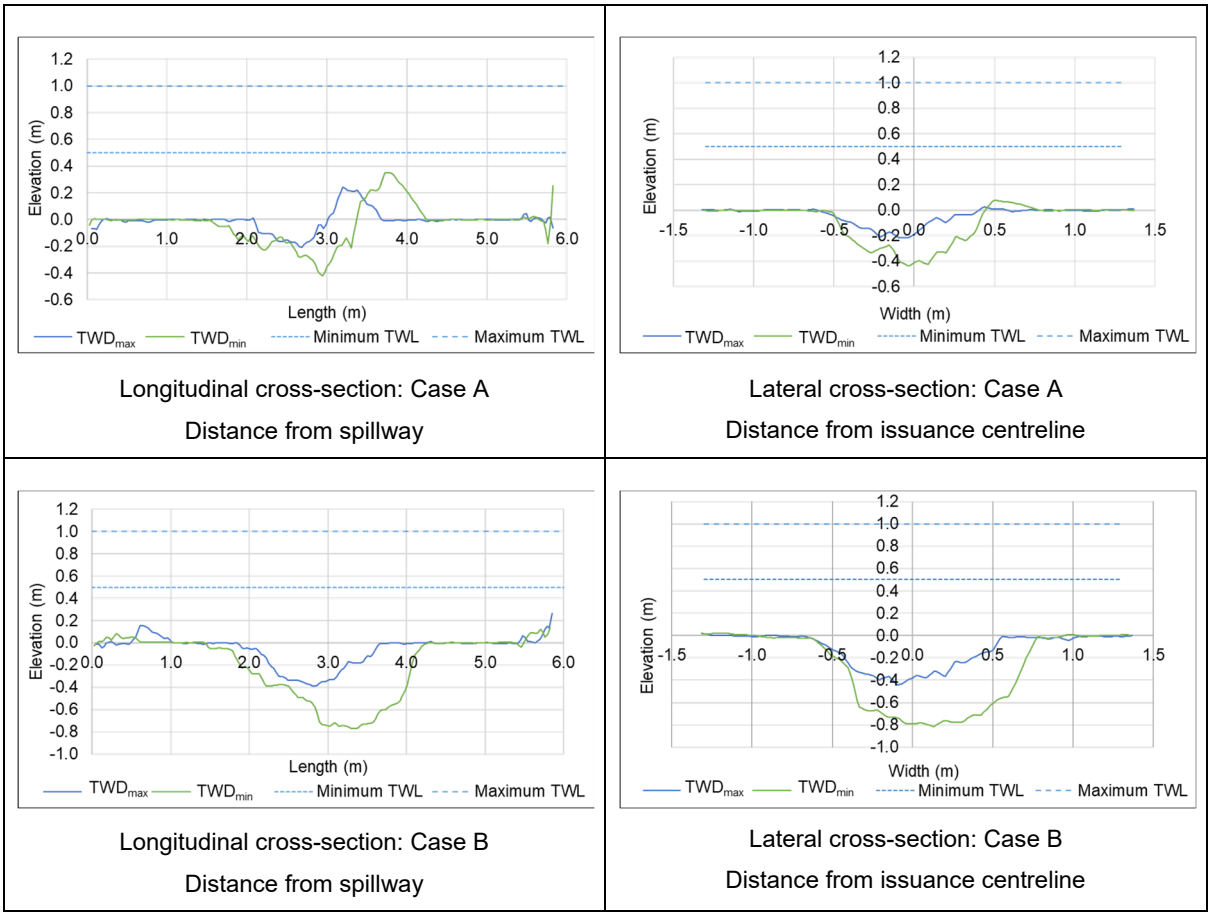

Longitudinal cross-section: Case A
Distance from spillway

Lateral cross-section: Case A
Distance from issuance centreline

Longitudinal cross-section: Case B
Distance from spillway

Lateral cross-section: Case B
Distance from issuance centreline

Figure 5.23: Observed model longitudinal and lateral equilibrium cross-section variation with tailwater depth (Q_{med}, H_{max})

5.7.3.4 Scour hole bed profile variation with rock size

The longitudinal and lateral bed profiles for different rock sizes are plotted on Figure 5.24 in order to analyse the that effect rock size has on rock removal.

The bed profiles depicted in Figure 5.24 indicate that the scour hole geometry (depth, length, width and volume) decreases as the rock block size increases. Larger rock blocks provide a greater erosive resistance than smaller blocks to the erosive capacity of the jet due to its submerged weight, in accordance to the literature (Section 3.4.1). The scour results in Figure 5.24 conclude that the scour hole geometry is dependent on the size of the rock block.

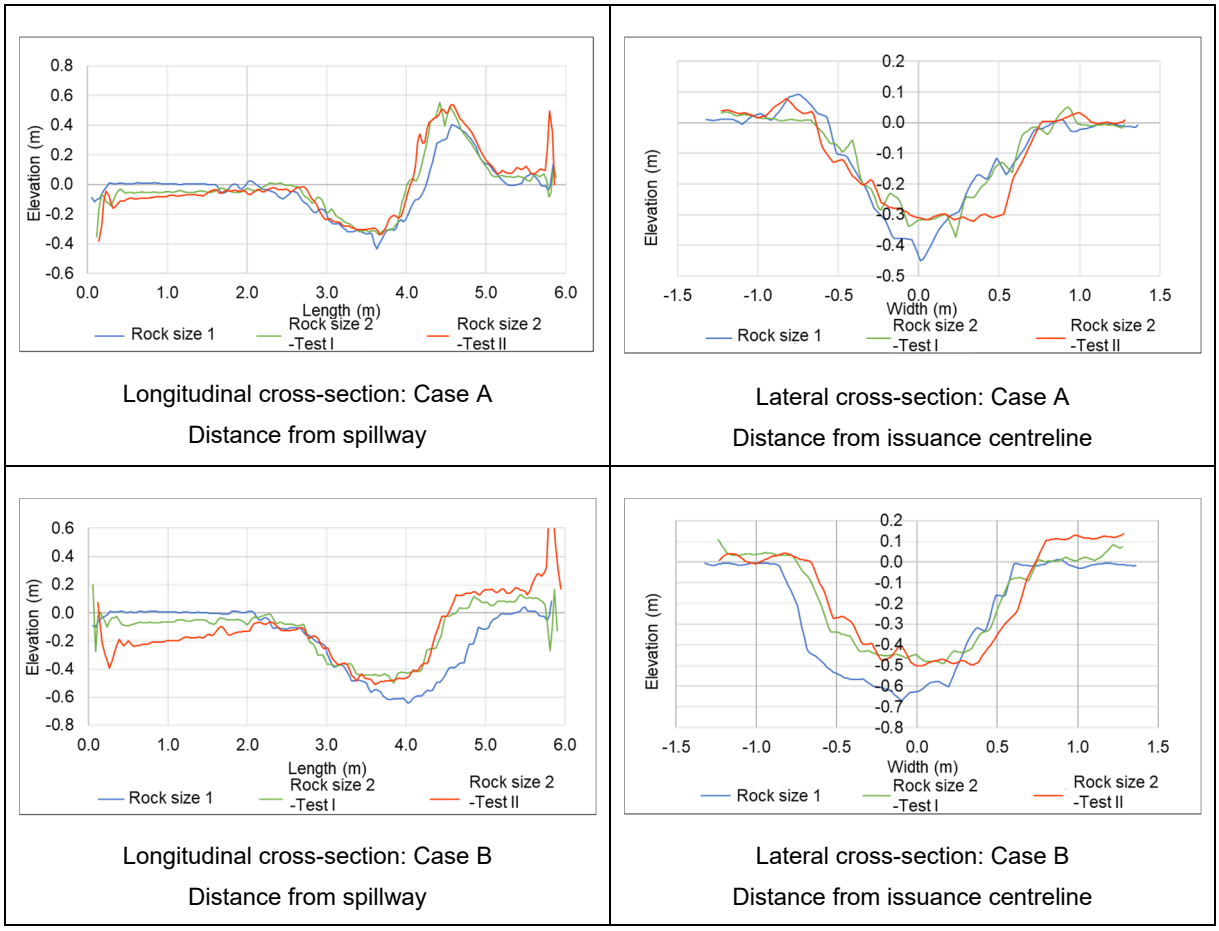

Figure 5.24: Observed model longitudinal and lateral equilibrium cross-section variation with rock size (Q_{max}, H_{max}, TWD_{max})

5.7.3.5 Scour hole bed profile variation with rock joint angle

The geologic structure of the rock can significantly influence the erodibility of the rock. The effect of the rock joint angle has on the bed profile was investigated by means of Figure 5.25. The three joint structure angles under investigation were 45º dipped against the flow direction, horizontal (0º to the horizontal axis), and 45º dipped in the direction of the flow (135º with the horizontal axis).

Similar to the well-known rock scour case of Ricobayo Dam in Spain (Annandale, 2006), the scour results in Figure 5.25 indicate that the rock is more conducive to scour failure when the dipping angle of the rock measured from the horizontal is dipped 45º in the direction of the flow. Sliding failure is enabled when the joint structure angle is dipped in the direction of the flow. The stability factors (refer to Table 5.9) indicate that the rock with the dipping anlge of the rock relative to the horizontal dipped 45º against the flow direction has a greater scour resistance to the erosive capacity of the jet.

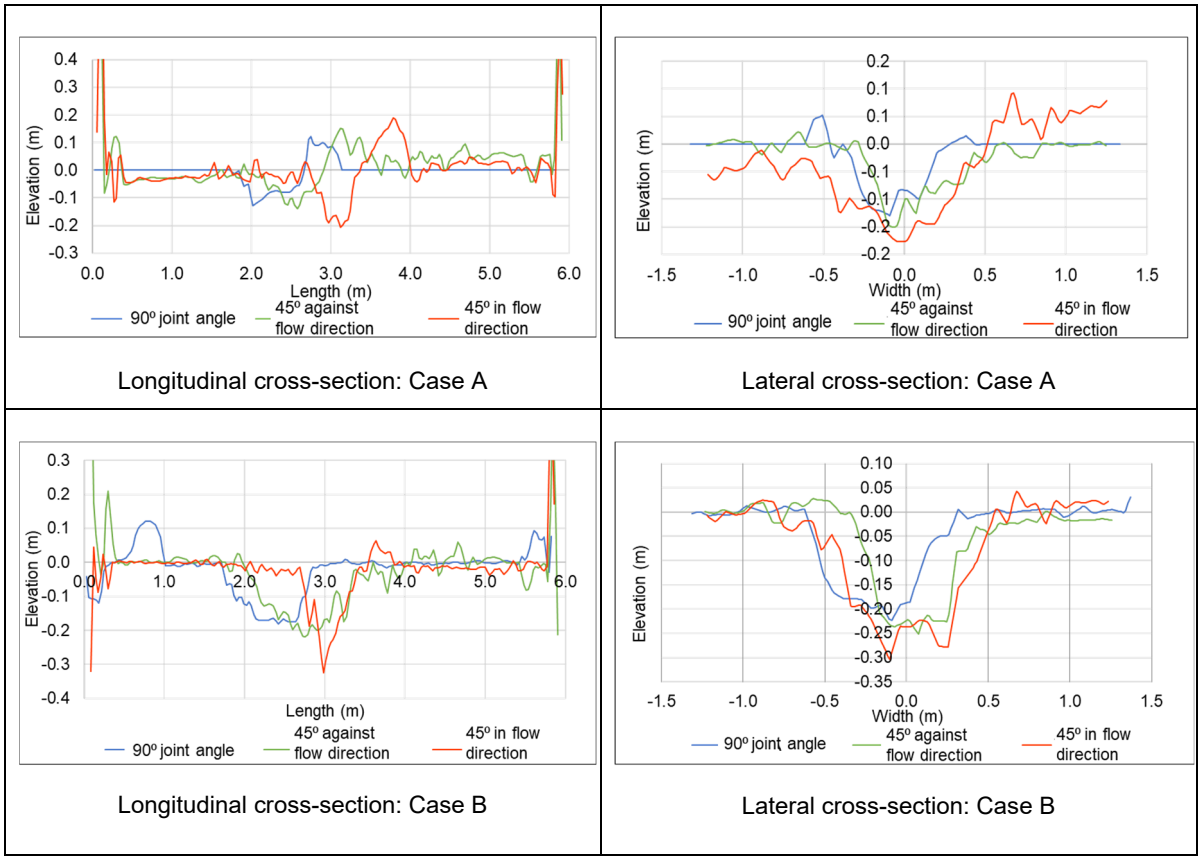

Figure 5.25: Observed model longitudinal and lateral equilibrium cross-section variation with rock joint angle (Q_{min}, H_{max}, TWD_{max})

5.7.4. *Air entrainment results*

The air concentration measured at the centreline of the jet for a discharge of 0.13 m^3/s (P: 45 $m^3/s/m$), fall height of 4 m (P: 80 m) and 1.0 m (P: 20 m) pool depth at the point of issuance and point of impingement with the pool water surface is shown in Figure 5.26. Although different flow rates, fall heights, and tailwater levels were tested, the air concentration measurements of all the tests followed similar trends as presented in Figure 5.26.

The recorded measurements indicate that the jet had a very low percentage air concentration at issuance, indicating that the jet consisted of a solid core of non-aerated water. However, the jet had a mean air concentration greater than 92% at the point of impingement with the pool surface for all the experimental tests. The high air concentration at impingement conditions indicates that the jet had become a developed jet, lacking a solid water core and comprises a conglomeration of water pockets as seen in Figure 5.27.

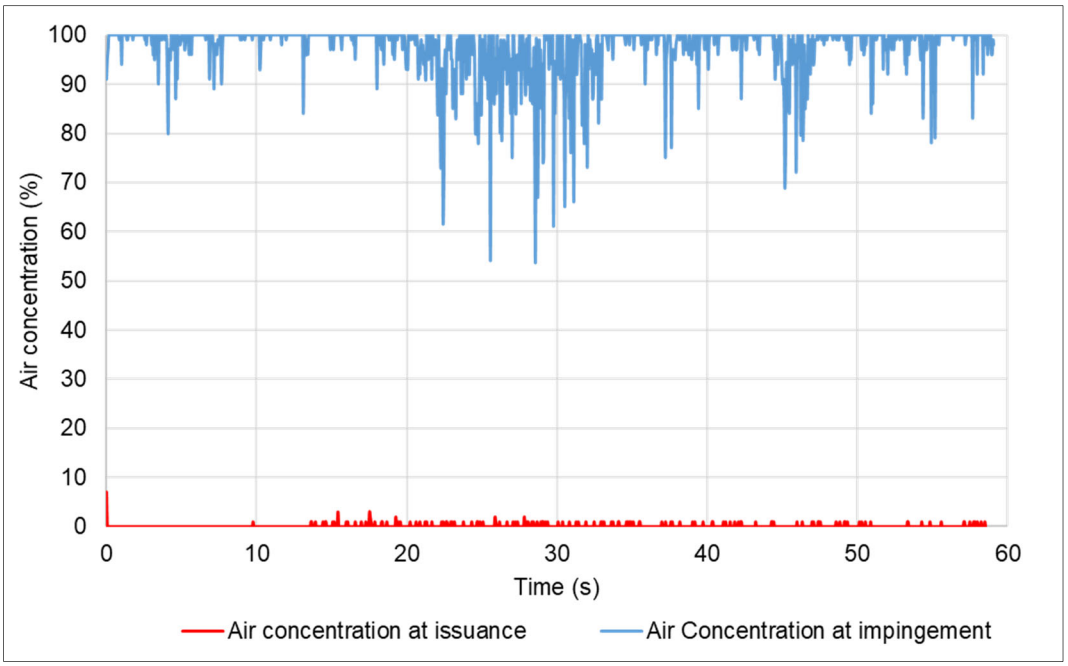

Figure 5.26: Observed air concentration at issuance and impingement with tailwater level observed for Q_{med}, H_{med}, TWD_{max}

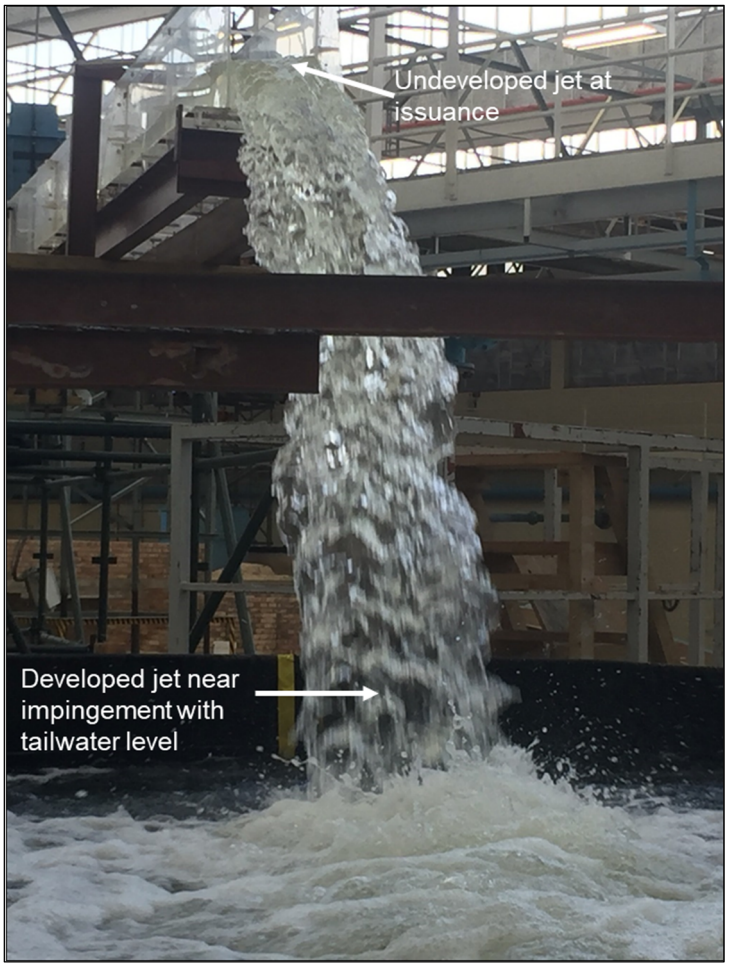

Figure 5.27: Undeveloped and developed regions of falling jet (Q_{min}, H_{min}, TWD_{max})

5.7.5. *Dynamic pressures at plunge pool bottom*

The superposition, propagation and reflection of the pressure waves at the rock joint entrance govern the water pressure magnitude experienced inside the rock joints. The behaviour of the pressure waves at the joint entrance is highly transient and cyclic, continuously changing between peak and low pressures as seen in Figure 5.9.

5.7.5.1 Discharge effect on pressure

Section 5.7.3.1 concluded that scour depth increases as the discharge increases, and is substantiated by the pressure results observed for tests performed at the lowest fall height (M: 3 m, P: 60 m) and deepest pool depth (M: 1.0 m, P: 20 m) summarised in Table 5.4. The 1% exceedance dynamic pressure head results in Table 5.4 indicates that as the discharge increased, the strength of the dynamic pressures on the plunge pool bottom surface increased (highlighted light pink to dark red), which resulted in greater rock scour occurring.

Table 5.4: Effect of discharge on 1% exceedance dynamic pressure head for test conducted at H_{min}, TWD_{min}

Unit discharge	$m^3/s/m$	Model	0.392	0.392	0.500	0.896
		Prototype	35.062	35.062	44.721	80.141
1% exceedance dynamic pressure head	m	Model	0.122	0.200	0.466	0.54
		Prototype	2.438	4.000	9.313	10.81

5.7.5.2 Fall height effect on pressure

The effect of the fall height on the dynamic pressures at the plunge pool bottom surface were analysed by comparing the 1% exceedance dynamic pressure head for the different fall heights, keeping the discharge and pool depth constant, as plotted in Figure 5.28. The data labels in Figure 5.28 indicate the pressure head values as prototype and model scale respectively. No prominent relationship occurred between the fall height and the pressure head experienced at the pool bottom. The pressure results substantiate the conclusion made in Section 5.7.3.2 and by Castillo et al. (2015) that the scour process is independent of the fall height, especially since the jet was fully developed at impingement with the tailwater level for the different fall heights tested as detailed in Section 5.7.4. The scour process is however dependent on the discharge and air entrainment that varies over the fall height.

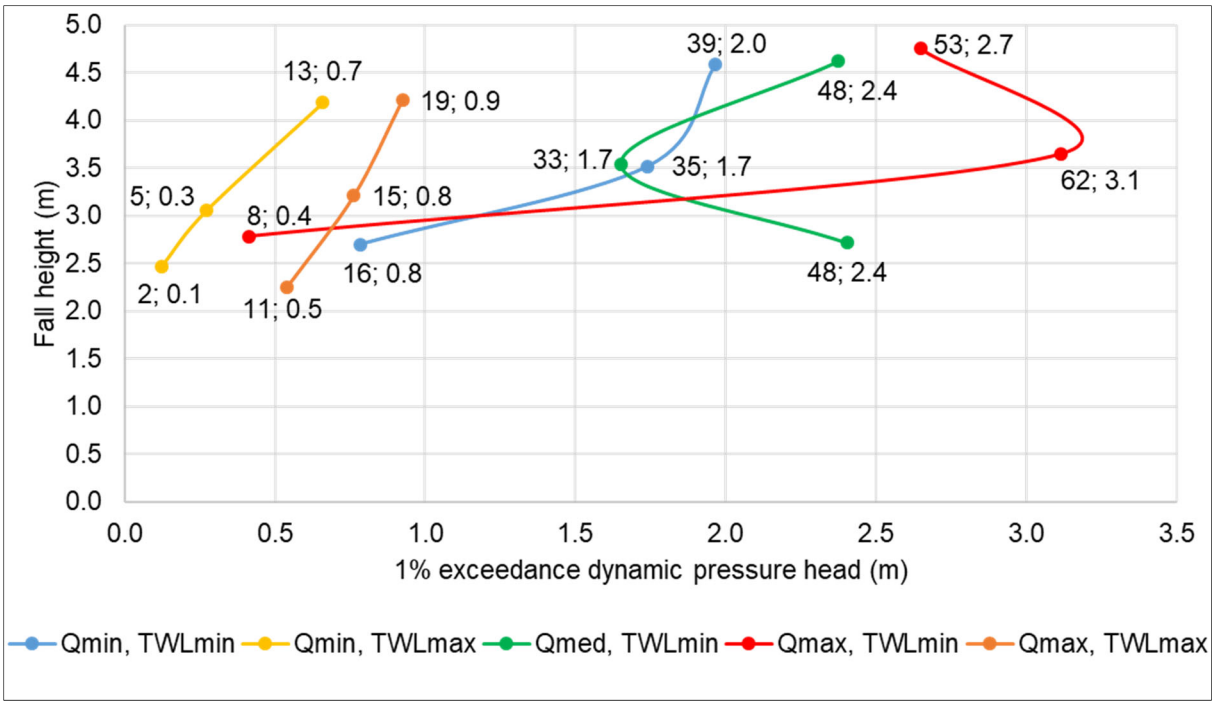

Figure 5.28: Observed dynamic pressure head (model and prototype values) for different fall height

5.7.5.3 Plunge pool depth effect on dynamic pressures

The effect of the plunge pool depth on the dynamic pressure head experienced at the pool bottom surface was analysed by comparing the dynamic pressure head values at the deepest scour hole location for the various pool depths and keeping the discharge and fall height constant. Table 5.5 summarises the 1% exceedance dynamic pressure head values for the maximum discharge (M: 0.896 $m^3/s/m$, P: 80 $m^3/s/m$) and maximum fall height (M: 5 m, P: 100 m) as an example.

Table 5.5: Effect of plunge pool depth on dynamic pressures for Q_{max}, H_{max}

Plunge pool depth (m)		**1% exceedance dynamic pressure head (m)**	
Model	**Prototype**	**Model**	**Prototype**
1.0	20.0	0.93	18.50
0.5	10.0	2.65	53.00

The observed 1% exceedance dynamic pressure head results indicate that the dynamic pressures experienced at the pool bottom increases with a decrease in the plunge pool depth. Deeper plunge pools therefore reduce the scour process more efficiently than shallow pools

by means of greater diffusion of the jet in the basin and reducing the dynamic pressures experienced at the pool bottom surface.

5.7.5.4 Mean and fluctuating dynamic pressure coefficients

Effective energy dissipation in the plunge pool occurs by means of diffusion for pool depths Y/B_j > 5 for rectangular jets. The dynamic pressure coefficients could be used to estimate the mean and fluctuating stream power decay coefficients by means of Equation 3.15 in Section 3.4.1. Thus, the disintegration of the jet through the air and its diffusion through the plunge pool could be determined using the mean and fluctuating dynamic pressure coefficients.

The total dynamic pressure (P_{max}) at the pool bottom comprises of the mean (C_p) and dynamic pressure (C_p') pressure coefficient as expressed in Equation 2.33 in Section 2.4.2. The mean and fluctuating pressure coefficients for the experimental tests as a function of the Y/B_j and H/L_b ratios are shown in Figure 5.29 and Figure 5.30 by the red curve, respectively, compared to results from previous studies. The mean percentage difference between the maximum dynamic pressure observed at the deepest point in the plunge pool compared to the total dynamic pressure (P_{max}) calculated with Equation 2.33 is 17%.

The mean dynamic pressure coefficients (C_p) for the current study correspond to the coefficients for developed jets for H/L_b > 1.6 by the other authors presented in Figure 5.29. The observed fluctuating dynamic pressure coefficients ($C_p{}'$) for the current study plot below the H/L_b > 1.6 graph proposed by the other authors as shown in Figure 5.30, due to the experimental tests of the current study having H/L_b > 1.85 (deduced from Equation 2.5) for all tests.

The maximum $C_p{}'$-values for the current study reaches an asymptotic value of 0.124 for H/L_b > 1.85. This finding is in contrast to that reported in literature (see Section 2.4.2) that said the fluctuating pressure coefficient is negligible for H/L_b > 2 (Castillo et al., 2015), since the magnitude of the fluctuations decrease for fully developed jets as the impingement area extends over a wider area. However, a C_p'-value of 0.124 can lead to a condition where the applied stream power in the plunge pool never crosses the threshold stream power of the rock for dams with significant discharge and deep plunge pools. Therefore a C_p'-value of zero should rather be used for deep plunge pools ($Y/D_j > 20$).

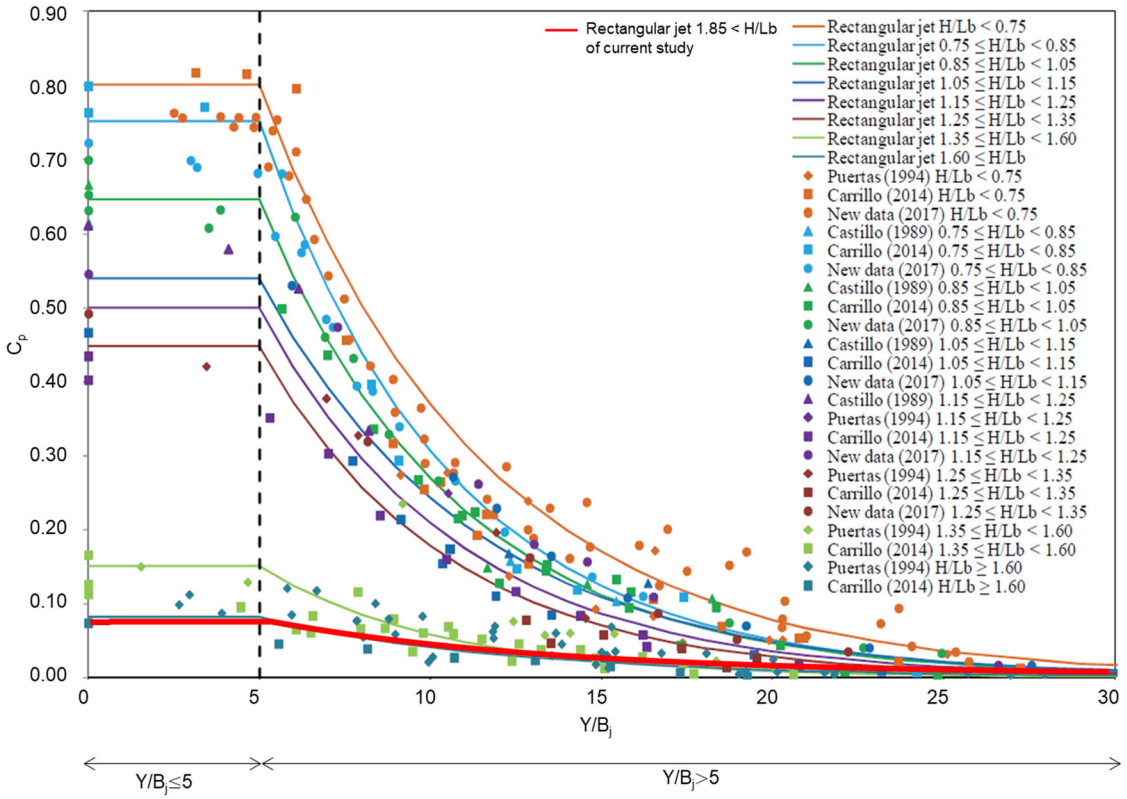

Figure 5.29: Mean dynamic pressure coefficients C_p of experimental tests as a function of Y/B_j and H/L_b ratios laid over results from previous studies (Castillo et al., 2018)

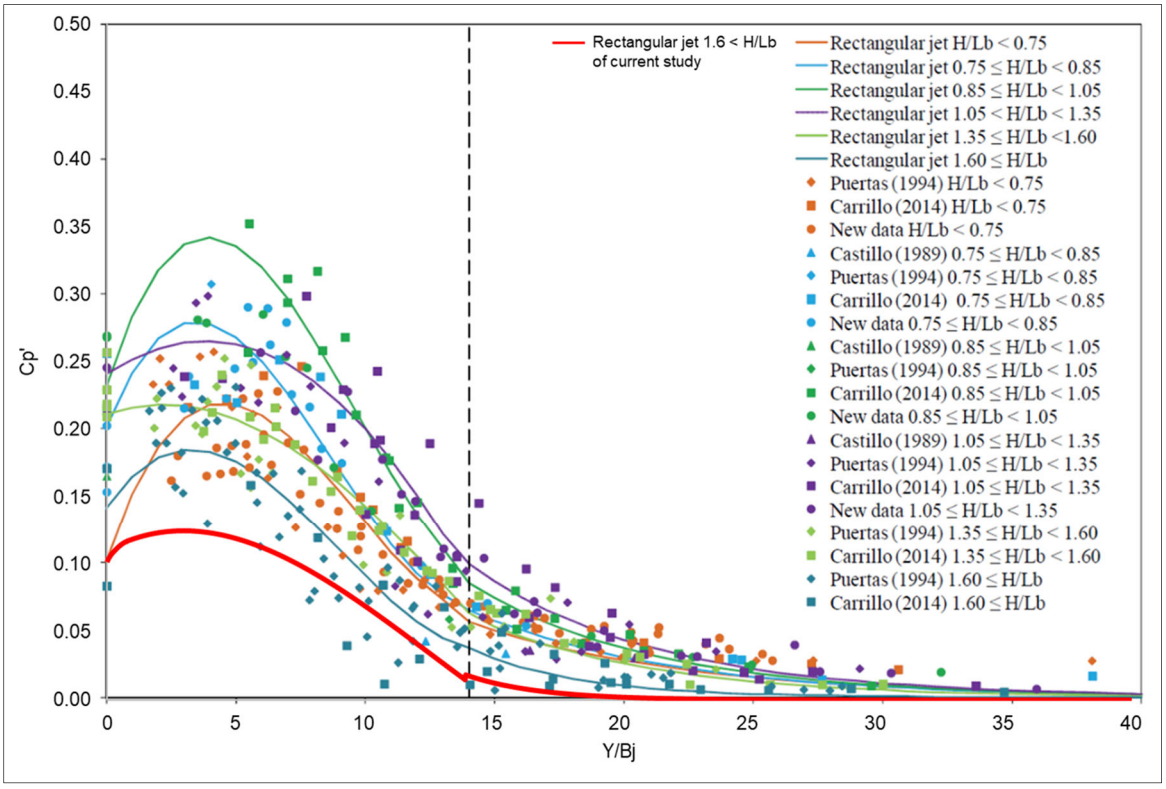

Figure 5.30: Fluctuating dynamic pressure coefficients $C_p{}'$ of experimental tests as a function of Y/B_j and H/L_b ratios laid over results from previous studies (Castillo et al., 2018)

5.8. Analysis of physical model results

5.8.1. *Derivation of formulae representing model data*

5.8.1.1 Regression models

An Ordinary Least Squares (OLS) regression analysis was performed on the collected physical model data to develop non-dimensional equations that predict the scour hole geometry (depth, length, width, and volume). Three regression models were each analysed for both Case A (scour and deposition) and Case B (scour with deposited rocks removed continuously), namely Linear, Logarithmic Transformed and Linear Logarithmic, represented by Equation 5.3 to Equation 5.6.

Linear model:

$$\pi_0 = k + a \cdot x_1 + b \cdot x_2 + c \cdot x_3 + \ldots \qquad \textit{Equation 5.3}$$

where:

π_0: dependent variable
$x_{1,2,3,\ldots}$: independent variables
k: intercept value (constant)
$a, b, c, \ldots$: coefficients

Logarithmic Transformed model:

$$\ln(\pi_0) = \ln(k) + a \cdot \ln(x_1) + b \cdot \ln(x_2) + c \cdot \ln(x_3) + \ldots \qquad \textit{Equation 5.4}$$

Equation 5.4 can be transformed to exponential form:

$$\pi_0 = k \cdot x_1^a \cdot x_2^b \cdot x_3^c \cdot \ldots \qquad \textit{Equation 5.5}$$

Linear Logarithmic model:

$$\pi_0 = k + a \cdot \ln(x_1) + b \cdot \ln(x_2) + c \cdot \ln(x_3) + \ldots \qquad \textit{Equation 5.6}$$

Specific statistical parameters of each model were analysed to distinguish between the models. The statistical parameters (formulae given in Annexure H) that were analysed were:

- Coefficient of determination, R^2. R^2 is a statistical measure of how close the data points fall within the fitted regression line. The R^2 value ranges from 0 to 1, with a value of 1 indicating that the model explains all of the variability of the observed data around its mean.

- The adjusted R^2 value is an amendment to the R^2 value that takes the number of independent variables in the data set into account. The adjusted R^2 value only increases if a new data point improves the regression model more than expected by chance.
- The probability value or p-value tests the null hypothesis that the coefficient is zero. The p-value ranges between 0 and 1. A low p-value (typically < 0.05) indicates that the null hypothesis can be rejected.
- Akaike Information Criterion (AIC) estimates the quality of a model compared to the other models. Thus, the AIC looks at the efficiency and simplicity of the model, providing a means of model selection. The smaller the AIC value, the better the quality of the model.
- Log-likelihood also provides a means for model selection by expressing how likely particular statistical parameter values are to the observation set. The higher the log-likelihood is, the closer the predicted and observed values are.

5.8.1.2 Dimensional analysis

Dimensional analysis is often used to reduce the complexity of fundamental equations describing a system to the simplest form. According to Albrecht et al. (2013) there are two main advantages associated with dimensional analysis, namely:

a) The number of independent variables can be reduced in a standard experiment.
b) Scalability of results are possible, since each variable set is made dimensionless.

The use of dimensional analysis in developing formulae representing the different scour hole geometrical variables is therefore advantageous, since the variables that have the smallest influence on the scour hole geometry are eliminated and scalability is made possible.

Several variables were incorporated in the regression analysis, such as rock diameter, discharge, fall height, plunge pool depth, stream power, submerged weight of the rock block, and uplift pressure and forces. The main variables influencing the flow and rock scour were selected based on the literature study and experimental tests (refer to Section 2.6).

Instead of incorporating bed shear stress explicitly, the movability number (Equation 5.7) based on the settling velocity (V_{ss}), as well as the particle Reynolds number, Re_p (Equation 5.8), were used in analysing the rock scour. The movability number and particle Reynolds number have the benefit that they are based on the shear velocity (V^*) that the particles experience due to the plunging jet, and the particle size (Armitage & Rooseboom, 2010). The movability number ranged between 0.176 and 0.76 for the experimental tests in the current

research. Rooseboom (1992) recommended a movability number greater than 0.12 for prefabricated paving blocks and Delport (2019) proposed movability numbers of 0.249 and 0.366 for Armorflex 140 installed on bed and side slopes, respectively. The minimum movability number of 0.176 determined in the current study is therefore similar to that recommended by Rooseboom (1992).

$$MN = \frac{V^*}{V_{ss}} \qquad \textit{Equation 5.7}$$

$$Re_p = \frac{V^* d_{50}}{\nu} \qquad \textit{Equation 5.8}$$

with ν the kinematic viscosity of water = 1 x 10^{-6} m²/s at 15˚C, and V^* the shear velocity (m/s) defined as

$$V^* = \sqrt{g \cdot y_{down} \cdot S_f} \qquad \textit{Equation 5.9}$$

with y_{down} denoting the wall jet thickness (m) downstream of the impingement region as illustrated in Figure 3.4. The energy slope S_f required for determining the shear velocity was determined from Chèzy (Equation 5.10) (Chadwick et al., 2013) by assuming the hydraulic radius $R = \frac{A_{wall\,jet}}{W_{j\,rock}}$ (area of jet deflected downstream of impingement/jet width at impingement with bedrock). The surface roughness was approximated as $k_s = d_{50}$ median particle size (Equation 4.2). The settling velocity was selected as representative of the transportability of large aggregate, since it accounts for size, shape, and density of the rock blocks. The median prototype settling velocity V_{ss} is 4.19 m/s and 4.99 m/s for the rock size 1 and 2 respectively.

$$Q_{down} = A_{wall\,jet} \times 18log\left(\frac{12R}{d_{50}}\right)\sqrt{R \cdot S_f} \qquad \textit{Equation 5.10}$$

with Q_{down} the respective discharge (m^3/s) downstream of the impingement region, based on the total flow and jet impinging angle, δ (Table 3.4), assumed equal to the jet impingement angle with the tailwater level (θ_j), R the hydraulic radius (m), and S_f the energy slope. The wall jet flow area defined as $A_{wall\,jet} = y_{down} \times W_{j\,rock}$, with $W_{j\,rock}$ the width of the jet at impingement with the rock bed (m), taking the jet outer spreading angle as 15º (Ervine & Falvey, 1987) for highly turbulent jets. The median particle size d_{50} (m) is defined by Equation 4.2.

The rock joint structure angle, α_r, did not form part of the regression analysis, since the joint angle only varied for a few tests. The regression analysis attributes variation in the dependent variable (π_0) to x-variables. The covariance matrices did not converge when the regression analysis was performed including the rock joint structure angle. It was therefore decided to

exclude the joint angle from the regression analysis and derive stability factors that take the joint angle into account (refer to Table 5.9).

The scour hole geometry (scour depth, length, width, and volume) could be expressed as a function of the following variables:

$$f\left(H_w, y_w, Q_w, \rho_r, \rho_w, d_{50}, V_{ss}, D_i, W_i, B_j, V_i, V_j, L_b, G_b, F_{uplift}, P_{SP}, P_{uplift}, Fr_i, g, P, P_{crit}, V^*\right) = 0 \qquad \textit{Equation 5.11}$$

where:

H_w	=	fall height	m
y_w	=	plunge pool depth	m
Q_w	=	discharge	m^3/s
ρ_r	=	rock density	kg/m^3
ρ_w	=	water density	kg/m^3
x, y, z, d_{50}	=	rock block size	m
V_{ss}	=	rock block settling velocity	m/s
D_i	=	flow depth at issuance	m
W_i	=	flow width at issuance	m
B_j	=	jet thickness at impingement	m
V_i	=	issuance velocity	m/s
V_j	=	velocity at impingement	m/s
L_b	=	breakup length	m
G_b	=	submerged weight of rock block	N
F_{uplift}	=	lift force	N
P_{SP}	=	stream power per area	kW/m^2
P_{uplift}	=	uplift pressure	Pa
Fr_i	=	Froude number at issuance	-
g	=	gravitational acceleration constant	$9.81\ m/s^2$
P	=	1% exceedance dynamic head	m
P_{crit}	=	critical pressure head	m
V^*	=	shear velocity	m/s

The dimensionless variables were obtained by applying the Buckingham π-theorem (Albrecht et al., 2013) on the scour hole variables listed in Equation 5.11 and choosing V_i, H_w and ρ_w as repeating variables, as shown in Table 5.6.

Table 5.6: Dimensionless variables used in regression analysis

Rock block dimension vs. fall height	$x_1 = \frac{d_{50}}{H_w}$	Pool depth vs. fall height	$x_8 = \frac{y_w}{H_w}$
Froude number at issuance	$x_2 = \frac{V_i}{\sqrt{gD_i}}$	Fluid Reynolds number at issuance	$x_9 = \frac{V_i D_i}{\nu}$
Fall height vs. jet breakup length	$x_3 = \frac{H_w}{L_b}$	Drop number (Khatsuria, 2004)	$x_{10} = \frac{q^2}{gH_w^3}$
Settling velocity vs. issuance velocity	$x_4 = \frac{V_{SS}}{V_i}$	Stream power vs. uplift pressure times settling velocity (Annandale, 2006)	$x_{11} = \frac{P_{SP}}{P_{uplift} \cdot V_{SS}} = \frac{\gamma Q_w H_w / (B_{jrock} \cdot W_{jrock})}{V_{SS} \cdot C_I \gamma V_j^2 / 2g}$
Pool depth vs. impinging jet thickness	$x_5 = \frac{y_w}{B_j}$	Pressure head	$x_{12} = \frac{P}{P_{crit}} = \frac{P}{P_{uplift}/\gamma}$
Uplift force vs. weight of rock block (Bollaert, 2002 and 2012)	$x_6 = \frac{F_{uplift}}{G_b} = \frac{C_I \gamma_w (x_b \cdot y_b) \frac{V_j^2}{2g}}{V_b(\rho_r - \rho_w)g}$	Movability number (Armitage & Rooseboom, 2010)	$x_{13} = \frac{V^*}{V_{ss}} = \frac{\sqrt{9.81 \cdot y_{down} \cdot S_f}}{V_{SS}}$
Stream power vs. uplift pressure times impingement velocity	$x_7 = \frac{P_{SP}}{P_{uplift} \cdot V_j} = \frac{\gamma Q_w H_w / (B_{jrock} \cdot W_{jrock})}{V_j \cdot C_I \gamma V_j^2 / 2g}$	Particle Reynolds number (Armitage & Rooseboom, 2010)	$x_{14} = \frac{V^* d_{50}}{\nu}$

For explanatory purposes, the relationship describing the dimensionless scour hole depth is then:

$$\frac{y_{scour}}{H_w} = f\left(\frac{d_{50}}{H_w}, \frac{V_i}{\sqrt{gD_i}}, \frac{H_w}{L_b}, \frac{V_{SS}}{V_i}, \frac{y_w}{B_j}, \frac{F_{lift}}{G_b}, \frac{P_{SP}}{P_{uplift} \cdot V_j}, \frac{y_w}{H_w}, \frac{\rho_w V_i H_w}{\mu}, \frac{q^2}{gH_w^2}, \frac{P_{SP}}{P_{uplift} \cdot V_{SS}}, \frac{P}{P_{uplift}}, \frac{V^*}{V_{ss}}, \frac{V^* d_{50}}{\nu}\right) \quad \textit{Equation 5.12}$$

5.8.1.3 Least squares regression analysis

The variables describing the scour hole geometry were calculated using ordinary least squares regressions, with consideration given to the parsimony principle. Due to the availability of many regressors, parsimony is emphasized to ensure avoiding over-fitting. The data points of the repeated tests (Tests 1B, 1C, 4B, 7B and 14B) did not form part of the regression analysis in order to confirm the developed formulae inside the ranges in which they were based on.

The regression modelling was started by performing a multi-regression analysis with all the variables (x_1 to x_{14}) on the physical model results for the horizontal and vertical rock joint structure network tests, excluding the repeated tests. Thereafter, the variables with the least significance were excluded one by one. The variables with a p-value > 0.05 were first excluded. Thereafter, the regression analysis options with high AIC-values and low Log-likelihood values were excluded. Finally, the regression analysis that was found not to have a good correlation to the experimental results was excluded by comparing the R^2-values of the different regression options and the percentage difference with the experimental data. A total of 168 regression analysis options were investigated. Table 5.7 shows the best performing regression analysis options according to the AIC, Log-likelihood and R^2 model selection methods for scour dimensions. The Logarithmic Transformed model provided the best fit for all the scour geometry dimensions (scour depth, length, width, and volume), except the scour hole depth for Case B was predicted best by the Linear Log model (highlighted red in Table 5.7).

Regression analysis options EQ60 and EQ83 (EQ: Regression analysis option equation) were both the best performing regression analysis options for determining the scour length for Case A with the lowest percentage difference between the observed and predicted values for all the tests (refer to Table 5.7). Analysis option EQ60 has a greater percentage difference for the repeated tests (23.9% difference) compared to 21.7% for EQ83. However, analysis option EQ60 was chosen to be the preferred formula to predict the scour length for Case A, since it incorporates the rock density in the submerged weight (G_b) variable, whereas analysis option EQ83 does not take the rock density into account.

The regression analysis indicated that by adding the intercept value k in Equation 5.3 to Equation 5.6, the coefficient of determination (R^2) decreased and the average difference increased for all three regression models. The dependent variable, π_0, is represented by the intercept value when all the independent variables ($x_{1,2,3,\dots}$) are zero. However, when the independent variables are zero, π_0 should also be zero, since no scour has occurred. The intercept value was removed from the analysis by forcing it to be zero.

Table 5.8 summarises the non-dimensional formulae for horizontal and vertical rock joint structures developed from the regression analysis. To apply these formulae the equilibrium scour depth should first be determined by a trial-and-error procedure using the scour formula in Table 5.8, initially for a jet impinging onto the original flat bed. Iteration ceases when a reasonable percentage difference between successive iterations is found. Thereafter, the scour variable (i.e. movability number and dynamic pressure head) at the equilibrium scour

depth can be used in order to obtain the other scour hole geometries (length, width, and volume) by using the developed formulae presented in Table 5.8.

The regression analysis results for the scour hole variables (depth, length, width and volume) for Case A (scour and deposition) and Case B (deposited rocks removed) are shown in Figure 5.31 and Figure 5.32 respectively with the 95% confidence band. The regression analysis results indicate that a good correlation was achieved between the predicted and observed values, which is a confirmation that the formulae are the best representation of the experimental data on which they were based. The derived regression formulae to determine the scour depth for Case A (Equation 5.13) and Case B (Equation 5.14) are compared to the experimental data in Figure 5.33 for confirmation of a good correlation between the formulae and model data.

The developed regression formulae were confirmed inside the ranges in which the developed formulae were based on for the experimental results that were not used for developing the formulae. The developed formulae correlate well with the observed validated data with percentage error (i.e. percentage difference between test values and that predicted by the developed formulae) ranging between 9.3% to 27.1% for Case A and 8.6% to 22.5% for Case B as detailed in Table 5.7.

The stabilising (or destabilising) factors for joint structure angles orientated 45º in and against the direction of the flow are summarised in Table 5.9. The joint structure angle factors should be applied to the predicted scour geometry results obtained for the horizontal and vertical joint formulae in Table 5.8.

Although the variation in the stabilising factors is small, additional experimental testing is required to ascertain whether linear interpolation is possible between the stabilising factors for different degrees of joint structures between 0° and 45° in and against the flow direction.

Table 5.7: Best performing regression models for scour dimensions (scour depth, length, width and volume)

Model selection method	Regression model	Depth Case A				Depth Case B			
		Winning equation	R^2	% diff. (all tests)	% diff. (repeated tests)	Winning option	R^2	% diff. (all tests)	% diff. (repeated tests)
AIC	Linear	EQ23	0.991	17.1%	23.3%	EQ9	0.991	71.9%	107.6%
	Log	**EQ60**	**0.998**	**13.6%**	**10.0%**	EQ58	0.997	7.6%	30.2%
	Linear Log	EQ116	0.994	13.8%	34.0%	**EQ113**	**0.992**	**7.1%**	**14.3%**
Log-Likelihood	Linear	EQ6	0.991	14.4%	21.8%	EQ9	0.991	71.9%	107.6%
	Log	**EQ60**	**0.998**	**13.6%**	**10.0%**	EQ60	0.997	7.3%	27.3%
	Linear Log	EQ116	0.994	13.8%	34.0%	**EQ113**	**0.992**	**7.1%**	**14.3%**
R^2	Linear	EQ6	0.991	14.4%	21.8%	EQ9	0.991	71.9%	107.6%
	Log	**EQ60**	**0.998**	**13.6%**	**10.0%**	EQ57	0.997	7.6%	30.2%
	Linear Log	EQ116	0.994	13.8%	34.0%	**EQ113**	**0.992**	**7.1%**	**14.3%**

Model selection method	Regression model	Length Case A				Length Case B			
		Winning equation	R^2	% diff. (all tests)	% diff. (repeated tests)	Winning option	R^2	% diff. (all tests)	% diff. (repeated tests)
AIC	Linear	EQ25	0.980	14.8%	32.5%	EQ9	0.995	19.2%	30.8%
	Log	**EQ83**	**0.976**	**12.2%**	**21.7%**	EQ108	0.977	8.2%	26.2%
	Linear Log	EQ164	0.974	15.3%	23.1%	EQ114	0.992	8.0%	32.8%
Log-Likelihood	Linear	EQ9	0.981	65.3%	56.7%	EQ9	0.995	19.2%	30.8%
	Log	**EQ60**	**0.987**	**12.2%**	**23.9%**	**EQ60**	**0.984**	**6.5%**	**22.5%**
	Linear Log	EQ116	0.985	15.8%	31.0%	EQ116	0.992	8.2%	33.4%
R^2	Linear	EQ6	0.981	27.9%	24.6%	EQ9	0.995	19.2%	30.8%
	Log	**EQ60**	**0.987**	**12.2%**	**23.9%**	**EQ60**	**0.984**	**6.5%**	**22.5%**
	Linear Log	EQ113	0.985	15.4%	29.4%	EQ113	0.992	8.4%	32.7%

* EQ: Regression analysis option equation

** Winning regression model is highlighted in red

Model selection method	Regression model	Width Case A				Width Case B			
		Winning equation	R^2	% diff. (all tests)	% diff. (repeated tests)	Winning option	R^2	% diff. (all tests)	% diff. (repeated tests)
AIC	Linear	EQ6	0.995	30.9%	35.1%	EQ43	0.998	52.9%	49.8%
	Log	**EQ60**	**0.998**	**5.0%**	**9.3%**	EQ60	0.996	4.9%	8.6%
	Linear Log	EQ127	0.994	7.9%	14.4%	EQ116	0.994	6.5%	11.5%
Log-Likelihood	Linear	EQ9	0.995	28.2%	31.7%	EQ9	0.998	46.7%	46.2%
	Log	**EQ60**	**0.998**	**5.0%**	**9.3%**	**EQ60**	**0.996**	**4.9%**	**8.6%**
	Linear Log	EQ116	0.995	6.8%	12.1%	EQ116	0.994	6.5%	11.5%
R^2	Linear	EQ6	0.995	30.9%	35.1%	EQ6	0.998	43.7%	42.8%
	Log	**EQ60**	**0.998**	**5.0%**	**9.3%**	**EQ60**	**0.996**	**4.9%**	**8.6%**
	Linear Log	EQ116	0.995	6.8%	12.1%	EQ116	0.994	6.5%	11.5%
Model selection method	**Regression model**	**Volume Case A**				**Volume Case B**			
		Winning equation	**R^2**	**% diff. (all tests)**	**% diff. (repeated tests)**	**Winning option**	**R^2**	**% diff. (all tests)**	**% diff. (repeated tests)**
AIC	Linear	EQ25	0.976	73.2%	62.7%	EQ15	0.993	225.7%	333.2%
	Log	**EQ60**	**0.999**	**13.5%**	**27.1%**	EQ97	0.998	97.6%	100.2%
	Linear Log	EQ122	0.942	66.8%	83.8%	EQ114	0.955	52.7%	153.8%
Log-Likelihood	Linear	EQ9	0.983	383.3%	139.7%	EQ9	0.994	240.7%	253.3%
	Log	**EQ60**	**0.999**	**13.5%**	**27.1%**	**EQ60**	**0.998**	**13.5%**	**14.4%**
	Linear Log	EQ116	0.945	63.1%	100.5%	EQ116	0.958	74.3%	154.3%
R^2	Linear	EQ6	0.983	618.8%	262.4%	EQ9	0.994	240.7%	253.3%
	Log	**EQ60**	**0.999**	**13.5%**	**27.1%**	EQ57	0.998	14.6%	11.8%
	Linear Log	EQ116	0.945	63.1%	100.5%	EQ116	0.958	74.3%	154.3%

* EQ: Regression analysis option equation

** Winning regression model is highlighted in red

*Table 5.8: Regression formulae for equilibrium scour hole geometry for horizontal and vertical open joints**

	Equation	R^2
Depth Case A *[Equation 5.13]*	$ln\left(\frac{Ds_{CaseA}}{H_W}\right) = -468.532ln\left(\frac{d_{50}}{H_W}\right) - 322.102\ln\left(\frac{V_i}{\sqrt{gD_i}}\right) + 4.502ln\left(\frac{H_w}{L_b}\right) - 483.385ln\left(\frac{V_{SS}}{V_i}\right) - 0.804ln\left(\frac{F_{lift}}{G_b}\right) - 0.817ln\left(\frac{y_w}{H_w}\right) - 473.991ln\left(\frac{V_iD_i}{\nu}\right) + 158.264ln\left(\frac{q^2}{gH_w^3}\right) - 0.419ln\left(\frac{P_{SP}}{P_{uplift}\cdot V_{SS}}\right) + 0.006ln\left(\frac{P}{P_{crit}}\right) - 473.536ln\left(\frac{V^*}{V_{ss}}\right) + 474.587ln\left(\frac{V^*d_{50}}{\nu}\right)$	0.998
Depth Case B *[Equation 5.14]*	$\frac{Ds_{CaseB}}{H_W} = -0.196ln\left(\frac{d_{50}}{H_W}\right) - 0.578\ln\left(\frac{V_i}{\sqrt{gD_i}}\right) - 0.942ln\left(\frac{V_{SS}}{V_i}\right) - 0.216ln\left(\frac{F_{lift}}{G_b}\right) - 0.129ln\left(\frac{P_{SP}}{P_{uplift}\cdot V_j}\right) - 0.079ln\left(\frac{y_w}{H_w}\right) - 0.279ln\left(\frac{V_iD_i}{\nu}\right) + 0.129ln\left(\frac{q^2}{gH_w^3}\right) + 0.006ln\left(\frac{P}{P_{crit}}\right) - 0.145n\left(\frac{V^*}{V_{ss}}\right) + 0.315ln\left(\frac{V^*d_{50}}{\nu}\right)$	0.992
Length Case A *[Equation 5.15]*	$\frac{Ls_{CaseA}}{H_W} = -416.262ln\left(\frac{d_{50}}{H_W}\right) - 281.275\ln\left(\frac{V_i}{\sqrt{gD_i}}\right) + 2.804ln\left(\frac{H_w}{L_b}\right) - 421.760ln\left(\frac{V_{SS}}{V_i}\right) + 0.666ln\left(\frac{F_{lift}}{G_b}\right) - 0.078ln\left(\frac{y_w}{H_w}\right) - 418.577ln\left(\frac{V_iD_i}{\nu}\right) + 140.444ln\left(\frac{q^2}{gH_w^3}\right) - 0.157ln\left(\frac{P_{SP}}{P_{uplift}\cdot V_{SS}}\right) - 0.076ln\left(\frac{P}{P_{crit}}\right) - 417.815ln\left(\frac{V^*}{V_{ss}}\right) + 418.985ln\left(\frac{V^*d_{50}}{\nu}\right)$	0.987
Length Case B *[Equation 5.16]*	$\frac{Ls_{CaseB}}{H_W} = \left(\frac{d_{50}}{H_W}\right)^{3.048}\cdot\left(\frac{V_i}{\sqrt{gD_i}}\right)^{-1.878}\cdot\left(\frac{H_w}{L_b}\right)^{1.427}\cdot\left(\frac{V_{SS}}{V_i}\right)^{-3.052}\cdot\left(\frac{F_{lift}}{G_b}\right)^{0.485}\cdot\left(\frac{y_w}{H_w}\right)^{-0.081}\cdot\left(\frac{V_iD_i}{\nu}\right)^{0.639}\cdot\left(\frac{q^2}{gH_w^3}\right)^{0.002}\cdot\left(\frac{P_{SP}}{P_{uplift}\cdot V_{SS}}\right)^{0.019}\cdot\left(\frac{P}{P_{crit}}\right)^{-0.001}\cdot\left(\frac{V^*}{V_{ss}}\right)^{0.872}\cdot\left(\frac{V^*d_{50}}{\nu}\right)^{-0.377}$	0.984
Width Case A *[Equation 5.17]*	$ln\left(\frac{Ws_{CaseA}}{H_W}\right) = -35.453\left(\frac{d_{50}}{H_W}\right) - 28.412\ln\left(\frac{V_i}{\sqrt{gD_i}}\right) + 2.079ln\left(\frac{H_w}{L_b}\right) - 43.005ln\left(\frac{V_{SS}}{V_i}\right) - 0.879ln\left(\frac{F_{lift}}{G_b}\right) + 0.102ln\left(\frac{y_w}{H_w}\right) - 37.850ln\left(\frac{V_iD_i}{\nu}\right) + 12.705ln\left(\frac{q^2}{gH_w^3}\right) - 0.229ln\left(\frac{P_{SP}}{P_{uplift}\cdot V_{SS}}\right) + 0.079ln\left(\frac{P}{P_{crit}}\right) - 37.585ln\left(\frac{V^*}{V_{ss}}\right) + 38.229ln\left(\frac{V^*d_{50}}{\nu}\right)$	0.998
Width Case B *[Equation 5.18]*	$\frac{Ws_{CaseB}}{H_W} = \left(\frac{d_{50}}{H_W}\right)^{-2.228}\cdot\left(\frac{V_i}{\sqrt{gD_i}}\right)^{4.390}\cdot\left(\frac{H_w}{L_b}\right)^{-1.844}\cdot\left(\frac{V_{SS}}{V_i}\right)^{6.531}\cdot\left(\frac{F_{lift}}{G_b}\right)^{0.853}\cdot\left(\frac{y_w}{H_w}\right)^{0.048}\cdot\left(\frac{V_iD_i}{\nu}\right)^{0.466}\cdot\left(\frac{q^2}{gH_w^3}\right)^{0.614}\cdot\left(\frac{P_{SP}}{P_{uplift}\cdot V_{SS}}\right)^{0.379}\cdot\left(\frac{P}{P_{crit}}\right)^{0.021}\cdot\left(\frac{V^*}{V_{ss}}\right)^{0.393}\cdot\left(\frac{V^*d_{50}}{\nu}\right)^{-0.565}$	0.996

	Equation	R^2
Scour volume Case A *[Equation 5.19]*	$ln\left(\frac{Vol_{CaseA}}{H_W^3}\right) = -131.752ln\left(\frac{d_{50}}{H_W}\right) - 106.469\ln\left(\frac{V_i}{\sqrt{gD_i}}\right) + 6.433ln\left(\frac{H_w}{L_b}\right) - 159.640ln\left(\frac{V_{SS}}{V_i}\right) + 1.567ln\left(\frac{F_{lift}}{G_b}\right) - 0.724ln\left(\frac{y_w}{H_w}\right) - 145.502ln\left(\frac{V_iD_i}{\nu}\right) + 47.595ln\left(\frac{q^2}{gH_w^3}\right) - 0.012ln\left(\frac{P_{SP}}{P_{uplift}\cdot V_{SS}}\right) - 0.134ln\left(\frac{P}{P_{crit}}\right) - 146.724ln\left(\frac{V^*}{V_{ss}}\right) + 146.313ln\left(\frac{V^*d_{50}}{\nu}\right)$	0.999
Scour volume Case B *[Equation 5.20]*	$\frac{Vol_{CaseB}}{H_W^3} = \left(\frac{d_{50}}{H_W}\right)^{3.061}\cdot\left(\frac{V_i}{\sqrt{gD_i}}\right)^{-5.062}\cdot\left(\frac{H_w}{L_b}\right)^{2.519}\cdot\left(\frac{V_{SS}}{V_i}\right)^{-8.050}\cdot\left(\frac{F_{lift}}{G_b}\right)^{1.330}\cdot\left(\frac{y_w}{H_w}\right)^{-0.470}\cdot\left(\frac{V_iD_i}{\nu}\right)^{-2.522}\cdot\left(\frac{q^2}{gH_w^3}\right)^{1.238}\cdot\left(\frac{P_{SP}}{P_{uplift}\cdot V_{SS}}\right)^{0.276}\cdot\left(\frac{P}{P_{crit}}\right)^{0.010}\cdot\left(\frac{V^*}{V_{ss}}\right)^{-2.566}\cdot\left(\frac{V^*d_{50}}{\nu}\right)^{2.966}$	0.998

* Ranges: Discharge: 35 $m^3/s/m$ – 80 $m^3/s/m$; Fall height: 60 m – 100 m; Tailwater depth: 10 m – 20 m; horizontal and vertical joint network

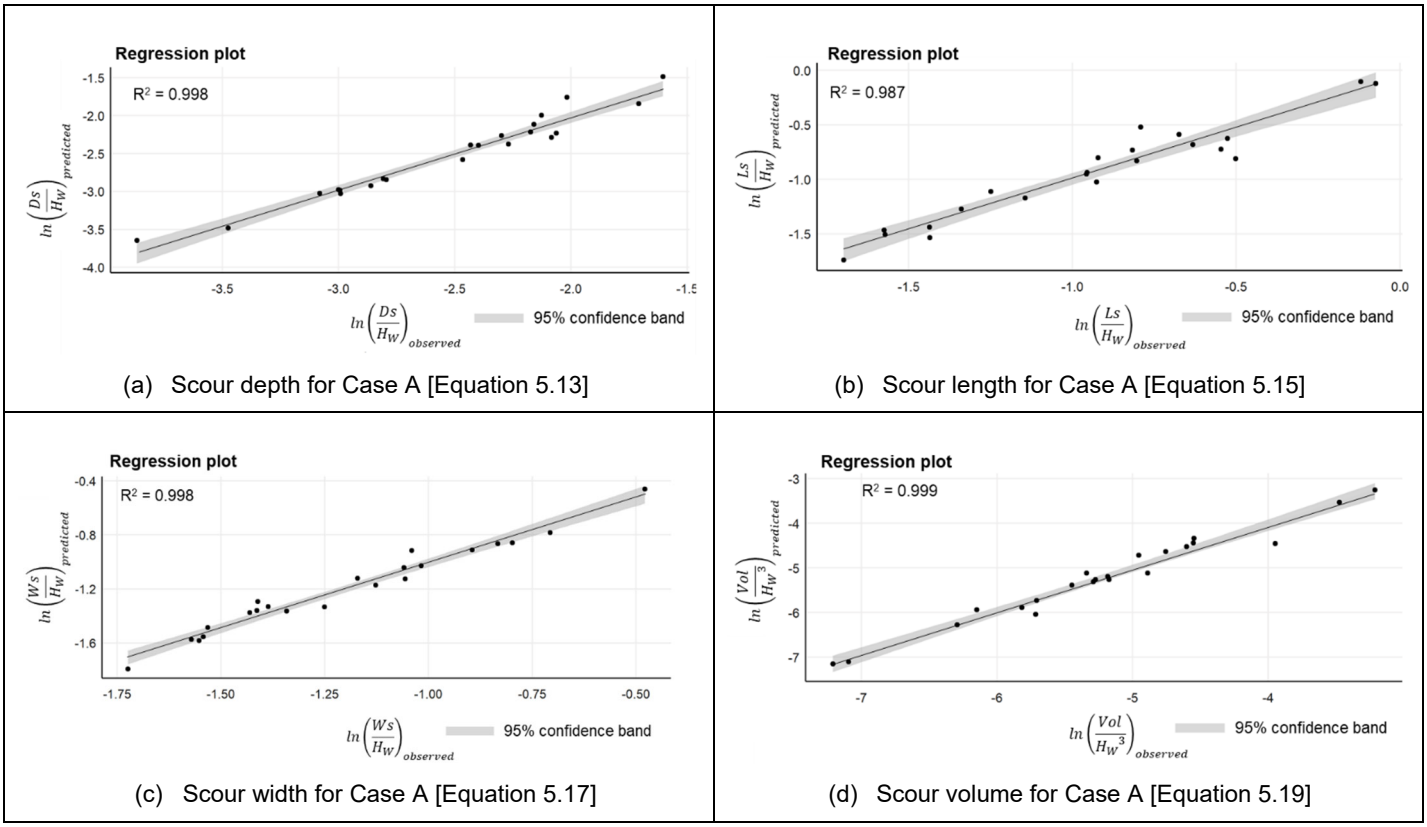

(a) Scour depth for Case A [Equation 5.13]

(b) Scour length for Case A [Equation 5.15]

(c) Scour width for Case A [Equation 5.17]

(d) Scour volume for Case A [Equation 5.19]

Figure 5.31: Regression analysis confirmation of Case A with 95% confidence band

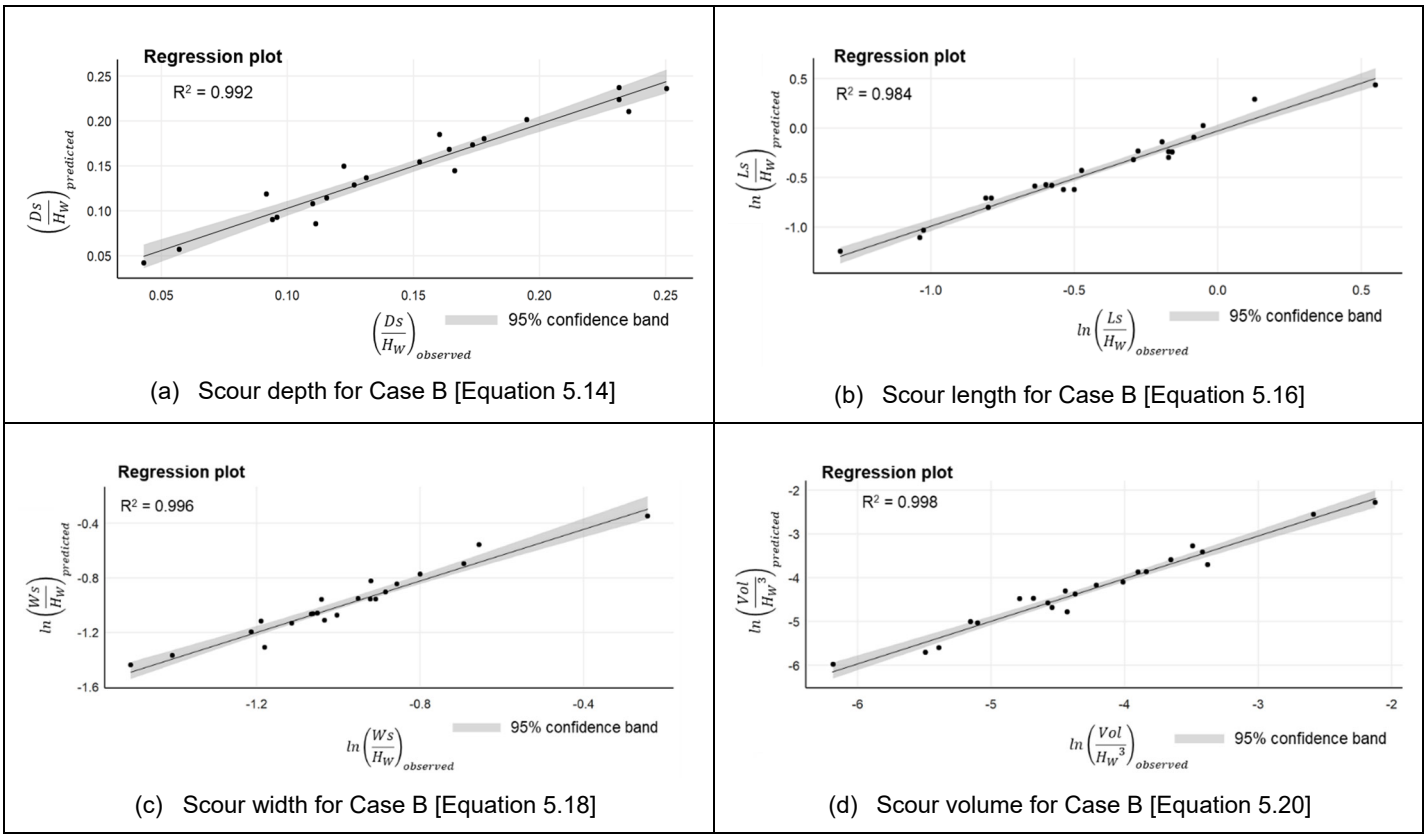

(a) Scour depth for Case B [Equation 5.14]

(b) Scour length for Case B [Equation 5.16]

(c) Scour width for Case B [Equation 5.18]

(d) Scour volume for Case B [Equation 5.20]

Figure 5.32: Regression analysis confirmation for Case B with 95% confidence band

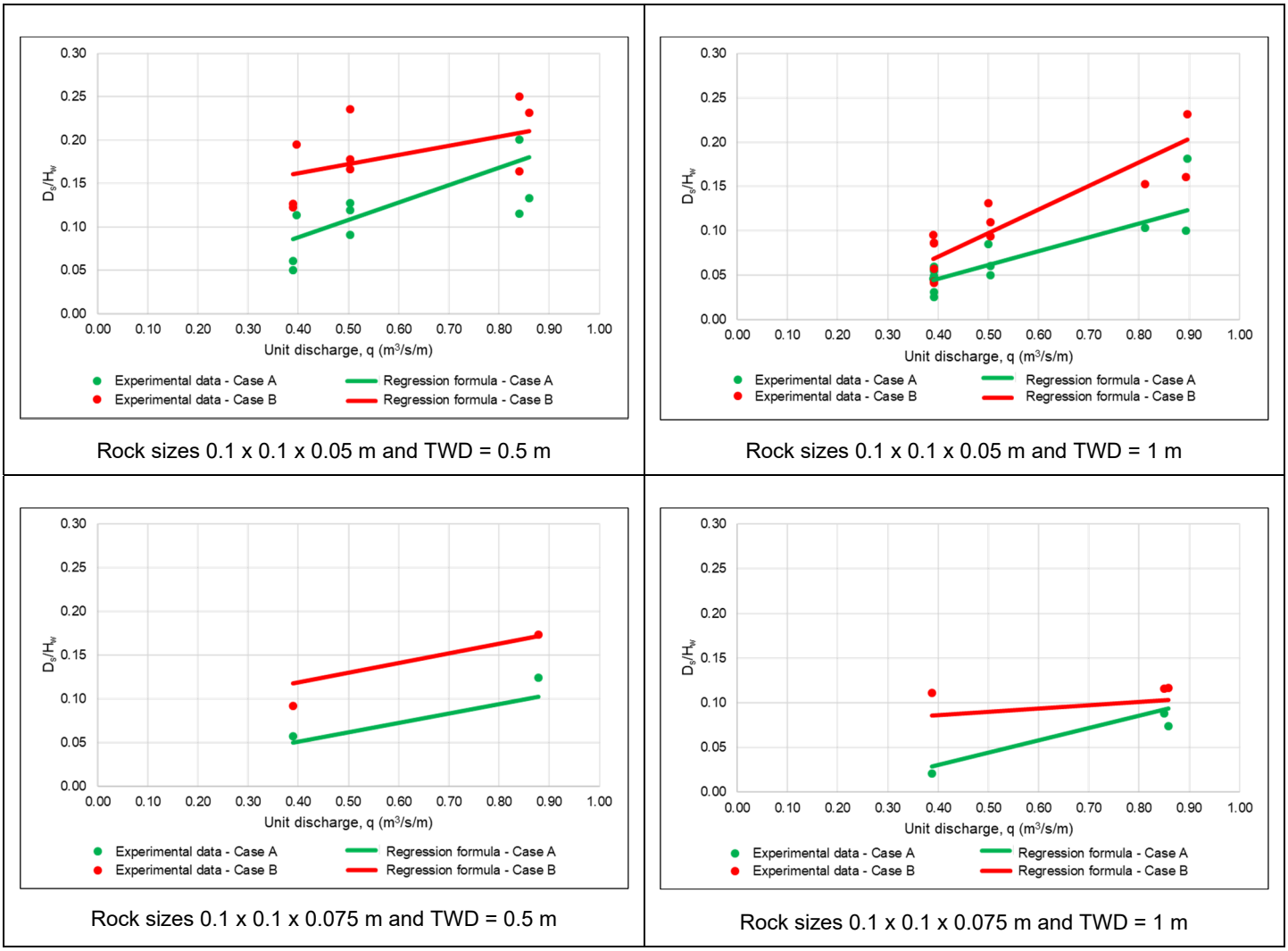

Rock sizes 0.1 x 0.1 x 0.05 m and TWD = 0.5 m

Rock sizes 0.1 x 0.1 x 0.05 m and TWD = 1 m

Rock sizes 0.1 x 0.1 x 0.075 m and TWD = 0.5 m

Rock sizes 0.1 x 0.1 x 0.075 m and TWD = 1 m

Figure 5.33: Comparison of derived scour depth formulae in this study with experimental data (model values)

Table 5.9: Stabilising factors due to joint angle

Scour hole geometry		**Dipping angle of rock relative the horizontal against flow direction**	**Dipping angle of rock relative to the horizontal in flow direction**	
		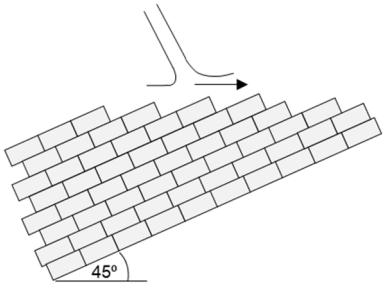	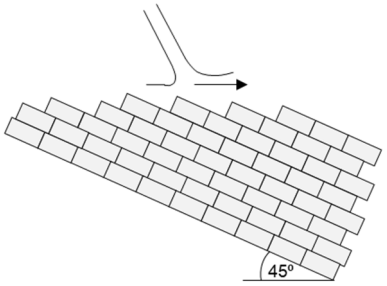	
Depth	Case A	0.93	1.29	
	Case B	0.89	1.06	
Length	Case A	0.98	0.77	
	Case B	0.82	Q < 45 $m^3/s/m$: 0.42	Q > 45 $m^3/s/m$: 0.89
Width	Case A	1.01	1.28	
	Case B	0.9	1.13	
Volume	Case A	0.83	Q < 45 $m^3/s/m$: 1.22	Q > 45 $m^3/s/m$: 0.48
	Case B	0.82	Q < 45 $m^3/s/m$: 1.09	Q > 45 $m^3/s/m$: 0.53

* Ranges: Discharge: 35 $m^3/s/m$ – 80 $m^3/s/m$; Fall height: 60 m – 100 m; Tailwater depth: 10 m – 20 m; 45º and 135º joints

5.8.2. *Application limitations of regression formulae derived from physical model data*

Relations (e.g. equations or formulae) derived from model tests, done in a particular variable test range, are normally assumed to be applicable over the tests' range as well as outside the tests' range (i.e. in the extrapolated zones). However, it is not always the case that the formulae derived from a range of model test conditions are also applicable outside of this range. Due to this uncertainty, the derived formulae in this study (Table 5.8), defining the relations between rock size, scour depth, fall height, discharge and plunge pool depth are,

strictly speaking, only applicable in the solution domain defined by ranges of the scaled-up physical model test conditions to a maximum model:prototype scale of 1:20. Therefore, formulae derived in this physical model study (Table 5.8) should be applied with caution outside the range as defined in Table 5.10. Table 5.10 demonstrates these application limits for different rock size ranges (all with densities of 2.65 kg/m³).

As an example, if the prototype rock falls in the 6th row rock size range in Table 5.10, the formulae in Table 5.8 are applicable within a fall height range of between 30 m and 50 m, a unit discharge range of between 12.4 m³/s/m and 28.3 m³/s/m and a stilling pool depth range of between 5 m and 10 m. Thus, if some of the variables are outside the relevant ranges, the results should be applied with caution.

Table 5.10: Definition of prototype application ranges of the formulae in Table 5.8

Rock size range							**Elevation range relative to bed,** $H_w + y_w$			**Unit discharge range, q**			**Plunge pool depth range, TWD**			**Prototype size relative to model (N)**	
x	**y**	**z**	**to**	**x**	**y**	**z**											
(m)							**(m)**			**(m³/s/m)**			**(m)**				
0.1	0.1	0.05	to	0.1	0.1	0.075	3	to	5	0.392	to	0.896	0.5	to	1	1	(model)
0.2	0.2	0.1	to	0.2	0.2	0.15	6	to	10	1.11	to	2.53	1	to	2	2	
0.4	0.4	0.2	to	0.4	0.4	0.3	12	to	20	3.14	to	7.17	2	to	4	4	
0.6	0.6	0.3	to	0.6	0.6	0.45	18	to	30	5.76	to	13.17	3	to	6	6	
0.8	0.8	0.4	to	0.8	0.8	0.6	24	to	40	8.87	to	20.27	4	to	8	8	
1	1	0.5	to	1	1	0.75	30	to	50	12.40	to	28.33	5	to	10	10	
1.2	1.2	0.6	to	1.2	1.2	0.9	36	to	60	16.30	to	37.25	6	to	12	12	
1.4	1.4	0.7	to	1.4	1.4	1.05	42	to	70	20.53	to	46.94	7	to	14	14	
1.6	1.6	0.8	to	1.6	1.6	1.2	48	to	80	25.09	to	57.34	8	to	16	16	
2	2	1	to	2	2	1.5	60	to	100	35.06	to	80.14	10	to	20	20	(target scale for this study)

5.8.3. *Regression analysis summary*

Formulae to predict the scour hole depth, length, width, and volume were developed by analysing 168 regression options. The AIC, Log-likelihood and R^2 model selection methods were used to determine the best performing regression analysis option.

The Logarithmic Transformed model provided the best fit for all the scour geometry dimensions (scour depth, length, width, and volume), except the scour hole depth for Case B, which was predicted best by the Linear Log model. The developed formulae all have a high coefficient of determination, R^2, indicating a good correlation between the predicted and observed values. The regression formulae were confirmed inside the ranges in which the developed formulae were based on.

For joint structure angles that are orientated 45º in and against the flow direction, stabilising (or destabilising) factors were derived.

5.9. Comparison of physical model results with scour prediction methods in literature

At present there is no universally agreed upon method to accurately predict the equilibrium scour hole depth due to plunging jets at dams, despite extensive research since the 1950s. The scour depth results from this study were compared to various analytical methods found in literature.

Twelve empirical formulae (Section 3.3), the EIM (Section 3.4.1), the Critical Pressure method (Section 3.4.3), the DI method (Section 3.4.2.2) and QSI method (Section 3.4.2.3) that are traditionally employed to predict rock scour due to plunging jets were evaluated against the results from the physical model study for a full-scale prototype. The CFM method (Section 3.4.2.1) was not applied to the physical model parameters, since the CFM method analyses fatigue failure and brittle fracturing of closed-ended joints, and the model's rock mass comprised a fully formed open-ended joint network.

The prototype scour hole depth formed in a movable bed based on the physical model study is compared to the scour prediction methods found in literature in Figure 5.34 for the 45 $m^3/s/m$ flow, a 100 m high fall height, a 20 m deep plunge pool, and horizontal and vertical aligned joints. The rock scour prediction methods from literature yield a wide range of scour depths for the same input conditions as shown in Figure 5.34. The methods that predicted a scour depth closest to the experimental results for Case B (deposited rocks removed continuously) for the example illustrated in Figure 5.34 in descending order are Veronese 2 (1984), Critical

Pressure method (Annandale, 2006), Mason and Arumugam empirical formula (Mason & Arumugam, 1985) and the EIM (Annandale, 2006).

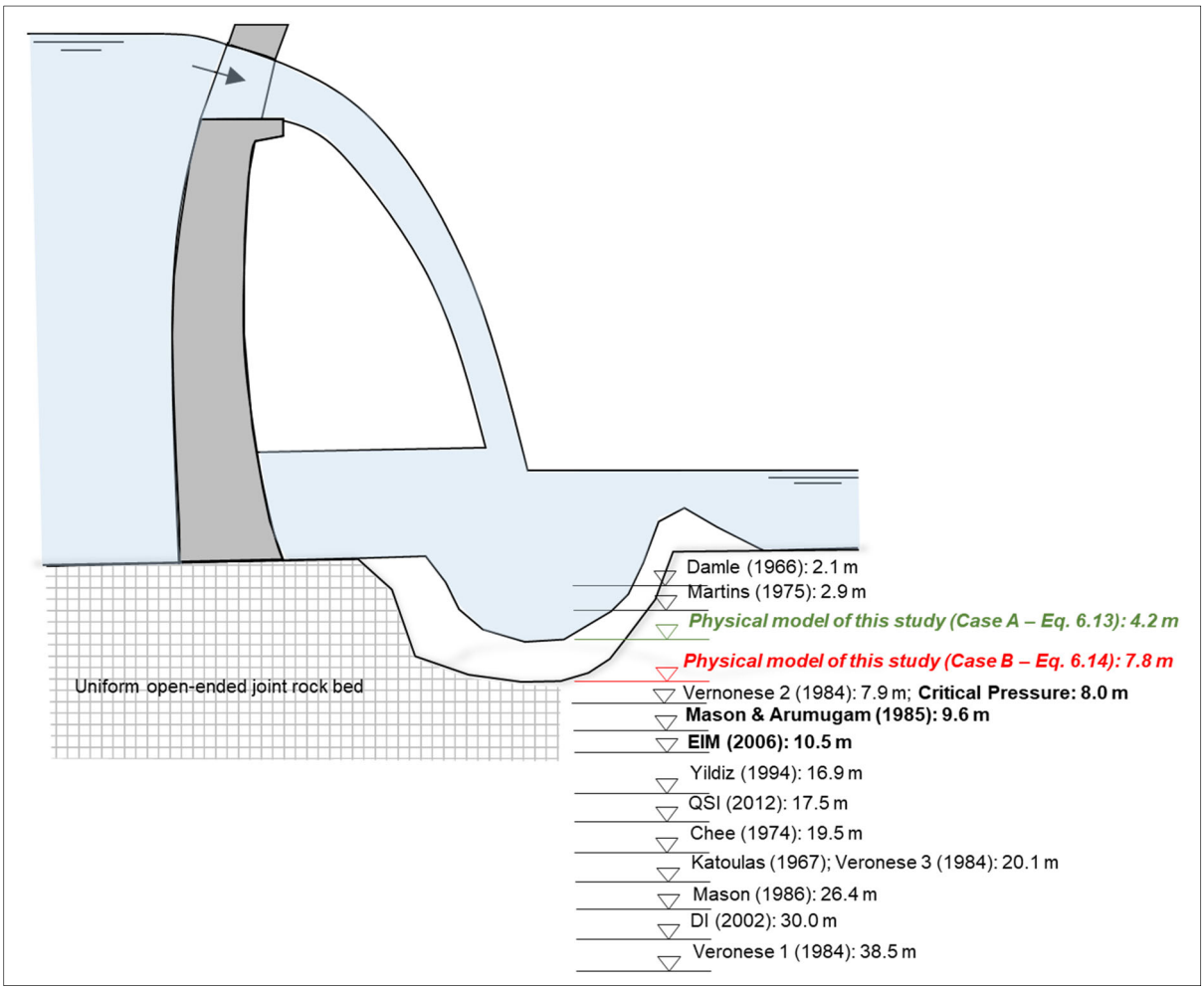

Figure 5.34: Prototype equilibrium scour depth for physical model and literature scour prediction methods for Q_{med}, H_{max}, TWD_{max} (not to scale)

Figure 5.35 is a correlation plot of scour depths observed in the experimental tests versus the scour depths predicted by 16 selected scour prediction methods from literature by applying prototype Case B physical model test conditions as input in the respective formulae or method. Figure 5.36 presents the statistical spread of the data in Figure 5.35. The percentage difference between the observed prototype depth from the experimental tests and the depths obtained from the respective literature methods is given by $\left({D_s}^{predicted} - {D_s}^{observed}\right)/{D_s}^{observed} \times 100$.

The percentage difference results shown in Figure 5.36 indicate that the scour prediction methods are in weak agreement with each other and generally overestimate the observed scour depths with a mean difference of 108% for Case B. The observed scour depths for Case A were also overestimated with a mean difference of 240%. The scour depth results of

the physical model are compared to the scour prediction method results for Case A for all the tests in Annexure G.3.

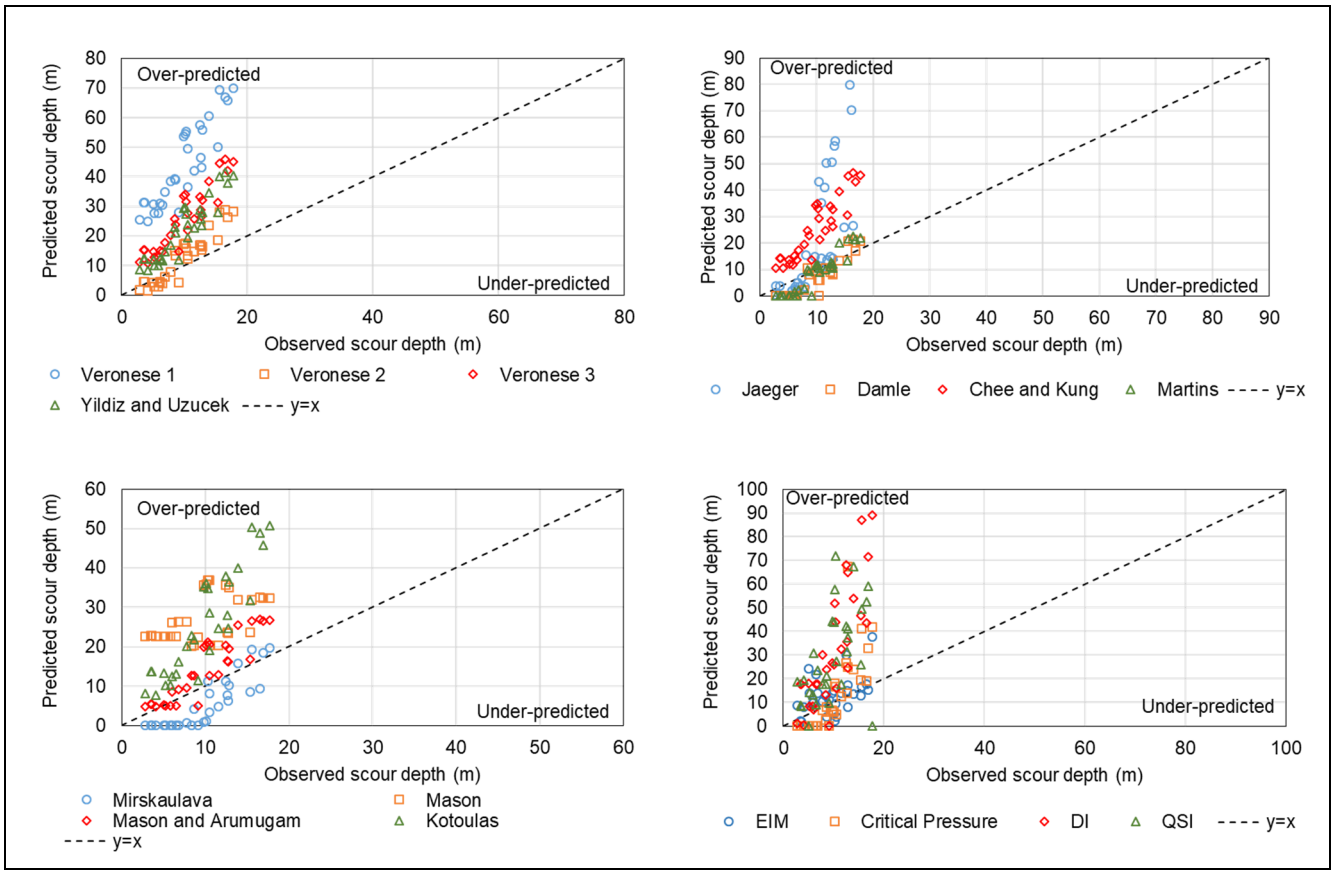

Figure 5.35: Comparison of equilibrium scour depths observed from experimental tests and predicted by the different methods for Case B

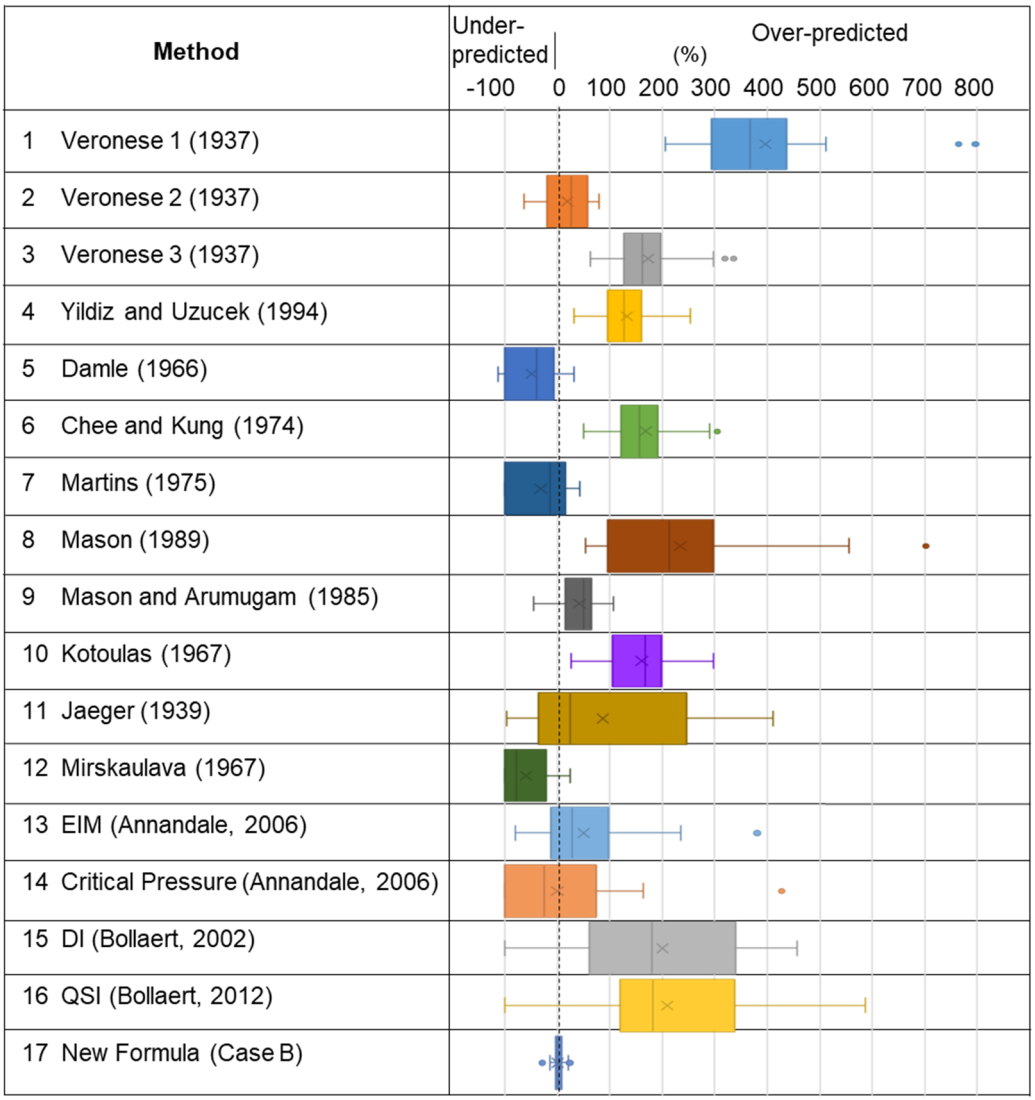

Figure 5.36: Scour depth distribution as a percentage difference for the different scour prediction methods from the experimental work for Case B

Figure 5.36 indicates that the analytical method agreeing the best with the experimental results is the Critical Pressure method (Annandale, 2006), since the median percentage difference is close to zero (-25.2%), and the method has the lowest mean percentage difference of 1% to the experimental scour depth results. However, the safest scour prediction method (accurate and conservative) would be the EIM (Annandale, 2006), followed by Mason and Arumugam's (1985) empirical equation, since the first quartile (25th percentile) nears the zero percentage difference (-12% and 15% respectively) with a narrow statistical spread. The EIM and Mason and Arumugam's empirical equation have a mean percentage difference of 50% and 42% to the experimental scour depth results respectively.

The Critical Pressure method (Annandale, 2006) proves to agree the closest with the laboratory data, presumably because this method relies on the critical pressure for scour initiation of a rock bed subjected to an impinging jet. This finding corresponds to the literature

that rock scouring is a process resulting from turbulent pressure fluctuations, and is not a shear process (Annandale, 2006). The critical pressure is dependent on the submerged weight of the rock block, block dimensions, uplift pressures inside the joints, diffusion of the jet through the air and plunge pool, as well as the velocity of the jet and fall height.

The EMI presumably performed well because it relies on rock material properties and stream power of the jet as it travels through the air and plunge pool. Figure 5.37 indicates that the EIM erosion threshold is compatible with the laboratory experimental data for Case B at prototype scale when the scoured blocks were continually removed, since the data plots above the threshold line in the “scour” region (green dots).

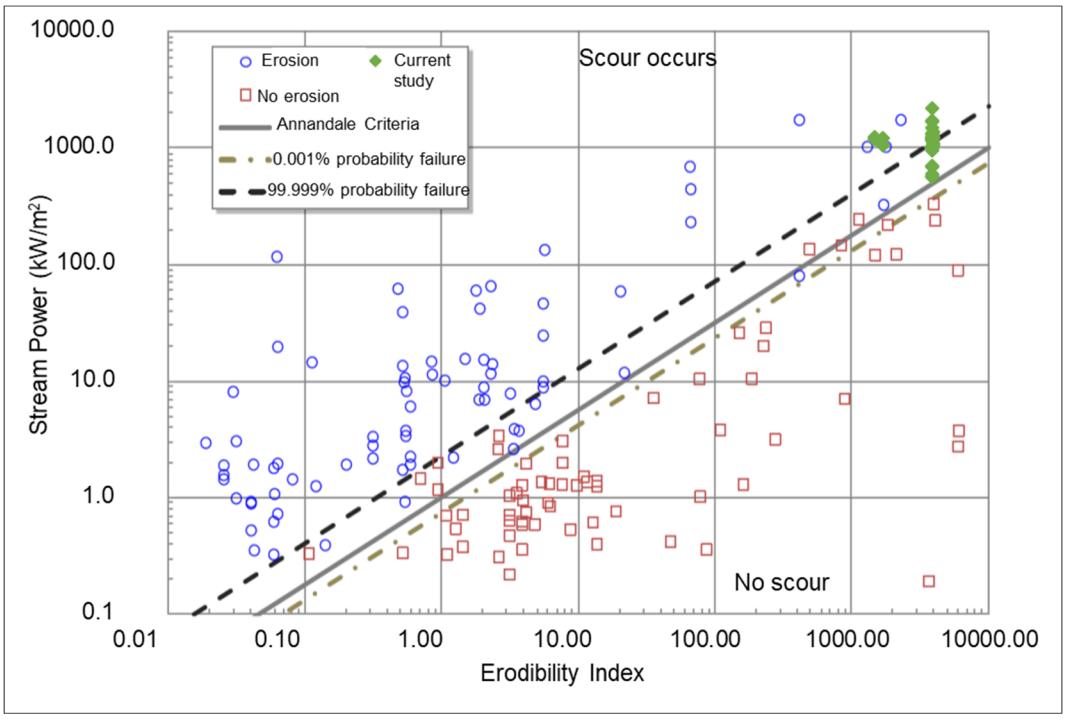

Figure 5.37: EIM erosion potential threshold (Annandale, 1995) overlaid with experimental data for Case B at prototype scale

Mason and Arumugam’s (1985) was one of two identified empirical formula that incorporates the plunge pool depth with gravity acceleration. The implication of this is that models taking the plunge pool depth, and consequently the dissipation of the jet’s energy through the plunge pool into consideration, could offer better scour depth predictions. The experimental test results reiterate the physical model finding that the scour depth depends on the plunge pool depth. Mason (1989) also incorporates the plunge pool depth with gravity acceleration, as well as the air entrainment defined by the air-to-water ratio, β. However, Mason’s empirical formula has a wide percentage difference of statistical spread compared to the observed scour depths, with a median percentage difference of 212%. A possible reason why Mason’s empirical formula overestimates the scour depth could be the ambiguous equation used to calculate the

total unit air discharge (q_a) entrained by the jet, presented by Equation 2.45. The Jaeger (1939, as cited in Castillo and Carrillo, 2014) equation also incorporates the plunge pool depth and has a median percentage difference close to zero (25%), however it has a wide percentage difference of statistical spread.

Yildiz and Uzucek (1994, as cited in Alias et al., 2008) and Mirskaulava (1967, as cited in Mason and Arumugam, 1985) rely on the impingement angle of the jet with the plunge pool surface. Both equations have a narrow statistical spread, however the Yildiz and Uzucek equation overestimates the scour depth, whereas the Mirskaulava equation underestimates the scour depth. Also, the median percentage difference calculated using the Mirskaulava equation (-78.6%) is closer to zero compared to the Yildiz and Uzucek equation (126.1%). A possible reason is that the Mirskaulava equation also incorporates the plunge pool depth and 90% percentile rock dimension whereas the Yildiz and Uzucek equation does not.

The remainder of the empirical formulae are based on the fall height and unit discharge with varying coefficients. A wide range in scour depths, both under- and over-predicted, were calculated indicating that the scour depth does not rely solely on the discharge and fall height, and that the scour depth is sensitive to the parameter coefficients. Furthermore, these equations do not incorporate the rock block size, thus the same scour depth would be predicted if the discharge and fall height are kept constant for various particle size scenarios. These empirical formulae are therefore considered less applicable for full-scale prototype cases.

The DI (2002) and QSI methods (Bollaert, 2012) demonstrated the most significant spread of percentage difference of all the methods. The DI method takes the uplift pulsating forces integrated over a pulse period into account. Whereas the QSI method is the only identified scour prediction model that takes wall jets into consideration. Both methods overestimated the scour depth, presumably due to the challenges posed by physical model scales and that the methods were developed for circular and vertical falling jets.

The developed regression formula (Equation 5.14) to predict the scour depth for Case B agreed well with the experimental results with a compact statistical range of differences with a median difference percentage close to zero (0.8%) with the first quartile just below zero (-3%: under-prediction) as seen in Figure 5.36 compared to the literature scour prediction methods. The developed regression scour depth formula performs well by achieving considerably less scatter about the line of equality, despite under-predictions, when compared to the EIM and Critical Pressure method in Figure 5.38 for Case B. Refer to Annexure G.3 for

the comparison between the new regression formula for Case A and the EIM and Critical Pressure method.

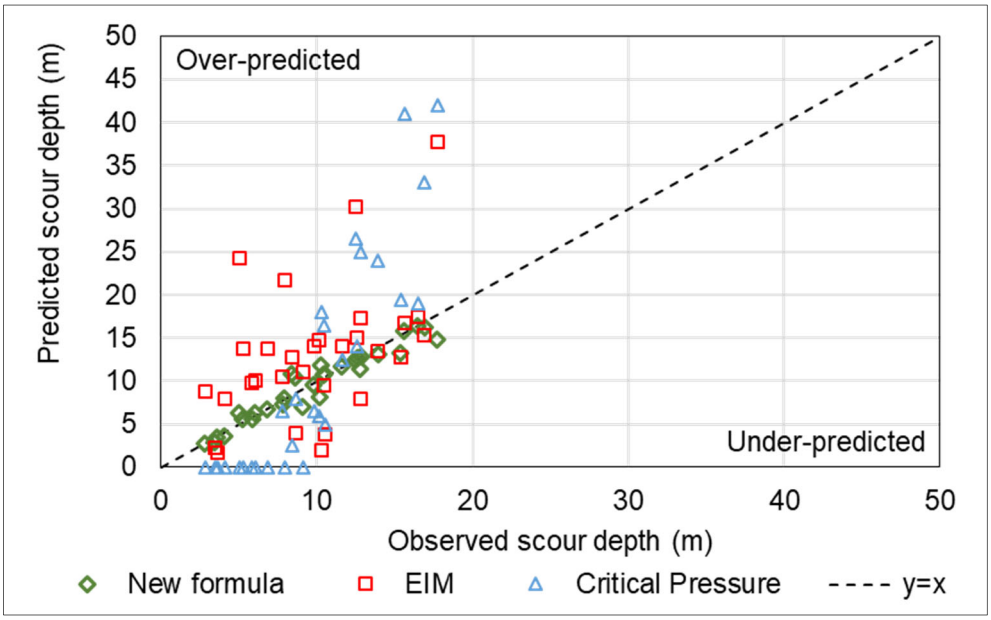

Figure 5.38: Scour hole depth comparison between regression formula from this study and EIM and Critical Pressure methods for Case B

The sum of squared residuals, as defined by Equation 5.21, was compared against the various scour prediction methods in Figure 5.39 for Case B (scour with deposited rocks removed). The data labels on Figure 5.39 indicate the under-predicted and over-predicated SSR values for each of the scour prediction methods. Refer to Annexure G.3 for the SSR plot for Case A (scour with deposition).

$$SSR = \sum \left(D_s^{observed} - D_s^{predicted}\right)^2 \qquad \textit{Equation 5.21}$$

The developed regression formula to determine the scour hole depth ranked the highest with the least total SSR 26;16 (under-predicted; over-predicted), followed by Martins (1975, as cited in Noret et al., 2012) and Damle (1966, as cited in Noret et al., 2012). However, Martins (1975) and Damle's (1966) empirical formulae have a high number of under-predictions. The EIM and Critical Pressure methods (Annandale, 2006) ranked seventh and eighth respectively in the least total SSR.

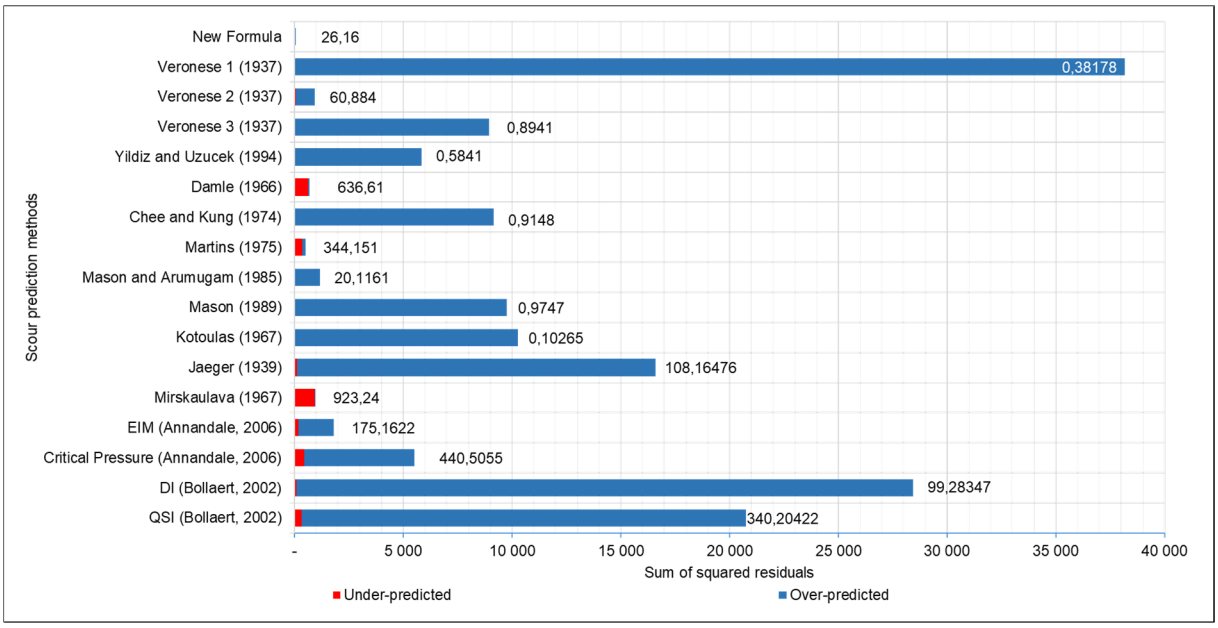

Figure 5.39: Comparison of the sum of squared residuals for the various scour prediction methods for Case B

5.10. Physical model investigation summary

This section presents the results of equilibrium plunge pool scour hole geometry obtained from a physical model study. A model scale (based on Froude scale laws) not exceeding 1:20 was recommended for the physical movable bed model in order to limit scale effects. Equilibrium scour hole geometries for different fissured bedrock dimensions (simulated with rectangular concrete blocks tightly prepacked in a regular rectangular matrix), were experimentally established with 31 model tests for the following conditions:

- Rectangular nappe plunging jets issuing horizontally.
- Fully developed jets plunging into a shallow plunge pool.
- Jet issuance levels of 3 m, 4 m, and 5 m (prototype: 60 m, 80 m and 100 m) above the rock bed level.
- Plunge pool tailwater depths of 0.5 m and 1.0 m (prototype: 10 m and 20 m).
- Unit discharges of 0.392 $m^3/s/m$ to 0.896 $m^3/s/m$ (prototype: 35 $m^3/s/m$ to 80 $m^3/s/m$).
- Two rock sizes of 0.1 m x 0.1 m x 0.075 m and 0.1 m x 0.1 m x 0.05 m (prototype: 2.0 m x 2.0 m x 1.5 m and 2.0 m x 2.0 m x 1.0 m).
- Rock joint structure angles of 0º, -45º, and 45º with the horizontal axis.

The analysis of the equilibrium scour hole topography indicated that the shape of the scour hole is highly dependent on the discharge and plunge pool depth, and to a lesser extent the rock size. The scour hole volume increases as the discharge increases, the plunge pool depth

decreases, and the rock size decreases. The scour results indicate that rock is more likely to fail due to scour when the rock joint structure dips in the direction of the flow.

Results from the physical model were used to develop non-dimensional multi-linear regression formulae to predict the scour hole geometry (depth, length, width, and volume). The proposed regression formulae were confirmed inside the ranges in which the formulae were developed and agree reasonably well with the experimental data upon which they are based.

The scour depth results from the physical model were compared to the results for various analytical methods found in literature. The equilibrium scour hole depth established in this study best agrees with that predicted by the Critical Pressure method, whereas the EIM method (Annandale, 2006) followed by Mason and Arumugam's (1985) empirical formula were more conservative than the formulae developed in this study.

6. 3D NUMERICAL SIMULATION OF PLUNGING JETS AND BEDROCK SCOUR

6.1. Background

Numerical modelling can simulate real world phenomena which enables the investigation of such phenomena. Numerical modelling remains a representation of the real world phenomena. The numerical model environment may have unintended inadequacies that could yield outcomes different from the experimental results or prototype behaviour. Therefore, the numerical model should preferably be calibrated with prototype data, or if not available, with experimental data to simulate more accurately the behaviour of the prototype or model in order to ascribe more certainty to the numerical results.

The purpose of the numerical modelling in this study was to investigate the hydrodynamic behaviour of rock scour downstream of a dam spillway. Scale restrictions of physical model studies do not limit numerical models. However, the limitations of numerical models include the assumptions made in the governing equations (including constants and coefficients in the equations), computer constraints in terms of memory capacity and processors, and the required computational effort to obtain the solution.

The model set up, computational software, model geometry and mesh, boundary conditions, and numerical solution technique are described in the first part of this section. The second part of this section presents the calibration process of the numerical simulation using the experimental measurements collected in Section 5.7. In the third part of this section the numerical simulation results are presented and compared with the experimental data and literature.

6.2. Modelling environment

The computational fluid dynamics (CFD) software used in the current research was ANSYS version 19.2, with a FLUENT module. FLUENT is a numerical model that has a wide range of functional components that can be used to simulate various flow scenarios. FLUENT has been widely used for modelling multi-phase flow with complex geometries by using the finite volume method. The current study aimed to build a three-dimensional, two-phased, transient, free-surface interaction model.

Other computer programs, such as Smooth Particle Hydrodynamics (SPH), FLOW-3D, Delft3D and Rocky were also considered for the current research. SPH does not have any form of fluid-structure interaction (FSI) modelling, thus modelling rock cracking and uplift is

impossible. Furthermore, SPH can only model rock if it is assumed to be a Newtonian fluid of high viscosity, thus ignoring any rock joints and steep angle of repose. By modelling the rock as a Newtonian fluid, it could potentially lead to a prohibitively small time step, thus jeopardising the use of SPH.

The sediment model of FLOW-3D is primarily empirical in nature, and the maximum particle size that can be simulated is 35 mm for version 11.1 according to Castillo and Carrillo (2016). In addition, the specific particle shape cannot be specified. FLOW-3D was therefore eliminated based on the aforementioned limitations.

Delft3D was deemed unfit to simulate rock scour due to a plunging jet since the program cannot simulate near-source problems.

Rocky is fully coupled with FLUENT (two-way coupling) which makes numerical modelling of granular-fluid systems possible. However, the 6 hours (actual time) to reach the equilibrium scour hole for Case A (scour and deposition) would require 6 months of computational time (E. Smuts, personal communication, 14 October 2019). This time limitation rendered Rocky undesirable.

Therefore, in the present research, a three-dimensional numerical model in FLUENT was used to simulate the hydrodynamic behaviour of the plunging jet and present the flow field at the plunge pool bottom. The 1% exceedance dynamic pressure and horizontal velocity results from the numerical model were used as input parameter in the regression formula for scour depth (Case B – Equation 5.14) presented in Table 5.8 (Section 5.8.1.3) to calculate the rock block movement.

The experimental tests proved that a greater scour hole is obtained if the deposited rocks downstream of the scour hole are continuously removed (Case B) compared to Case A where the deposited rocks were not removed. Therefore, rock block movement for Case B was determined by means of the numerical model in order to reach the static scour limit (maximum equilibrium scour hole dimensions).

6.3. Computational hardware

The numerical simulations were set up and tested in ANSYS Workbench Release R19.2 on a 10 core Intel®Core™ i7 CPU 2.93 GHz with 16 GB of RAM.

For the actual computations, the numerical simulation set up was transferred to the Centre of High Performance Computing (CHPC) of the Council for Scientific and Industrial Research (CSIR) in Cape Town, South Africa. The CHPC houses a petaflop level cluster containing

23832 Intel®Xeon® CPU cores each with a 2.6 GHz clock speed and 148.5 TB memory. The system limits normal researches to 10 nodes, comprising of 24 cores and 128 GB of memory, for a maximum elapsed time of 48 hours. The computation time was reduced by more than an order of magnitude due to ANSYS's built-in parallel processing algorithms when comparing the two platforms. The typical number of elements used in this study was 2 million. FLUENT could simulate 30 seconds of model data of the hydrodynamic aspects of the plunging jet in approximately 16 hours. No bed changes were simulated, but were calculated with Equation 5.14 using the simulated results as input data.

6.4. Numerical model concepts

The numerical model used physical model boundary conditions as input to simulate the physical model data to enable calibration of the numerical model with the physical model results. The numerical procedure followed for setting up the model was:

1. Define a three-dimensional computational domain by creating the model geometry.
2. Generate a mesh in order to divide the computational area into smaller elements.
3. Set up the model boundary conditions.
4. Adopt a solution technique and simulation of the problem.
5. The post-processing and analyses of simulation results.
6. The calibration of geometry, meshing and solver set ups.

The abovementioned steps are discussed in detail in the following sections.

6.4.1. *Model domain geometry and mesh*

FLUENT first discretised the flow domain into smaller cell volumes and then FLUENT Solver solved the governing equations (refer to Section 4.4.2 for more detail) in each generated cell.

The three-dimensional numerical model had to accurately simulate the various experimental results (recorded in Annexure G.1) under the same laboratory conditions as discussed in Section 5. Thus, the numerical model was modelled with the same dimensions as the physical model set up.

The laboratory issuance canal was 9.5 m long in order to obtain fully developed uniform flow. However, only 0.10 m of the issuance canal was modelled in the numerical model, by specifying the fully developed logarithmic velocity profile at the inlet as seen in Figure 6.1. The number of generated mesh cells decreased considerably by shortening the issuance canal and consequently, significantly reduced the computational time.

Figure 6.1 indicates the model geometry of the laboratory model set up as presented in ANSYS DesignModeler. The geometric domain was divided into three bodies, namely the inlet, air body (plunging jet) and plunge pool. The three bodies were maintained as one part to ensure conformal meshing at the surface boundaries.

The fixed scoured plunge pool bottom was created by surface triangulation between the topography data points gathered from the laser survey. Figure 6.2 shows the representation of the plunge pool bottom surface created in ANSYS DesignModeler for the calibration test, C1 (Q_{max}, H_{max}, TWD_{max}).

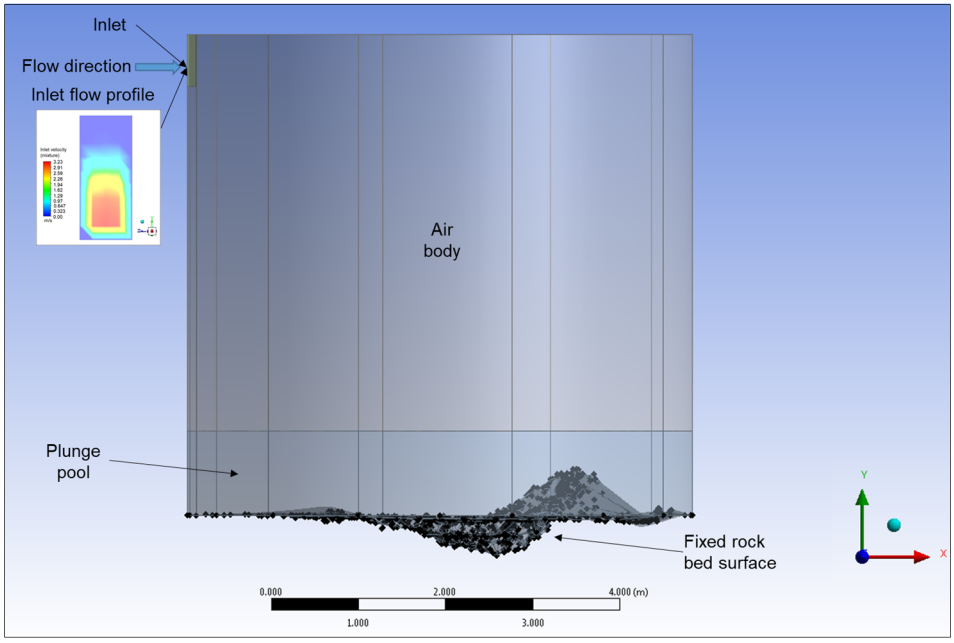

Figure 6.1: CFD model geometry for Test C1

The construction of an appropriate computational mesh is an essential step in developing a numerical model to obtain a stable and grid independent solution. The governing equations are iteratively solved at the nodes of the mesh until convergence is reached for the important model parameters (i.e. flow velocity and dynamic pressures). The construction of a very fine mesh increases the number of cells, and subsequently increases the computational time for a single solution. Thus, to be most effective, the domain set up and mesh should be prepared considering the abovementioned aspects.

The mesh size was a sensitive component of the numerical model, due to the irregular shape of the rock bed surface. A mesh refinement exercise was performed to ensure that the simulation is grid independent and capable of simulating the desired phenomena. The individual mesh cell size is reduced until the relevant metric (dynamic pressures on the plunge pool bottom) does not change more than a specific percentage. A finer mesh would not

contribute significantly to the accuracy of the results, since an asymptotic value is reached. The model domain was discretised into a hybrid mesh containing both hexahedron and tetrahedron meshes, since it provides a high-quality solution. Numerical diffusion denotes the overestimation of the diffusion coefficient by the model. Figure 6.3 indicates the generated mesh used and Table 6.1 provides some details of the mesh.

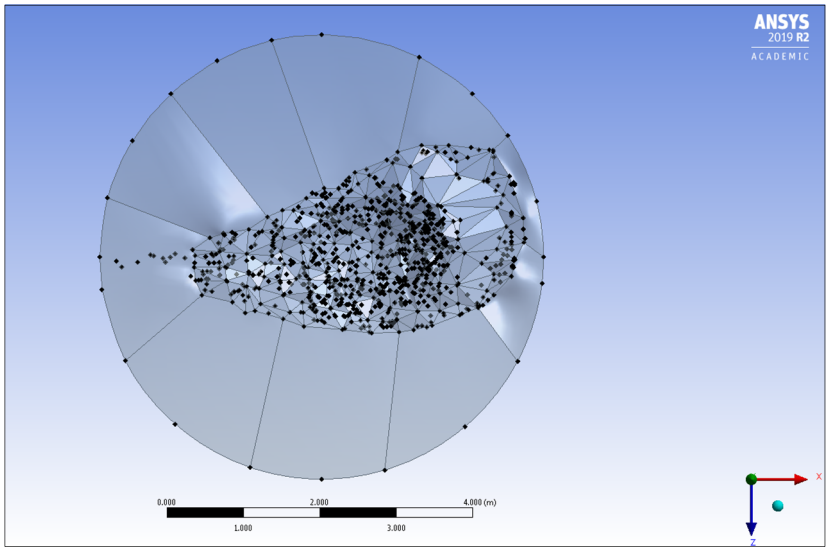

(a) Plan view of pool bottom of the numerical model

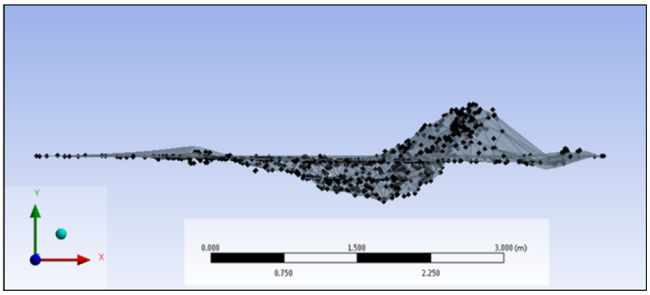

Numerical representation of rock bed

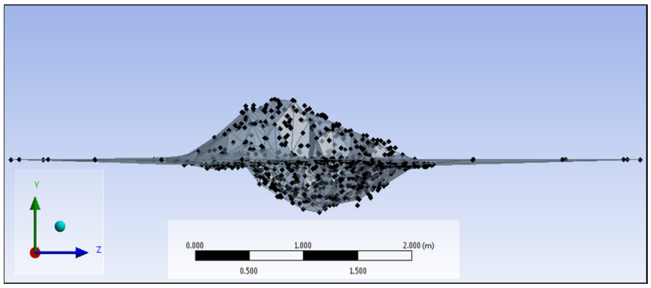

Numerical representation of rock bed

Experimental test

(b) Side view

Experimental test

(c) Front view

Figure 6.2: Numerical plunge pool bottom created by triangulation compared to the physical model pool bottom

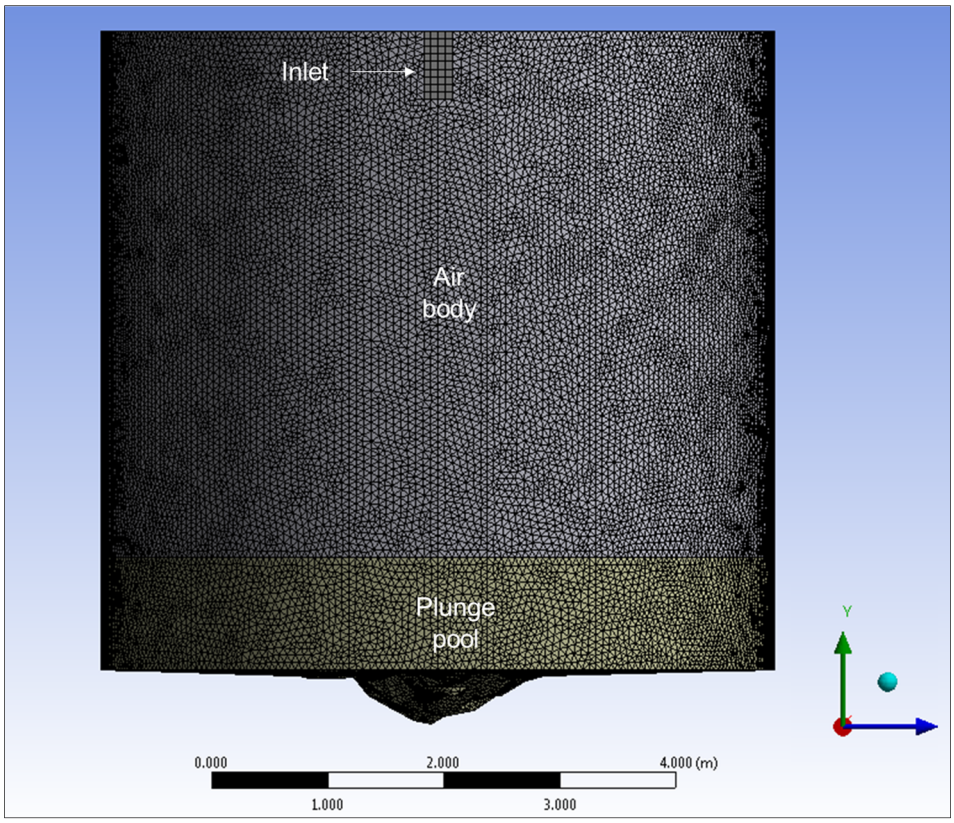

Figure 6.3: Conformal mesh viewed normal to inlet

A good quality mesh is defined when the average orthogonal quality is close to 1, and as poor when the value is 0. The average orthogonal quality of the generated mesh is 0.7847 (Table 6.1), which is close to 1, indicating that the mesh used was of good quality.

Table 6.1: Mesh details

Metric	**Value**
Number of cells	347 577
Number of nodes	1 940 340
Element size (m)	0.0625
Maximum cell size (m)	0.1000
Average skewness	0.2140
Average aspect ratio	1.814
Average orthogonal quality	0.7847

6.4.2. *Model boundary conditions*

Boundary conditions specify physical values at the boundaries of the computational domain. Boundary conditions have a direct impact on the quality of the final simulation results, thus the boundary conditions should be defined correctly and their role in the numerical simulation should be understood. Three boundary conditions were applied, namely velocity-inlet, outlet-pressure, and wall boundary as shown in Figure 6.4.

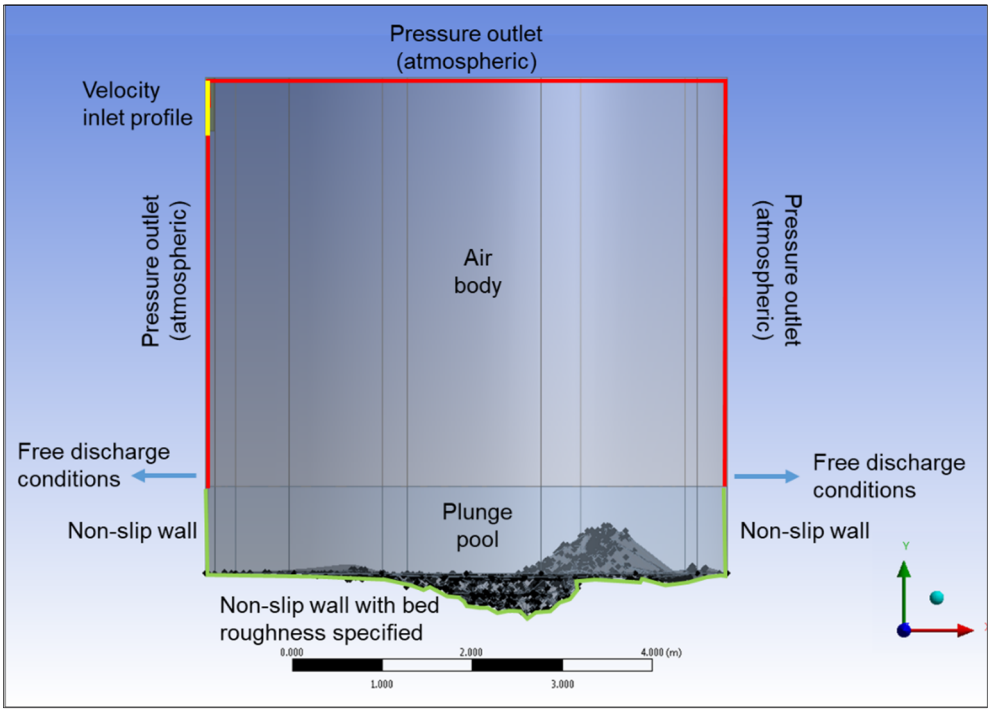

Figure 6.4: Boundary conditions

The inlet-velocity boundary type was set at the issuance canal by specifying the fully developed logarithmic velocity profile (magnitude and direction) and turbulence intensity. The inlet discharge and velocity profile prescribed at the inlet boundary, as seen in Figure 6.1, were the same as for the laboratory tests, including the friction effect of the spillway sides. The flow direction was specified as normal to the inlet boundary. The turbulence intensity (T_u) at the inlet-boundary was specified as 4% (Bollaert, 2002). The hydraulic diameter $\left(D_h = \frac{4A}{P}\right)$, where A denotes the inlet cross-section area and P its perimeter, was also specified to account for the inlet turbulence. Water was specified as the primary phase and the volume fraction of the secondary phase, air, was set as zero at the inlet.

The pressure-outlet boundary type was set at the air body boundaries with the gauge pressure set to 0 Pa. In FLUENT the absolute pressure is equal to the sum of the gauge pressure (set to 0 Pa) and a reference pressure, which was set to atmospheric pressure. The default

turbulent intensity value of 5% and viscosity ratio of 10 were prescribed at the outlet boundary. The backflow condition of the air volume fraction was set to one, ensuring that water backflow could not occur.

The sidewalls of the plunge pool and rock bed surface were set as a wall boundary type with non-slip condition specified. The roughness height (K_s) and roughness constant (C_s) for the pool bottom surface were calibrated and validated as detailed in Section 6.5.5.

The sidewall of the plunge pool acted as an uncontracted weir, creating the outflow boundary from the plunge pool. In order to obtain the correct plunge pool depth, White's empirical discharge formula (Equation 6.1) developed for uncontracted weirs under free discharge conditions was used (Chadwick et al., 2013).

$$Q = 0.562(1 + 0.153h_1/P_s)b\sqrt{g}(h_1 + 0.001)^{3/2} \qquad \textit{Equation 6.1}$$

with h_1 the flow depth above the weir, P_s the weir crest height and b the weir width. Equation 6.1 is valid for $h_1 > 20$ mm, $P_s > 150$ mm, and $h_1 < 2.2P_s$. The plunge pool wall height (P_s) was adjusted in order to obtain the correct plunge pool depth ($Y = h_1 + P_s = 0.5$ m or 1.0 m) that was tested in the physical model.

6.4.3. *Numerical solution technique and procedure*

The different settings for the numerical model were selected through the Graphical User Interface (GUI) of FLUENT by launching a three-dimensional, double precision, and parallel processing platform. The parameters shown in Table 6.2 were used to set up the FLUENT model. The type of flow being simulated, namely open-channel turbulent flow with air-water interaction, governed most of the FLUENT parameters. However, some parameters had to be calibrated, which included the turbulence model, solution methods and bed roughness parameters.

The standard operating conditions for air-water phase flow were applied, which included a constant surface tension coefficient of 0.072 N/m to define the interaction between the two phases, gravitational acceleration, and atmospheric pressure and density of 1.225 kg/m^3 and 998.2 kg/m^3 for air and water respectively.

Before the simulation was commenced, the starting conditions were specified as a still standing volume of water in the plunge pool up to the desired tailwater level. The inlet velocity profile was also specified at the inlet boundary as accurately as possible to ensure that scouring errors are not generated by an erroneous flow pattern.

A time step size of 0.001 seconds was specified with a maximum of 10 iterations per time step. The time step size was obtained after several trial runs which were found adequate to achieve solution stability and convergence. The time step size of 0.001 seconds also satisfies the guideline that the Courant number be less than one (according to Equation 4.1) despite the use of an implicit solver for model stability. The number of iterations per time step was selected in order for the residuals to decrease by two to three orders of magnitude within each time step (ANSYS, 2015). The number of time steps used in the analyses were 30 000, which equates to 30 seconds (physical model time). Data was collected at 1 second intervals.

The flow discharged from the spillway remained constant throughout the test, meaning the flow scenario was steady. However, the hydrodynamic behaviour of the pressures and velocities experienced at the pool bottom was transient in nature, thus the transient solver was selected.

Table 6.2: Spatial discretisation schemes used

Aspect	**Parameter**	**Value**
Solver	Type	Pressure-based
Solver	Time	Transient
Flow model	Multi-phase	Volume of Fluid (VOF)
Flow model	Viscous flow	SST $k-\omega$
Material (primary phase)	Fluid	Water-liquid
Material (secondary phase)	Fluid	Air
Solution method	Pressure-velocity coupling	PISO
Solution method	Spatial Discretisation: Gradient	Least Squares Cell Based
Solution method	Spatial Discretisation: Pressure	PRESTO!
Solution method	Spatial Discretisation: Momentum	2nd order upwind
Solution method	Spatial Discretisation: Volume Fraction	Geo-reconstruct
Solution method	Turbulent Kinetic Energy	1st order upwind
Solution method	Specific Dissipation Rate	1st order upwind
Solution method	Transient formulation	2nd order upwind
Solution method	Under-relaxation factors	Default
Solution method	Time step	Constant

6.5. Model calibration

Numerical models must be calibrated to reduce the risk of the numerical model not predicting the physical flow behaviour correctly. The experimental results from the physical model were used to calibrate the numerical model. The experimental tests listed in Table 6.3 were used for calibration and confirmation by simulating the equilibrium scoured bed profile for Case A as a rigid bed boundary with specified bed roughness parameters. The numerical model was set up with the identical conditions of the physical model experiments, i.e. the numerical model was set up to simulate the physical model to eliminate the influence of scaling effect.

Table 6.3: Calibration and confirmation tests

Rock block size $x \times y \times z$	**Test name**		**Discharge, Q**	**Fall height, H**	**Plunge pool depth, TWD**
0.1 m x 0.1 m x 0.05 m (2.0 m x 2.0 m x 1.0 m)	Calibration 1	C1	0.894 m^3/s Q_{max}	5 m H_{max}	1 m TWD_{max}
	Calibration 2	C2	0.391 m^3/s Q_{min}	3 m H_{min}	0.5 m TWD_{min}
	Confirmation 1	CF1	0.513 m^3/s Q_{med}	4 m H_{med}	1 m TWD_{max}
	Confirmation 2	CF2	0.391 m^3/s Q_{min}	4 m H_{med}	0.5 m TWD_{min}
	Confirmation 3	CF3	0.513 m^3/s Q_{med}	5 m H_{max}	0.5 m TWD_{min}
0.1 m x 0.1 m x 0.075 m (2.0 m x 2.0 m x 1.5 m)	Calibration 3	C3	0.894 m^3/s Q_{max}	5 m H_{max}	1 m TWD_{max}
	Confirmation 4	CF4	0.391 m^3/s Q_{min}	5 m H_{max}	0.5 m TWD_{min}

The main calibration factors were as follows:

- mesh cell size,
- turbulence model,
- pressure-velocity coupling,
- pressure gradient scheme,
- plunge pool bottom roughness,
- inlet velocity profile, and
- visual appearance and behaviour of the plunging jet.

The parameters chosen for calibration and confirmation were the 1% exceedance (99 percentile) dynamic pressures at the plunge pool bed surface (recommended by Lopardo,

1988, as cited in Castillo et al., 2018), and the 1% exceedance velocity field 50 mm from the water-rock interface.

Attention was given to ensure that the data intervals recorded when the model simulation was still converging or stabilising were disregarded. The time to reach convergence, as well as how long it would take a drop of water to pass through the whole model domain with a safety factor of 1.5 was less than 10 seconds for all the simulations. A constant pressure pattern was established on the plunge pool bottom between 10 seconds and 30 seconds, and was analysed in the same manner as the physical model.

6.5.1. *Mesh size*

Five different mesh sizes were simulated to investigate the sensitivity of the mesh size on the results as listed in Table 6.4. Finer and coarser mesh sizes relative the mesh described in Section 6.4.1 (Mesh B) were used in the mesh refinement exercise. The element size of 0.0625 m ensured at least four cells over the width of the inlet.

Table 6.4: Mesh refinement sizes

Mesh name	**Size**	**Mesh Type**
Mesh A	Element size = 0.0625 m Maximum cell size = 0.25 m	Hybrid mesh (hexahedron and tetrahedron shapes)
Mesh B	Element size = 0.0625 m Maximum cell size = 0.1 m	Hybrid mesh (hexahedron and tetrahedron shapes)
Mesh C	Element size = 0.050 m Maximum cell size = 0.1 m	Hybrid mesh (hexahedron and tetrahedron shapes)
Mesh D	Element size = 0.03125 m Maximum cell size = 0.1 m	Hybrid mesh (hexahedron and tetrahedron shapes)
Mesh E	Element size = 0.0625 m Maximum cell size = 0.1 m	Multi-block grid, with the inlet canal and air modelled with a hexahedron mesh, and the plunge pool with a tetrahedron mesh.

Table 6.5 indicates the percentage difference in the dynamic pressures on the plunge pool floor for the different mesh sizes (mesh A to D). The results indicate that the percentage difference in the dynamic pressures reach an asymptote and that mesh C and D would not contribute significantly to the accuracy of the results. Furthermore, the distance from the

plunge pool bottom to the centroid of the adjacent cell is greater than the block size used for mesh B (refer to Section 4.3.1), which is not true for mesh C and D.

Table 6.5: Percentage difference due to mesh size

Mesh A and B	Mesh B and C	Mesh C and D
142%	16%	8%

Mesh E divided the model domain into two regions with different mesh types. The inlet and air were discretised into a hexahedron mesh and the plunge pool into a tetrahedron mesh. The mesh generated poor quality cells to such an extent that the simulation was unable to run.

Mesh B was selected based on the mesh refinement results.

6.5.2. *Turbulence model*

The majority of numerical modelling conducted on rock scour due to plunging jets made use of the Reynolds Averaged Navier-Stokes (RANS) methodology. The dynamic pressures generated on the plunge pool bottom resulting from the standard $k-\varepsilon$ and SST $k-\omega$ turbulence models were evaluated. The standard $k-\varepsilon$ and SST $k-\omega$ turbulence models over-predict the dynamic pressures by 310% and 206% respectively (without considering bed roughness calibration). The SST $k-\omega$ turbulence model therefore simulates flow separation and shear flow at the plunge pool bottom more accurately and in a faster time than the standard $k-\varepsilon$ turbulence model.

6.5.3. *Pressure-velocity coupling*

The pressure-based Piso scheme provided similar results in a faster time compared to the SIMPLE scheme, corresponding to the literature in Section 4.3.4. The Piso scheme over-predicted the dynamic pressures by 206% (not considering bed roughness calibration), compared to 212% for the SIMPLE scheme. The Piso scheme was therefore selected.

6.5.4. *Pressure scheme*

The PRESTO! discretisation scheme provided higher quality results in a faster time compared to the Body Force Weighted scheme. The simulation time required to run one second of the model time was 0.75 hours for the PRESTO! scheme and 1.5 hours for the Body Force Weighted scheme. Furthermore, the average percentage differences between the dynamic pressures on the plunge pool bottom measured in the experimental tests compared to the numerical model for the PRESTO! and Body Force Weighted schemes were respectively

206% and 376% (not considering bed roughness calibration). The PRESTO! scheme was therefore used to solve the pressure gradient.

6.5.5. *Surface roughness*

The plunge pool bed roughness effects are simulated in FLUENT by specifying the roughness height (K_S) and roughness constant (C_s) described in Section 4.3.2.

Rooseboom and Van Vuuren (2013) specified a Chèzy roughness value of 0.04 m for random "stone in mortar", and 0.2 m for "hand placed pitching". The perpendicular distance from the triangular cavities between the scoured rock bed to the pseudo-bottom (Figure 4.1) was measured as 0.0535 m. The median diameter (d_{50}) for the 0.1 m x 0.1 m x 0.05 m rock block was calculated with Equation 4.2 as 0.0985 m. Two additional bed roughness values were used for calibration, namely half the scour depth ($D_s/2$) and the scour depth (D_s) observed for Case A (scour and deposition).

Four roughness coefficients were (C_s) were simulated, namely 0.2, 0.5, 0.8, and 1.0.

The 1% exceedance dynamic pressures at the plunge pool bed surface, and the velocity magnitude 50 mm from the water-rock interface from 10 seconds to 30 seconds in 1 second intervals at the same sensor locations as in the experimental tests were used for calibrating the bed roughness parameters.

The mean percentage differences between the numerical and physical model of the 1% exceedance dynamic pressures for the different roughness coefficients (C_s) and roughness heights (K_S) for test C1 (Q_{max}, H_{max}, TWD_{max}) are shown in Figure 6.5. The percentage difference results indicate that a roughness constant of C_s = 0.8 is more appropriate for simulating a plunge pool bottom surface, corresponding to a non-uniform bed as detailed in Section 4.3.2.

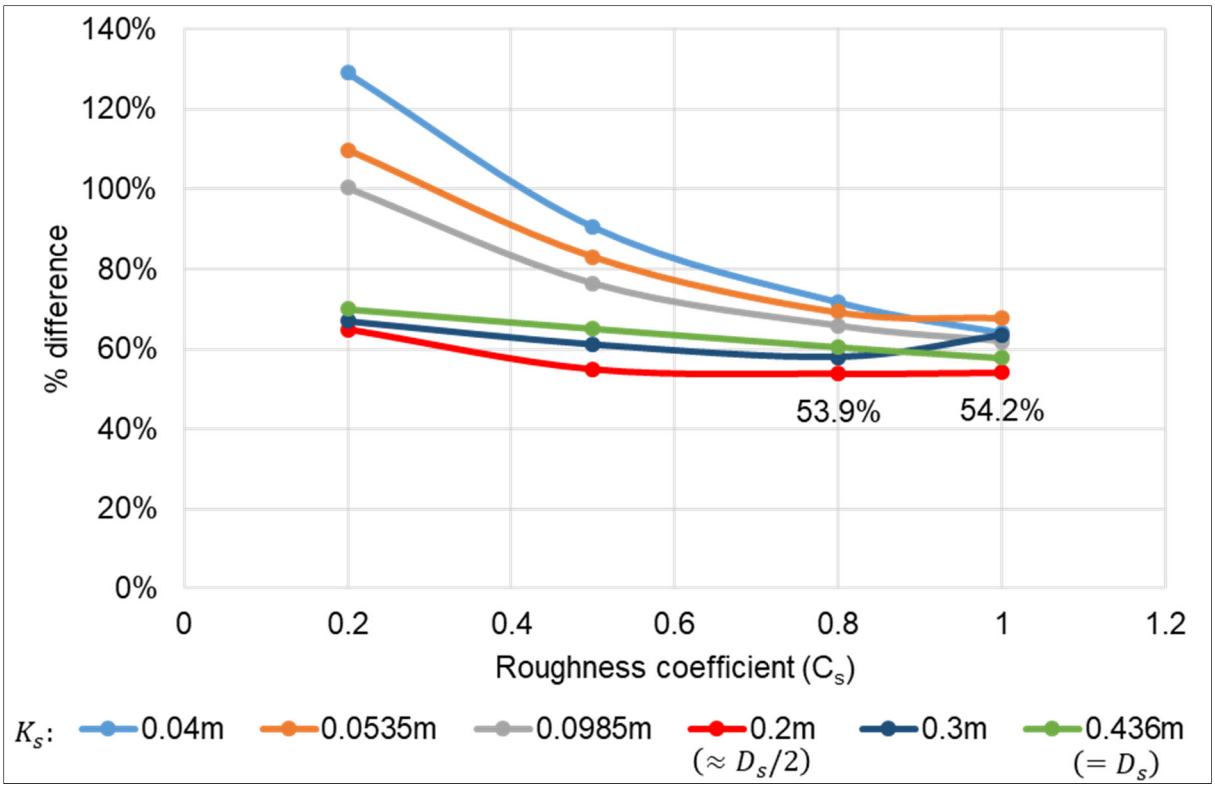

Figure 6.5: Mean of 1% exceedance dynamic pressure as a percentage difference for different C_s- and K_s-values from the experimental work for test C1 (Q_{max}, H_{max}, TWD_{max})

Only the calibration and confirmation tests with a 0.5 m plunge pool depth could use both the 1% exceedance velocity and dynamic pressures to calibrate the surface roughness due to the limiting length of the ADV equipment. The percentage difference of the mean of 1% exceedance dynamic pressures and velocity magnitude for a C_s-value equal to 0.8 for different roughness K_S-values between the numerical and physical model for tests C2 and CF2 are shown in Figure 6.6 (a) and (b), respectively. The surface roughness K_s-values that predicted both the dynamic pressures and velocity magnitude the best (lowest percentage difference) are indicated by the dotted line boxes in Figure 6.6 (a) and (b).

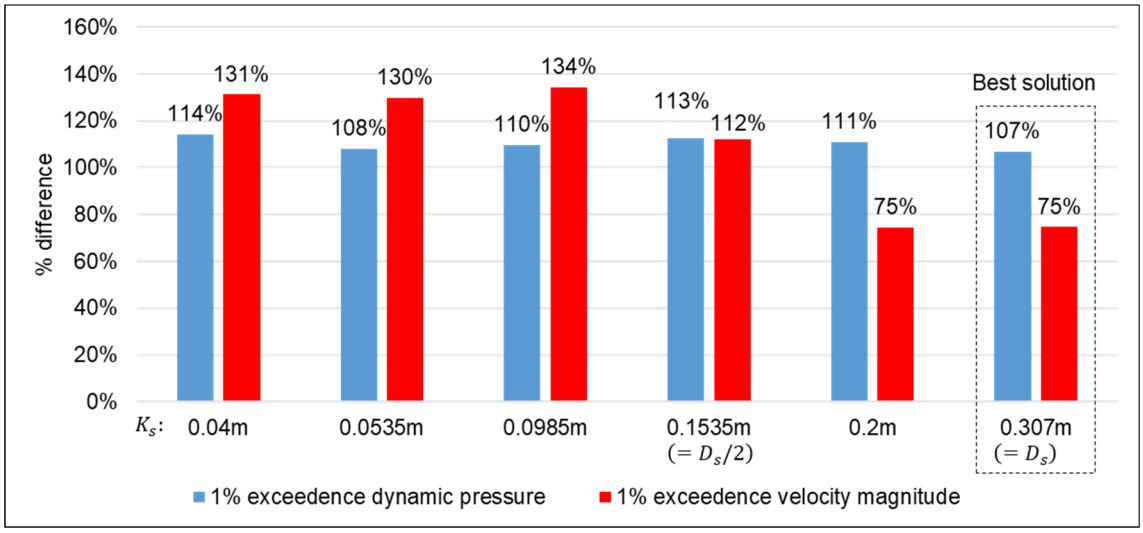

(a) Calibration Test 2: Q_{min}, H_{min}, TWD_{min}

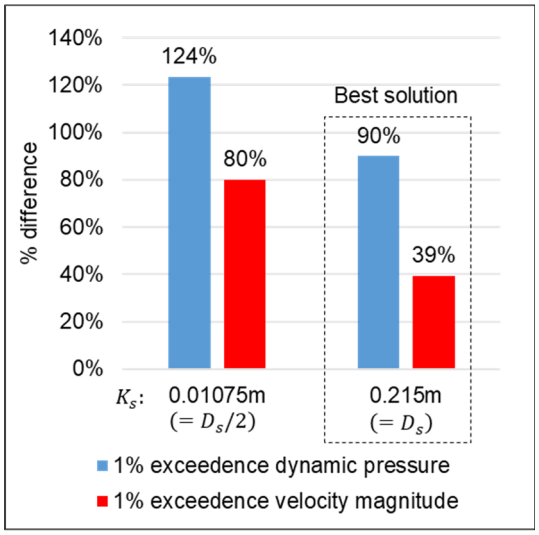

(b) Confirmation Test 2: Q_{min}, H_{med}, TWD_{min}

Figure 6.6: Mean of 1% exceedance dynamic pressure and velocity magnitude as a percentage difference for different K_s-values from the experimental work for test C2 and CF2

The surface roughness K_s-values that predicted the dynamic pressures and velocity magnitude the best with a C_s-value equal to 0.8 for the different calibration and validation tests are shown in Table 6.6. The surface roughness parameter for the 0.1 m x 0.1 m x 0.05 m rock blocks was determined to be approximately 0.2 m, corresponding to a Chèzy roughness value of 0.2 m for “hand placed pitching” according to Rooseboom and Van Vuuren (2013). The surface roughness parameter was determined to be 0.4 m for the 0.1 m x 0.1 m x 0.075 m rock blocks. Thus, the calibrated surface roughness to rock block height ratio (K_s/z_b) is 4 and 5.3 for the 0.1 m x 0.1 m x 0.05 m rock block and 0.1 m x 0.1 m x 0.075 m rock block respectively.

Table 6.6: Calibrated surface roughness values

Rock block size $x \times y \times z$	**Test**		**Surface roughness** (K_s)
0.1 m x 0.1 m x 0.05 m	Calibration 1	Q_{max}, H_{max}, TWD_{max}	0.200 m
	Calibration 2	Q_{min}, H_{min}, TWD_{min}	0.307 m
	Confirmation 1	Q_{med}, H_{med}, TWD_{max}	0.187 m
	Confirmation 2	Q_{min}, H_{med}, TWD_{min}	0.215 m
	Confirmation 3	Q_{med}, H_{max}, TWD_{min}	0.210 m
0.1 m x 0.1 m x 0.075 m	Calibration 3	Q_{max}, H_{max}, TWD_{max}	0.400 m
	Confirmation 4	Q_{min}, H_{max}, TWD_{min}	

6.5.6. *Influence of inlet velocity profile on dynamic pressures at the scour bottom*

This section explains how the prescribed inflow boundary influences the dynamic pressure results experienced at the plunge pool bottom. The velocity inlet boundary can be prescribed as a constant inflow value or as a fully developed logarithmic velocity profile that takes friction of the spillway sidewalls into account.

The velocity profile of water exiting a dam spillway is characterized by a logarithmic shape with a zero velocity at the spillway floor and sides, and the maximum velocity occurring near the water surface as illustrated by Figure 4.2. The logarithmic velocity profile shape follows from the postulate that water being a viscous fluid experiences shearing when encountering a solid surface such as a spillway bed or sides. A thin layer of water adjacent to the surface decelerates until the layer comes to rest. A shearing action develops between the static water layer and the subsequent layer, causing the second water layer to decelerate to a lesser degree. The decelerating process continues to form a boundary layer zone. Outside of the boundary layer the flow is free of shear and the velocity may therefore be assumed to remain unaffected (Chadwick et al., 2013).

The dynamic plunge pool bed pressures for a constant inflow velocity with that of a fully developed velocity profile were compared to establish the influence of inlet velocity profiles on

the dynamic bed pressures in the scour hole. The percentage difference between the 1% exceedance dynamic bottom pressures from the experimental tests and numerical models simulated with a constant inflow velocity and with a fully developed velocity profile for the three deepest points on the scour hole centre line are summarised in Table 6.7.

The percentage difference results in Table 6.7 indicate that the numerical model with the fully developed velocity profile specified more accurately predicted the dynamic pressures at the plunge pool bottom compared to when a constant velocity is specified at the inlet boundary. Thus, to accurately predict the plunge pool scour, the correct velocity profile at the inflow boundary should be specified.

Table 6.7: Percentage difference between simulated and observed dynamic bottom pressures at scour bottom for a constant inlet velocity and velocity profile

Deepest pressure sensors	**Constant velocity**	**Velocity profile specified**
Pressure sensor 1	-88%	-68%
Pressure sensor 2	-55%	25%
Pressure sensor 3	116%	34%
Absolute average	**86%**	**42%**

6.5.7. *Plunging jet*

The simulated jet trajectories for the calibration and confirmation tests were compared with the experimental and empirical jet trajectory formula (Equation 2.4) results in Figure 6.7. The jet trajectory was well predicted by the numerical model for all the tests. However, the numerical model and the empirical jet trajectory formula show a shorter projection of the jet compared to the experimental trajectories.

Table 6.8 compares the simulated jet velocity (V_j), jet thickness (B_j), and jet width (W_j) at impact with the plunge pool water surface with experimental data. The experimental impinging jet velocity (V_j) was calculated using Equation 2.29.

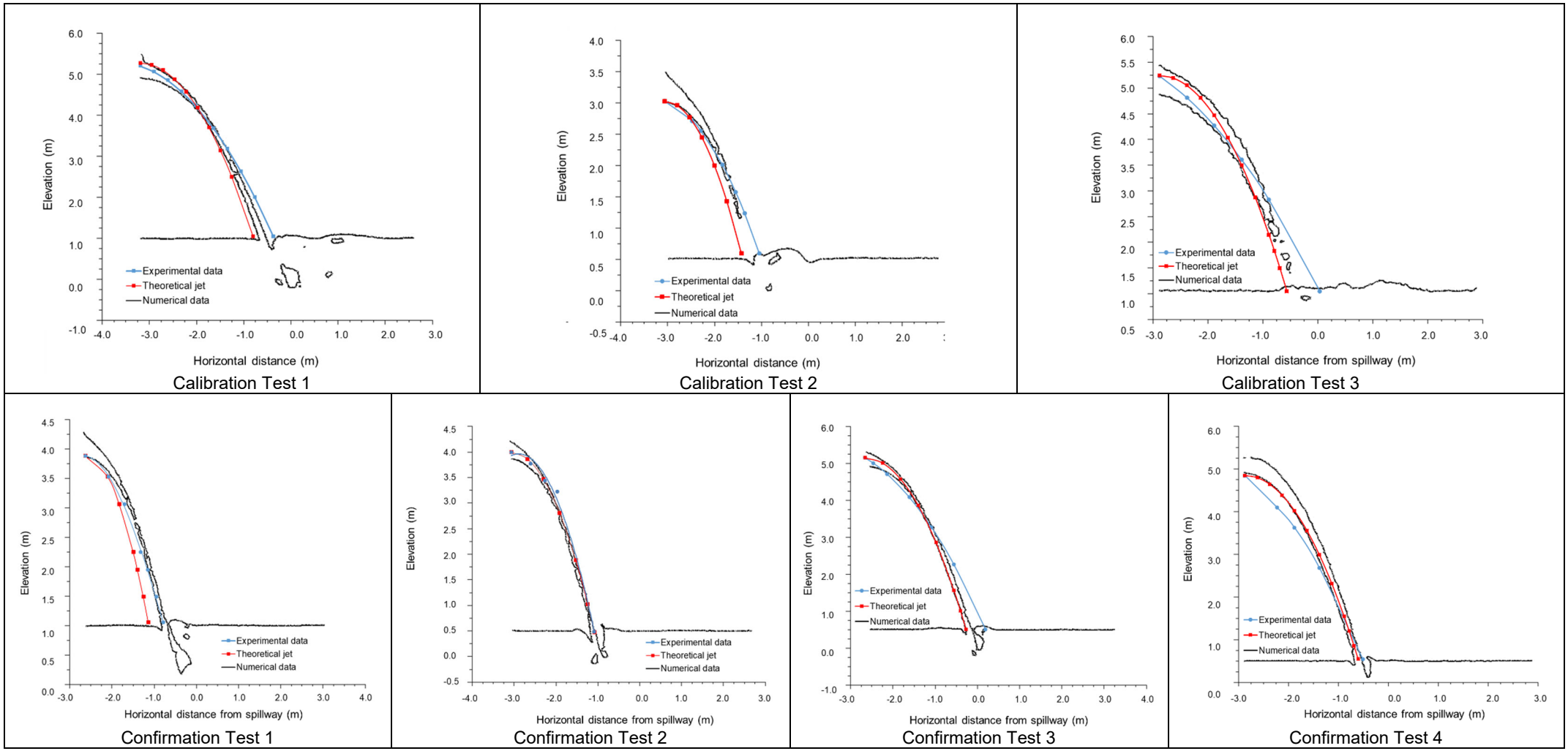

Figure 6.7: Jet trajectory comparison between physical model, numerical model and theoretical formula for the calibration and confirmation tests

Table 6.8: Plunging jet result comparisons (model values)

Test	Parameter	Experimental data	Numerical data	% difference
Calibration Test 1	Impinging velocity (V_j)	9.48 m/s	9.35 m/s	-1.3%
[Q_{max}, H_{max}, TWD_{max}]	Impinging jet thickness (B_j)	0.68 m	0.50 m	-26.5%
[Rock size: 0.1 m x 0.1 m x 0.05 m]	Impinging jet width (W_j)	0.87 m	0.80m	-8%
Calibration Test 2	Impinging jet velocity (V_j)	7.57 m/s	7.12 m/s	-5.9%
[Q_{min}, H_{min}, TWD_{min}]	Impinging jet thickness (B_j)	0.5 m	0.438 m	-12.4%
[Rock size: 0.1 m x 0.1 m x 0.05 m]	Impinging jet width (W_j)	0.7 m	0.5 m	-28.6%
Confirmation Test 1	Impinging jet velocity (V_j)	8.08 m/s	8.48 m/s	5.0%
[Q_{med}, H_{med}, TWD_{max}]	Impinging jet thickness (B_j)	0.35 m	0.42 m	20.0%
[Rock size: 0.1 m x 0.1 m x 0.05 m]	Impinging jet width (W_j)	0.60 m	0.58 m	-2.8%
Confirmation Test 2	Impinging jet velocity (V_j)	8.66 m/s	12.21 m/s	40.9%
[Q_{min}, H_{med}, TWD_{min}]	Impinging jet thickness (B_j)	0.61 m	0.5 m	-18%
[Rock size: 0.1 m x 0.1 m x 0.05 m]	Impinging jet width (W_j)	0.74 m	0.58 m	-21%
Confirmation Test 3	Impinging jet velocity (V_j)	9.81 m/s	9.83 m/s	0.2%
[Q_{med}, H_{max}, TWD_{min}]	Impinging jet thickness (B_j)	0.64 m	0.50 m	-21.9%
[Rock size: 0.1 m x 0.1 m x 0.05 m]	Impinging jet width (W_j)	0.72 m	0.75 m	4.9%
Calibration Test 3	Impinging jet velocity (V_j)	9.47 m/s	9.44 m/s	-0.3%
[Q_{max}, H_{max}, TWD_{max}]	Impinging jet thickness (B_j)	0.77 m	0.50 m	-34.6%
[Rock size: 0.1 m x 0.1 m x 0.075 m]	Impinging jet width (W_j)	1.02 m	0.92 m	-9.4%
Confirmation Test 4	Impinging jet velocity (V_j)	9.76 m/s	10.31 m/s	5.6%
[Q_{min}, H_{max}, TWD_{min}]	Impinging jet thickness (B_j)	0.56 m	0.42 m	-25.6%
[Rock size: 0.1 m x 0.1 m x 0.075 m]	Impinging jet width (W_j)	0.53 m	0.38 m	-28.6%

The simulated impinging jet velocity, V_j, agrees well with the experimental measurements shown in Table 6.8 with a mean percentage difference of 6%. The jet thickness and width at impact with the tailwater level were under-predicted compared to the experimental measurements with a mean percentage difference of -17% and -13%, respectively.

The disparity between the simulated jet footprint at impingement with the plunge pool water surface and the observed measurements could be due to the rate at which air is entrained into the jet is under-predicted by the numerical model. In order to find a solution why the numerical model's jet through the air entrains lower quantities of air compared to the physical model, the following procedures were followed:

- A finer mesh size was used to resolve the water-air mixing, however no improvement was made to the thickness (B_j) and width (W_j) of the jet at impingement with the plunge pool surface.
- The initial turbulence (T_u) at the inlet boundary was increased from 4% to 9%, however, no improvement was made to the impinging jet's footprint with the tailwater level.

6.6. Transient hydrodynamic results

This section presents the hydrodynamic results of tests C1 and C2 for Case A. Refer to Annexure I.1 for the hydrodynamic results of all the Calibration and Confirmation tests used to calibrate the numerical model parameters.

6.6.1. *Plunging jet output*

The condition of the simulated plunging jet was determined by examining the volume fraction contour plots of the water and air phases. The volume fraction contour plots for tests C1 and C2 are shown in Figure 6.8 with red indicating water and blue indicating air. The volume fraction contour plots indicate that the plunging jet becomes developed for all the conditions tested, which correspond

ds to the experimental tests. The volume fraction contour plots also indicate that air entrainment occurs as the jet plunges through the air, as well as when the jet travels through the plunge pool.

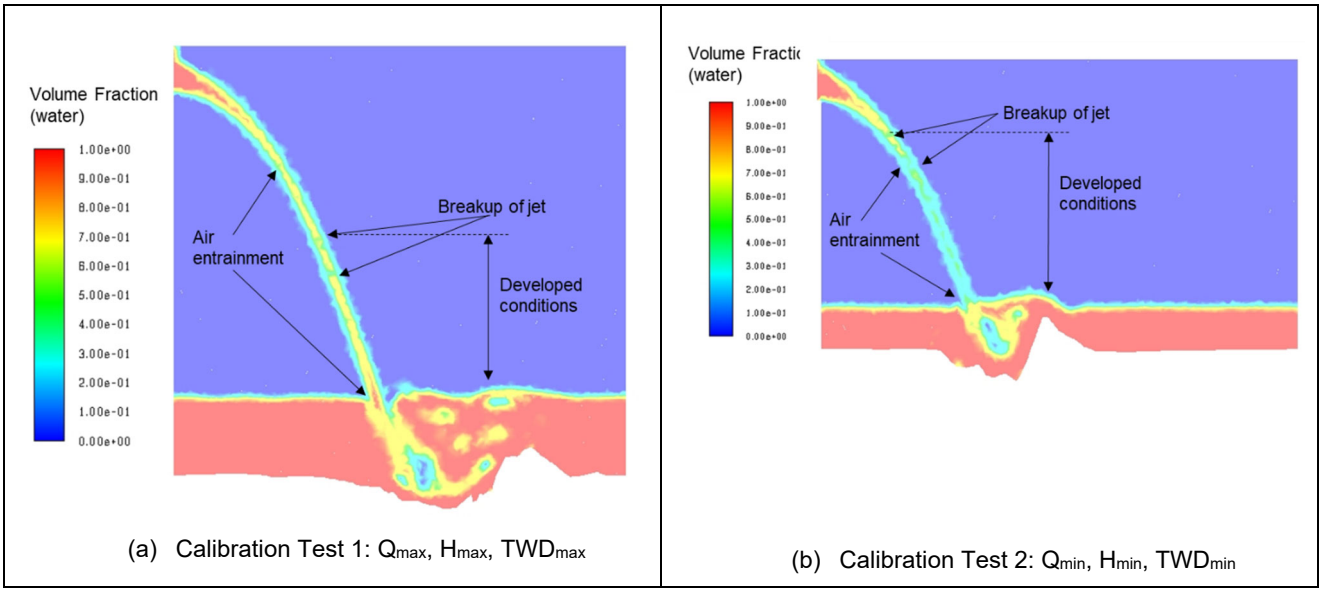

(a) Calibration Test 1: Q_{max}, H_{max}, TWD_{max}

(b) Calibration Test 2: Q_{min}, H_{min}, TWD_{min}

Figure 6.8: Volume fraction contour plot of plunging jet for tests C1 and C2 (red = water and blue = air)

6.6.2. *Streamlines*

Figure 6.9 displays the streamlines for tests C1 and C2 as determined in the numerical model for Case A (scour and deposition). The streamlines are characterised from a global perspective, as well as in more detail in the plunge pool. The streamlines presented in Figure 6.9 present several relevant flow patterns:

- The jet is deflected both upstream and downstream after impingement with the plunge pool bottom. Only a small portion of the total flow is deflected upstream from the impingement point.
- The streamlines represented by the red, purple and green lines indicate that mixing of the flow occurs, especially in the turbulent plunge pool. The height at which the flow is discharged from the spillway does not determine the flow direction in the plunge pool due to the high mixing occurring in the plunge pool.
- The streamlines indicate that recirculation occurs for testing higher discharges due to the influence of the reservoir sides.

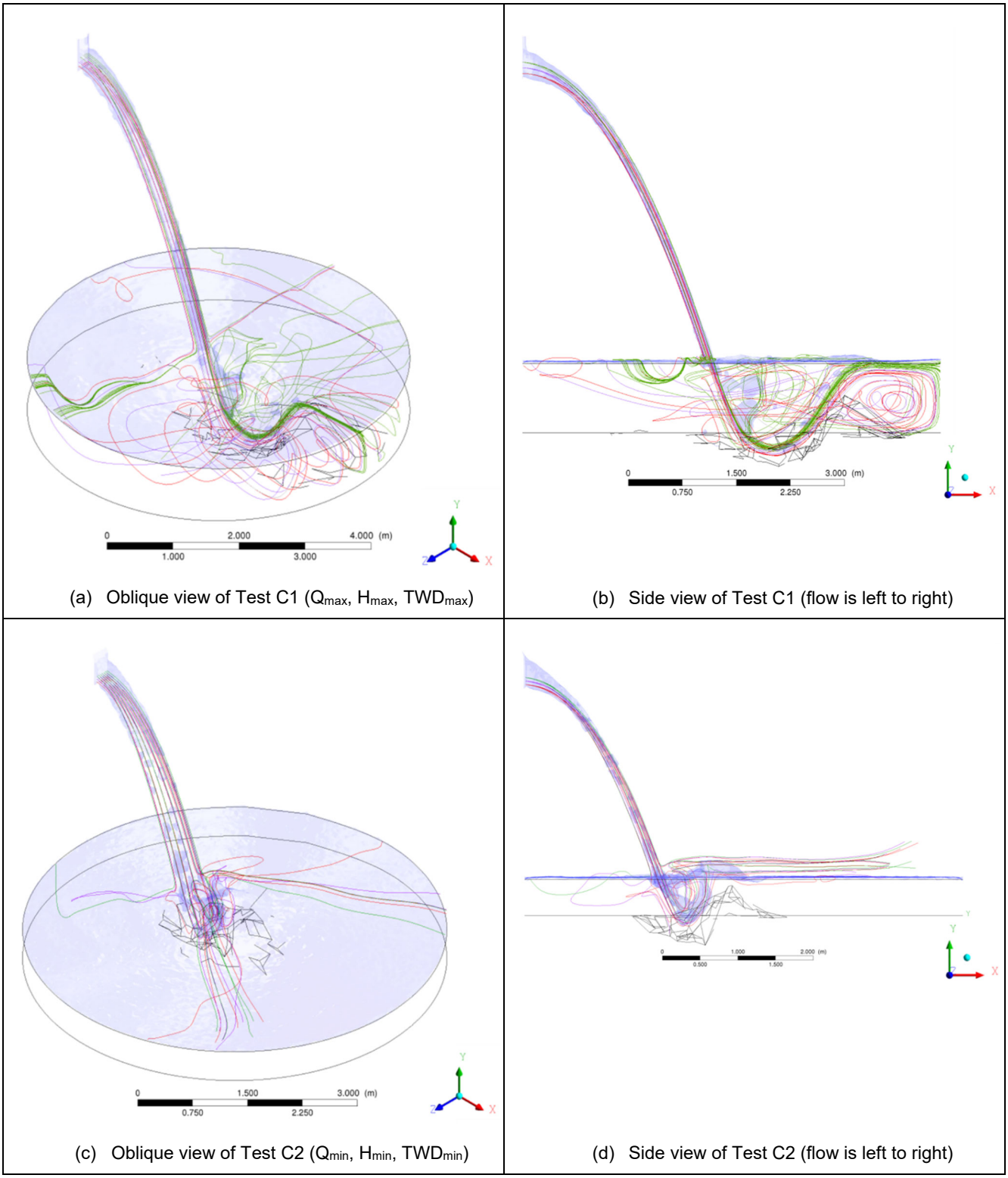

(a) Oblique view of Test C1 (Q_{max}, H_{max}, TWD_{max})

(b) Side view of Test C1 (flow is left to right)

(c) Oblique view of Test C2 (Q_{min}, H_{min}, TWD_{min})

(d) Side view of Test C2 (flow is left to right)

Figure 6.9: Streamlines from issuance canal to plunge pool for tests C1 and C2 for Case A

6.6.3. *Flow velocity*

The flow velocity magnitude along the symmetry plane for tests C1 and C2 for Case A are presented in Figure 6.10 (a) and (b) respectively. The vector magnitude is indicated by the colour bands. Flow arrows are presented in both figures to give an indication of the flow vector direction at that point. The flow velocity just above the impingement zone with the tailwater level is the highest. Near bed flows in the plunge pool exhibit weak upward flow due to the high diffusion rate in the plunge pool.

6.6.4. *Pressures on plunge pool bottom*

The total pressures (static and dynamic pressures) on the plunge pool bottom are a function of not only the static pressure head due to the plunge pool depth but also the dynamics at the pool bottom. Thus, even though the pressure field at the pool bottom is a macroscopic quantity, localised pressure fluctuations can affect it. The local pressure fluctuations are of crucial importance as the dynamic pressures will impose uplift forces on the rock blocks causing scour.

Figure 6.11 shows the total pressure contour distribution (sum of static and dynamic pressures) on the plunge pool bottom for tests C1 and C2 for Case A (scour and deposition). The total pressures on the pool bed inside the scour hole are higher due to the impinging jet on the plunge pool bottom.

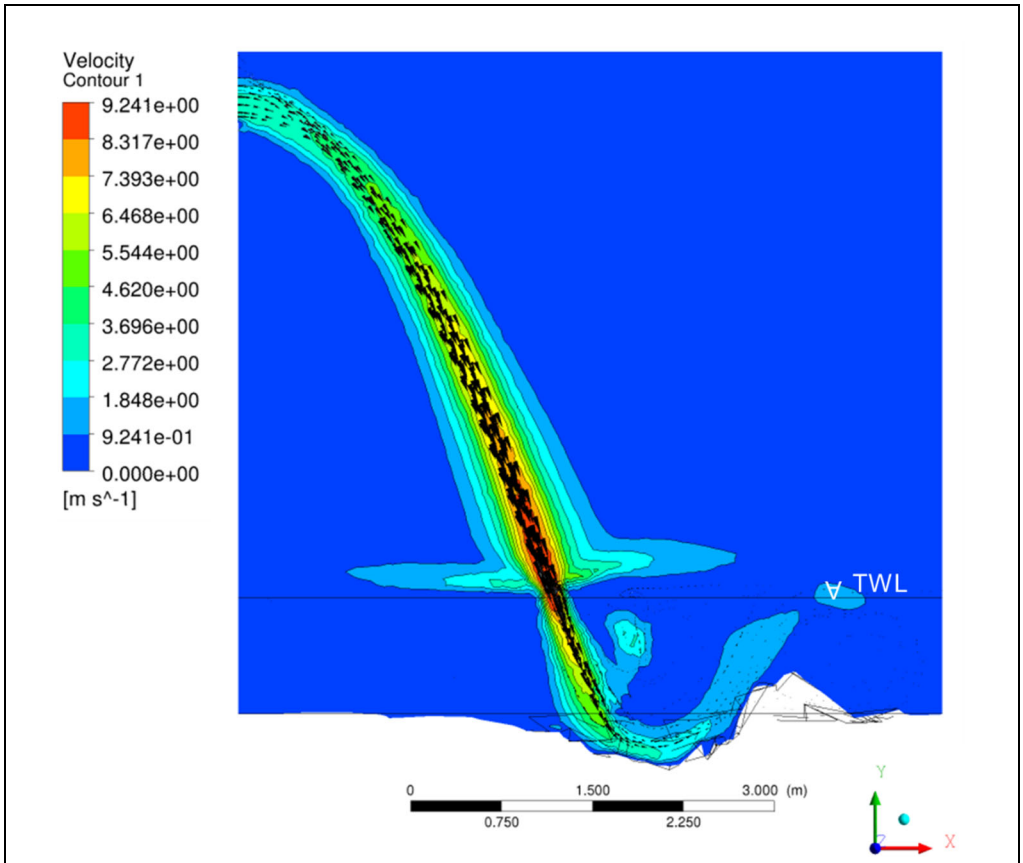

(a) Calibration Test 1: Q_{max}, H_{max}, TWD_{max}

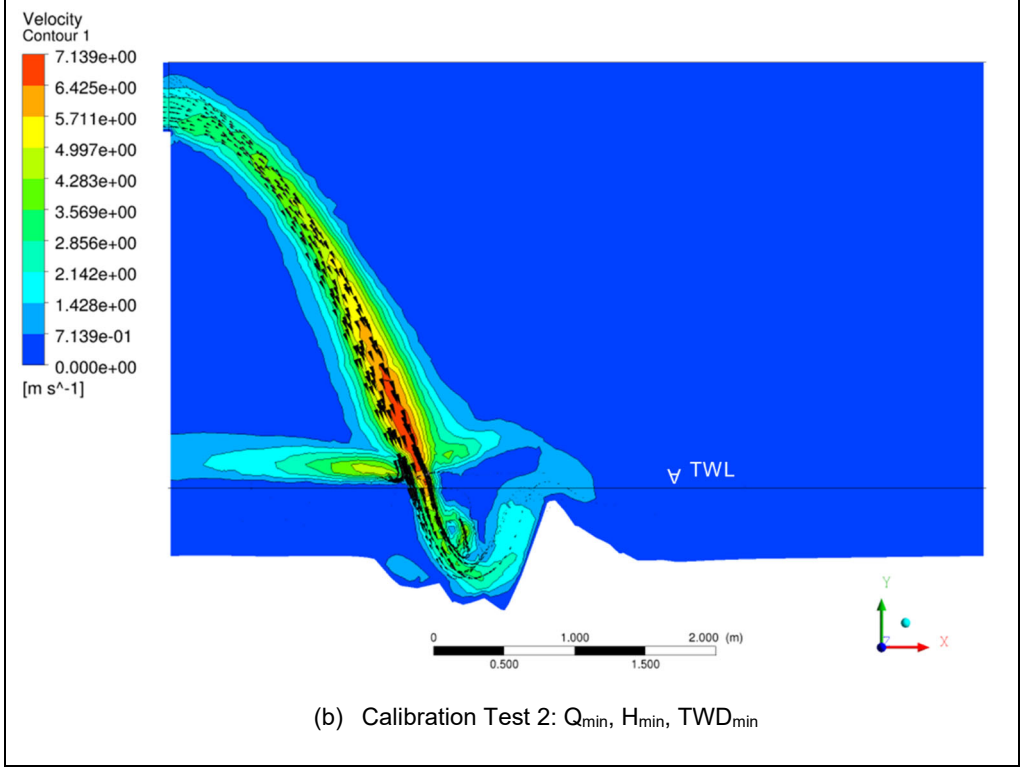

(b) Calibration Test 2: Q_{min}, H_{min}, TWD_{min}

Figure 6.10: Velocity magnitude (m/s) in flow direction for test C1 and C2 for Case A

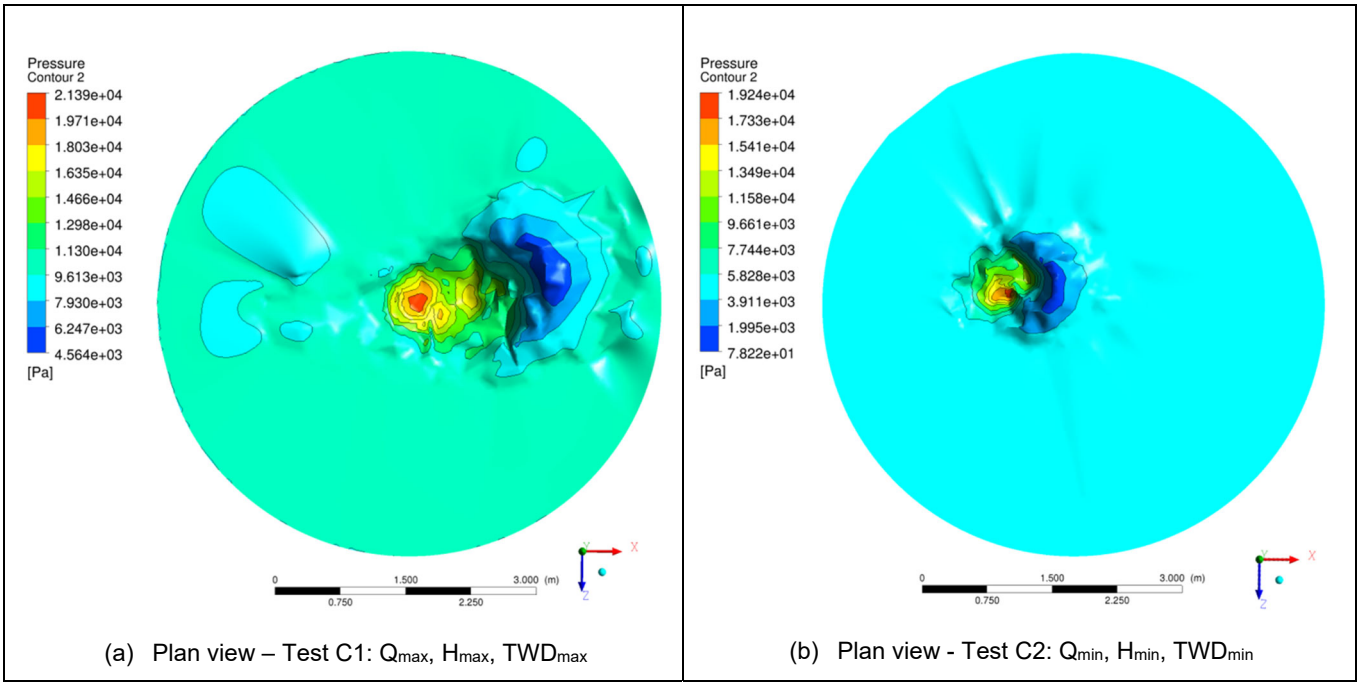

(a) Plan view – Test C1: Q_{max}, H_{max}, TWD_{max}

(b) Plan view - Test C2: Q_{min}, H_{min}, TWD_{min}

Figure 6.11: Total pressures on the plunge pool bottom for tests C1 and C2 (Case A)

6.7. Numerical set up summary

A fully three-dimensional numerical model was used to simulate the rock scour of a plunge pool bottom downstream of a dam. The numerical model set up and techniques used are discussed in the first part of this section. The numerical model was calibrated and confirmed in terms of dynamic pressures and velocity magnitudes against data collected from the physical model until there was good agreement between the numerical and physical models which is presented in the second part of this section. The calibration analysis shows that the turbulence model, pressure-velocity coupling and pressure scheme used to simulate plunging jets are in agreement with what is reported in literature. To accurately replicate the dynamic pressures and velocity magnitudes at the plunge pool bottom, the flow should be initialised as accurately as possible, which includes specifying a fully developed velocity profile at the inlet boundary. The calibration analysis proved that a surface roughness constant (C_s) of 0.8 should be used for simulating a scoured plunge pool bottom surface. The surface roughness parameters (K_s) for the 0.1 m x 0.1 m x 0.05 m and 0.1 m x 0.1 m x 0.075 m rock blocks were determined to be 0.2 m and 0.4 m respectively. The K_s/z_b ratio is therefore 4 and 5.3 for the respective block sizes.

6.8. Numerical solution procedure using regression scour formula to determine scour depth

The equilibrium scour hole geometry was determined by applying the scour depth regression formula (Equation 5.14) for Case B (deposited rocks removed continuously) in Table 5.8 iteratively in order to obtain the static scour limit (maximum scour hole dimensions). The FLUENT model was compiled according to the procedure described in Section 6.4, initially for a jet impinging onto the original flat bed.

The numerical data was collected in a grid fashion, at 0.2 m longitudinal intervals and 0.2 m across the width along the erodible area of the plunge pool bottom. The 1% exceedance dynamic pressures at the plunge pool bottom and the horizontal velocity (x-direction) in the plunge pool were recorded at each grid point. The mean horizontal velocity (V_{mean}) between the pool bottom and the maximum velocity for the specific grid point, together with the flow depth to the maximum velocity ($y_{V_{max}}$) were used to determine the movability and particle Reynolds numbers as illustrated in Figure 6.12. The movability and particle Reynolds numbers were solved for each grid point according to the procedure summarised in Section 5.8.1.2.

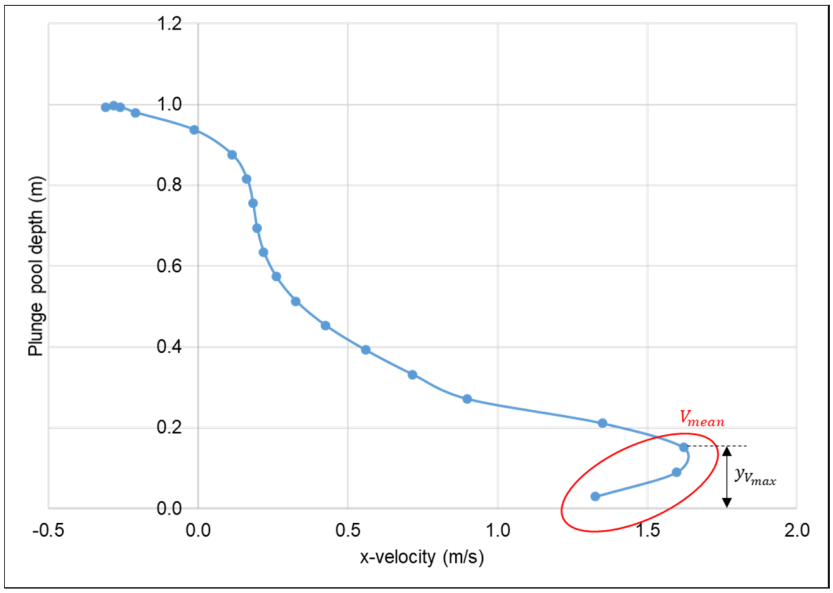

Figure 6.12: Simulated velocity and flow depth used for determining the movability and particle Reynolds numbers

Finally, the block movement calculations were performed manually with post-processing (uncoupled bed deformation). The scour depth regression equation (Equation 5.14) was solved for each grid point. According to the regression formula set up, a positive value indicates scour, and a negative value is taken as zero scour. The numerical simulation was repeated with the newly calculated scoured pool bottom, with additional scour added to the

previous scour depth at the specific grid point. Iteration ceased when a reasonable percentage difference was found (i.e. 0% for the maximum scour depth and < 3% for all the grid points). Figure 6.13 shows the progression of the longitudinal and lateral cross-sections for the different simulation iterations for CF3 test (Q_{med}, H_{max}, TWD_{min}). The numerical procedure followed to obtain the equilibrium scour hole by using the scour depth regression formula (Equation 5.14) is presented as a flow chart in Figure 6.14.

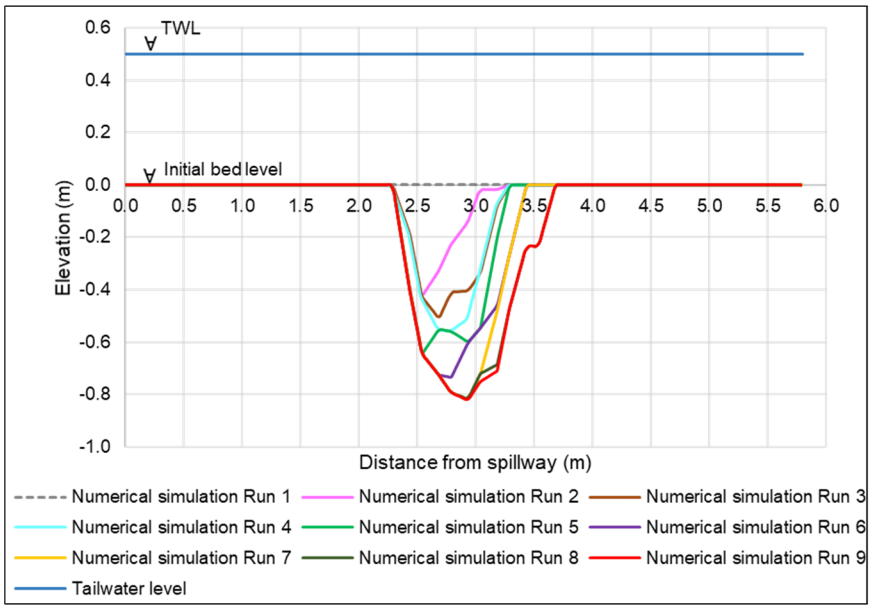

(a) Longitudinal cross-section: Case B

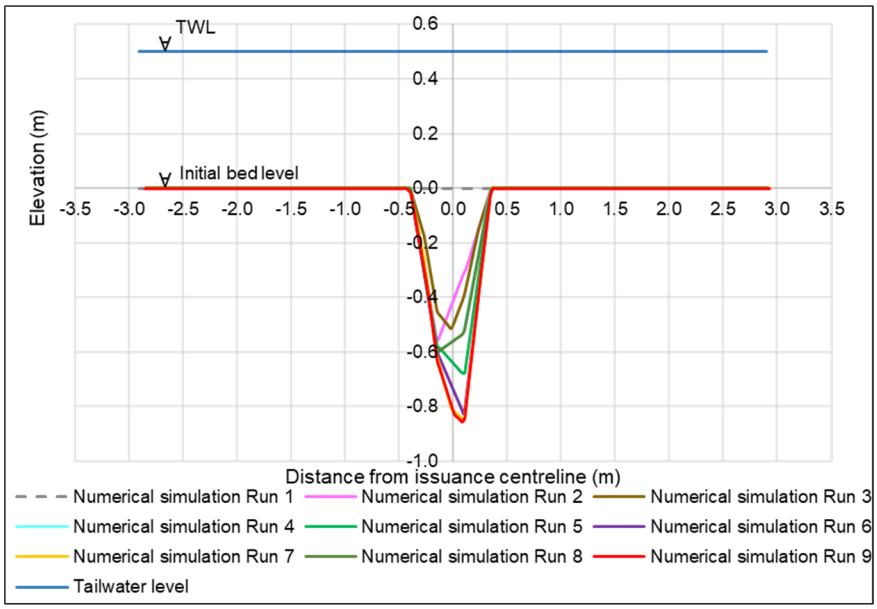

(b) Lateral cross-section: Case B

Figure 6.13: Progression of longitudinal and lateral cross-sections between the different numerical iterations for CF3

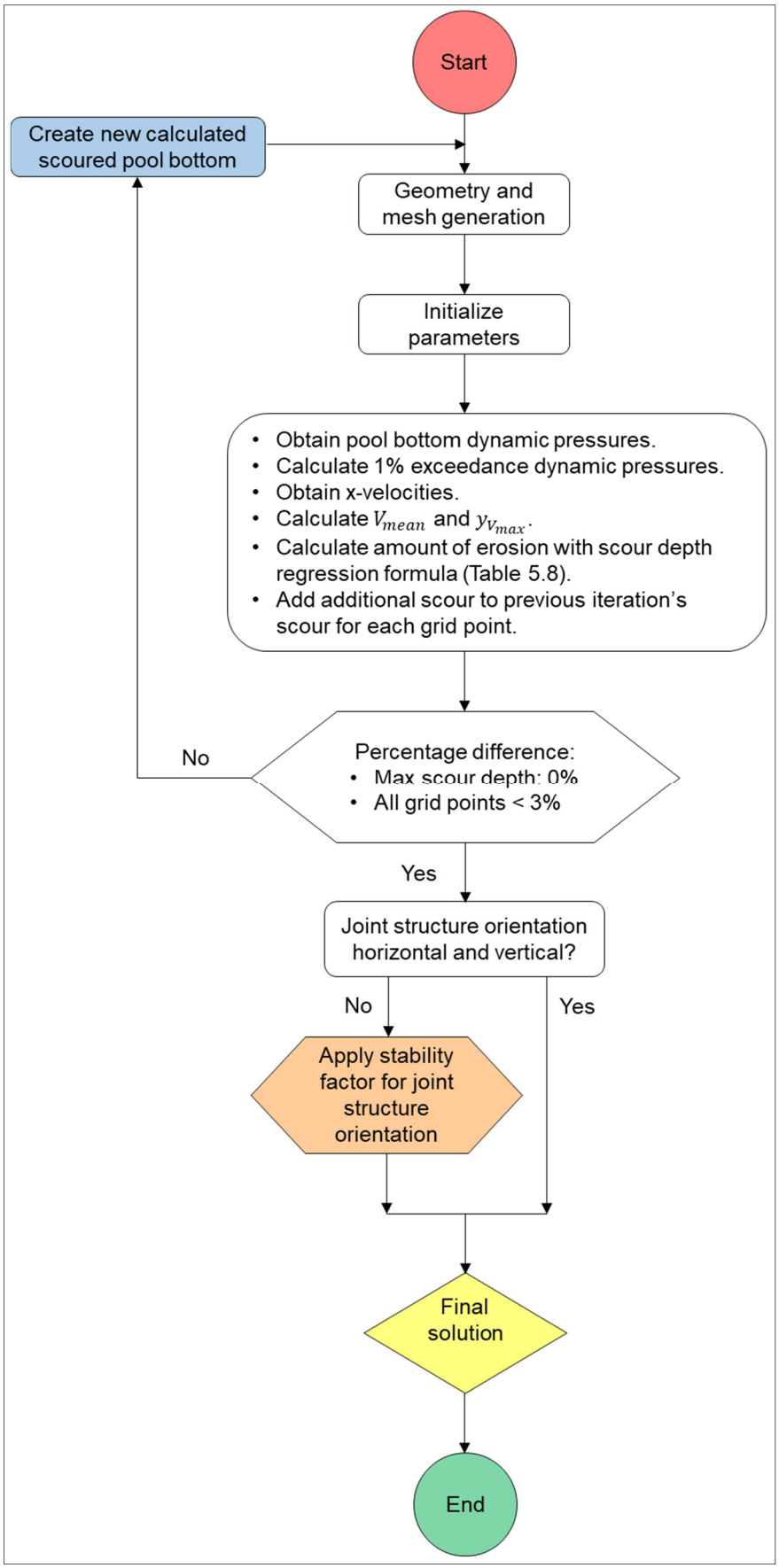

Figure 6.14: Applied flow chart for the numerical solution procedure using the regression scour formula

6.9. Analysis of numerical simulation results

The ability of the proposed numerical model to simulate the complex flow field and calculating the resultant plunge pool bottom scour downstream of a dam spillway was evaluated and compared to the experimental work. Refer to Annexure I.2 for the hydrodynamic results of all the simulated tests with a jet initially impinging onto the original flat bed for Case B.

6.9.1. *Comparison of bed deformation results*

Table 6.9 records the bed deformation as longitudinal and lateral cross-sections, as well as contour maps for the experimental tests for Case B (deposited rocks removed continuously) and numerical model for each of the Calibration and Confirmation tests using the scour depth regression formulae, Equation 5.14, including two additional tests with joint structures dipped in and against the flow direction using Table 5.9, and one test (CF1) also simulated for Case A (scour and deposition) using the scour depth regression formula, Equation 5.13. Negative values on the contour maps represent scouring with warmer colours (red) indicating shallow scouring and cooler colours (purple and blue) indicating deep scouring. Contours upstream and downstream of the scour hole for the experimental tests indicate small surface irregularities recorded by the laser scanner.

Although the scour profiles in Table 6.9 from the experimental and numerical tests are not identical, the simulated scour contours reasonably agree with the experimental test measurements in terms of maximum scour depth and the scour width. The numerical model has been equally successful in capturing the variation in the scour hole size for different discharges, fall height, tailwater levels, rock sizes and joint structure orientation. The simulated scour hole contours are not entirely symmetrical, suggesting that the numerical model is able to incorporate the randomness of scouring in nature.

The maximum scour depth observed from the experimental tests and the proposed numerical model for Case B are compared in Figure 6.15 (blue round markers). The maximum scour depths plotted on Figure 6.15 tend towards the line of equality, indicating that the proposed numerical model is able to predict the maximum scour depth downstream of a spillway for different discharges, fall heights, tailwater levels, rock sizes and joint structure orientation. A low SSR value of 0.103 (model scale) also indicates that the simulated maximum scour depth for all the tests is in good agreement with the observed measurements. The simulated maximum scour was generally over-predicted with a mean percentage error of 11%.

The extent of the simulated scour hole (length and width) compared with the experimental measurements for Case B (deposited rocks removed continuously) are also shown in

Figure 6.15. Although the numerical model is capable of predicting the maximum scour depth downstream of a dam spillway well, the width (round green markers) of the scour hole is predicted with less accuracy and the length (round red markers) poorly, as seen in the bed deformation graphs in Table 6.9 and the high SSR values indicated in Figure 6.15. The length of the scour hole in the direction of the flow, is under-predicted for all the tests. The numerical scour lengths and widths for Case B compared to the experimental measurements for Case B, plotted on Figure 6.15, has a mean percentage difference of -33% and -13% respectively, with large SSR values.

Similarly, Figure 6.16 compares the scour hole volume for Case B simulated by the proposed numerical model with the experimental measurements. The scour hole volume required for energy dissipation was under-predicted for all the tests for Case B, demonstrating a mean percentage difference of -55% and a large SSR value of 5.696.

In general, the scour hole predicted by the numerical model is deeper, shorter and narrower compared to the experimental measurements. The disparity in the scour hole dimensions could be due to the diffusion of the jet through the air being less than in the physical model, with the simulated jet being more compact at impingement with the plunge pool water surface as concluded from Table 6.8. A possible reason for the lower jet diffusion being simulated could be that the simulated water-air mixing of the jet in the air and plunge pool of the numerical model is less than in the physical model. Due to the more compact jet simulated at the tailwater level and in the plunge pool, a smaller area on the plunge pool bottom experiences fluctuating pressures and uplifting forces, leading to a deeper, shorter and narrower scour hole being calculated.

Out of all the tests simulated for Case B (scour with rocks removed continuously), the proposed numerical model best predicted the scour hole extent (length and width) for test CF1, as seen from the longitudinal and lateral cross-sections in Table 5.9. Only for test CF1, the numerical model over-predicted the jet thickness (B_j) at impact with the plunge pool water surface and the jet impinging width (W_j) having the lowest percentage difference with the experimental jet width (refer to Table 6.8). In order to establish whether a more accurate prediction of the impinging jet footprint would better simulate the scour hole extent, test CF1 was also simulated for Case A (scour and deposition) by calculating the scour depth with the regression formula, Equation 5.13. The last row in Table 6.9 shows the simulated bed deformation results for test CF1 for Case A compared to the experimental results. The deposition of the scoured material downstream of the hole was manually achieved by depositing the scoured volume directly downstream of the calculated scour hole, since the transport capability of the numerical model has not yet been automated.

The maximum scour depth, length and width for test CF1 for Case A are in good agreement with the observed measurements. Considering that the numerical model and scour depth regression formulae (Equation 5.13 for Case A and Equation 5.14 for Case B) were able to simulate the scour hole dimensions for test CF1, this validates the use of the regression formulae when the spreading behaviour of the plunging jet is simulated accurately.

Table 6.9: Bed deformation results

C1 test	Q_{max}, H_{max}, TWD_{max} Small blocks, horizontal/ vertical joints Case B	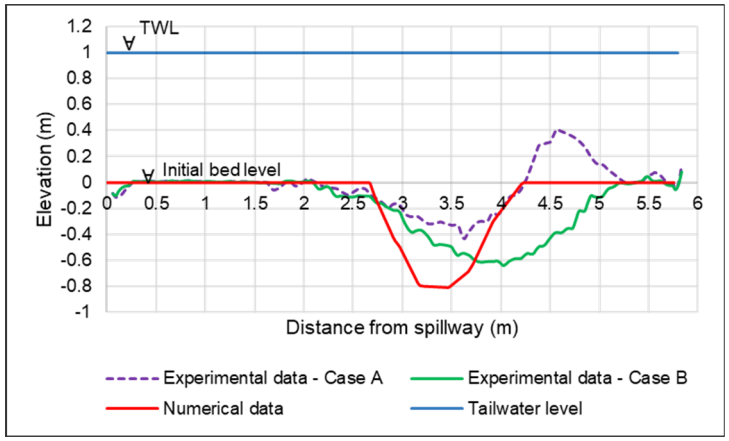 Longitudinal cross-section: Case B	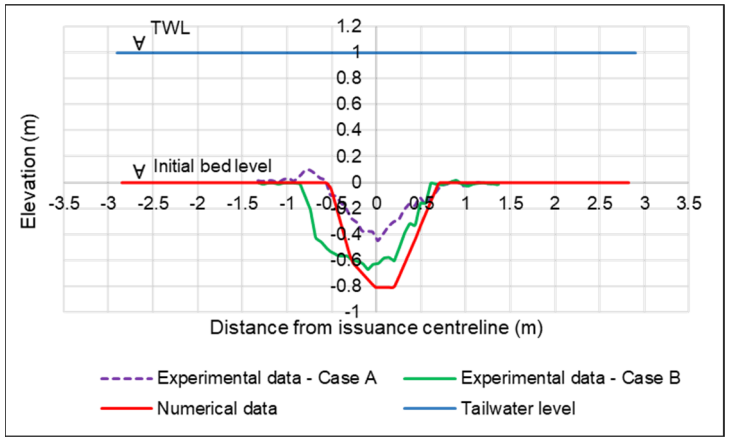 Lateral cross-section: Case B
		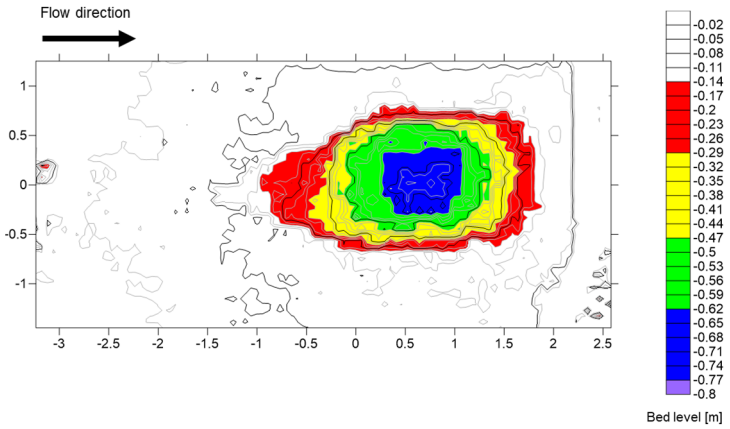 Experimental test contours	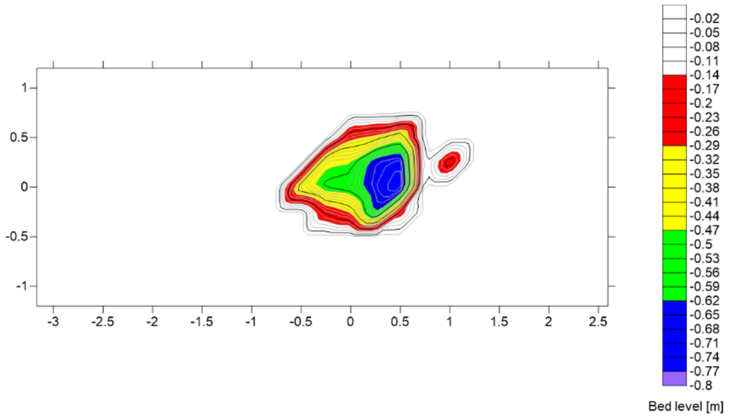 Numerical test contours

C2 test	Q_{min}, H_{min}, TWD_{min} Small blocks, horizontal/ vertical joints Case B	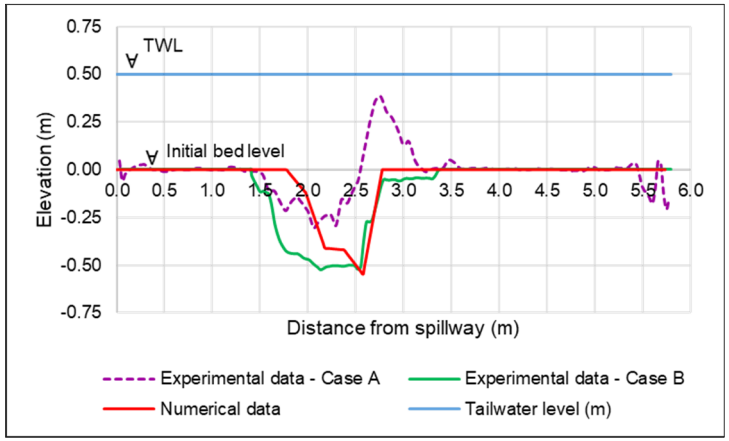 Longitudinal cross-section: Case B	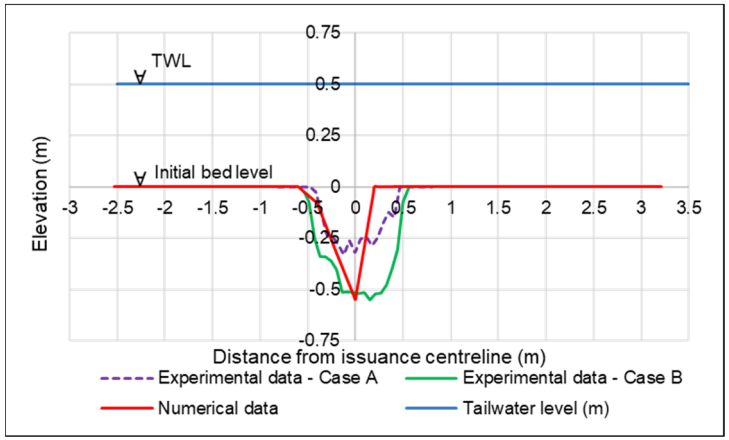 Lateral cross-section: Case B
		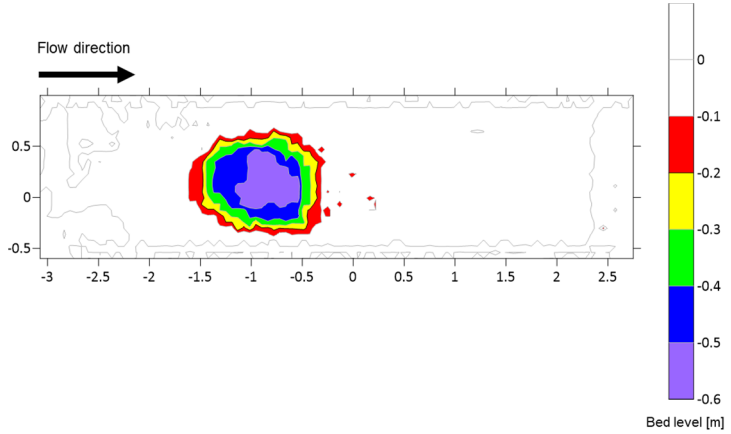 Experimental test contours	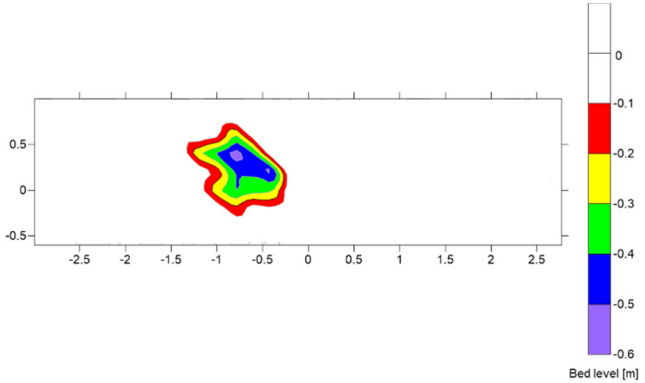 Numerical test contours

CF1 test	Q_{med}, H_{med}, TWD_{max} Small blocks, horizontal/ vertical joints Case B	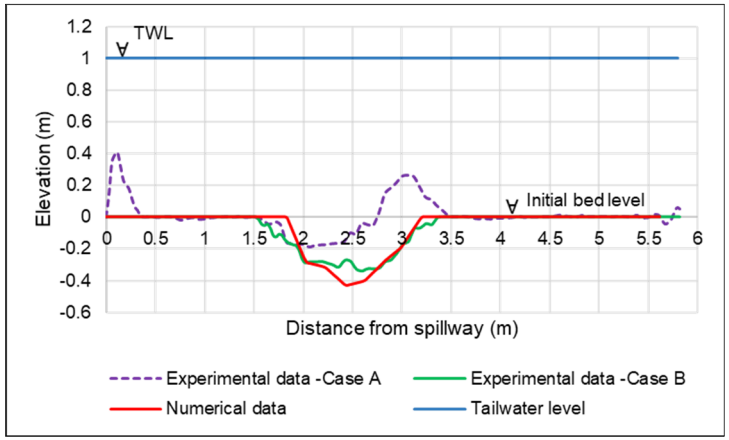 Longitudinal cross-section: Case B	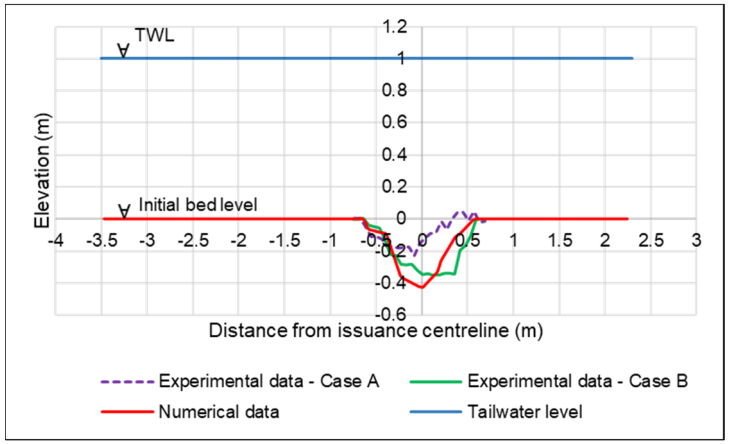 Lateral cross-section: Case B
		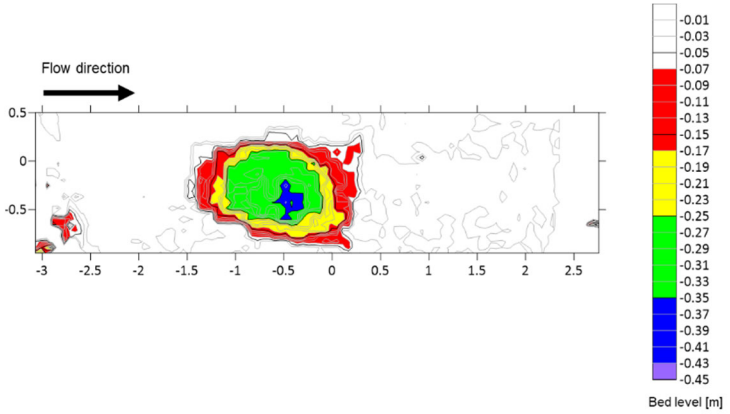 Experimental test contours	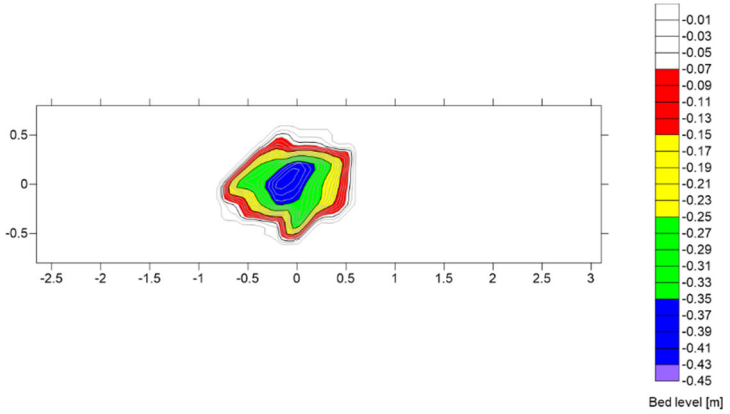 Numerical test contours

CF2 test	Q_{min}, H_{med}, TWD_{min} Small blocks, horizontal/ vertical joints Case B	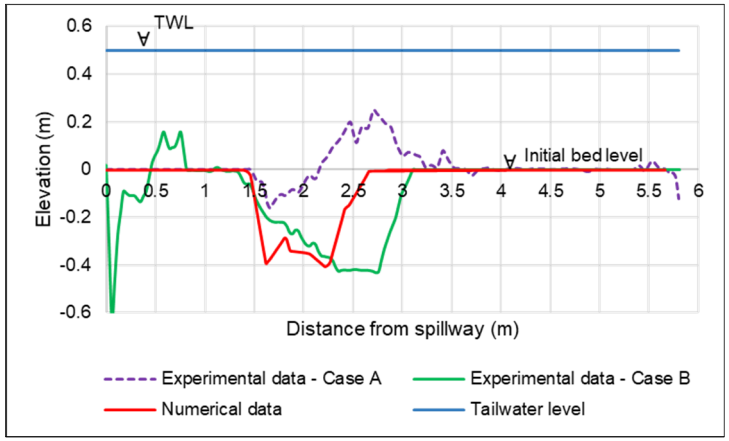 Longitudinal cross-section: Case B	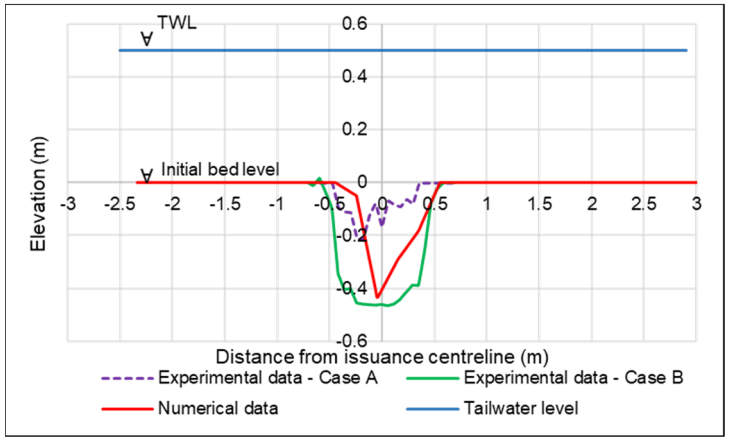 Lateral cross-section: Case B
		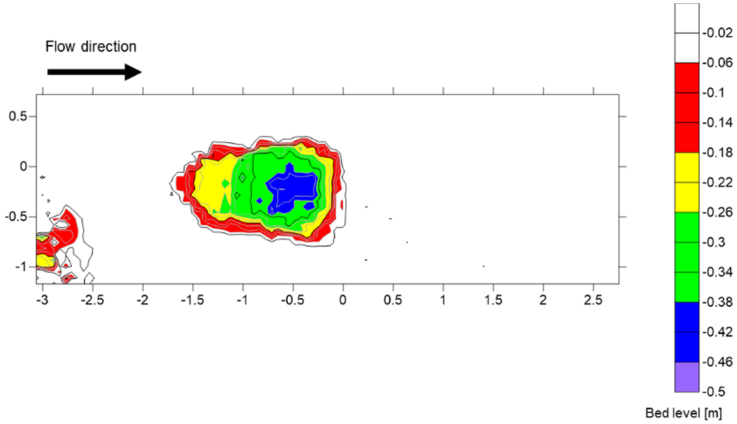 Experimental test contours	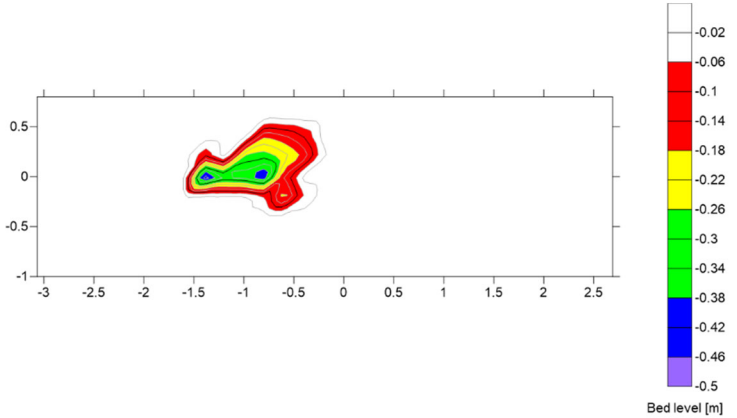 Numerical test contours

CF3 test	Q_{med}, H_{max}, TWD_{min} Small blocks, horizontal/ vertical joints Case B	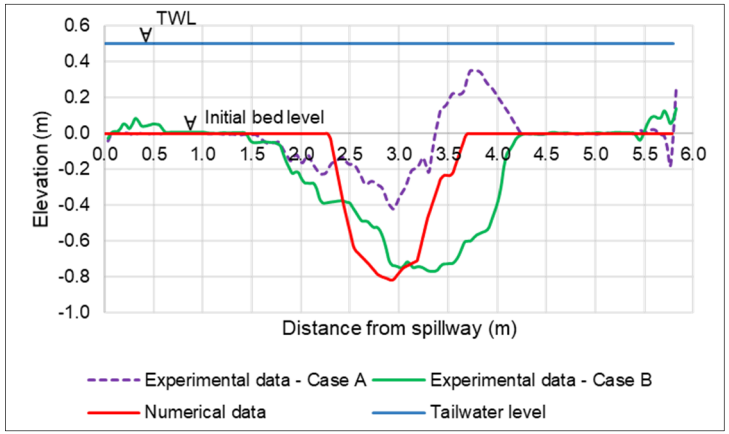 Longitudinal cross-section: Case B	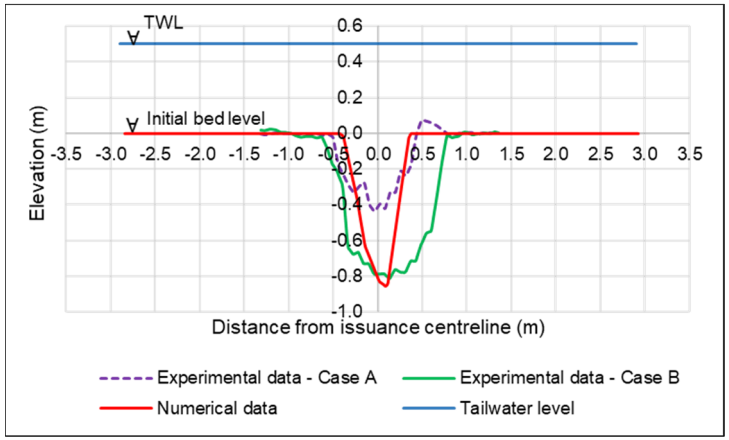 Lateral cross-section: Case B
		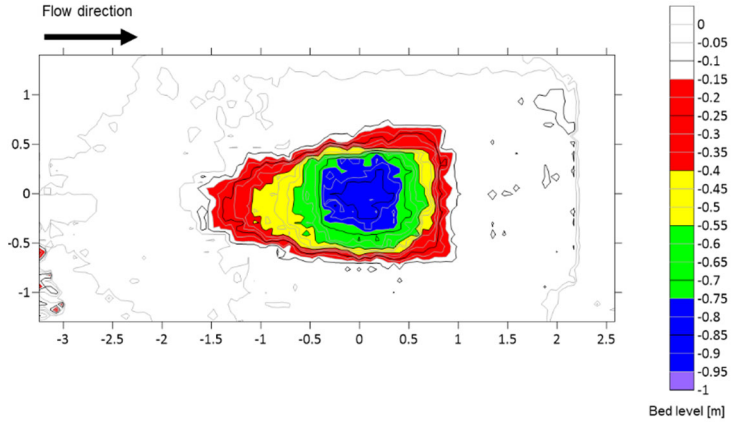 Experimental test contours	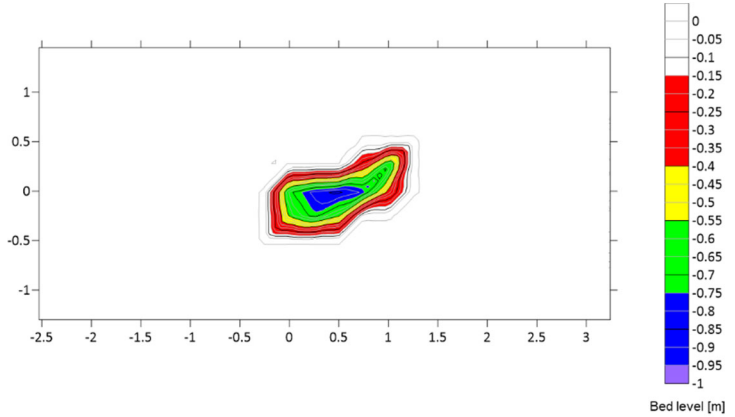 Numerical test contours

C4 test	Q_{max}, H_{max}, TWD_{max} Large blocks, horizontal/ vertical joints Case B	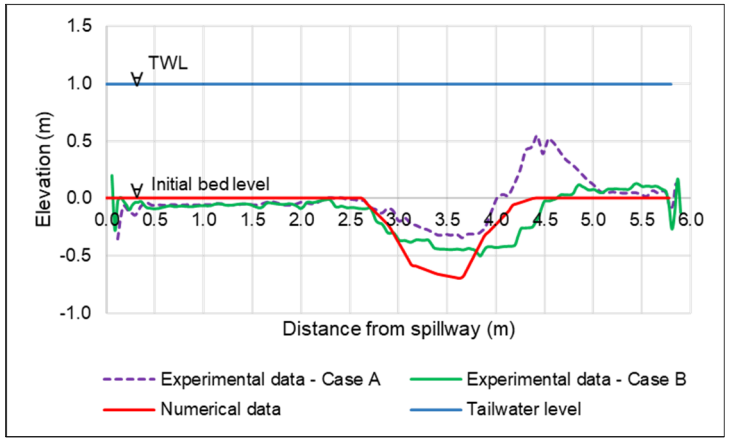 Longitudinal cross-section: Case B	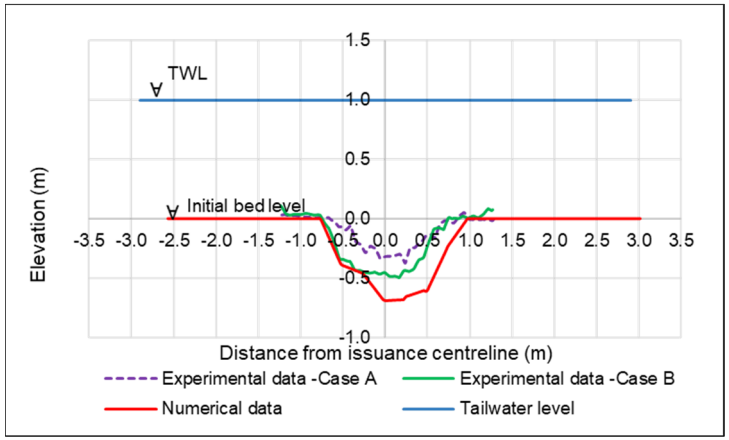 Lateral cross-section: Case B
		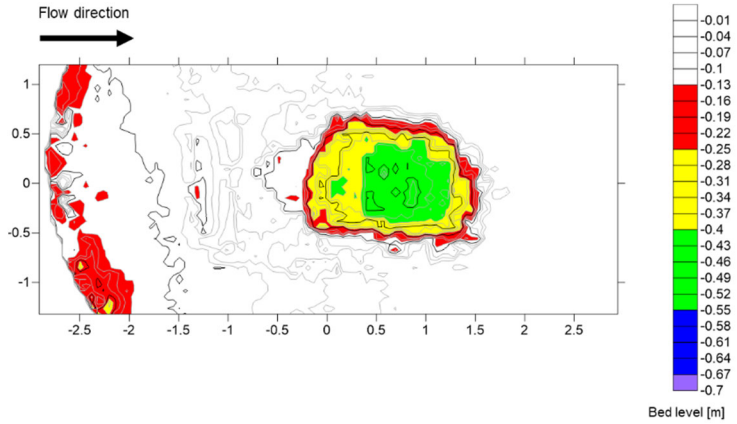 Experimental test contours	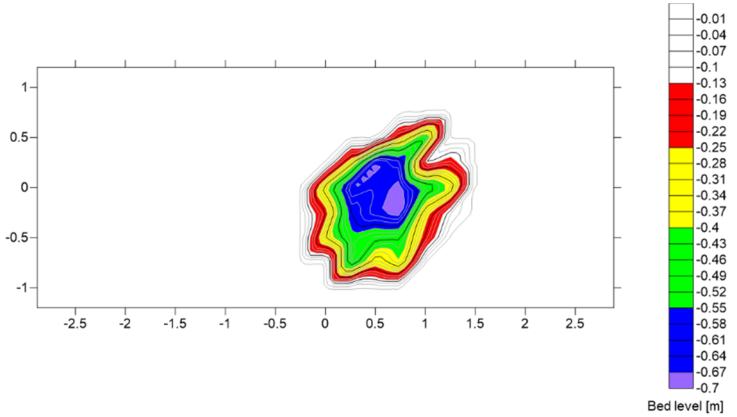 Numerical test contours

CF4 test	Q_{min}, H_{max}, TWD_{min} Large blocks, horizontal/ vertical joints Case B	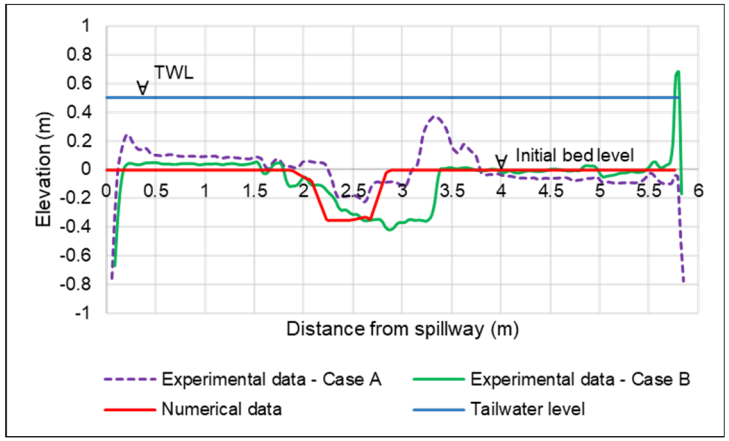 Longitudinal cross-section: Case B	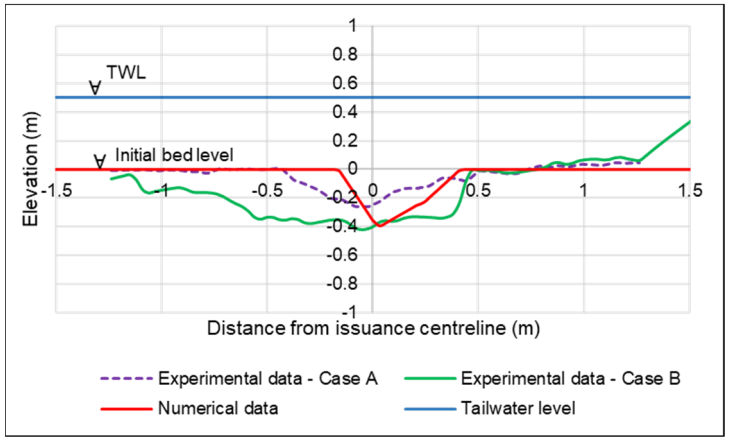 Lateral cross-section: Case B
		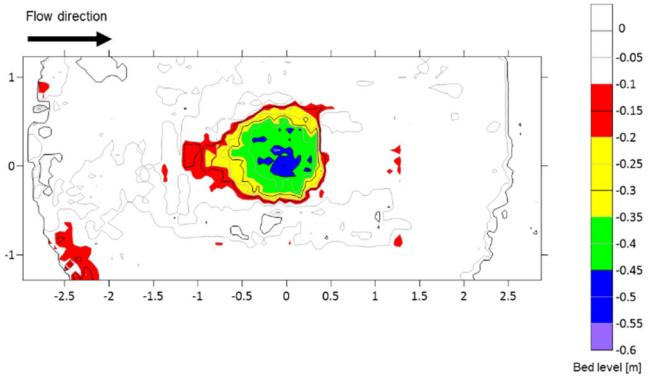 Experimental test contours	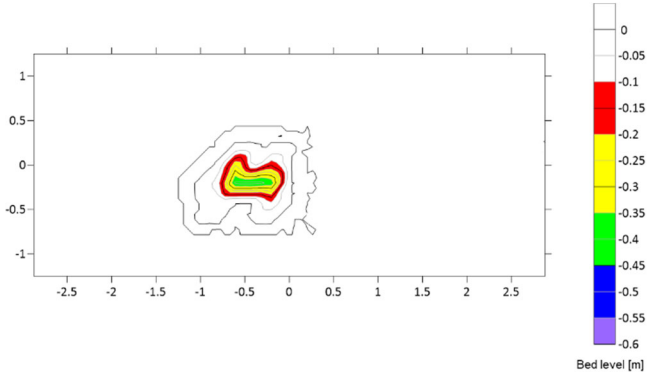 Numerical test contours

Joint angle test 1	Q_{min}, H_{max}, TWD_{max} Small blocks, joint structure dip against flow direction Case B	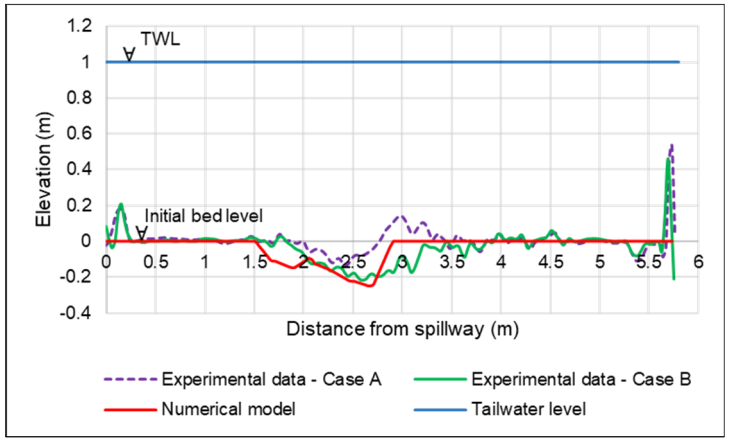 Longitudinal cross-section: Case B	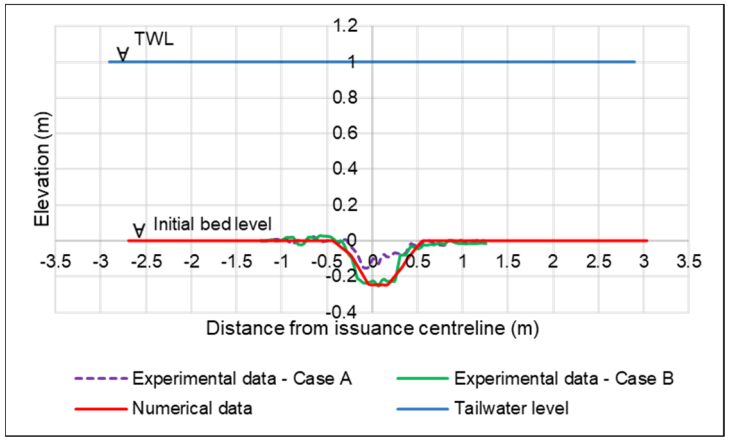 Lateral cross-section: Case B
		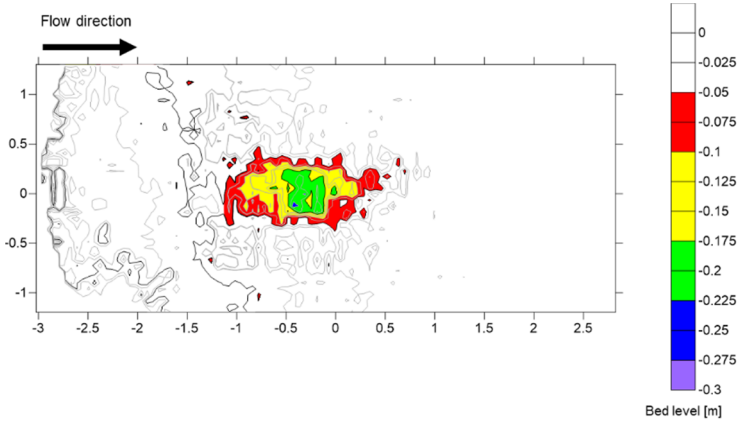 Experimental test contours	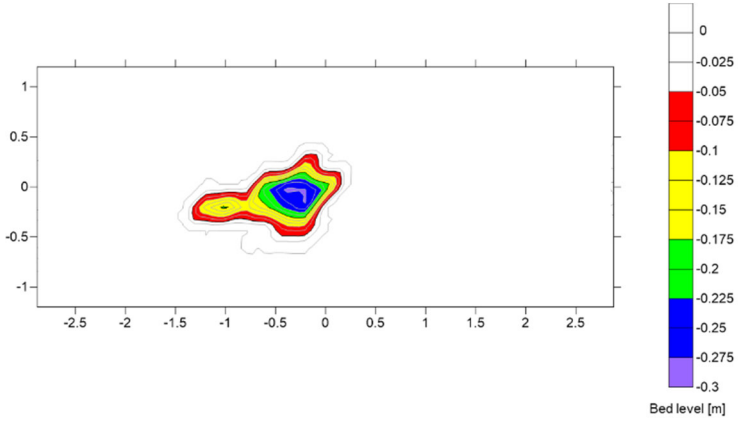 Numerical test contours

Joint angle test 2	Q_{max}, H_{max}, TWD_{max} Small blocks, joint structure dip with flow direction Case B	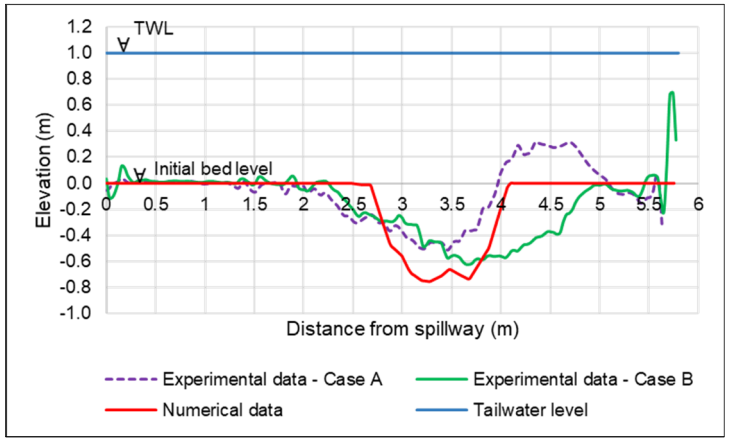 Longitudinal cross-section: Case B	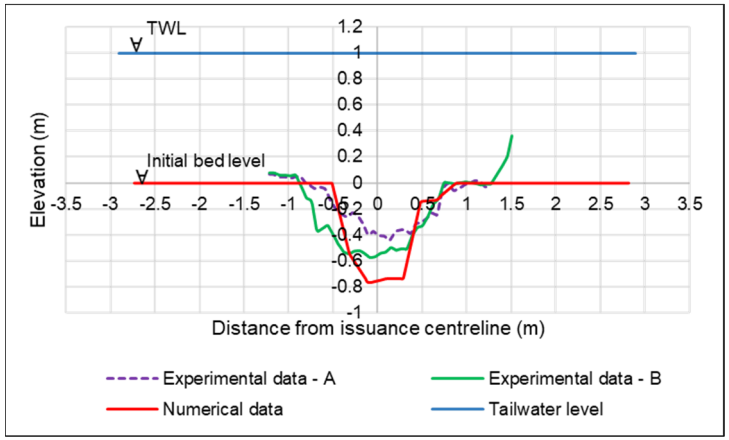 Lateral cross-section: Case B
		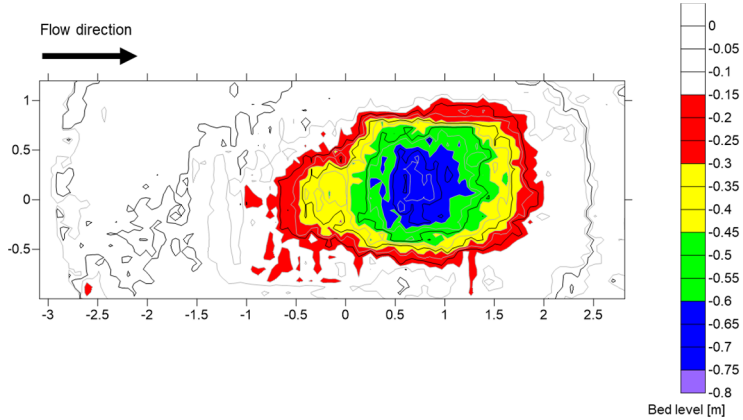 Experimental test contours	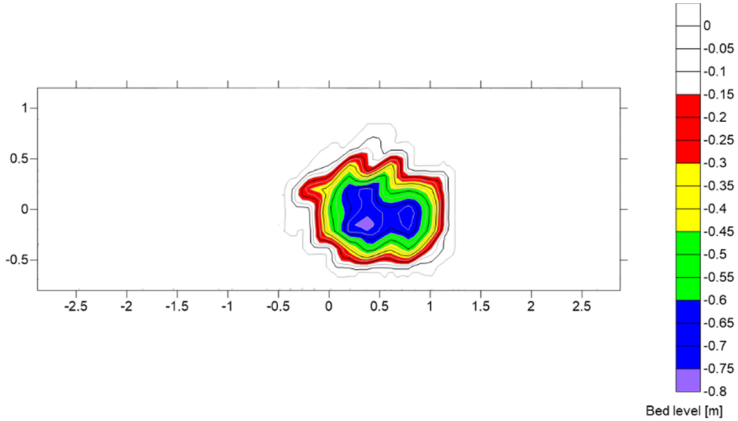 Numerical test contours

CF1 test	Q_{med}, H_{med}, TWD_{max} Small blocks, horizontal/ vertical joints Case A	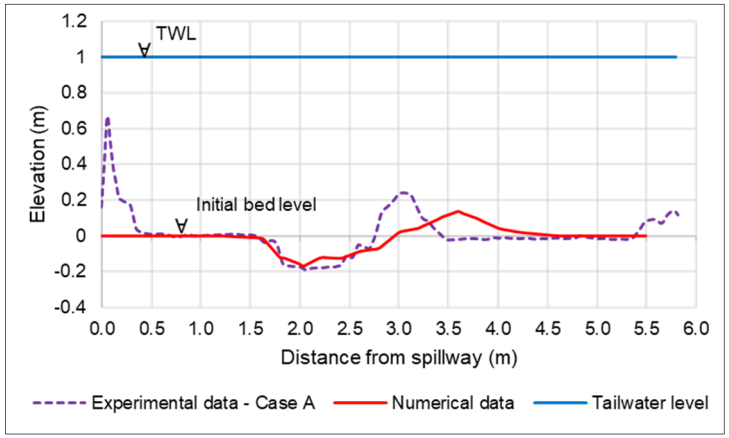 Longitudinal cross-section: Case A	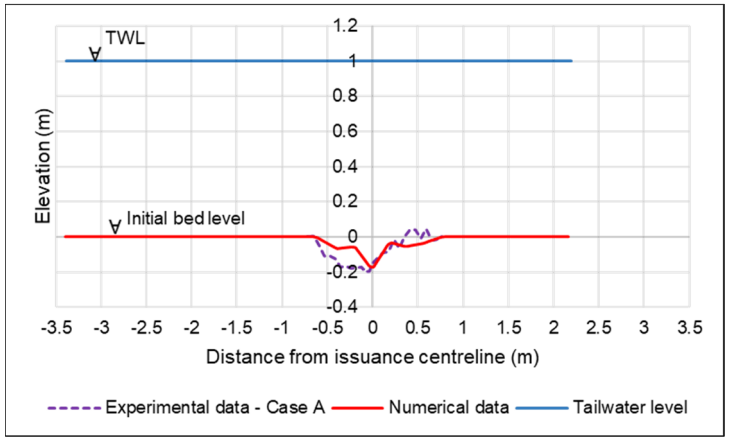 Lateral cross-section: Case A
		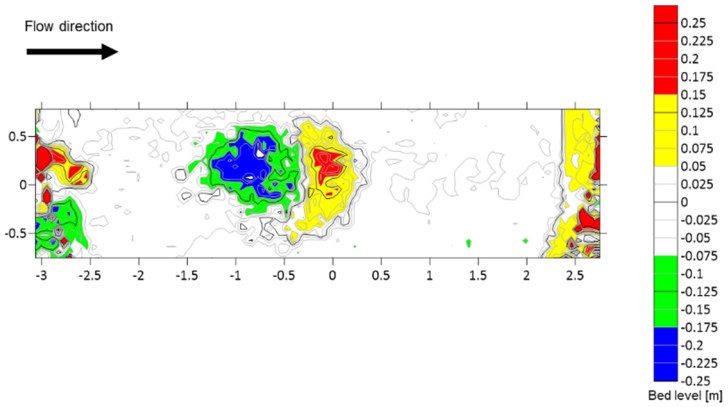 Experimental test contours for Case A	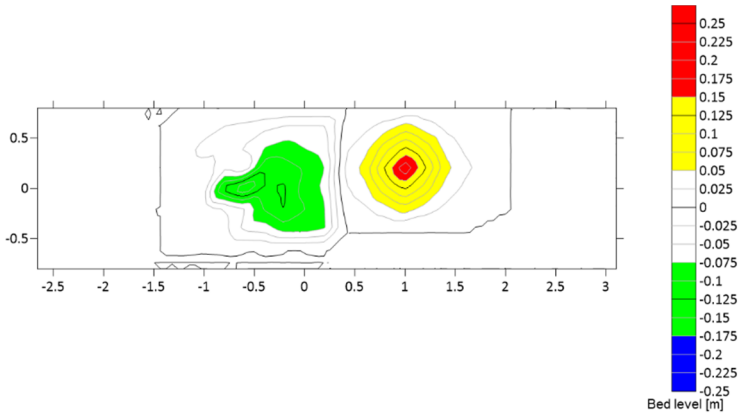 Numerical test contours for Case A

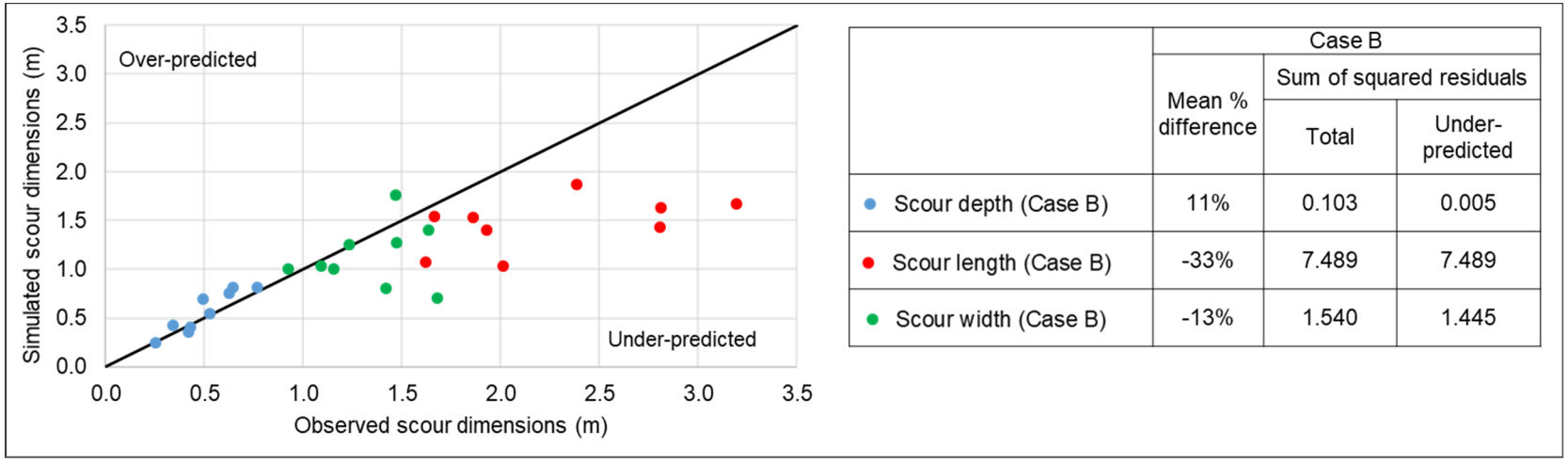

	Case B		
	Mean % difference	Sum of squared residuals	
		Total	Under-predicted
Scour depth (Case B)	11%	0.103	0.005
Scour length (Case B)	-33%	7.489	7.489
Scour width (Case B)	-13%	1.540	1.445

Figure 6.15: Comparison of scour depth, length and width observed from the experimental tests and simulated by proposed numerical model for Case B (model values)

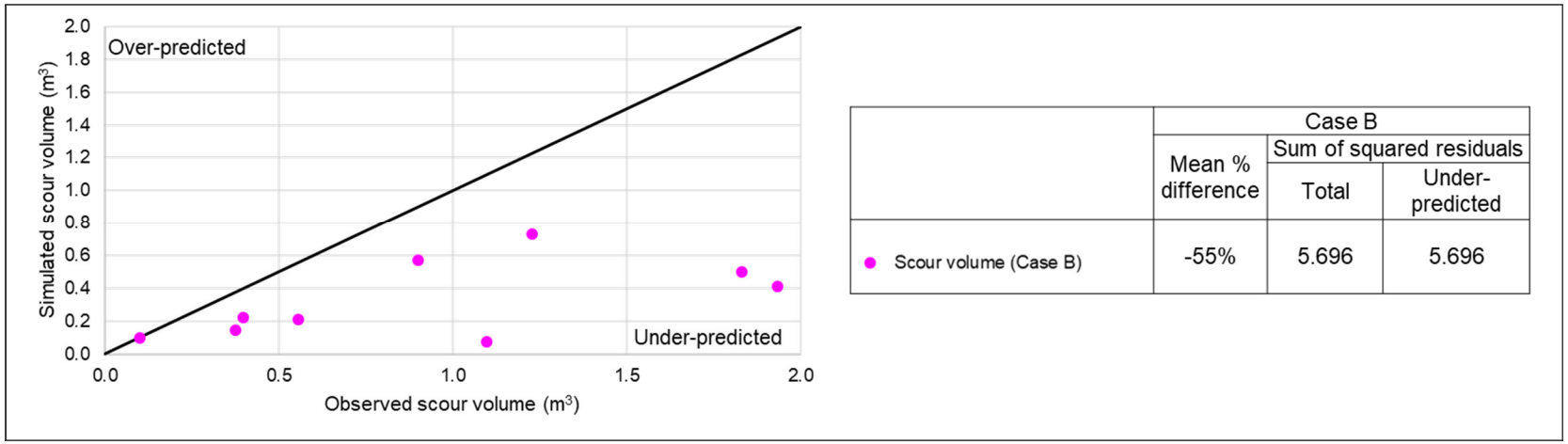

	Case B		
	Mean % difference	Sum of squared residuals	
		Total	Under-predicted
Scour volume (Case B)	-55%	5.696	5.696

Figure 6.16: Comparison of scour volume observed from the experimental tests and simulated by the proposed numerical model for Case B (model values)

6.9.2. *Comparison of simulated scour depth with literature*

Figure 6.17 presents the SSR values for the Calibration and Confirmation Tests for the proposed numerical model scour depths and the scour prediction methods evaluated in Section 5.9 on a 1:20 prototype scale for Case B (deposited rocks removed continuously). The proposed numerical model performs well in predicting the relative scour depths for Case B compared to the scour prediction methods, regardless of the perceived limitations of the numerical model. The proposed numerical model has the second lowest total SSR of 41 and is one of the methods with the least under-predictions (2) of the experimental data for Case B on a prototype scale. The low SSR values prove that numerical models are physically sound and able to capture different parameters, such as tailwater depth and two phase flow (air and water), to predict scour depths that tend to the line of equality shown in Figure 6.15.

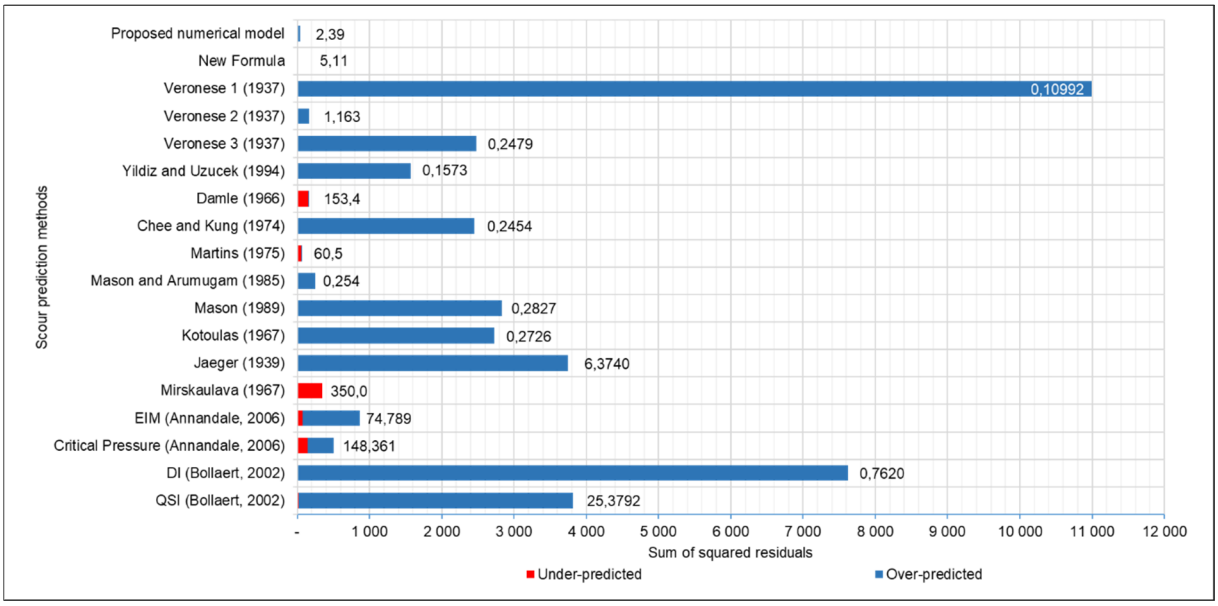

Figure 6.17: The SSR for the proposed numerical model scour depths and for the various scour prediction methods for Case B for the Calibration and Confirmation tests on a 1:20 prototype scale

The proposed numerical model is considered safe for plunge pool scour determination downstream of a spillway inside the prototype ranges on which the regression formulae (Equation 5.14 in Table 5.8, Section 5.8.1.3) were based (discharge: 35 $m^3/s/m$ – 80 $m^3/s/m$; fall height: 60 m – 100 m; tailwater depth: 10 m – 20 m; 0°, 45º and 135º joints). When the model fails to be accurate, it predominantly over-predicts the maximum scour depth with a mean percentage difference of 11%. However, further research is proposed to evaluate the capability of the numerical model to simulate field data, i.e. a prototype spillway and plunge pool calibrated to incorporate the in-situ rock material and joint structure orientation, including the required mesh resolution. Furthermore, the performance of the proposed numerical model

to simulate plunge pool scour could be compared with other numerical models, such as Rocky and FLOW-3D.

6.9.3. *Comparison of dynamic pressures*

The 1% exceedance dynamic pressures at the plunge pool bed surface were used for calibrating the bed roughness parameters in Section 6.5.5. The simulated dynamic pressures at the plunge pool bed surface had to be calibrated against the experimental pressures recorded in order to ascribe more certainty to the results.

The magnitude of the pressures experienced at the pool bottom is predominantly dependent on the distribution of the extreme values, which depend on the turbulence characteristics in the plunge pool and the observation time length (Castillo et al., 2018). A comparison of the 1% exceedance dynamic pressure head at the centreline of the scour hole predicted by the proposed numerical model and observed from the experimental tests is presented in Figure 6.18 for different discharges, fall heights and tailwater levels.

The magnitude of the peak dynamic pressure head values simulated by the proposed numerical model are in agreement with the measured values, excluding C1 test (Q_{max}, H_{max}, TWD_{max}). However, the numerical model predicted the minimum dynamic pressure fluctuations, which corresponds to the location of entrained air incorrectly. The discrepancy between the simulated and measured negative dynamic pressures could be due to the simulation of the jet diffusion through the air and plunge pool being less than in the physical model, due to the water-air mixing simulated by the numerical model being less than for the physical model.

The location of the peak dynamic pressure head predicted by the numerical model differs to that of the experimental tests. The discrepancy in the peak dynamic pressure location could be attributed to the difference of the jet trajectory and jet impingement point with the pool bottom between the numerical model and experimental tests as seen in Figure 6.7.

The dynamic pressure head results presented in Figure 6.18 also indicate that the magnitude of the simulated and observed peak dynamic pressure head values are greater for shallow pool depths (Figure 6.18a) compared to greater pool depths (Figure 6.18b) that dampen the scour process more. The numerical model is therefore capable of resolving the variation in the pool bottom pressures for different pool depths.

Although the pressure fluctuations were not modelled properly, the proposed numerical model is capable of simulating the peak dynamic pressure head magnitudes. The model was

therefore able to capture the scour process and calculate the scour depth, since rock scour in turbulent flow is caused by fluctuating pressures and not shear processes (Annandale, 2006).

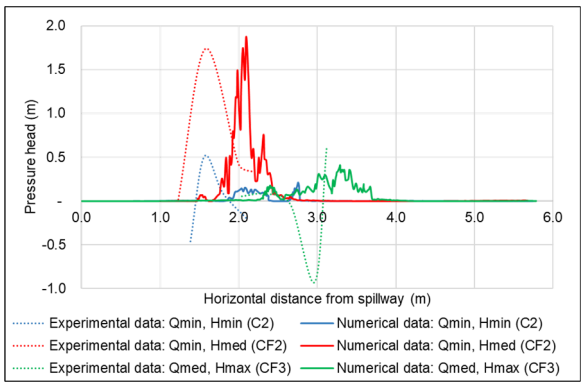

(a) Minimum tailwater level (M: 0.5 m, P: 10 m)

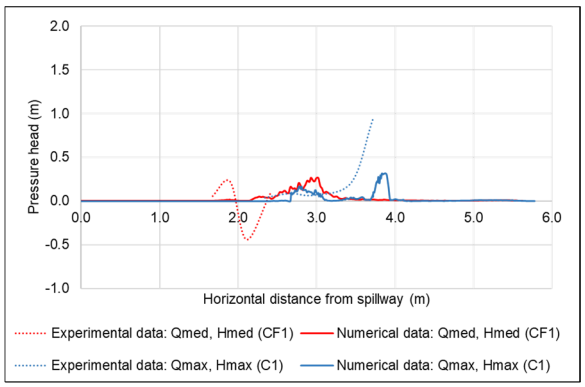

(b) Maximum tailwater level (M: 1.0 m, P: 20 m)

Figure 6.18: Comparison of simulated and observed centreline dynamic pressure head at pool bottom as model scale values

6.9.4. *Comparison of flow velocity*

Figure 6.19 depicts the velocity profiles located at the deepest point of the scour hole simulated by the proposed numerical model for the shallow and deep plunge pool depths. The horizontal velocities were made non-dimensional by using the maximum horizontal velocity, V_{max}, of each vertical cross-section. In general, the numerical model yields horizontal velocity profiles similar to that of a free-flow velocity profile close to the plunge pool bed.

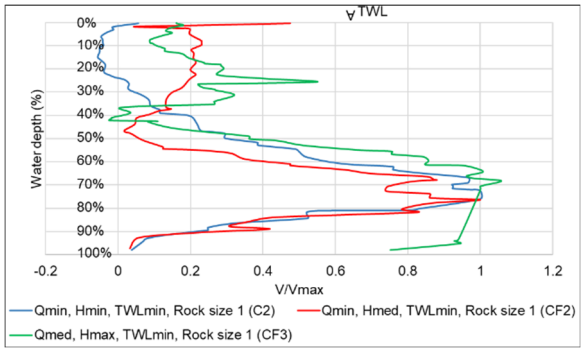

Velocity variation for shallow pool depth (M: 0.5 m, P: 10 m)

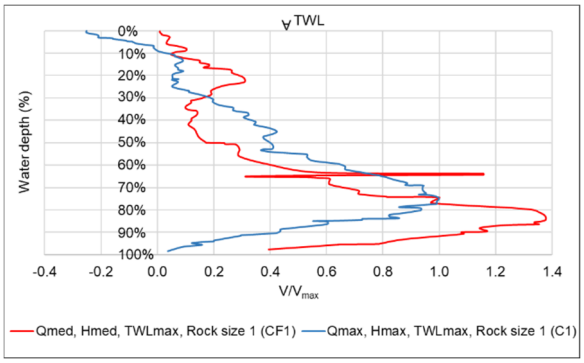

Velocity variation for deep pool depth (M: 1.0 m, P: 20 m)

Figure 6.19: Simulated horizontal flow velocity over flow depth

The horizontal flow velocity near the plunge pool bottom located at the jet centreline simulated by the numerical model and observed in the experimental tests is shown in Figure 6.20. The numerical simulation for Calibration Test 2 (Figure 6.20a) shows the same behaviour as the flow velocity values obtained in the experimental test. The discrepancy in the flow velocity

location between the numerical and experimental results is attributed to the difference in the jet trajectory and impingement point of the jet with the pool bottom as outlined in Figure 6.7.

A prominent dissimilarity in the simulated and observed horizontal flow velocity magnitudes of the wall jet flow located at the jet centreline for Confirmation Test 2 (Q_{min}, H_{med}, TWD_{min}) is indicated in Figure 6.20b. The numerical model yields horizontal flow velocity magnitudes that are distinctly over-predicted near the boundary surface. The behaviour could be attributed to laboratory measurements by the ADV taken at too shallow depths and not in the wall jet boundary region, due to the highly turbulent flow in the plunge pool that made visibility difficult and moving cobblestones that could damage the equipment.

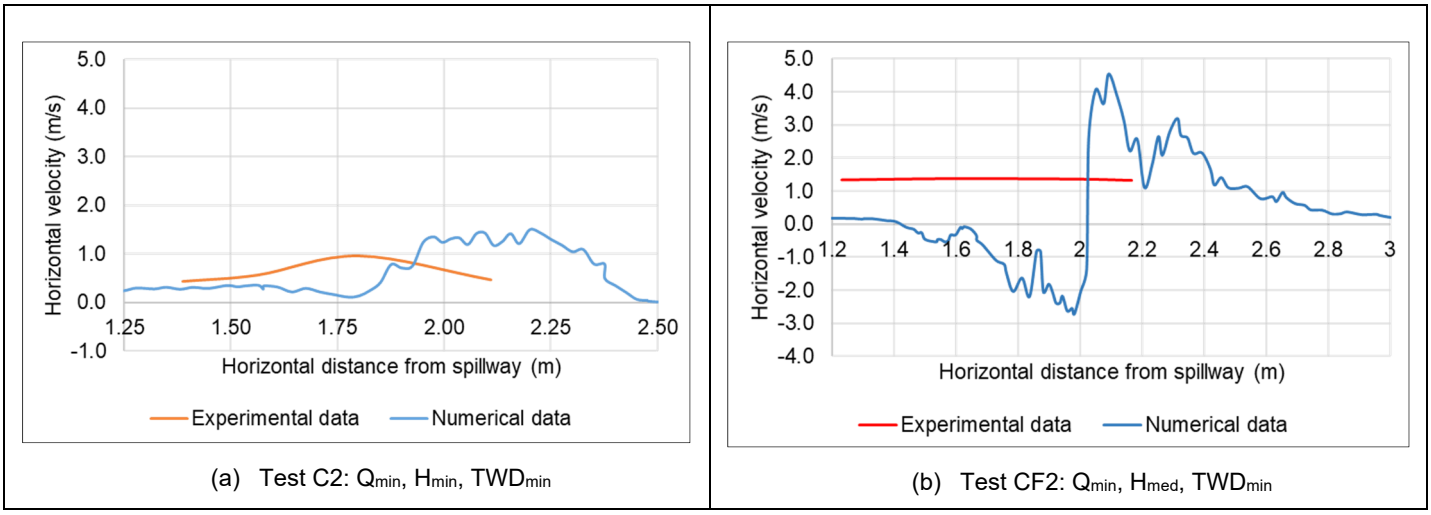

(a) Test C2: Q_{min}, H_{min}, TWD_{min}

(b) Test CF2: Q_{min}, H_{med}, TWD_{min}

Figure 6.20: Horizontal velocity near the pool bottom along the jet centreline at model scale

The simulated turbulent kinetic energy at different sections of the plunge pool is shown in Figure 6.21 for Calibration Test 2 (Q_{min}, H_{min}, TWD_{min}). The turbulent kinetic energy dissipates quickly as the flow moves further downstream from the impact zone (X = -1 m). The simulated results obtained by the numerical model emulates the evolution of the kinetic energy dissipation trends established by Castillo et al. (2018).

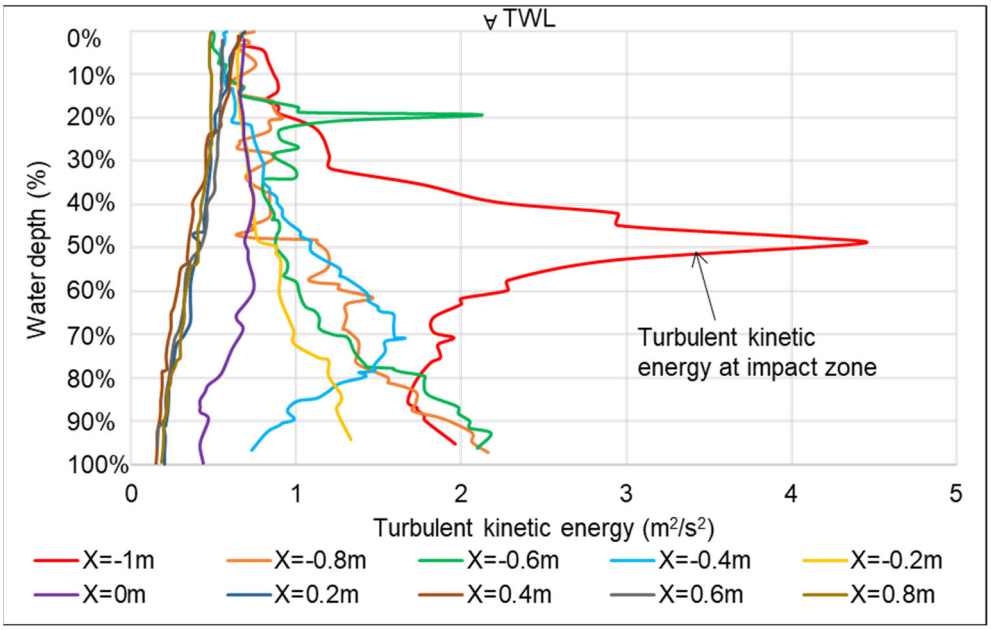

Figure 6.21: Simulated turbulent kinetic energy for different sections of the plunge pool at scale model for test C2 (Q_{min}, H_{min}, TWD_{min})

Figure 6.22 shows the comparison between the simulated and observed relative energy dissipation in the plunge pool and the impinging Froude number, $Fr_j = V_j/(gB_j)^{0.5}$, laid over the experimental data recorded by Castillo et al. (2018). The impingement Froude number of the current study is between 2.70 to 5.10 and 3.65 to 4.69 for the experimental test and numerical simulations respectively. The impingement Froude number for the experimental tests performed by Castillo et al. (2018) were between 13 to 20. The experimental results of all 31 physical model tests of the current study show energy dissipation values larger than 39% of the impingement jet energy for shallow pool depths and 42% for deeper pool depths determined with Equation 6.2. Whereas the numerical simulation results of the current study show energy dissipation values larger than 42% for shallow pool depths and 56% for greater pool depths for the Calibration and Confirmation tests. The relative energy dissipation results are in agreement with the literature that greater pool depths dissipate more of the energy of the plunging jet and damping the scour formation compared to shallow pool depths as discussed in Section 2.4.1. The relative energy data is summarised in Table G.3 in Annexure G.1.

The formula proposed to determine the relative energy dissipation in the plunge pool is as follows (Castillo et al., 2018):

$$\frac{H_L}{H_0} = \frac{2\left(\frac{y_w + y_s}{y_{down}} - \frac{y_w}{y_{down}}\right) + \left(1 - \frac{1}{(y_w/y_{down})^2}\right) Fr_0^2}{2([y_w + y_s]/y_{down}) + Fr_0^2} \qquad \textit{Equation 6.2}$$

with H_L the total energy dissipation (m), H_0 the energy of jet upstream of the submerged hydraulic jump that forms due to the impacting jet with the pool bottom (m), y_w the plunge pool depth (m), y_s the scour depth (m), y_{down} the contracted flow depth of the wall jet upstream of the submerged hydraulic jump (m), and Fr_0 the Froude number upstream of the submerged hydraulic jump, approximated as Fr_j in the current study.

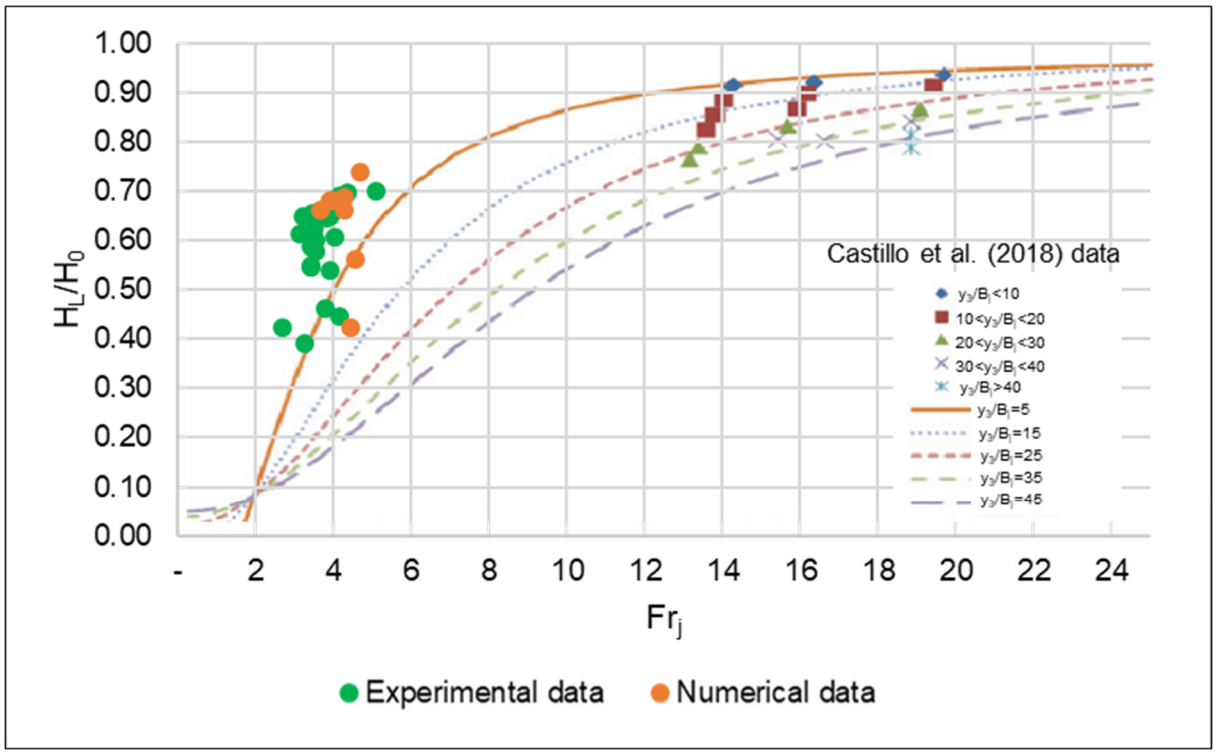

Figure 6.22: Relative energy dissipation simulated and observed in the plunge pool as a function of the Froude number at impingement with tailwater level at model scale

Figure 6.23 shows the relative energy dissipation in the plunge pool as a function of the ratio $(y_w + y_s)/B_j$ and are summaries in Table G.3 in Annexure G.1. The energy dissipation results for the seven numerical Calibration and Confirmation tests and all 31 physical model tests are laid over the experimental results obtained by Castillo et al. (2018). The simulated and observed energy dissipation results from the current study tend toward Castillo et al's. (2018) curve for Fr_j = 5, which corresponds to the impingement Froude number (Fr_j) for the current study. The energy dissipation in the plunge pool for the experiments performed by Castillo et al. (2018) was greater than 75% of the energy of the impinging jet. A possible reason for the lower energy dissipation results from the current study could be the lower impingement Froude numbers and shallower pool depths compared to the experiments performed by Castillo et al. (2018).

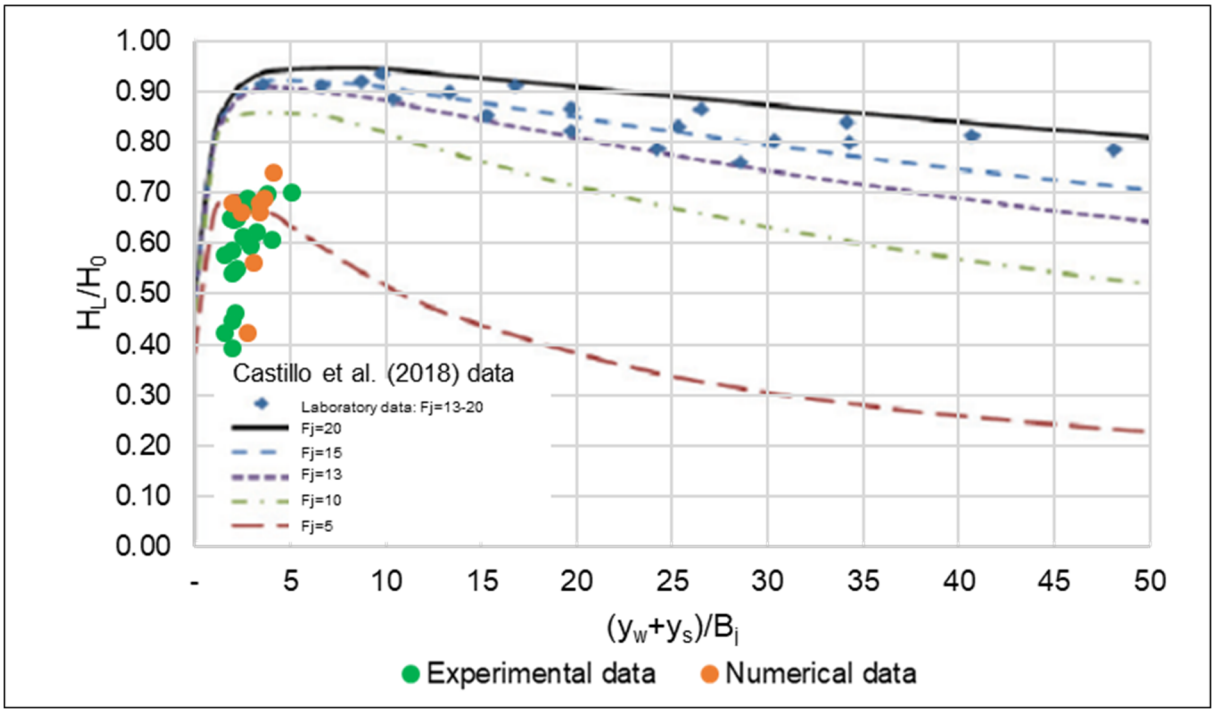

Figure 6.23: Relative energy dissipation simulated and observed in the plunge pool as a function of the ratio $(y_w + y_s)/B_j$ at impingement with tailwater level as model scale

6.10. Numerical model summary

The dynamic behaviour of rock scour due to a plunging jet was investigated using both experimental testing and numerical models. Data recorded from the physical model was used to calibrate the numerical model and to study tendencies beyond the physical model scope. Experimental test observations not used in the calibration process of the numerical model were used to visually validate the ability of the numerical model to simulate the hydrodynamics of the flow correctly.

The three-dimensional numerical model is capable of simulating the maximum scour depth and peak dynamic pressure head magnitudes from the physical model. However, some differences between the physical and numerical models remain, especially in the horizontal velocity of the wall jet region and scour hole length.

In general, the scour hole predicted by the numerical model is deeper, shorter and narrower compared to the experimental measurements. The disparity in the scour hole dimensions could be that the air entrainment of the jet in the air and plunge pool of the numerical model is less than in the physical model. In the numerical model the more compact jet simulated at the tailwater level and in the plunge pool creates a smaller jet footprint area on the plunge pool bottom that experiences fluctuating pressures and uplifting forces, which leads to a deeper, shorter and narrower scour hole.

The energy dissipation of the falling jet was greater than 54% for shallow pool depths and greater than 65% for the deeper pool depths for the physical model, compared to 42% and 56% simulated by the numerical model, respectively.

Regardless of the perceived limitation of the numerical model, it performs well in predicting the maximum scour depth compared to any of the rock scour prediction methods evaluated in Section 5.9.

7. CONCLUSIONS

7.1. Overview

A free falling jet from a high head dam requires significant energy dissipation to limit scouring of the foundations downstream of a dam. A scour hole will form in the plunge pool bed downstream of the dam if the energy dissipation of the jet is underestimated. A large scour hole downstream of a dam could endanger the foundation of the dam. Scouring of the plunge pool bottom downstream of the dam has been reported at several dam sites worldwide. The assessment of the equilibrium scour hole geometry is therefore important in the hydraulic design of high head dams to ensure that the foundations of the dam are not endangered by the scour hole during its lifetime.

An extensive literature review pertaining to rock scour downstream of a dam embankment due to a free falling jet showed that most studies on rock scour are based on semi-empirical formulas and physical model tests, although sophisticated computer models is available. The reason being because rock scour is a complex phenomenon, involving the interaction of different physical factors that are not easily modelled numerically.

The overall goal of researching rock scour downstream of dam spillways is to examine scientifically the cause of scouring, understand the regression of a scour hole and the prevention of scouring of a dam's foundations. The main purpose of this investigation was thus to contribute to the body of knowledge on the prediction of the equilibrium scour hole geometry downstream of high head dams.

The scope of the study did not allow for conducting an exhaustive assessment of the rock scour phenomena or provide a characterisation of all potential parameters affecting rock scour. The assessment of rock scour was limited to fully developed jets plunging into shallow plunge pools for different discharges, fall heights, rock block sizes and joint structure orientation that may be commonly found at prototypes.

Rock scour can be apportioned into two main parts, comprising hydrodynamic and geo-mechanical aspects. Both physical and numerical modelling were used to investigate both aspects, as well as any plausible interaction between them by collecting data and to make observations. The physical model was set up in the Hydraulics Laboratory of Stellenbosch University in order to investigate rock scouring due to a high-velocity impinging jet in a controlled environment. The proposed three-dimensional numerical model parameters were calibrated against the experimental results. The numerical model was used in an iterative manner with the scour depth regression formula (Equation 5.14) to manually calculate the

scour depths on a grid with post-processing. The experimental tests proved that a greater scour hole is obtained if the deposited rocks downstream of the scour hole are continuously removed (Case B) compared to Case A where the deposited rocks were not removed. Therefore, rock block movement for Case B was determined by means of the numerical model in order to reach the static scour limit (maximum equilibrium scour hole dimensions).

The numerical simulation results were satisfactory. The proposed three-dimensional numerical model developed in this study is capable of accurately simulating the scour hole depth, and to a lesser extent the scour length, width, and volume.

7.2. Findings

7.2.1. *Physical modelling of rock scour*

A three-dimensional physical model (based on Froude scale laws) of the high-velocity free falling jet, the plunge pool and the underlying bedrock with open-ended joints was constructed. A model scale not exceeding 1:20 is recommended for the experimental results from this study to limit scale effects. The free falling jets were modelled with a rectangular horizontal issuance canal, replicating an uncontrolled spillway. The broken-up bedrock mass was modelled by using tightly hand-packed concrete paver blocks (cobblestones) emulating a uniform three-dimensional open-ended horizontal and vertical rock joint network. The plunging jets generated correct aeration in the plunge pool and realistic dynamic pressures at the pool bottom.

The constructed scaled physical model was used to observe the rock scour under a range of conditions and to collect pressure and velocity data at the plunge pool bottom. Rock scour due to a high-velocity free falling jet was successfully modelled by 31 laboratory tests. Repeatability was tested by repeating 10% of the tests and the maximum percentage repeatability error was quantified as 15% for the scour depth.

The experimental results showed that the shape of the scour hole is highly dependent on the discharge and plunge pool depth, as well as the rock size. The scour hole volume increases as the discharge increases, the plunge pool depth decreases, and the rock block size decreases. The experimental results also indicated that a much greater scour hole would occur if the deposited rocks downstream of the scour hole are removed by floodwaters.

Rock scour due to a plunging jet is not a shear process, but is initiated by turbulent and fluctuating pressures at the pool bottom (Annandale, 2006). In this study, the strength of the dynamic pressures at the pool bottom increased with an increase in the discharge, resulting in an increase in the scour hole volume.

No unique relationship could be established between the fall height and the dynamic pressures experienced at the pool bottom, as well as with the scour hole geometries. The dynamic pressure results substantiate this conclusion that for fully developed jets the fall height becomes less dominant in the scour process, since the mean and fluctuating dynamic pressure coefficients become very low as proved by Castillo et al. (2015).

The dynamic pressures experienced at the pool bottom decrease with an increase in pool depth. The observed dynamic pressure results showed that the plunge pool acts as a water cushion and lessens the scour process. Greater diffusion of the jet occurs in a deep plunge pool in comparison to a shallow plunge pool, thus reducing the pressures experienced at the pool bottom.

The scour analysis proved that rock is more conducive to scour failure when the horizontal rock joint is dipped in the direction of the flow. The scour results for the different rock joint structure orientations were similar to that of the case study of the Ricobayo Dam in Spain (Annandale, 2006).

7.2.2. *Regression analysis*

The experimental test results were used to develop non-dimensional regression formulae to predict the scour hole geometry (scour depth, length, width, and volume). The prototype ranges in which the regression formulae were developed are as follows:

- Discharge: 35 $m^3/s/m$ – 80 $m^3/s/m$
- Fall height: 60 m – 100 m
- Tailwater depth: 10 m – 20 m
- Joint orientation angle: horizontal and vertical (0°), 45º and 135º

The parameters describing the scour hole geometry were determined using ordinary least squares regressions, with due consideration given to the parsimony principle. The parameters were made dimensionless by applying the Buckingham π-theorem.

The main parameters influencing the hydrodynamics of the jet and rock scour that were incorporated in the regression analysis were selected based on literature and experimental tests. Some of the main parameters incorporated into the regression analysis were discharge, fall height, pool depth, rock size, stream power, submerged weight of the rock block, and uplift pressures and forces.

Since rock scour is not a shear process, but is caused by turbulent and fluctuating pressures at the pool bottom, the regression analysis did not explicitly incorporate the bed shear stress.

Rather, the regression analysis of rock scour made use of the movability number based on the settling velocity of the rock, and the particle Reynolds number, thus incorporating the shear velocity the rocks experience due to the falling jet. The minimum movability number of 0.176 determined for the experimental tests is similar to the minimum movability number of 0.12 recommended by Rooseboom (1992).

Stabilising (or destabilising) factors were derived for joint structure orientations that are orientated 45° in and against the flow direction. The proposed regression formulae were confirmed inside the ranges in which the formulae were developed and agree reasonably well with the experimental data on which they are based.

7.2.3. *Comparison to scour prediction methods found in literature*

The scour depth results from the physical model were evaluated against twelve of the better-known empirical formulae, the EIM, the Critical Pressure method, the DI and QSI methods traditionally employed to predict rock scour due to a free falling jet for a full-scale prototype. The scour prediction methods were found not to agree with each other well, yielding a wide range of varying scour depths for the same input conditions. The mean percentage difference between the scour prediction methods and observed scour depth was 240% for Case A (scour and deposition) and 108% for Case B (scour with deposited rocks removed continuously during test). No single scour prediction method is conclusively superior, however the Critical Pressure method (Annandale, 2006), followed by the EIM (Annandale, 2006) method and Mason and Arumugam's (1985) empirical formula are recommended.

The Critical Pressure method agreed the best with the experimental results from this study with the a mean percentage difference of 1%, presumably because this method relies on the critical pressures at the pool bottom that initiates rock scour due to an impinging jet. This finding corresponds with the literature that rock scouring is caused by turbulent pressure fluctuations and not shear processes (Annandale, 2006). The critical pressure may be considered the main parameter affecting rock scour and is directly dependent on the submerged weight of the rock block, block size, uplift pressures inside the joints, diffusion of the jet through the air and plunge pool, the impinging velocity of the jet and air entrainment over the fall height.

The EIM method (Annandale, 2006), followed by Mason and Arumugam's (1985) empirical formula were more conservative in predicting the rock scour compared to the regression formula developed in this study.

The developed regression formula to predict the scour depth (95% confidence) agreed well with the experimental results. The developed regression formula had the least total SSR and lowest mean percentage difference of 0.5% compared to the other scour prediction methods, which is acceptable compared to the physical model test repeatability error of 15%.

Despite extensive research done over the last seven decades on rock scour by a plunging jet, very few studies have involved detailed three-dimensional numerical modelling of rock scour processes. Even though regression formulae are proposed to determine the scour hole geometry (depth, length, width, and volume), numerical modelling could possibly overcome any shortcomings associated with the empirical formulae and experimental work. Therefore, numerical modelling of rock scour should be the primary subject of further studies.

7.2.4. *Numerical modelling of rock scouring*

The hydrodynamics of the flow could be determined in a much greater level of detail in the numerical model than in the physical model. The hydrodynamics were modelled by selecting the Reynolds Averaged Navier-Stokes (RANS) methodology in conjunction with the SST $k-\omega$ turbulence model.

The scaled physical model results were used to calibrate the transient, three-dimensional, multi-phase numerical model. The following improvements to the numerical model set up were done to achieve a more accurate and numerically stable solution:

- A fine computation mesh size (0.0625 m to 0.1 m) was required to resolve the turbulent and fluctuating pressures on the pool bottom that are crucial for scour development. Mesh independency was also established.
- The surface roughness parameters for the plunge pool bottom were calibrated using the 1% exceedance dynamic pressures at the pool bed surface, and the 1% exceedance velocity magnitude of the wall jet (50 mm above the water-rock interface). The calibration results showed that a roughness constant of C_s = 0.8 should be used for simulating a plunge pool bottom surface, which corresponds to a non-uniform bed. The surface roughness parameter (K_s) was determined through the calibration process to be approximately 0.2 m for the 0.1 m x 0.1 m x 0.05 m rock block, and 0.4 m for the 0.1 m x 0.1 m x 0.075 m rock block, with the calibrated surface roughness to rock block height ratio (K_s/z_b) being 4 and 5.3, respectively.
- In order to replicate the dynamic pressures at the pool bottom, and therefore the rock scour, the flow at the inlet boundary should be initialised as accurately as possible. Thus, a fully developed velocity profile that takes the friction effects of the spillway

sides into account, should be defined at the inflow boundary, compared to a constant inflow velocity.

The scour depth regression formula for Case B (deposited rocks removed continuously – Equation 5.14) made it possible to relate the impacting jet's hydrodynamic loading and velocity to the resistance and movement of the rock under the impacting jet. The FLUENT model was initially set up with a flat bed. The numerical data was collected in a grid fashion. The scour depth regression formula was solved for each grid point, determining the irregular shape of the scour hole. The numerical simulation was repeated with the calculated scour hole shape. The iterations ceased when a reasonable percentage difference was found between the new and previous scour hole shape.

The capability of the proposed three-dimensional numerical model was evaluated and compared against the experimental data. The scour contours and profiles of the simulated and experimental tests are not identical, but agree well in terms of the maximum scour depth and width, however less accurately in terms of the length and volume.

The proposed numerical model, in conjunction with the regression formula (Equation 5.14), is considered safe for predicting the maximum scour depth due to a high-velocity free falling, fully developed jet that is inside the ranges in which the regression formula was developed. The reason is because if the numerical model fails to be accurate, it predominantly over-predicts the maximum scour depth with a mean percentage difference of 11% compared to the observed data.

The numerical model under-predicted the scour hole width for Case B (scour with deposited rocks removed continuously during test) with a mean percentage difference of -13% compared to the observed data. The length (in the flow direction) and volume of the scour hole were poorly predicted for Case B. The simulated scour length and volume were under-predicted with a mean percentage difference of -33% and -55% respectively in comparison to the experimental measurements.

In general, a deeper, shorter and narrower scour hole was predicted with the numerical model and the regression scour depth formula (Equation 5.14) compared to the experimental measurements for Case B (scour with deposited rocks removed continuously). The disparity in the scour hole dimensions could be due to the diffusion of the jet through the air and the plunge pool being less than in the physical model, with the simulated jet being more compact at impingement with the plunge pool water surface and bottom. Due to the more compact jet, a smaller area on the plunge pool bottom experiences dynamic pressures and uplifting forces,

leading to a deeper, shorter and narrower scour hole being calculated by the numerical model and regression scour depth formula. In order to support this statement, test CF1 was also simulated for Case A, since the jet outspread for test CF1 is similar to the jet outspread of the physical model. The scour hole depth, length and width for test CF1 for Case A agree with the experimental measurements well, validating the use the scour depth regression formulae developed (Equation 5.13 for Case A and Equation 5.14 for Case B) with the proposed numerical model, if the spreading (diffusion) of the plunging jet is simulated accurately.

The simulated dynamic pressure peaks at the rock-water interface also agree well with the dynamic pressures measured in the physical model. Thus, the numerical model is representative for model pressures in open-ended joints.

Compared to the scour prediction methods found in literature, the proposed numerical model performs well in predicting the equilibrium scour depth for Case B for a 1:20 prototype scale. Despite the limitations of the proposed numerical model, the simulated results demonstrate that numerical models are able to capture different parameters, discover hydrodynamic trends and explore factors that affect the scouring process.

7.3. Contributions to engineering science

The main aim of the study was to contribute to the body of knowledge on the phenomena of rock scour due to a high-velocity impinging jet, concerning the cause and extent of the scouring. Specific contributions toward the hydraulic design of high head spillways that are novel to science made by the research for fully developed rectangular nappe jets and shallow plunge pool depths ($Y/D_j < 5.5$) include:

- The physical model results indicated that a much greater scour hole is formed if the deposited rocks downstream of the scour hole are removed by floodwaters.
- The influence on the pressure characteristics at the water-rock interface by the highly irregular shape of the pool bottom was accounted for by using a movable bed with open-ended joints. The rock mass consisting of multiple blocks represents the bedrock of a real case scenario better compared to a fixed bed.
- A complex joint structure was investigated where several joints were interconnected with one another. Joint structures with tilted beds were also investigated.
- The turbulence of the jet at impingement defines the turbulent characteristics of the pressures experienced at the water-rock interface. In turn, the turbulence of the jet depends on the jet trajectory through the air and the jet's stability characteristics. Low-frequency turbulent jets would generate higher turbulent intensities and pressure

fluctuations at the water-rock interface. The research studied the scour hole geometry formed by a low-frequency turbulent jet issued from a horizontal canal, compared to previous studies that used circular jets discharged from a nozzle.

- The equilibrium scour hole geometry was simulated by using a three-dimensional, multi-phase, transient numerical model.
- The proposed numerical model can predict the scour hole depth, length, width and volume, whereas most previous scour prediction methods are only able to predict the maximum scour depth.

7.4. Further research

The conducted research on rock scour due to a high-velocity plunging jet can be improved to contribute on aspects not explored in this study. The additional recommended improvements are:

- Additional experimental testing is required to establish whether linear interpolation could be used between the derived stabilising factors derived in this study for different degrees of joint structures between 0º and 45º in and against the flow direction. Further testing is also required to determine the influence joint structure orientations greater than 45° have on the pool bottom pressures and scour process.
- Physical modelling was only conducted on a U-shaped rock joint, which is the simplest possible joint geometry. Further research is required on more complex joint geometries.
- Future physical model studies should use ADV equipment capable of measuring the flow velocity in pool depths greater than 0.9 m. The ADV equipment should also be capable of measuring the flow velocity at multiple elevations simultaneously to obtain a vertical velocity profile at different points in the plunge pool.
- Additional experimental testing is required for plunging jets with various breakup length ratios (L_j/L_b), tending towards less than one, and for deep plunge pools ($Y/D_j > 6$).
- The influence the turbulence intensity of the plunging jet has on the pool bottom pressures and scour process should be quantified. Also, the dissipation of the jet turbulence along the pool depth should be quantified.
- The capability of the proposed numerical model to simulate rock scour should be compared with the performance of other numerical models, such as Rocky and FLOW-3D.
- Further studies should investigate the possibility of developing a fully coupled three-dimensional numerical model that models the rock scour and deposition over time by means of a movable bed. The standard FLUENT code should be used to solve the

hydrodynamic aspects of the plunging jet as in the current study. However, the immersed boundary method should be used to simulate the surface deformation of the bedrock. User Defined Function (UDF) is a special design feature of FLUENT that allows the user to define their own code to specify customised parameters. Thus, the developed scour regression formula from this research could be defined as a UDF, operating as the rock scour sub-model. The deformation of the bedrock would therefore be calculated automatically.

- By defining a UDF rock scour sub-model to simulate the deformation of the bed surface for the proposed numerical model, an additional improvement can be made by modifying the rock scour sub-model to be able to simulate different rock block sizes at the same time, as well as various joint structure orientations to progressively approach a real case scenario.
- Further studies are recommended to investigate performance of the proposed numerical model using multiple spillways simultaneously.
- The SST $k-\omega$ turbulence model used in this research assumes the turbulence creation and dissipation to be the same in all directions, whereas the RSM model can assume different turbulence for different directions. Future studies should investigate whether using the RSM turbulence model would increase the diffusion of the simulated jet through the air and plunge pool to predict the scour hole extent more accurately.

7.5. Closing comments

The findings from this research showed that numerical modelling is capable of predicting the dynamic pressures at the water-rock interface due to a high-velocity free falling jet. The proposed three-dimensional numerical model in conjunction with the scour depth regression formula developed in this study, is capable of simulating the scour hole geometry if the diffusion of the falling jet through the air and plunge pool is modelled accurately.

8. REFERENCES

Albrecht, MC., Nachtsheim, CJ., Albrecht, TA., & Cook, RD. (2013). Experimental Design for Engineering Dimensional Analysis. *Technometrics, 55(3)*, 257-270. DOI: 10.1080/00401706.2012.746207.

Alias, NA., Mohamed, TA., Ghazali, AH., & Mohd, MJM. (2008). Impact of Takeoff Angle of Bucket Type Energy Dissipater on Scour Hole. *American Journal of Applied Sciences, 5(2)*, 117-121.

Annandale, GW. (1995). Erodibility. *Journal of Hydraulic Research, 33(4)*, 471-494. DOI: 10.1080/00221689509498656.

Annandale, GW. (2006). *Scour Technology: Mechanics and Engineering Practice.* New York: McGraw-Hill Companies.

Annandale, GW. (2010). Wall Jet Scour in Rock. *International Conference on Scour and Erosion* (pp. 715-723. DOI: 10.1061/41147(392)70). San Francisco, United States: American Society of Civil Engineers.

Annandale, GW., & George, MF. (2011). Closure problem to jet scour. *Journal of Hydraulic Research, 49(2), DOI: 1080/00221686.2011.568205*, 276-277.

Annandale, GW., Smith, SP., Nairns, R., & Jones, JS. (1996). Scour Power. *Civil Engineering, 66(7)*, 58-60.

ANSYS, I. (2015). *ANSYS FLUENT Theory Guide Release 16.* Canonsburg, PA: ANSYS, Inc.

Armitage, N., & Rooseboom, A. (2010). The link between Movability Number and Incipient Motion in river sediments. *Water SA, 36(1)*, 89-96.

Asadollahi, P., & Tonon, F. (2010). Stability of rock blocks subjected to high-velocity water jet impact. *44th US Rock Mechanics Symposium and 5th US-Canada Rock Mechanics Symposium.* Salt Lake City: American Rock Mechanics Association.

Asadollahi, P., Tonon, F., Federspiel, MPEA., & Schleiss, AJ. (2011). Prediction of rock block stability and scour depth in plunge pools. *Journal of Hydraulic Research, 49(6)*, 750-756. DOI: 10.1080/00221686.2011.618055.

Avila, H., & Pitt, R. (2008). The Calibration and use of CFD Models to Examine Scour from Stormwater Treatment Devices – Hydrodynamic Analysis. *11th International Conference on Urban Drainage*, (pp. 1-10). Edinburgh, Scotland, UK.

Azamathulla, HM., Ghani, AA., & Zakaria, NA. (2009). ANFIS-based approach to predicting scour location of spillway. *Water Management, 162(6)*, 399-407.

Bastier, E. (Director). (2018). *A technical challenge realized by Razel-Bec on the Kariba Dam of Zambesi* [Motion Picture].

Biń, AK. (1984). Air entrainment by plunging liquid jets. *Symposium on Scale Effects in Modeling Hydraulic Structures* (pp. 1-6). Esslingen, 3-6 September, Paper 5.5: IAHR.

Bohrer, JG., Abt, SR., & Wittler, RJ. (1998). Predicting Plunge Pool Velocity Decay of Free Falling, Rectangular Jet. *Journal of Hydraulic Engineering, 124(10)*, 1043-1048. DOI: 10.1061/(ASCE)0733-9429(1998)124:10(1043) .

Bollaert, E. (2002). *Transient water pressures in joints and formation of rock scour due to high-velocity jet impact.* Lausanne, Switzerland: PhD Thesis, Ecole Polytechnique Fédérale de Lausanne (EPFL).

Bollaert, E. (2004). A comprehensive model to evaluate scour formation in plunge pools. *International Journal on Hydropower and Dams, 11(1)*, 94-101.

Bollaert, E. (2005). The influence of geomechanic and hydrologic uncertainties on scour at large dams: Case study of Kariba Dam (Zambia-Zimbabwe). *73rd Annual Meeting of ICOLD. 1-6 May.* Tehran, Iran: CIGB, ICOLD.

Bollaert, EFR. (2010a). A prototype scaled rock scour prediction model. *USSD Conference*, (pp. 1269-1283). Sacramento.

Bollaert, EFR. (2010b). Rock scour at hydraulic structures: a practical engineering approach. *Geo-Strata, July-August*.

Bollaert, EFR. (2010c). The Comprehensive Scour Model: Theory and Feedback from Practice. *5th International Conference on Scour and Erosion.* San Francisco.

Bollaert, EFR. (2011). Penstock Scour Formation at Bluestone Dam. 21st Century Dam Design - Advances and Adaptions. *31st Annual United States Society on Dams Conference* (pp. 325-338). San Diego, California: U.S. Society on Dams.

Bollaert, EFR. (2012). Wall jet rock scour in plunge pools: a quasi-3D prediction model. *International Journal on Hydropower & Dams*, 1-9.

Bollaert, EFR., & Hofland, B. (2004). The influence of flow turbulence on particle movement due to jet impingement. *2nd International Conference on Scour and Erosion.* Singapore.

Bollaert, EFR., & Lesleighter, EJ. (2014). Spillway Rock Scour Experience and Analysis - the Australian Scene over the past Four Decades. *11th National Conference on Hydraulics in Civil Engineering & 5th International Symposium on Hydraulic Structures: Hydraulic Structures and Society - Engineering Challenges and Extremes*, (p. 189). Brisbane, Australia.

Bollaert, E., & Schleiss, A. (2001). A new approach for better assessment of rock scouring due to high velocity jets at dam spillways. *ICOLD European Symposium.* Geiranger, Norway, 25-27 June.

Bollaert, E., & Schleiss, A. (2003a). Scour of rock due to the impact of plunging high velocity jets Part I: A state-of-the-art review. *Journal of Hydraulic Research, 41(5)*, 451-464.

Bollaert, E., & Schleiss, A. (2003b). Scour of rock due to the impact of plunging high velocity jets Part II: Experimental results of dynamic pressures at pool bottoms and in one- and two-dimensional closed end rock joints. *Journal of Hydraulic Research, 41(5)*, 465-480.

Bollaert, EFR., & Schleiss, AJ. (2005). Physically based model for evaluation of rock scour due to high-velocity jet impact. *Journal of Hydraulic Engineering, 131(3)*, 153-165. DOI: 10.1061/(ASCE)0733-9429(2005)131:3(153).

Bollaert, EFR., Duarte, R., Pfister, M., Schleiss, A., & Mazvidza, D. (2012a). Physical and numerical model study investigating plunge pool scour at Kariba Dam. *24th Congress of CIGB-ICOLD*, (pp. 241-248). Kyoto, Japan.

Bollaert, EFR., Manso, PA., & Schleiss, AJ. (2004). Dynamic pressure fluctuations at real-life plunge pool bottoms. *International Conference on Hydraulics of Dams and River Structures* (pp. 117-124). Tehran, Iran: A.A. Balkema Publishers.

Bollaert, EFR., Munodawafa, MC., & Mazvidza, DZ. (2012b). Kariba Dam Plunge Pool Scour: quasi-3D Numerical Predictions. *6th International Conference on Scour and Erosion*, (pp. 627-634). Paris.

Bollaert, EFR., Stratford, CS., & Lesleighter, EJ. (2015). Numerical modelling of rock scour: Case study of Wivenhoe Dam (Australia). *7th International Conference on Scour and Erosion* (pp. 397-404). Perth, Australia: CRC Press. DOI: 978-1-138-02732-9.

Borghei, SM., & Zarnani, P. (2008). Jet impact geometry and plunge pool dimensions effects on dynamic pressures at pool sidewalls. *Canadian Journal of Civil Engineering, 35(4)*, 408-417. DOI: 10.1139/L07-141.

Boroomand, MR., Salehi Neyshabouri, SAA., & Aghajanloo, K. (2007). Numerical simulation of sediment transport and scouring by an offset jet. *Canadian Journal of Civil Engineering, 34(10)*, 1267-1275.

Boushaba, F., Manso, P., Schleiss, AJ., Yachouti, A., & Daoudi, S. (2013). Numerical and Experimental High-Reynolds Jet Diffusion and Impact Pressures in Flat and Laterally Confined Aerated Pools. *International Journal of Hydraulic Engineering, 2(6)*, 133-141.

Calitz, JA. (2015). *Investigation of air concentration and pressures of a stepped spillway equipped with a crest pier.* Master's Thesis, Stellenbosch, South Africa: Stellenbosch University.

Castillo, LG. (2007). Pressures characterization of undeveloped and developed jets in shallow and deep pool. *Congress-International Association of Hydraulic Engineering and Research, 32(2)*, (p. 645). Venice, Italy.

Castillo, LG., & Carrillo, JM. (2014). Scour analysis downstream of Paute-Cardenillo Dam. *3rd IAHR Europe Congress*, (pp. 1-10). Porto-Portugal.

Castillo, LG., & Carrillo, JM. (2016). Scour, velocities and pressures evaluations produced by spillway and outlets of dam. *Water, 8(3)*, 68. DOI: 10.3390/w8030068.

Castillo, LG., & Carrillo, JM. (2017). Comparison of methods to estimate the scour downstream of a ski jump. *International Journal of Multiphase Flow, 92*, 171-180. DOI: 10.1016/j.ijmultiphaseflow.2017.03.006.

Castillo, LG., Carillo, JM., & Blàzquez, A. (2015). Plunge pool dynamic pressures: a temporal analysis in the nappe flow case. *Journal of Hydraulic Research, 53(1)*, 101-118. DOI: 10.1080/00221686.2014.968226.

Castillo, LG., Carrillo, JM., & Marco, F. (2018). Advances in the characterization of pressures and velocities in the overtopping of arch and gravity dams. *3rd International Conference on Protection against Overtopping (6-8 June)*, (pp. 1-9). United Kingdom.

Chadwick, A., Morfett, J., & Borthwick, M. (2013). *Hydraulics in civil and environmental engineering.* CRC PRess.

Chanel, PG., & Doering, JC. (2007). An Evaluation of Computational Fluid Dynamics for Spillway Modelling. *16th Australasian Fluid Mechanics Conference*, (pp. 1201-1206). Gold Coast, Australia.

Chanson, H., & Carosi, G. (2007). Advanced post-processing and correlation analyses in high-velocity air-water flows. *Environ Fluid Mech, 7(6)*, 495-508. DOI: 10.1007/s10652-007-9038-3.

Dasgupta, B., Basu, D., Das, K., & Green, R. (2011). Development of computational methodology to assess erosion damage in dam spillways. *31st Annual United States Society on Dam Conference*, (pp. 11-15). San Diego, CA, April 11-15.

De Padova, D., Mossa, M., Sibilla, S., & Toriti, E. (2013). 3D SPH modelling of hydraulic jump in a very large channel. *Journal of Hydraulic Research, 51(2)*, 158-173. DOI: 10.1080/00221686.2012.736883.

Delport, K. (2019). *Incipient motion of Armorflex articulating concrete blocks on steep slopes, Master's thesis.* Stellenbosch: Stellenbosch University.

Dey, D., & Eldho, TI. (2009). Effect of spacing of two offset jets on scouring phenomena. *Journal of Hydraulic Research, 47(1)*, 82-89. DOI: 10.3826/jhr.2009.3044.

Duarte, R. (2014). *Influence of air entrainment on rock scour development and block stability in plunge pools.* Lausanne, Switzerland: PhD Thesis, EPFL.

Epely-Chauvin, G., De Cesare, G., & Schwindt, S. (2014). Numerical Modelling of Plunge Pool Scour Evolution in Non-Cohesive Sediments. *Engineering Applications of Computational Fluid Mechanics, 8(4)*, 447-487. DOI: 10.1080/19942060.2014.11083301.

Ervine, DA. (1976). The entrainment of air in water. *Water Power and Dam Construction, 28(12)*, 27-30.

Ervine, DA. (1998). Air entrainment in hydraulic structures: A review. *Proceedings of the Institution of Civil Engineers - Water Maritime and Energy, 130(3)* (pp. 142-153). ICE.

Ervine, DA., & Falvey, HT. (1987). Behaviour of turbulent water jets in the atmosphere and in plunge pools. *Proceedings of the Institution of Civil Engineers, 83(1)*, (pp. 295-314).

Ervine, DA., Falvey, HT., & Withers, W. (1997). Pressure fluctuations on plunge pool floors. *Journal of Hydraulic Research, 35(2)*, 257-279. DOI:10.1080/00221689709498430.

Federspiel, MPEA. (2011). *Response of an embedded block impacted by high-velocity jets.* Lausanne, Switzerland: PhD Thesis, Ecole Polytechnique Fédérale de Lausanne (EPFL).

Ferrari, A. (2010). SPH simulation of free surface flow over a sharp-crested weir. *Advances in Water Resources, 33(3)*, 270-276.

George, MF. (2015). *3D Block erodibility: Dynamics of rock-water interaction in rock scour.* Berkeley: PhD Thesis, University of California.

Ghodsian, M., Faradonbeh, AA., & Abbasi, AA. (1999). Scour downstream of free overfall spillway. *28th IAHR Conference.* Iran: Tarbiat Modarres University.

Ghodsian, M., Mehraein, M., & Ranjbar, H. (2012). Local scour due to free fall jets in non-uniform sediment. *Scientia Iranica, 19(6)*, 1437-1444. DOI: 10.1016/j.scient.2012.10.008.

Guven, A. (2011). A multi-output descriptive neural network for estimation of scour geometry downstream from hydraulic structures. *Advances in Engineering Software, 42(3)*, 85-93. DOI: 10.1016/j.advengsoft.2010.12.005.

Häusler, E. (1983). Spillways and outlets with high energy concentration. *International Symposium on the lay-out of dams in narrow gorges* (pp. 77-194). ICOLD.

Heller, V. (2011). Scale effects in physical hydraulic engineering models. *Journal of Hydraulic Research, 49(3)*, 293-306. DOI: 10.1080/00221686.2011.578914.

Heng, S., Tingsanchali, T., & Suetsugi, T. (2012). Analysis of plunge pool scour hole formation below a chute spillway with flip bucket using a physical model. *ASEAN Engineering Journal*, 88-101.

Hickin, EJ. (2004). Chapter 6: Sediment Transport. In *River hydraulics and channel form.*

Hoffmans, GJCM. (1998). Jet scour in equilibrium phase. *Journal of Hydraulic Engineering, 124(4)*, 430-437.

Horeni, P. (1956). Disintegration of a free jet of water in air. *Byzkumny ustav vodohospodarsky prace a studie, Sesit 93*.

Kabiri-Samani, AR., & Borghei, SM. (2013). Effects of anti-vortex plates on air entrainment by free vortex. *Scientia Iranica, 20(2)*, 251-258. DOI: 10.1016/j.scient.2012.10.041.

Kamanbedast, AA., & Aghamajidi, R. (2013). Cup Ski Jump Length of the Spillway Using FLOW3D Mathematical Model (Case Study: Gotvand Dam). *Technical Journal of Engineering and Applied Sciences, 3(23)*, 3399-34040.

Karim, OA., & Ali, KHM. (2000). Prediction of flow patterns in local scour holes caused by turbulent water jets. *Journal of Hydraulic Research, 38(4)*, 279-287. DOI: 10.1080/00221680009498327.

Kerman-Nejad, J., Fathi-Moghadam, M., Lashkarara, B., & Haghighipour, S. (2011). Dynamic pressures of flip bucket jets. *World Applied Sciences Journal, 12(8)*, 1165-1171.

Khatsuria, RM. (2004). Ogee or overflow spillway. In *Hydraulics of spillways and energy dissipators* (pp. 41-62). Boca Raton: CRC Press.

Kieffer, DS., & Goodman, RE. (2012). Assessing scour potential of unlined rock spillways with the Block Scour Spectrum. *Geomechanics and Tunnelling, 5(5)*, 527-536. DOI: 10.1002/geot.201200039.

Kirsten, HAD. (1982). A classification system for excavation in natural materials. *The Civil Engineering in South Africa, 24(7)*, 293-308.

Lewis, TM., Abt, SR., Wittler, FRJ., & Annandale, GW. (1999). Predicting Impact Velocities of Developed Jets. *Water International, 24(3)*, 255-265. DOI: 10.1080/02508069908692169.

Liu, PQ., Dong, JR., & Yu, C. (1998). Experimental investigation of fluctuation uplift on rock blocks at the bottom of the scour pool downstream of Three-Gorges spillway. *Journal of Hydraulic Research, 36(1)*, 55-68. DOI: 10.1080/00221689809498377.

Maleki, S., & Fiorotto, V. (2019). Block Stability in Plunge Pools under Turbulent Rectangular Jets. *Journal of Hydraulic Engineering, 145(4)*, 04019007.1 - 04019007.13. DOI: 10.1061/(ASCE)HY.1943-7900.0001573.

Manso, PFA. (2006). *The influence of pool geometry and induced flow patterns in rock scour by high-velocity plunging jets.* Lausanne, Switzerland: PhD Thesis: Ecole Polytechnique Fédérale de Lausanne (EPFL).

Manso, PFA., Bollaert, EFR., & Schleiss, AJ. (2008). Evaluation of high-velocity plunging jet-issuing characteristics as a basis for plunge pool analysis. *Journal of Hydraulic Research, 46(2)*, 147-157. DOI: 10.1080/00221686.2008.9521852.

Manso, PA., Bollaert, EFR., & Schleiss, AJ. (2009). Influence of plunge pool geometry on high-velocity jet impact pressures and pressure propagation inside fissured rock media. *Journal of Hydraulic Engineering, 135(10)*, 783-792.

Manso, PA., Fiorotto, V., Bollaert, E., & Schleiss, AJ. (2003). Discussion of "Effect of Jet Air Content on Plunge Pool Scour" by Stefano Canepa and Willi H. Hager. *Journal of Hydraulic Engineering, 129(5)*, 358-365. DOI: 10.1061/(ASCE)0733–9429(2003)129:5(358).

Mason, PJ. (1989). Effects of air entrainment on plunge pool scour. *Journal of hydraulic Engineering, 115(3)*, 385-399. DOI: 10.1061/(ASCE)0733-9429(1989)115:3(385).

Mason, PJ., & Arumugam, K. (1985). Free jet scour below dams and flip buckets. *Journal of Hydraulic Engineering, 111(2)*, 220-235. DOI: 10.1061/(ASCE)0733-9429(1985)111:2(220).

Melo, JF. (2002). Reduction of plunge pool floor dynamic pressures due to jet air entrainment. *Rock Scour, AJ Schleiss and E Bollaert Editors*, 125-136.

Menter, FR. (1994). Two-equation eddy-viscosity turbulence models for engineering applications. *AIAA Journal Volume, 32(8)*, 1598-1605. DOI: 10.2514/3.12149.

Mirtskhoulava, TE. (1991). Scouring by flowing water of cohesive and noncohesive beds. *Journal of Hydraulic Research, 29(3)*, 341-354.

Mok, CMW., Aw, E., Wright, R., & Cooley, J. (2014). Probabilistic Dam Erosion Risk Evaluation. *Vulnerability, Uncertainty, and Risk: Quantification, Mitigation, and Management*, 2459-2467. DOI: 10.1061/9780784413609.247.

Monfette, M. (2004). *Comprehensive review of plunge pool performance at four of the BC Hydro dam sites and assessment of scour extent.* Vancover, Canada, Master's Thesis, University of British Columbia.

Morgans, RC., Dally, BB., Nathan, GJ., Lanspeary, PV., & Fletcher, DF. (1999). Application of the revised Wilcox (1998) k-ω turbulence model to a jet in co-flow. *Second International Conference on CFD in the Minerals and Process Industries* (pp. 479-484). Melbourne, Australia, 6-8 December: CSIRO.

Munodawafa, MC., & Mhlanga, SZ. (2014). Kariba Dam at 54: Rehabilitation of the spillway upstream control facility and reshaping of the plunge pool. *SANCOLD Conference: Towards Sustainable Dams in South Africa*, (pp. 1-10 (Paper 35)). Johannesburg.

Neyshabouri, AAS., Da Suva, AMF., & Barron, R. (2003). Numerical simulation of scour by a free falling jet. *Journal of Hydraulic Research, 41(5)*, 533-539. DOI: 10.1080/00221680309499998.

Noret, C., Girard, JC., Munodawafa, MC., & Mazvidza, DZ. (2012). Kariba Dam on Zambezi River: Stabilizing the natural plunge pool. *6th International Conference on Sediment and Erosion*, (pp. 34-41). Paris, France.

Odgaard, AJ. (1986). Free-surface air-core vortex. *Journal of Hydraulic Engineering, ASCE, 112(7)*, 610-620. DOI: 10.1061/(ASCE)0733-9429(1986)112:7(610) .

Pabst, W., & Gregorová, E. (2007). Characterization of particles and particle systems. *ICT Prague, 122*, 122.

Padmanabhan, M., & Hecker, GE. (1984). Scale effects in pump sump models. *Journal of Hydraulic Engineering, 110(11)*, 1540-1556.

Pagliara, S., Hager, WH., & Minor, HE. (2004). Plunge pool scour in prototype and laboratory. *International Conference on Hydraulics of Dams and River Structures*, (pp. 165-172). Lisse, The Netherlands: Balkema.

Pagliara, S., Hager, WH., & Minor, HE. (2006). Hydraulics of plane plunge pool scour. *Journal of Hydraulic Engineering, 132(5)*, 450-461. DOI: 10.1061/(ASCE)0733-9429(2006)132:5(450) .

Pan, YW., Li, KW., & Liao, JJ. (2014). Mechanics and response of a surface rock block subjected to pressure fluctuations: A plucking model and its application. *Engineering Geology, 171*, 1-10. DOI: 10.1016/j.enggeo.2013.12.008.

Peiqing, L., & Aihua, L. (2007). Fluctuating uplift acting on rock blocks at the bottom of river bed and estimation of the limiting scour depth. *Journal of Hydraulic Research, 45(4)*, 478-485. DOI: 10.1080/00221686.2007.9521782.

Pells, S. (2016). *Erosion of rock in spillways, Ph.D. Thesis.* Kensington, NSW, Australia: UNSW Australia.

Pells, SE., Pells, PJN., Peirson, WL., Douglas, K., & Fell, R. (2015). Erosion of unlined spillways in rock - does a "scour threshold" exist? *Annual Australian National Committee on Large Dams, ANCOLD: Contemporary Challenges for Dams, 4(8).* Brisbane.

Pfister, M., & Hager, WH. (2009). Deflector-generated jets. *Journal of Hydraulic Research, 47(4)*, 466-475.

Pfister, M., Hager, W., & Boes, RM. (2014). Trajectories and air flow features of ski jump-generated jets. *Journal of Hydraulic Research, 52(3)*, 336-346.

Puertas, J., & Dolz, J. (2005). Plunge Pool Pressures due to a Falling Rectangular Jet. *Journal of Hydraulic Engineering, 131(5)*, 404-407. DOI: 10.1061/(ASCE)0733-9429(2005)131:5(404).

Rashidian, S., & Asadollahi, P. (2012). Assessment of Rock Scour Depth in Plunge Pools. *6th International Conference on Sedimentation and Erosion*, (pp. 1121-1126). Paris.

Rooseboom, A. (1992). *Sediment Transport in Rivers and Reservoirs - A Southern African Perspective.* Pretoria: Water Research Commission Report No. 297/1/92.

Rooseboom, A., & Van Vuuren, S. (2013). *Drainage Manual. 6th Edition. Chapter 5 - Surface drainage.* South Africa: The South African National Roads Agency SOC Ltd Drainage Manual.

Savage, BM., & Johnson, MC. (2001). Flow over ogee spillway: Physical and numerical model case study. *Journal of Hydraulic Engineering, 127(8)*, 640-649. DOI: 10.1061/(ASCE)0733-9429(2001)127:8(640) .

Schleiss, A. (2002). Scour evaluation in space and time - the challenge of dam designers. *Proceedings of International Workshop on Rock Scour due to falling high-velocity jets (No. LCH-ARTICLE-2002-017)*, (pp. 3-22). Lausanne, Switzerland, 25-28 September.

Schleiss, A. (2016). High Head Spillways - the challenge of energy dissipation and scour control downstream. *ICOLD Bulletin - Technical Advancements in Spillway Design, Progress and Innovation from 1985 to 2015* (pp. 41-68). Johannesburg, South Africa: ICOLD.

Stratford, CE., Bollaert, EFR., & Lesleighter, EJ. (2013). Plunge pool rock scour analysis techniques: Wivenhoe dam spillway, Australia. *Hydro 2013 Conference.* Innsbruck, Austria.

Toombes, L., & Chanson, H. (2007). Free-surface aeration and momentum exchange at a bottom outlet. *Journal of Hydraulic Research, 45(1)*, 100-110. DOI: 10.1080/00221686.2007.9521748.

Van Aswegen, WJ., Dunkley, E., & Blake, KRK. (2001). *Plunge pool scour reproduction in physical hydraulic models.* Stellenbosch, South Africa: Water Research Commission, Report No 502/1/01.

Van Schalkwyk, A., Dooge, N., & Pitsiou, S. (1995). Rock Mass Characteristics for Evaluation of Erodability. *Proceedings of the 11th European Conference on Soil Mechanics and Foundation Engineering, Volume 3.* Copenhagen.

Van Schalkwyk, A., Jordaan, JM., & Dooge, N. (1994). *Die erodeerbaarheid van verskillende rotsformasies onder variërende vloeitoestande (WNK Verslag No. 302/1/95).* Verslag aan die Waternavorsingskommissie deur die Departement Geologie, Universiteit van Pretoria, Suid-Afrika: Universiteit van Pretoria, Suid-Afrika.

Versteeg, HK., & Malalasekera, W. (2007). *An Introduction to Computational Fluid Dynamics: the finite volume method, 2nd Edition.* England: Pearson Education Limited.

Vonkeman, JK. (2019). *Coupled fully three-dimensional hydro-morphodynamic modelling of bridge pier scour in an alluvial bed.* Stellenbosch, South Africa: PhD Thesis, Stellenbosch University.

Wahl, TL., Frizell, KH., & Cohen, EA. (2008). Computing the Trajectory of Free Jets. *Journal of Hydraulic Engineering*, 256-260.

Webber, NB. (1971). *Fluid Mechanics for Civil Engineers, S.I. Edition.* London: Champman and Hall Ltd.

Whittaker, JG., & Schleiss, A. (1984). *Scour Related to Energy Dissipators for High Head Structures.* Zürich: Eidgenössischen Technischen Hochschule.

Wibowo, JL., Yule, DE., Villanueva, E., & Temple, DM. (2005). Earth and Rock Surface Spillway Erosion Risk Assessment. *Alaska Rocks 2005, The 40th US Symposiym on Rock Mechanics.* American Rock Mechanics Association.

Wittler, RJ., Mefford, BW., Abt, SR., Ruff, JF., & Annandale, GW. (1995). Spillway and dam foundation erosion: predicting progressive erosion extents. *1st International Conference on Water Resources Engineering* (pp. 1-5). San Antionio, Texas, 14-18 August: US Department of the Interior, Bureau of Reclamation.

Zhu, Y., Oğuz, HN., & Prosperetti, A. (2000). Air entrainment by impinging liquid jets. *Journal of Fluid Mechanics, 404*, 151-177. DOI: 10.1017/S0022112099007090.

Zubeldia, E., Fourtakeas, G., & Rogers, B. (2016). Modelling sediment erosion in fluvial channels using SPH. *11th International SPHERIC Workshop*, (pp. 345-352). Munich, Germany.

ANNEXURE A: HYDRODYNAMIC CHARACTERISTICS OF DIFFERENT SPILLWAYS

Table A.1: Hydrodynamic characteristics of typical spillways and orifice configurations (Manso et al., 2008)

Case	schematic	Type of jet	Type of intake	Boundary development layer	Outlet structure	Hydrodynamics	Aeration	Angle of lower nappe	Angle of upper nappe	Turbulence intensity T_u (%)	Kinetic energy correction factor (-)
1			WES weir (gated or non-gated)	Fully or partially developed	Ski-jump (plane bucket)	$P(n)$ concave $V(n)$ deformed Logarithmic tending to uniform	Partially or fully aerated core	Tang(lip)	Approx. tange(lip), eventual correction	4-8%, take 4% for high velocities	Tending toward 1.0 for high velocities
2		Trajectory	Orifice, low head	Non-developed	Curved lip	$P(n)$ hydrostatic $V(n)$ turbulent ev. Swirling tending to uniform flor high V	Depending on submergence	Tang(lip)	Approx. tange(lip), eventual correction	3-8%	Tending toward 1.0 for high velocities
3			Orifice, high head	Non-developed	Curved lip	$P(n)$ hydrostatic $V(n)$ quasi-uniform	None	Tang(lip)	Approx. tange(lip), eventual correction	2-4%	Approx. 1.0
4			WES weir, short chute	Partially developed	Straight lip	$P(n)$ approximately parabolic, $V(n)$ almost uniform	None	Tang(lip)	Approx tang(lip)	Low, <3%	Approx. 1.0
5		Overfall	WES weir, long chute	Partially or fully developed	Straight or Curved lip	$P(n)$ hydrostatic, $V(n)$ turbulent uniform	Partially aerated	Tang(lip)	Approx tang(lip)	4-5%	Approx. 1.1
6			Broad-crested weir	Non-developed	Straight lip	$P(n)$ approx. parabolic, $V(n)$ freefall quadratic	None	Horizontal	Approx. 4-5°	Low, <3% but may depend on crest details	Approx. 1.0
7		Complex	WES weir	Partially or fully developed	Blocks or deflectors	Mixed	Partially or fully aerated	Tang(lip)	Approx tang(lip)	8% overall or more	-

$P(n)$ and $V(n)$ stand for pressure and velocity profile at issuance, respectively. Initial jet turbulence intensity and kinetic energy correction factor α are according to the type of outlet based on experimental results with high-velocity jet flows.

ANNEXURE B: PHYSICAL MODEL SCALE EFFECTS

Generally, it is not financially viable to construct a physical model of a dam at the full-scale system (prototype). Physical models are constructed at a smaller scale than the prototype and are used to investigate the critical aspects that could influence the performance of the system. Therefore, the model should represent the behaviour of the prototype accurately.

The relationship between the prototype and the model's performance is governed by hydraulic similarity. However, simultaneous compliance with all the laws of similitude is impossible, thus some discrepancies are inevitable between the performance of the model and that of the prototype, which are known as scale effects. The scale effects could be minimised by ensuring that the model is large enough, or by ensuring the necessary compensatory steps are taken (Webber, 1971).

B.1 Hydraulic similarity

The performance of the model must relate to the performance of the prototype in order to obtain accurate prototype conditions. The two flow systems must be hydraulically similar in order to extrapolate the results from the model to the prototype. Hydraulic similarity entails that geometric similarity of the boundaries be retained and that kinematic and dynamic similarity be established by ensuring that the forces impacting on the motion of the water particles in the model and in the prototype be of constant ratio to each other. Therefore, the water particles in the model and in the prototype must flow in similar geometrical patterns in proportional times (U.S. Army Corps of Engineers, 1963).

B.1.1 Geometric similarity

Geometric similarity indicates similarity of shape, which denotes that the model and prototype are identical in shape but differ in size. Thus, the ratio of any two dimensions of the model corresponds to the ratio of the prototype and can be expressed as follows (U.S. Army Corps of Engineers, 1963):

$$\frac{(L_1)_m}{(L_2)_m} = \frac{(L_1)_p}{(L_2)_p} \qquad \textit{Equation B.1}$$

where

L: linear dimensions of model (m)

m: model

p: prototype

B.1.2 Kinematic similarity

Kinematic similarity is similarity of motion and is obtained if the velocity, acceleration and time intervals at congruent points in both systems have the same ratio. The direction of the fluid motion in the two systems must also be the same. The following ratios will apply between the model and prototype for kinematic similarity (Webber, 1971):

$$\frac{(V_1)_m}{(V_2)_m} = \frac{(V_1)_p}{(V_2)_p} \text{ and } \frac{(a_1)_m}{(a_2)_m} = \frac{(a_1)_p}{(a_2)_p} \qquad \textit{Equation B.2}$$

where

V: velocity (m/s)

a: acceleration of fluid (m/s^2)

Geometric similarity of the boundaries is a prerequisite to obtain similar streamlines to achieve kinematic similarity.

B.1.3 Dynamic similarity

Dynamic similarity is similarity of forces capable of influencing the motion of the fluid. The forces at congruent points in both systems that are dynamically similar must have the same ratio and act in the same direction. The ratio to comply with dynamic similarity is as follows (Webber, 1971):

$$\frac{(F_1)_m}{(F_2)_m} = \frac{(F_1)_p}{(F_2)_p} \qquad \textit{Equation B.3}$$

where

F: forces acting on fluid (kN)

The forces acting on the fluid in both systems could be gravity, surface tension, elasticity, fluid viscosity or pressure.

B.2 Conformance with similarity laws

The connotations of the similarity laws that could be applicable to hydraulic models are discussed in this section.

B.2.1 Euler law

The Euler law depicts the relationship between velocity (V) and pressure (P) $\left(E_u = V/\sqrt{2\Delta P/\rho}\right)$. The Euler number is relevant to enclosed systems where the turbulence of the fluid is fully developed and gravity and surface tension forces are absent (Webber, 1971).

B.2.2 Froude law

The Froude law is applicable to systems where gravity is the dominant force influencing the motion of the fluid and a free surface gradient is present. Open channels, spillways, rivers and weirs are typical examples of systems where gravity is the dominant force. The Froude number is defined as (U.S. Army Corps of Engineers, 1963):

$$Fr = \frac{V}{\sqrt{gL}} \qquad \textit{Equation B.4}$$

where

Fr: Froude number (dimensionless)

g: acceleration of gravity (9.81 m/s^2)

The corresponding velocities in the two systems must satisfy Equation B.5 to comply with the Froude law (Webber, 1971).

$$\frac{V_p}{V_m} = \frac{(L_p)^{1/2}}{(L_m)^{1/2}} = x^{1/2} \qquad \textit{Equation B.5}$$

with x being the scale factor.

B.2.3 Reynolds law

The Reynolds law is applicable to systems where viscosity and inertia forces are the only forces present. The Reynolds number $(Re = VL/v)$ is used to reproduce the surface irregularities affecting the fluid motion.

According to the Reynolds law the corresponding velocities in the model and prototype must satisfy Equation B.6 (Webber, 1971):

$$\frac{V_p}{V_m} = \frac{v_p}{v_m}\frac{L_m}{L_p} = \frac{v_p}{v_m}\frac{1}{x} \qquad \textit{Equation B.6}$$

where v is the kinematic viscosity (m^2/s) = 1 x 10^{-6} m^2/s.

The scalar relationships according to the Froude and Reynolds' laws are summarised in Table B.1.

B.2.4 Weber law

The Weber law $\left(W = V/\sqrt{\sigma/L\rho}\right)$ describes the relationship between flow velocity and surface tension. Surface tension is rarely a significant force, however it could become important where an air-water boundary exists. Compliance with the Weber law is achieved when the corresponding velocities in the model and prototype relate as follows (Webber, 1971):

$$\frac{V_p}{V_m} = \frac{{\sigma_p}^{1/2}}{{\sigma_m}^{1/2}} \frac{{\rho_m}^{1/2}}{{\rho_p}^{1/2}} \frac{{L_m}^{1/2}}{{L_p}^{1/2}} = \frac{{\sigma_p}^{1/2}}{{\sigma_m}^{1/2}} \frac{{\rho_m}^{1/2}}{{\rho_p}^{1/2}} \frac{1}{x^{1/2}} \qquad \textit{Equation B.7}$$

where

σ: surface tension of liquid (kN/m^2)

ρ: density of liquid (kg/L)

The physical model for the current research of rock scour downstream of a high head dam is an open channel with a free surface. Gravitational forces are therefore the dominant forces and the Froude law was the criterion to be satisfied. However, it was important to ensure sufficiently high Reynolds and Weber numbers to mitigate the potential scale effects due to viscosity and surface tension respectively.

Table B.1: Scalar relationships for Reynolds and Froude Laws (Webber, 1971)

Hydraulic Similarity	Quantity	Dimensions	Reynolds law	Froude law	
			Natural scale 1:x	Natural scale 1:x	Distorted scales 1:x horiz.; 1:y vert
Geometric	Length	L	x	x	x (horiz.) y (vert.)
	Area	L^2	x^2	x^2	x^2 (plan) xy (sect.)
	Volume	L^3	x^3	x^3	x^2y
Kinematic	Time	T	x^2/v_r	$x^{1/2}$	$x/y^{1/2}$
	Velocity	L/T	v_r/x	$x^{1/2}$	$x/y^{1/2}$ (horiz.) $y^{3/2}/x$ (vert.)
	Acceleration	L/T^2	v_r^2/x^3	1	y/x (horiz.) y^2/x^2 (vert.)
	Discharge	L^3/T	v_rx	$x^{5/2}$	$xy^{3/2}$
Dynamics	Pressure	M/LT^2	$\rho_r v_r^2/x^2$	$\rho_r x$	$\rho_r y$ (sect.)
	Force	M/LT^2	$\rho_r v_r^2$	$\rho_r x^3$	$\rho_r xy^2$ (sect.)
	Energy	M^2/LT^2	$\rho_r v_r^2 x$	$\rho_r x^4$	$\rho_r xy^3$ (sect.)
	Power	M^2/LT^3	$\rho_r v_r^3/x$	$\rho_r x^{7/2}$	$\rho_r y^{7/2}$ (sect.)

* v_r: Velocity (m/s) $\left(\frac{V_p}{V_m}\right)$

ρ_r: Density $\left(\frac{\rho_p}{\rho_m}\right)$

B.3 References for Annexure B

Engineers, U. A. (1963). Hydraulic Design of Reservoir Outlet structures, Em 1110-2-1602.

Webber, NB. (1971). Fluid Mechanics for Civil Engineers, S.I. Edition. London: Chapman and Hall Ltd.

ANNEXURE C: EMPIRICAL FORMULAE

Table C.1: Lesser-known empirical formulae

Formula (Empirical)	Author	Equation number
$y_s + y_w = K\frac{q^{0.67}H_w^{0.67}y_w^{0.15}}{g^{0.33}d_{90}^{0.33}}\left(\frac{\rho_w}{\rho_r - \rho_w}\right)$	Bombardelli and Gioia (2006, as cited in Castillo and Carrillo (2014))	*Equation C.0.1*
$y_s + y_w = \left[\frac{5.65q}{\sqrt{gd_{90}}\left(\frac{y_w}{d_{90}}\right)^{1/6}} - 9(B_u)\right]\frac{sin\theta_j}{1 - 0.215cot\theta_j}$	Mikhalev (as cited in Whittaker & Schleiss, 1984)	*Equation C.2*
Scour length: $L_{sc} = 2.7\frac{H_w{}^{0.45}q^{0.9}}{d_{95}{}^{0.8}g^{0.45}}$ Horizontal distance where maximum scour occurs: $x_1 = 3.9\frac{H_w{}^{0.27}q^{0.54}}{d_{95}{}^{0.27}g^{0.08}}$	Kotoulas (1967) (as cited in Whittaker & Schleiss, 1984)	*Equation C.3* *Equation C.4*
$\frac{y_s}{y_w} = 0.75F_r^{0.524}\left(\frac{d_{50}}{y_w}\right)^{-3.66}\left(\frac{H_w}{y_w}\right)^{0.255}$ Width of scour: $\frac{W_S}{y_w} = 2.83F_r^{0.225}\left(\frac{d_{50}}{y_w}\right)^{-0.188}\left(\frac{H_w}{y_w}\right)^{0.62}$ Horizontal distance where maximum scour occurs: $\frac{L_S}{y_w} = 2.5F_r^{0.122}\left(\frac{d_{50}}{y_w}\right)^{0.127}\left(\frac{H_w}{y_w}\right)^{0.581}$ $F_r = \frac{q}{(y_w^3 g)^{0.5}}$	Ghodsian et al. *(1999)*	*Equation C.5* *Equation C.6* *Equation C.7* *Equation C.8*
$y_s + y_w = \frac{1804qsin\theta_j}{1 - 0.215cot\theta_j}\left(\frac{1}{d_{90}^{0.33}y_w^{0.50}} - \frac{1.126}{H_w}\right)$	Mikhalev (1960, as cited in Castillo & Carrillo, 2017)	*Equation C.9*
$y_s + y_w = y_w + 0.19\left(\frac{H_w + y_w}{d_{90}}\right)^{0.75}\left(\frac{q^{1.20}}{H_w^{0.47}y_w^{0.33}}\right)$	Rubinstein (1963, as cited in Castillo & Carrillo, 2017)	*Equation C.10*
$y_s + y_w = 0.14\left(\frac{Q^3H_w^{1.5}}{d_m^2}\right)^{1/7} - 0.73\frac{y_w^2}{\left(\frac{Q^3H_w^{1.5}}{d_m^2}\right)^{\frac{1}{7}}} + 1.7y_w$	Martins (1973, as cited in Castillo & Carrillo, 2017)	*Equation C.11*
$y_s + y_w = (6.42 - 3.10H_w^{0.10})\frac{g^{0.60-(\frac{H_w}{300})}H_w{}^{0.15+(\frac{H_w}{200})}y_w^{0.15}}{g^{0.30}d_{50}^{0.1}}$	Mason & Arumugam (1985)	*Equation C.12*

In Table C.1, d_{50}, d_{90} and d_{95} are the rock diameters (m) representing the 50%, 90% and 95% percentile respectively, θ_j is the impingement angle with plunge pool surface (degrees), ρ_w and ρ_r the water and rock density (kg/m^3) respectively, and B_u is half of the diameter/thickness of the jet at impact with the tailwater level (m).

ANNEXURE D: ERODIBILITY INDEX METHOD TABLES

M_s (Mass Strength Number):

Table D.1: Mass strength number for rock (Annandale, 2006)

Strength	Description of condition	Unconfined compressive strength (MPa)	Mass Strength Number (Ms)
Very soft rock	Material crumbles under firm (moderate) blows with sharp end of a geological pick and can be peeled with a knife, too hard to cut tri-axial sample by hand.	Less than 1.7	0.87
		1.7 - 3.3	1.86
Soft rock	Can just be scraped and peeled with a knife; indentations 1 mm to 3 mm show in the specimen with firm (moderate) blows with the pick point.	3.3 - 6.6	3.95
		6.6 - 13.2	8.39
Hard rock	Cannot be scraped or peeled with a knife; handheld specimen can be broken with hammer end of geological pick with a single firm (moderate) blow.	13.2 - 26.4	17.7
Very hard rock	Handheld specimen breaks with hammer end of pick under more than one blow.	26.4 - 53.0	35.0
		53.0 - 106.0	70.0
Extremely hard rock	Specimen requires many blows with a geological pick to break through intact material.	Larger than 212.0	280.0

K_b (block/particle size number)

$$K_b = \frac{RQD}{J_n}$$

The joint set numbers (J_n) for rock is summarised in Table D.2.

Table D.2: Joint set number (J_n) for rock (Annandale, 2006)

Number of Joint Sets	Joint Set Number (J_n)
Intact, no, or few joints/fissures	1.00
One joint/fissure set	1.22
One joint/fissure set plus random	1.50
Two joint/fissure set	1.83
Two joint/fissure set plus random	2.24
Three joint/fissure set	2.73
Three joint/fissure set plus random	3.34
Four joint/fissure set	4.09
Multiple joint/fissure sets	5.00

RQD can be calculated in various ways as shown in the formulae below (Annandale, 2006):

$$RQD = (115 - 3.3J_C)$$

$$J_C = \left(\frac{3}{D}\right) + 3 = \left(\frac{3}{\left(J_x \cdot J_y \cdot J_z\right)^{0.33}}\right) + 3$$

$$RQD = \left(105 - \frac{10}{D}\right) = \left(105 - \frac{10}{\left(J_x \cdot J_y \cdot J_z\right)^{0.33}}\right)$$

where

D: mean block diameter (≥ 0.1m)

$J_x.J_y.J_z$: average spacing of joint sets (m)

RQD values are between 5 and 100 while the joint set number (J_n) values fall between 1 and 5, thus the block size number (K_d) ranges between 1 and 100 for rock. General RQD and joint set numbers (J_c) are summarised in Table D.3.

Table D.3: General RQD and joint set numbers (Annandale, 1995)

Number of joints per m^3 (J_c)	Ground Quality Designation (RQD)	Number of joints per m^3 (J_c)	Ground Quality Designation (RQD)
33	5	18	55
32	10	17	60
30	15	15	65
29	20	14	70
27	25	12	75
26	30	11	80
24	35	9	85
23	40	8	90
21	45	6	95
20	50	5	100

Discontinuity or interparticle bond shear strength number (K_d) for rock

$$K_d = \frac{J_r}{J_a}$$

Joint roughness number (J_r): The degree of roughness of the rock discontinuity's opposing faces are described by this parameter. Refer to Table D.4 for the joint roughness number for different joint conditions, and to Figure D.1 for a schematic presentation of joint roughness.

Joint alteration number (J_a): Represents the degree of alteration of the discontinuity faces. Refer to Table D.5 for joint alteration numbers for different joint types.

Joints with a spacing of 1 mm are effectively in contact while for a joint spacing of 5 mm joints do not come into contact upon shear.

Table D.4: Joint roughness number (J_r) (Annandale, 2006)

Joint separation	Condition of joint	Joint roughness number (J_r)
Joints tight or closing during excavation	Stepped joints	4.0
	Rough or irregular, undulating	3.0
	Smooth undulating	2.0
	Slickensided undulating	1.5
	Rough or irregular, planar	1.5
	Smooth planar	1.0
	Slickensided planar	0.5
Joints open and remain open during excavation	Joints either open or containing relatively soft gouge of sufficient thickness to prevent joint wall contact upon excavation.	1.0
	Shattered or micro-shattered clays	1.0

Figure D.1 is a schematic presentation of conventional descriptions of joint roughness.

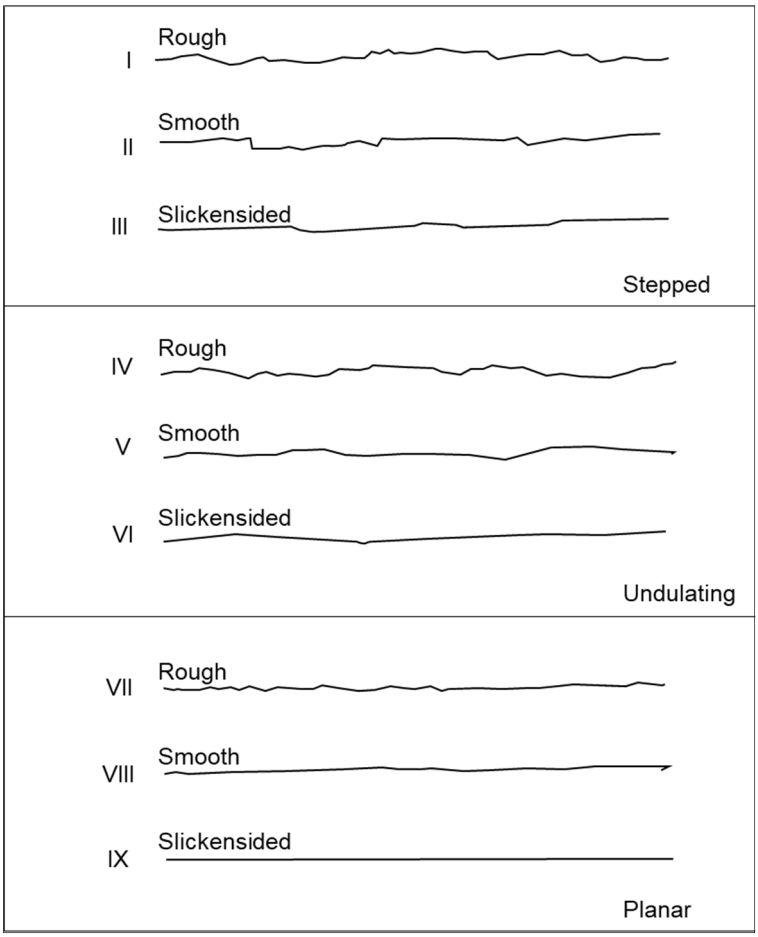

Figure D.1: Schematic presentation of joint roughness (Annandale, 2006)

Table D.5: Joint alteration number (J_a) (Kirsten, 1982)

Description of gouge	**Joint alteration number (J_a) for joint separation (mm)**		
	1.0*	**1.0 - 5.0†**	**5.0‡**
Tightly healed, hard, non-softening impermeable filling	0.75	-	-
Unaltered joint walls, surface staining only	1.0	-	-
Slightly altered, non-softening, non-cohesive rock mineral or crushed rock filling	2.0	2.0	4.0
Non-softening, slightly clayey non-cohesive filling	3.0	6.0	10.0
Non-softening, strongly over-consolidated clay mineral filling, with or without crushed rock	3.0	6.0§	10.0
Softening or low friction clay mineral coatings and small quantities of swelling clays	4.0	8.0	13.0
Softening moderately over-consolidated clay mineral filling, with or without crushed rock	4.0	8.0§	13.0
Shattered or micro-shattered (swelling) clay gouge, with or without crushed rock	5.0	10.0§	18.0

NOTE:
* Joint walls effectively in contact
† Joint walls come into contact after approximately 100 mm shear
‡ Joint walls do not come into contact at all upon shear
§ Also applies when crushed rock occurs in clay gouge without rock wall contact

Relative ground structure number (J_s)

The joint spacing ratio r defines the rock block shape. The joint spacing is determined by the quotient of the mean spacing of the two most prominent high angle joint sets in the vertical plane ($r = \frac{z}{x}$) as illustrated in Figure D.2.

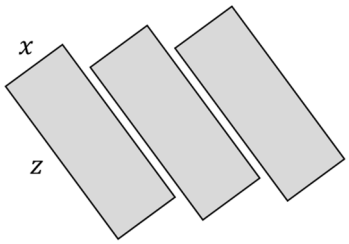

Figure D.2: Joint spacing ratio r (Annandale, 2006)

For intact material the value of J_s is 1, and when the r-value is higher than 8 the J_s value is that of r = 8. The relative ground structure number for different dip angles are summarised in Table D.6.

Table D.6: Relative ground structure number (J_S) (Annandale, 2006)

Dip direction of closer spaced joint set (degrees)	Dip angle of closer spaced joint set (degrees)	Ratio of joint spacing, r			
		1:1	1:2	1:4	1:8
180/0	Vertical 90	1.14	1.20	1.24	1.26
In direction of stream flow 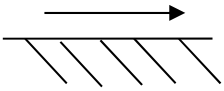	89	0.78	0.71	0.65	0.61
	85	0.73	0.66	0.61	0.57
	80	0.67	0.60	0.55	0.52
	70	0.56	0.50	0.46	0.43
	60	0.50	0.46	0.42	0.40
	50	0.49	0.46	0.43	0.41
	40	0.53	0.49	0.46	0.45
	30	0.63	0.59	0.55	0.53
	20	0.84	0.77	0.71	0.67
	10	1.25	1.10	0.98	0.90
	5	1.39	1.23	1.09	1.01
	1	1.50	1.33	1.19	1.10
0/180	Horizontal 0	1.14	1.09	1.05	1.02
Against direction of stream flow 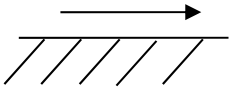	-1	0.78	0.85	0.90	0.94
	-5	0.73	0.79	0.84	0.88
	-10	0.67	0.72	0.78	0.81
	-20	0.56	0.62	0.66	0.69
	-30	0.50	0.55	0.58	0.60
	-40	0.49	0.52	0.55	0.57
	-50	0.53	0.56	0.59	0.61
	-60	0.63	0.68	0.71	0.73
	-70	0.84	0.91	0.97	1.01
	-80	1.26	1.41	1.53	1.61
	-85	1.39	1.55	1.69	1.77
	-89	1.50	1.68	1.82	1.91
180/0	Vertical -90	1.14	1.20	1.24	1.26

ANNEXURE E: QUASI-STEADY UPLIFT PRESSURE COEFFICIENTS

The net uplift pressure coefficient (C_{uplift}) must be calibrated based on the shape and scour extent at the specific site. Net uplift pressure coefficients of 0.1 to 0.2 have been proposed for low to very low block protrusions, and coefficients of 0.3 to 0.5 for moderate to significant block protrusions, which are typically encountered in fractured rock. Bollaert (2012) indicated that the latter values are considered most plausible for a real water-rock interface. Stabilising coefficients are obtained for joint angles that are orientated against the flow.

Table E.1: Quasi-steady uplift pressure coefficients (Bollaert, 2012)

	h_{block}/e_{block}	β_{block}	C_{uplift}
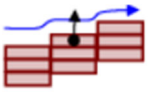	17 - 29	0°	0.220
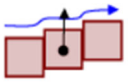	17 - 29	0°	0.220
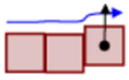	17 - 29	0°	0.085
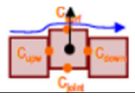	17 - 34	0°	0.155
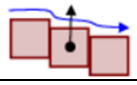	4 - 9	0°	-0.070
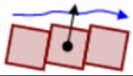	4 - 10	3°	0.310
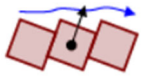	2 - 4	9°	0.37 – 0.47
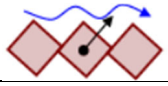	1 – 2.5	18°	0.25 – 0.45
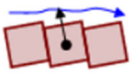	4.2 – 8.7	-3°	-0.070
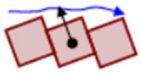	1 – 2.3	-18°	-0.150

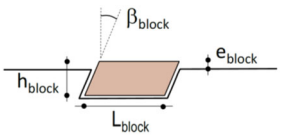

ANNEXURE F: EXPERIMENTAL DETAILS

F.1 Physical model photographs

Figure F.1: View of model for highest fall height

Figure F.2: Pressure box with air valve and flow straighteners

Figure F.3: Reservoir outlet valves

Figure F.4: ADV equipment set up

Figure F.5: Rod used to adjust ADV equipment depth for each grid point

Figure F.6: Flow velocity measurements with ADV during testing

F.2 Model schematics

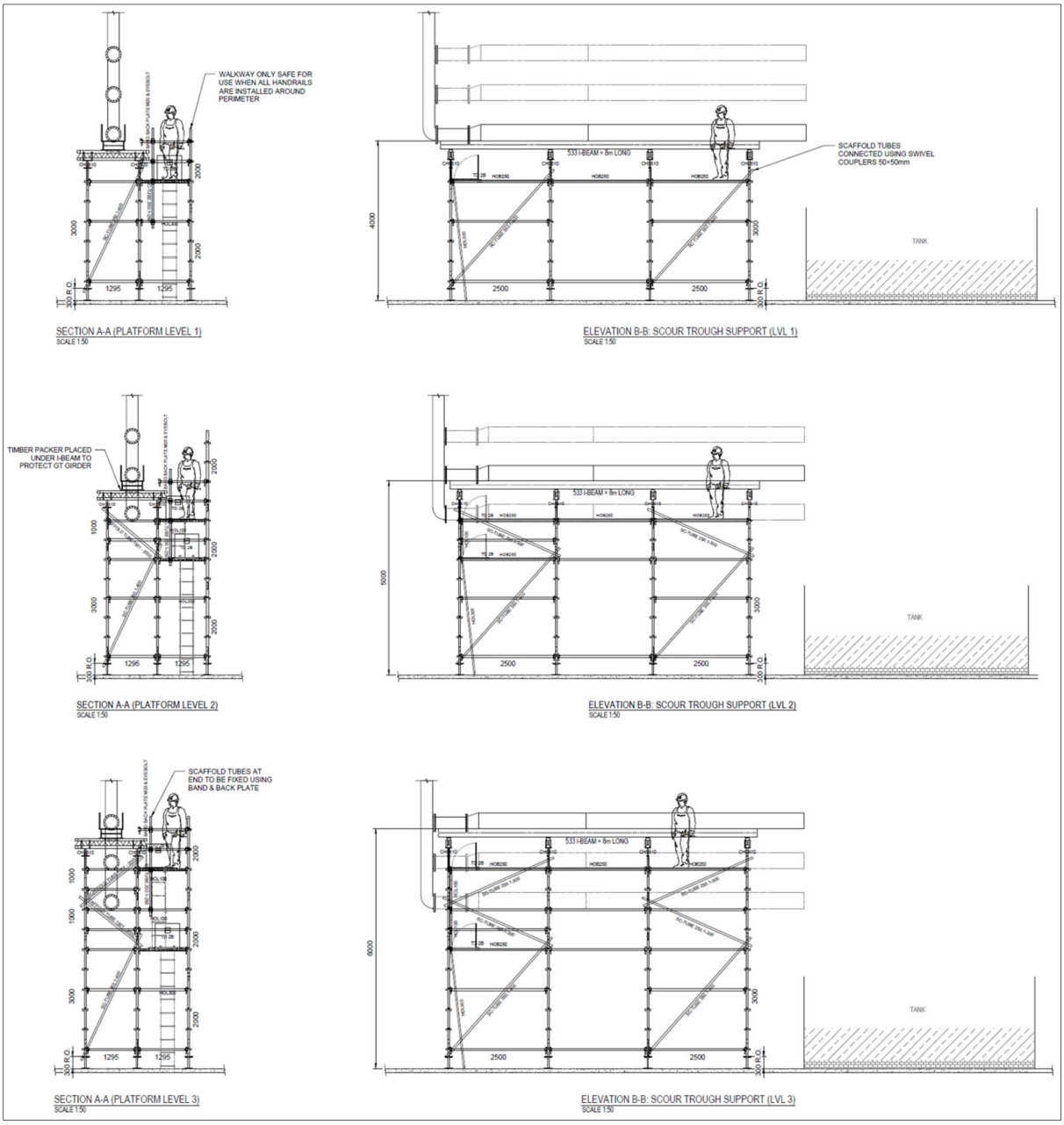

Figure F.7: Schematics of model for the three different fall heights

ANNEXURE G: PHYSICAL MODEL RESULTS

G.1 Experimental test schedule and results

Table G.1: Experimental test schedule and results

Test	Target flow	Actual flow	Elevation	Tailwater depth	Rock size	Joint angle	Flow depth at issuance	Jet thickness at impingement	Jet width at impingement	Issuance velocity	Velocity at impingement	Impingement jet angle	Scour depth		Scour length		Scour width		Scour volume		Ratio		Time exposure	
	Q_{target}	Q_{actual}	H	TWD	z_b		D_i	D_j	W_j	V_i	V_j	Θ_j	D_s (m)		L_s (m)		W_s (m)		V_s (m)		L/(W/2)		T_s (hours)	
	(m^3/s/m)	(m^3/s/m)	(m)	(m)	(m)	(°)	(m)	(m)	(m)	(m/s)	(m/s)	(°)	Case A	Case B	Case A	Case B	Case A	Case B	Case A	Case B	Case A	Case B	Case A	Case B
1A	0.391	0.392	3.01	1.0	0.5	0°	0.454	0.40	0.45	0.9	7.0	68	0.12	0.14	1.09	1.35	0.60	1.02	0.11	0.14	3.6	2.7	1.0	5
1B	0.391	0.392	3.01	1.0	0.5	0°	0.314	0.39	0.44	1.2	6.9	69	0.14	-	1.40	-	0.93	-	0.24	-	3.0	-	2.6	-
1C	0.391	0.392	3.01	1.0	0.5	0°	0.357	0.30	0.60	1.1	6.9	77	0.13	0.20	1.75	2.28	0.80	1.11	0.15	0.22	4.4	4.1	5.5	16
2A	0.513	0.500	3.01	1.0	0.5	0°	0.300	0.40	0.50	1.7	6.9	66	0.20	0.30	1.34	1.95	1.04	1.16	0.24	0.42	2.6	3.4	5.0	18
3A	0.894	0.896	3.01	1.0	0.5	0°	0.247	0.60	0.80	3.6	7.6	58	0.41	0.52	2.00	3.91	1.40	1.77	0.46	1.38	2.9	4.4	5.5	21
1.1A	0.391	0.396	3.01	0.5	0.5	0°	0.190	0.50	0.70	2.1	7.6	87	0.31	0.53	1.07	2.01	0.94	1.09	0.17	0.42	2.3	3.7	6.0	16
2.1A	0.513	0.504	3.01	0.5	0.5	0°	0.205	0.52	0.61	2.5	7.7	70	0.32	0.64	1.44	2.24	1.18	1.22	0.21	0.66	2.4	3.7	6.0	20
3.1A	0.894	0.840	3.01	0.5	0.5	0°	0.272	0.62	0.70	3.1	8.0	55	0.56	0.70	2.58	3.16	1.37	1.44	0.67	1.62	3.8	4.4	6.0	22
4A	0.391	0.390	3.86	1.0	0.5	0°	0.195	0.40	0.55	2.0	8.0	61	0.14	0.29	0.88	1.79	0.74	1.05	0.14	0.30	2.4	3.4	5.5	18
4B	0.391	0.392	3.86	1.0	0.5	0°	0.200	0.25	0.50	2.0	8.0	62	0.17	0.26	1.02	1.69	0.94	1.12	0.14	0.29	2.2	3.0	5.5	18
5A	0.513	0.504	3.86	1.0	0.5	0°	0.240	0.35	0.60	2.1	8.1	68	0.19	0.34	1.19	1.93	1.00	1.23	0.14	0.35	2.4	3.1	6.0	20
6A	0.894	0.894	3.86	1.0	0.5	0°	0.350	0.97	1.20	2.6	8.3	57	0.32	0.51	1.90	2.95	1.31	1.36	0.35	0.86	2.9	4.3	6.0	20
4.1A	0.391	0.390	3.86	0.5	0.5	0°	0.160	0.61	0.74	2.4	8.7	59	0.22	0.43	0.73	1.86	0.84	1.16	0.19	0.36	1.7	3.2	6.0	16
5.1A	0.513	0.504	3.86	0.5	0.5	0°	0.185	0.54	0.44	2.7	8.8	63	0.45	0.63	2.15	3.03	1.23	1.25	0.34	0.90	3.5	4.8	6.0	20
6.1A	0.894	0.860	3.86	0.5	0.5	0°	0.290	0.75	0.79	3.0	9.0	56	0.49	0.85	1.65	3.47	1.29	1.45	0.49	1.48	2.6	4.8	6.0	16
7A	0.391	0.392	4.91	1.0	0.5	0°	0.280	0.59	1.11	1.4	9.2	70	0.13	0.18	1.00	1.50	0.75	0.93	0.24	0.30	2.7	3.2	5.0	18
7B	0.391	0.392	4.91	1.0	0.5	0°	0.280	0.56	1.13	1.4	9.2	69	0.11	0.17	0.88	1.04	0.79	0.90	0.22	0.29	2.2	2.3	6.0	20
8A	0.513	0.504	4.91	1.0	0.5	0°	0.235	0.51	0.90	2.1	9.3	65	0.21	0.39	1.09	1.85	1.08	1.23	0.15	0.41	2.0	3.0	6.0	24
9A	0.894	0.812	4.91	1.0	0.5	0°	0.305	0.87	0.68	2.7	9.5	60	0.44	0.64	2.15	3.19	1.31	1.47	0.42	1.11	3.3	4.3	5.5	27
7.1A	0.391	0.389	4.91	0.5	0.5	0°	0.180	0.56	0.53	2.2	9.7	66	0.23	0.58	1.09	2.09	0.95	1.12	0.18	0.59	2.3	3.7	6.0	20
8.1A	0.513	0.504	4.91	0.5	0.5	0°	0.215	0.64	0.72	2.3	9.8	63	0.42	0.77	1.83	2.80	1.00	1.42	0.33	1.18	3.7	3.9	6.0	24
9.1A	0.894	0.840	4.91	0.5	0.5	0°	0.345	0.77	1.02	2.4	10.0	62	0.55	0.78	2.13	4.01	1.36	1.69	0.60	1.95	3.1	4.7	6.0	26
10A	0.391	0.388	4.9	1.0	0.5	+45°	0.180	0.56	0.53	2.2	9.2	66	0.15	0.25	1.00	1.67	0.87	0.92	0.12	0.34	2.3	3.6	6.0	20
10.1A	0.894	0.852	4.9	0.5	0.5	+45°	0.335	0.77	1.02	2.5	10.0	62	0.57	0.89	2.34	2.87	1.39	1.53	0.51	1.33	3.4	3.7	6.0	20
11A	0.391	0.384	4.9	1.0	0.5	-45°	0.175	0.56	0.53	2.2	9.2	66	0.21	0.40	0.69	0.80	1.21	1.23	0.18	0.38	1.1	1.3	6.0	24
12A	0.894	0.840	4.9	1.0	0.05	-45°	0.320	0.77	1.02	2.6	9.5	62	0.44	0.62	1.73	2.81	1.59	1.64	0.21	0.59	2.2	3.4	6.0	28
13A	0.391	0.388	4.9	1.0	0.075	0°	0.175	0.56	0.53	2.2	9.2	66	0.09	0.45	0.75	1.10	0.87	1.24	0.05	0.14	1.7	1.8	5.3	12
13.1A	0.391	0.390	4.9	0.5	0.075	0°	0.165	0.56	0.53	2.4	9.8	66	0.26	0.42	0.95	1.62	0.97	1.68	0.08	0.44	2.0	1.9	6.0	18
14A	0.894	0.850	4.9	1.0	0.075	0°	0.340	0.77	1.02	2.5	9.5	62	0.37	0.49	1.63	2.38	1.54	1.47	0.39	0.79	2.1	3.2	6.0	24
14B	0.894	0.858	4.9	1.0	0.075	0°	0.440	0.77	1.02	2.0	9.4	62	0.32	0.51	1.33	2.24	1.41	1.39	0.44	0.60	1.9	3.2	6.0	26
14.1A	0.894	0.878	4.9	0.5	0.075	0°	0.345	0.77	1.02	2.5	10.0	62	0.59	0.82	1.51	2.14	1.19	1.84	0.32	1.36	2.5	2.3	5.3	28

Repeated tests are indicated with “B” in the test name.

Table G.2: Experimental and theoretical impingement jet angle

Test	Target flow	Actual flow	Elevation	Tailwater depth	Experimental impingement jet angle	Theoretical impingement jet angle (Wahl et al., 2008)
	Q_{target}	Q_{actual}	H	TWD	Θ_j	Θ_j
	($m^3/s/m$)	($m^3/s/m$)	(m)	(m)	(°)	(°)
1A	0.391	0.392	3.01	1.0	68	87
1B	0.391	0.392	3.01	1.0	69	84
1C	0.391	0.392	3.01	1.0	77	86
2A	0.513	0.500	3.01	1.0	66	82
3A	0.894	0.896	3.01	1.0	58	64
1.1A	0.391	0.396	3.01	0.5	87	77
2.1A	0.513	0.504	3.01	0.5	70	73
3.1A	0.894	0.840	3.01	0.5	55	69
4A	0.391	0.390	3.86	1.0	61	77
4B	0.391	0.392	3.86	1.0	62	76
5A	0.513	0.504	3.86	1.0	68	72
6A	0.894	0.894	3.86	1.0	57	75
4.1A	0.391	0.390	3.86	0.5	59	74
5.1A	0.513	0.504	3.86	0.5	63	71
6.1A	0.894	0.860	3.86	0.5	56	70
7A	0.391	0.392	4.91	1.0	70	84
7B	0.391	0.392	4.91	1.0	69	85
8A	0.513	0.504	4.91	1.0	65	78
9A	0.894	0.812	4.91	1.0	60	76
7.1A	0.391	0.389	4.91	0.5	66	79
8.1A	0.513	0.504	4.91	0.5	63	78
9.1A	0.894	0.840	4.91	0.5	62	78

Table G.3: Relative energy dissipation in the plunge pool

Test	Tailwater depth	Experimental data			Numerical data		
		Impinging Froude number	Relative energy dissipation	Pool depth to jet impingement thickness ratio	Impinging Froude number	Relative energy dissipation	Pool depth to jet impingement thickness ratio
	TWD	Fr_j	H_L/H_0	$(y_w+y_s)/Bj$	Fr_j	H_L/H_0	$(y_w+y_s)/Bj$
	(m)	(-)	(-)	(-)	(-)	(-)	(-)
1A	1.0	3.54	0.60	2.85	-	-	-
1B	1.0	3.51	0.59	2.92	-	-	-
1C	1.0	4.02	0.61	4.01	-	-	-
2A	1.0	3.50	0.62	3.26	-	-	-
3A	1.0	3.12	0.61	2.54	-	-	-
1.1A	0.5	3.42	0.54	2.05	3.65	0.66	2.41
2.1A	0.5	3.41	0.55	2.19	-	-	-
3.1A	0.5	3.25	0.39	1.93	-	-	-
4A	1.0	4.04	0.67	3.23	-	-	-
4B	1.0	5.10	0.70	5.05	-	-	-
5A	1.0	4.36	0.70	3.83	3.98	0.68	3.41
6A	1.0	2.70	0.42	1.56	-	-	-
4.1A	0.5	3.54	0.58	1.53	3.91	0.68	1.96
5.1A	0.5	3.81	0.46	2.09	-	-	-
6.1A	0.5	3.31	-0.03	1.79	-	-	-
7A	1.0	3.83	0.65	2.02	-	-	-
7B	1.0	3.91	0.65	2.10	-	-	-
8A	1.0	4.14	0.69	2.73	-	-	-
9A	1.0	3.24	0.65	1.89	4.28	0.69	3.64
7.1A	0.5	4.15	0.45	1.93	-	-	-
8.1A	0.5	3.92	0.54	1.98	4.43	0.42	2.75
9.1A	0.5	3.64	0.02	1.67	-	-	-
10A	1.0	3.93	0.65	2.24	4.56	0.56	3.09
10.1A	0.5	3.64	0.04	1.81	-	-	-
11A	1.0	3.93	0.67	2.36	-	-	-
12A	1.0	3.46	0.65	2.12	4.69	0.74	4.14
13A	1.0	3.93	0.68	2.60	-	-	-
13.1A	0.5	4.17	0.66	1.64	4.83	-2.05	2.25
14A	1.0	3.46	0.65	1.95	4.27	0.66	3.40
14B	1.0	3.45	0.59	1.97	-	-	-
14.1A	0.5	3.65	0.02	1.73	-	-	-

G.2 Contour maps of bed deformation

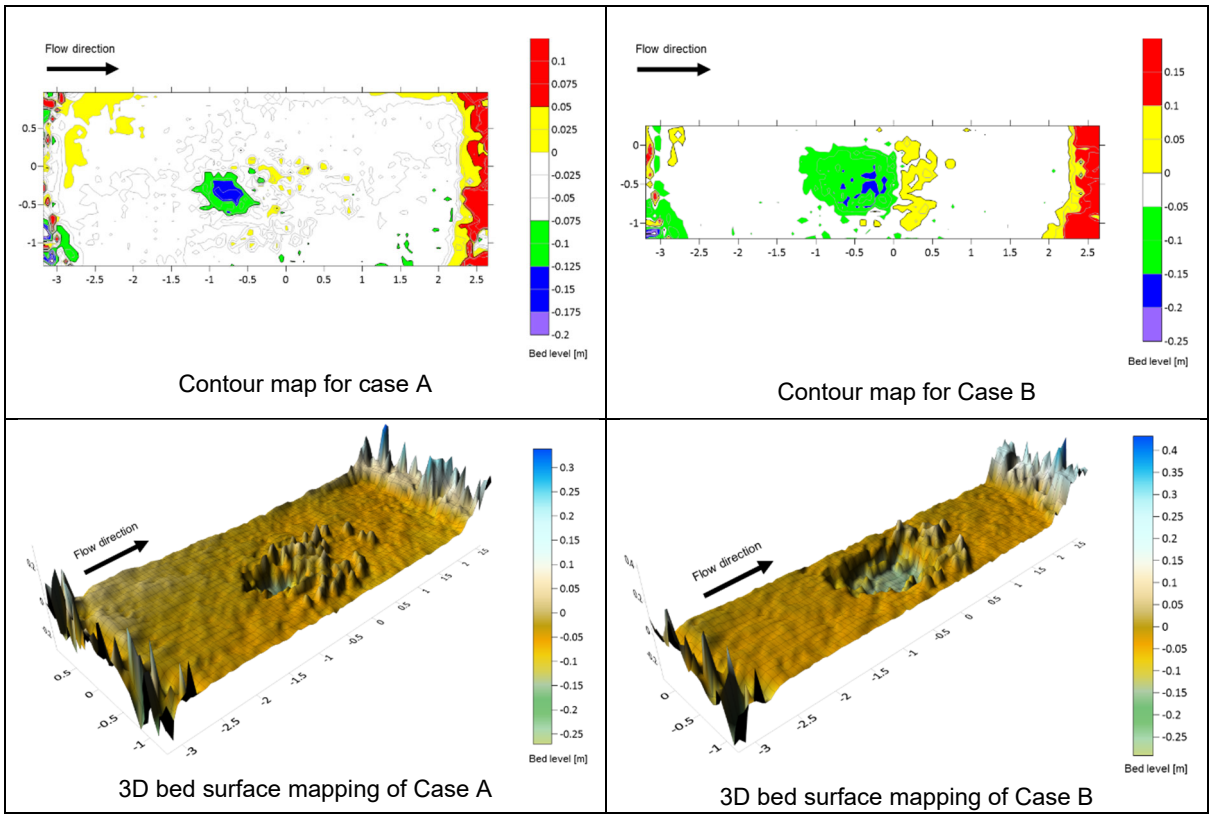

Figure G.1: Equilibrium bed levels for Test1A (Q_{min}, H_{min}, TWD_{max}) for Case A (scour and deposition) and B (scour with deposited rocks removed)

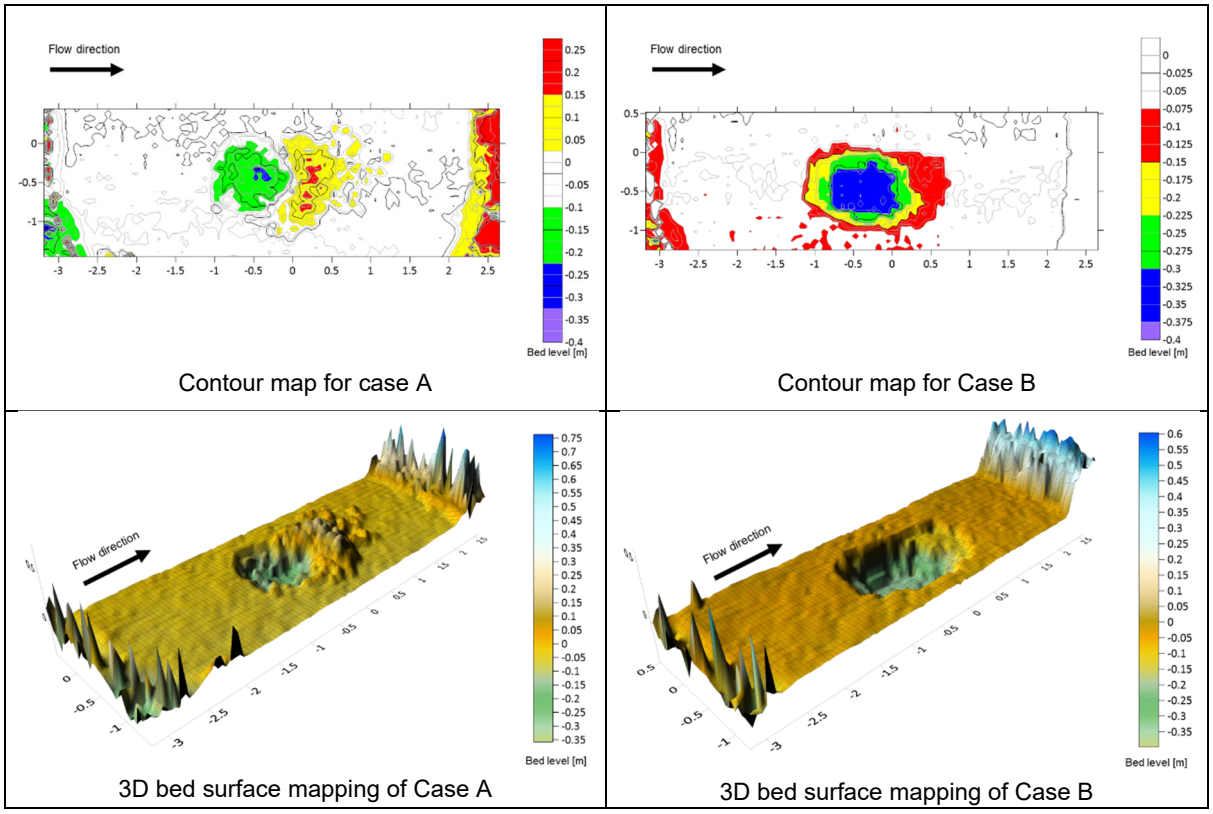

Figure G.2: Equilibrium bed levels for Test2A (Q_{med}, H_{min}, TWD_{max}) for Case A (scour and deposition) and B (scour with deposited rocks removed)

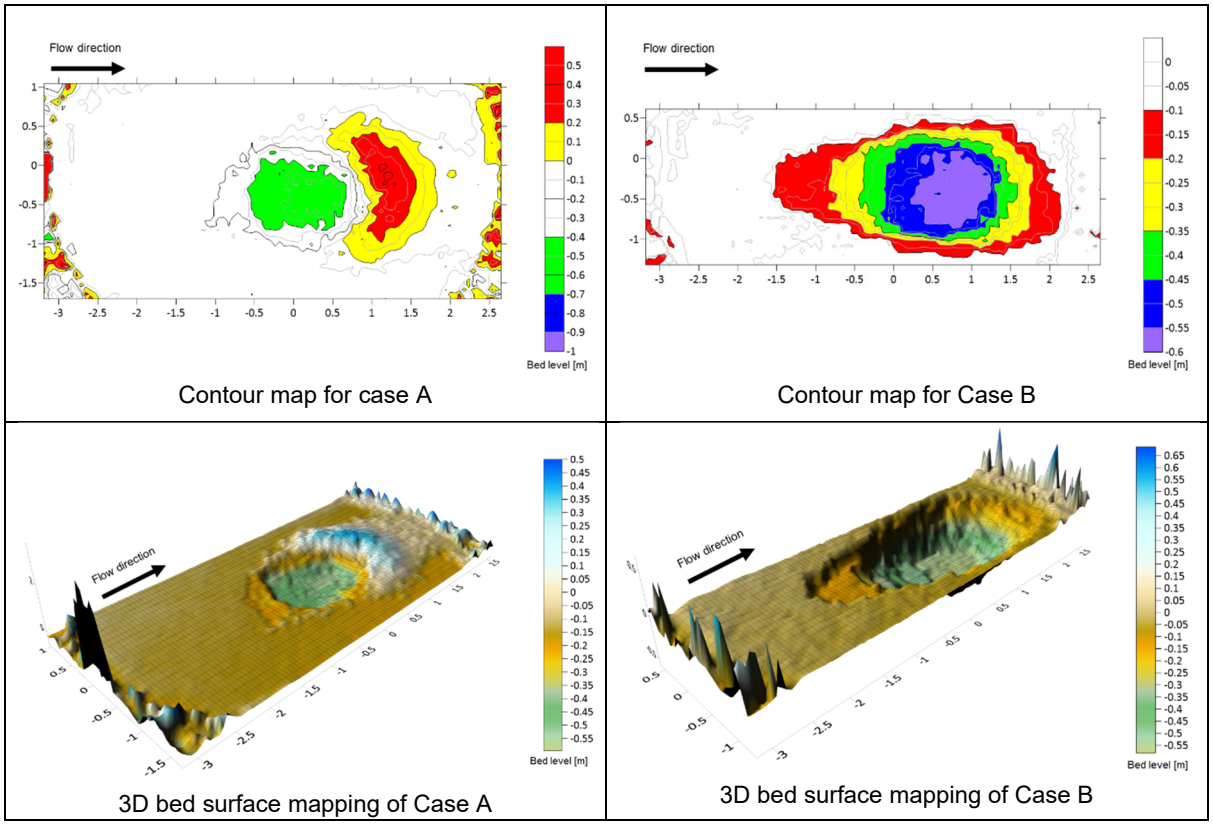

Figure G.3: Equilibrium bed levels for Test3A (Q_{max}, H_{min}, TWD_{max}) for Case A (scour and deposition) and B (scour with deposited rocks removed)

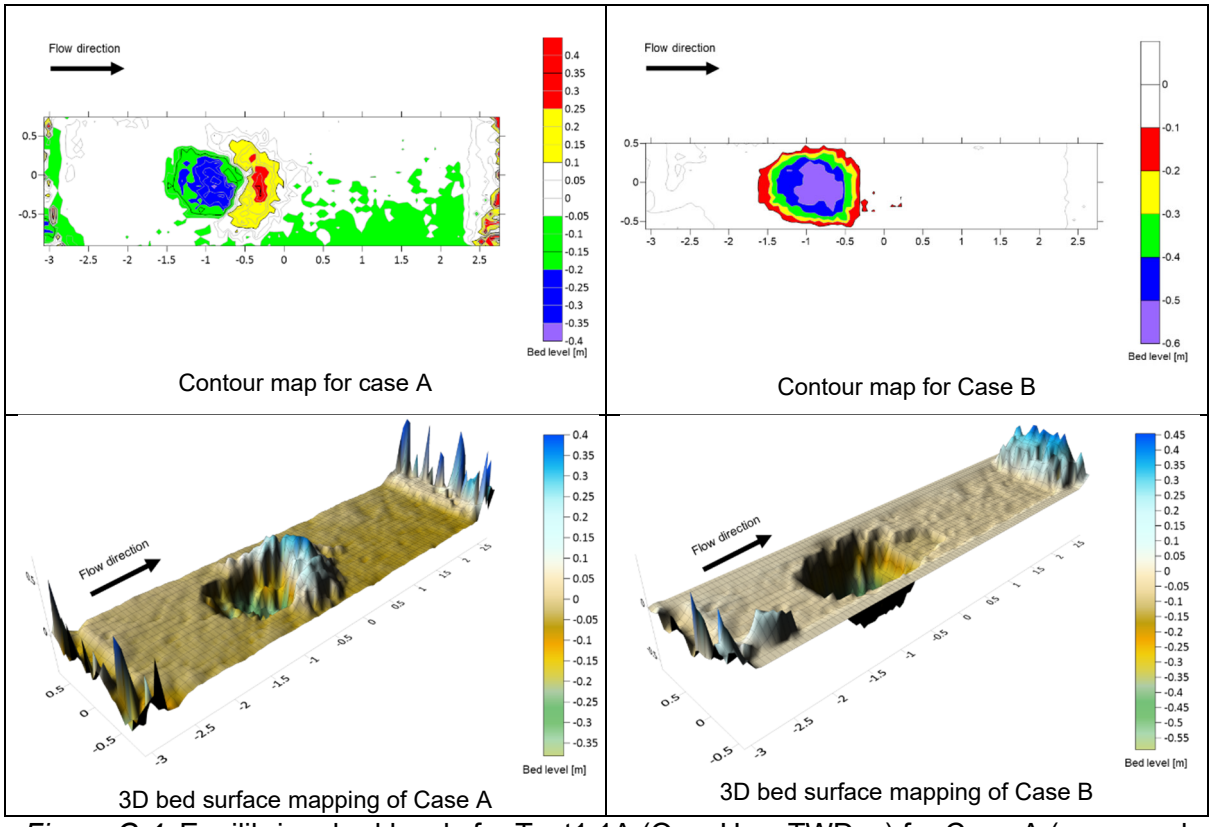

Figure G.4: Equilibrium bed levels for Test1.1A (Q_{min}, H_{min}, TWD_{min}) for Case A (scour and deposition) and B (scour with deposited rocks removed)

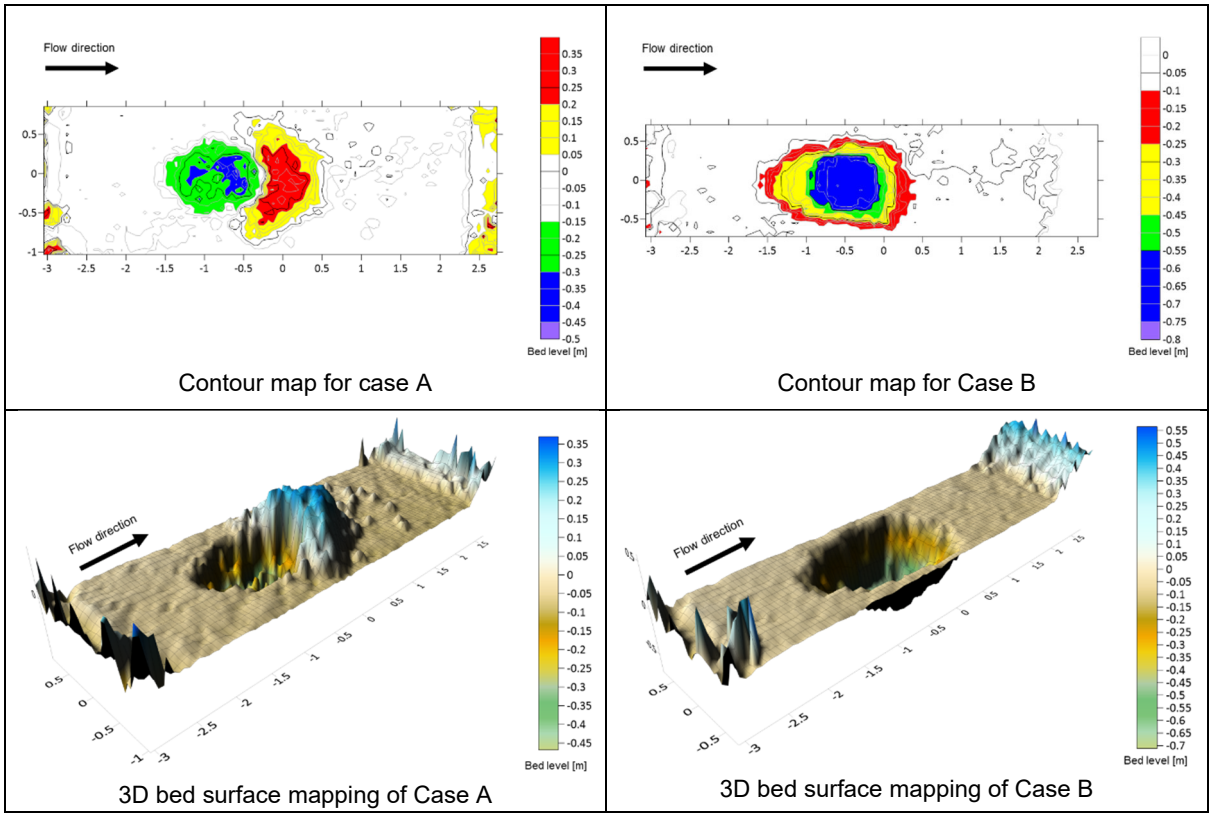

Figure G.5: Equilibrium bed levels for Test2.1A (Q_{med}, H_{min}, TWD_{min}) for Case A (scour and deposition) and B (scour with deposited rocks removed)

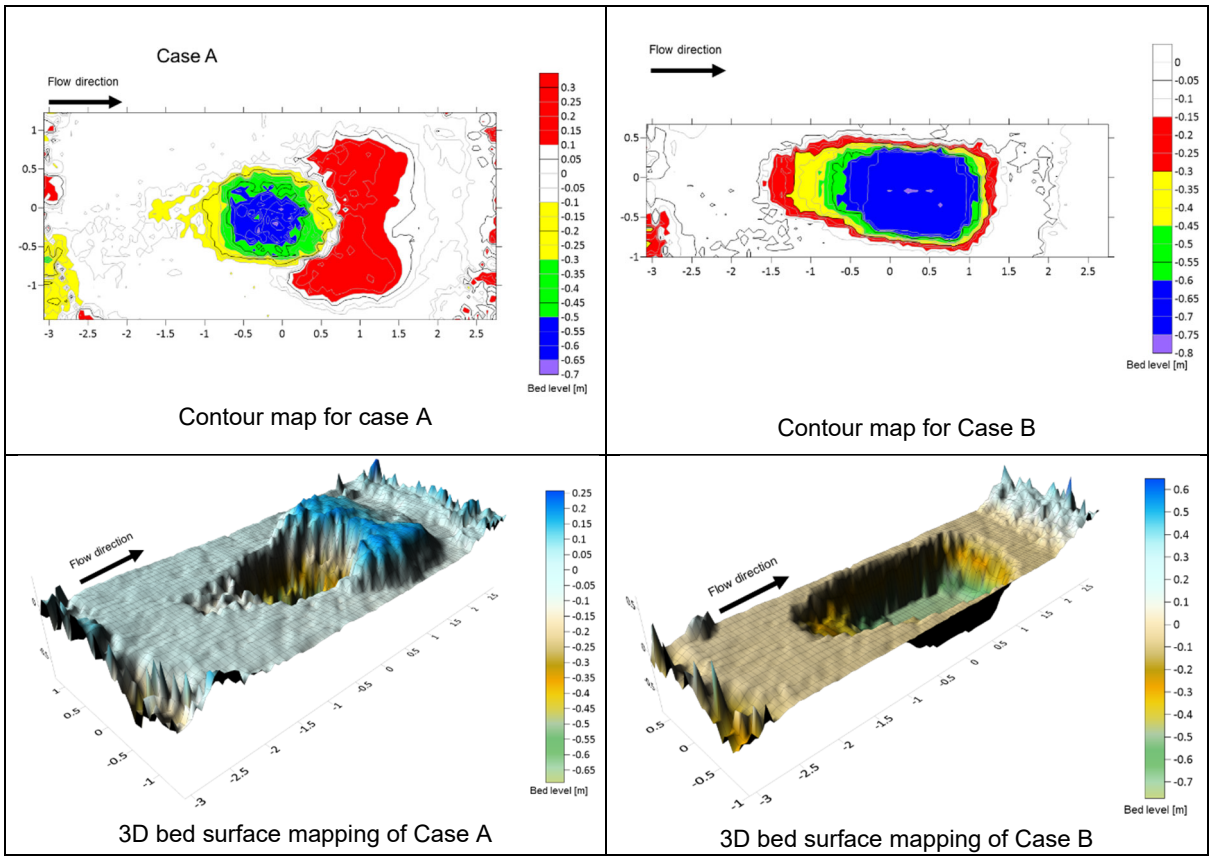

Figure G.6: Equilibrium bed levels for Test3.1A (Q_{max}, H_{min}, TWD_{min}) for Case A (scour and deposition) and B (scour with deposited rocks removed)

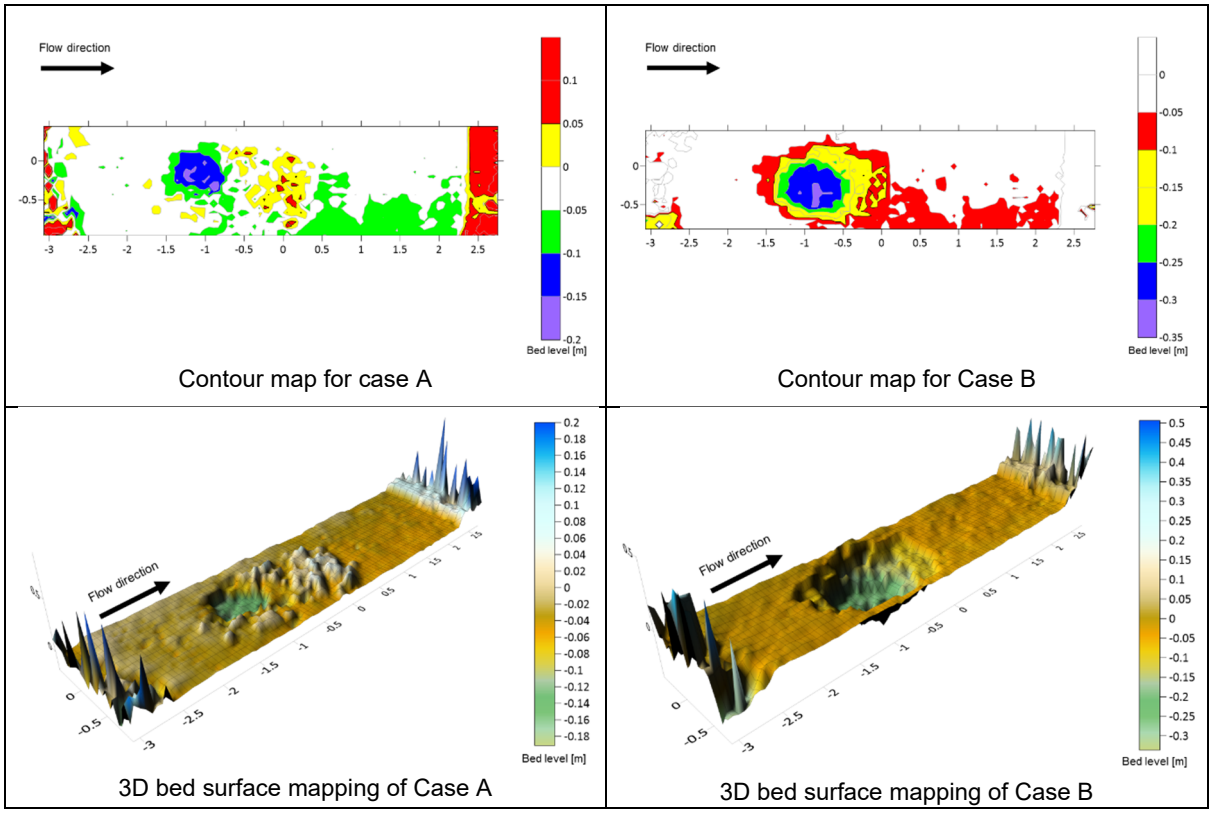

Figure G.7: Equilibrium bed levels for Test4A (Q_{min}, H_{med}, TWD_{max}) for Case A (scour and deposition) and B (scour with deposited rocks removed)

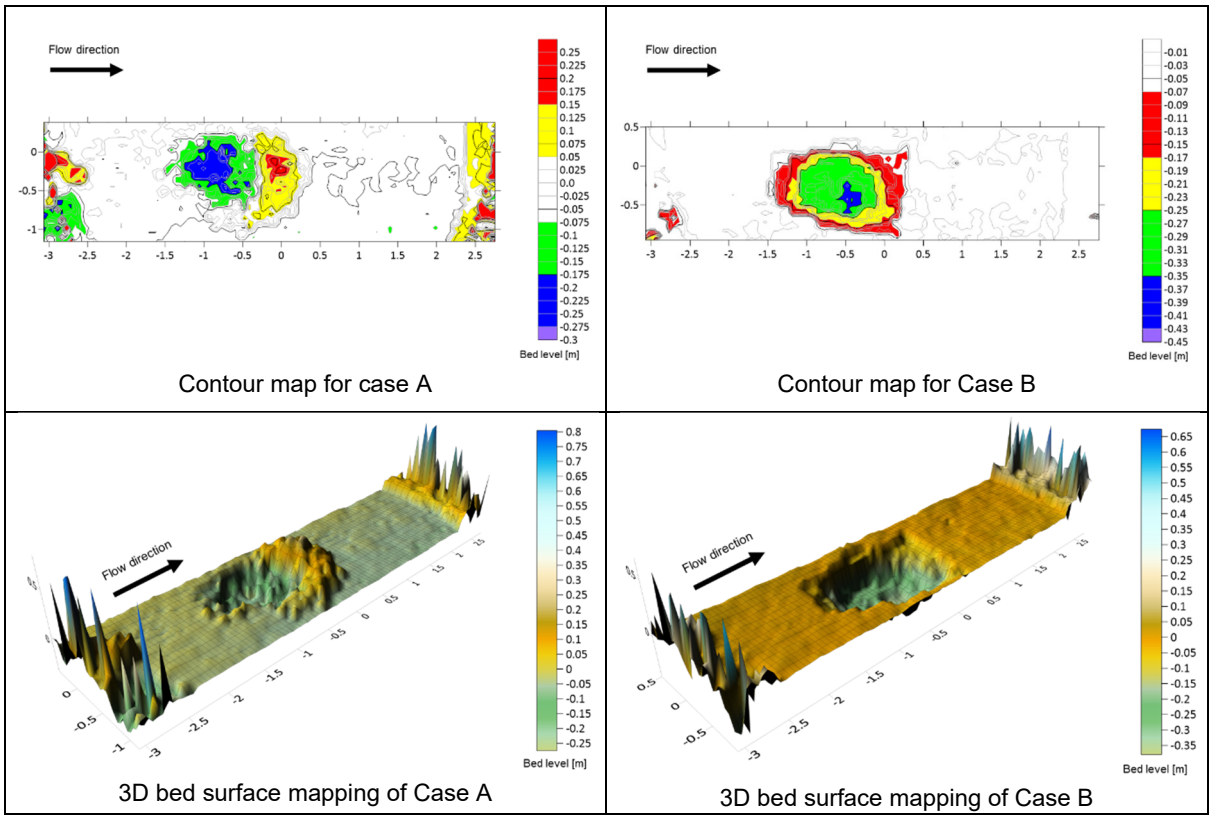

Figure G.8: Equilibrium bed levels for Test5A (Q_{med}, H_{med}, TWD_{max}) for Case A (scour and deposition) and B (scour with deposited rocks removed)

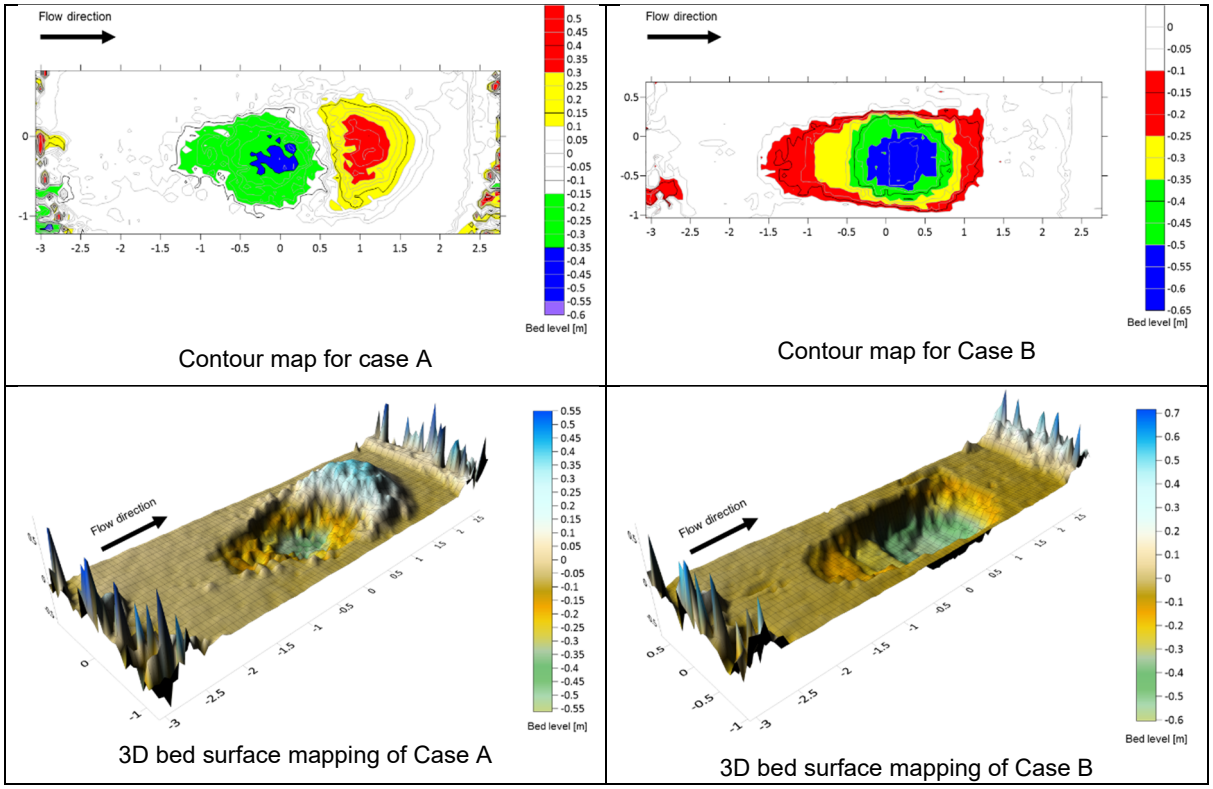

Figure G.9: Equilibrium bed levels for Test6A (Q_{max}, H_{med}, TWD_{max}) for Case A (scour and deposition) and B (scour with deposited rocks removed)

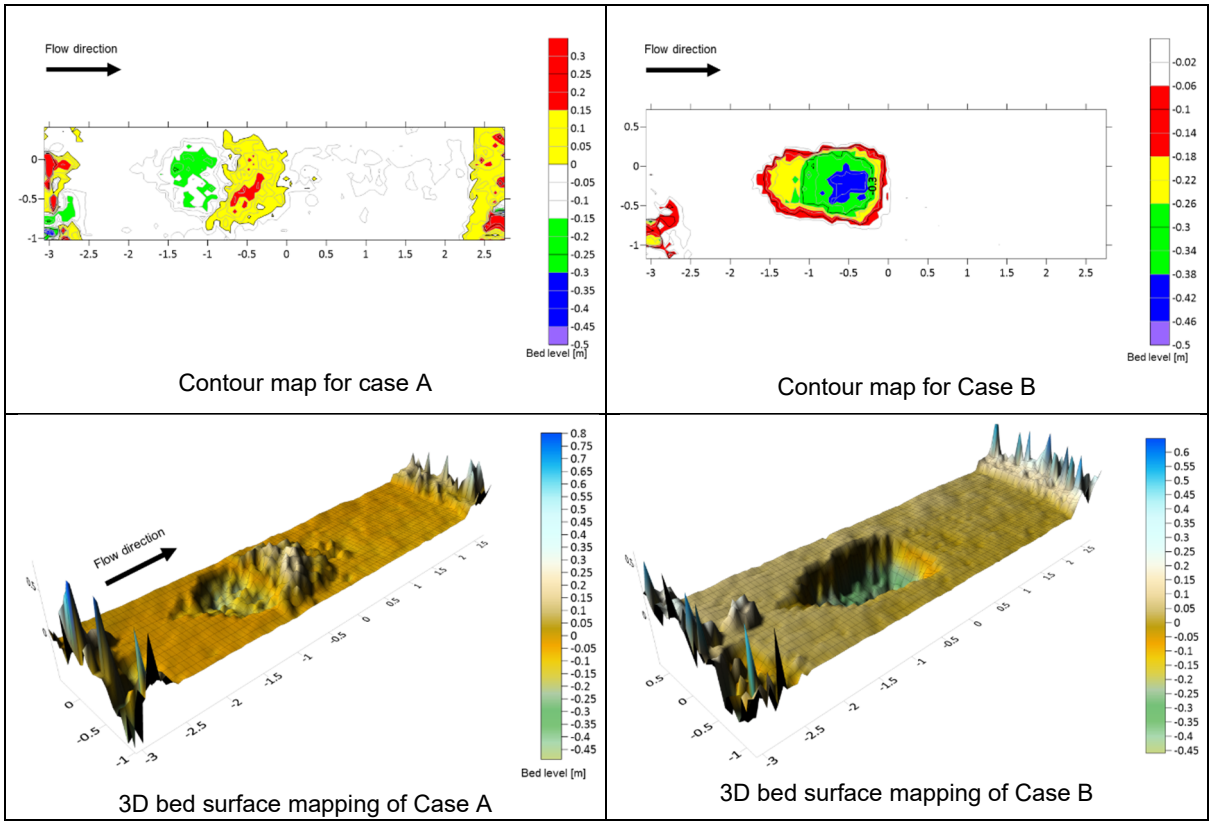

Figure G.10: Equilibrium bed levels for Test4.1A (Q_{min}, H_{med}, TWD_{min}) for Case A (scour and deposition) and B (scour with deposited rocks removed)

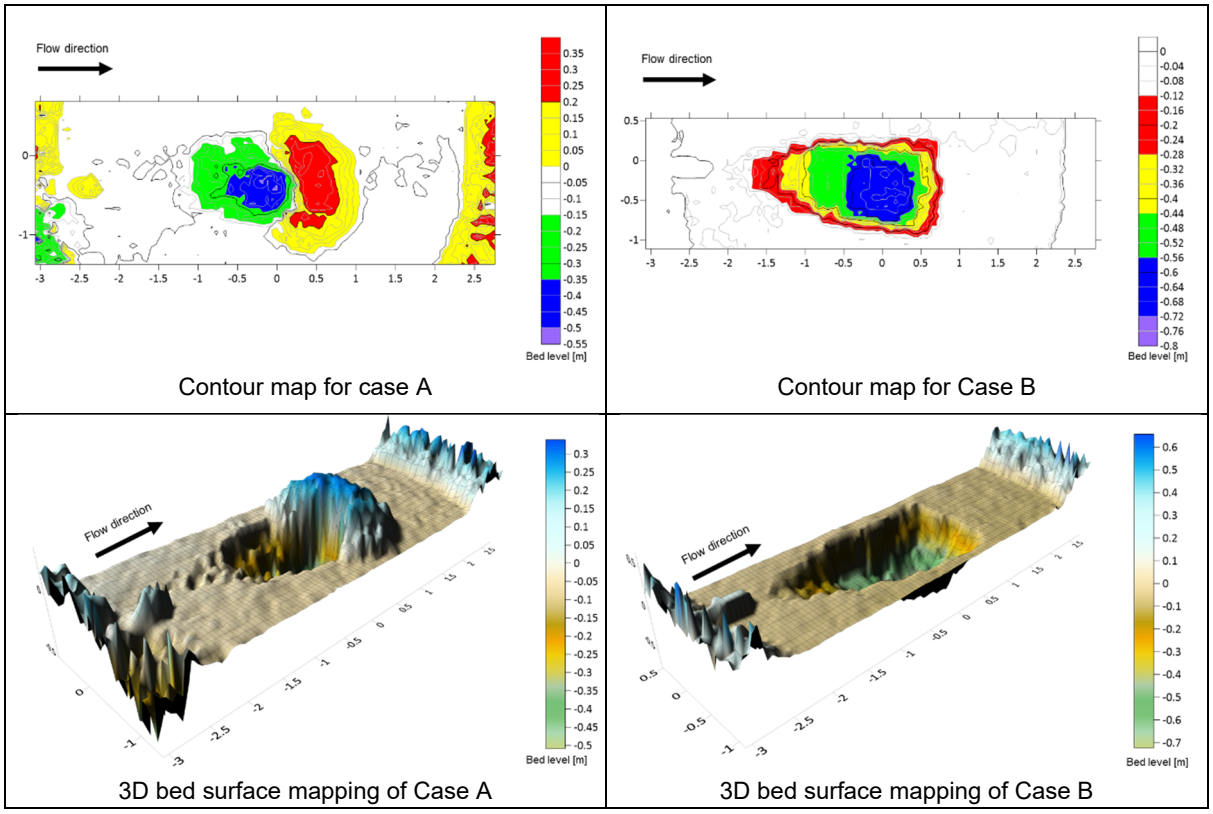

Figure G.11: Equilibrium bed levels for Test5.1A (Q_{med}, H_{med}, TWD_{min}) for Case A (scour and deposition) and B (scour with deposited rocks removed)

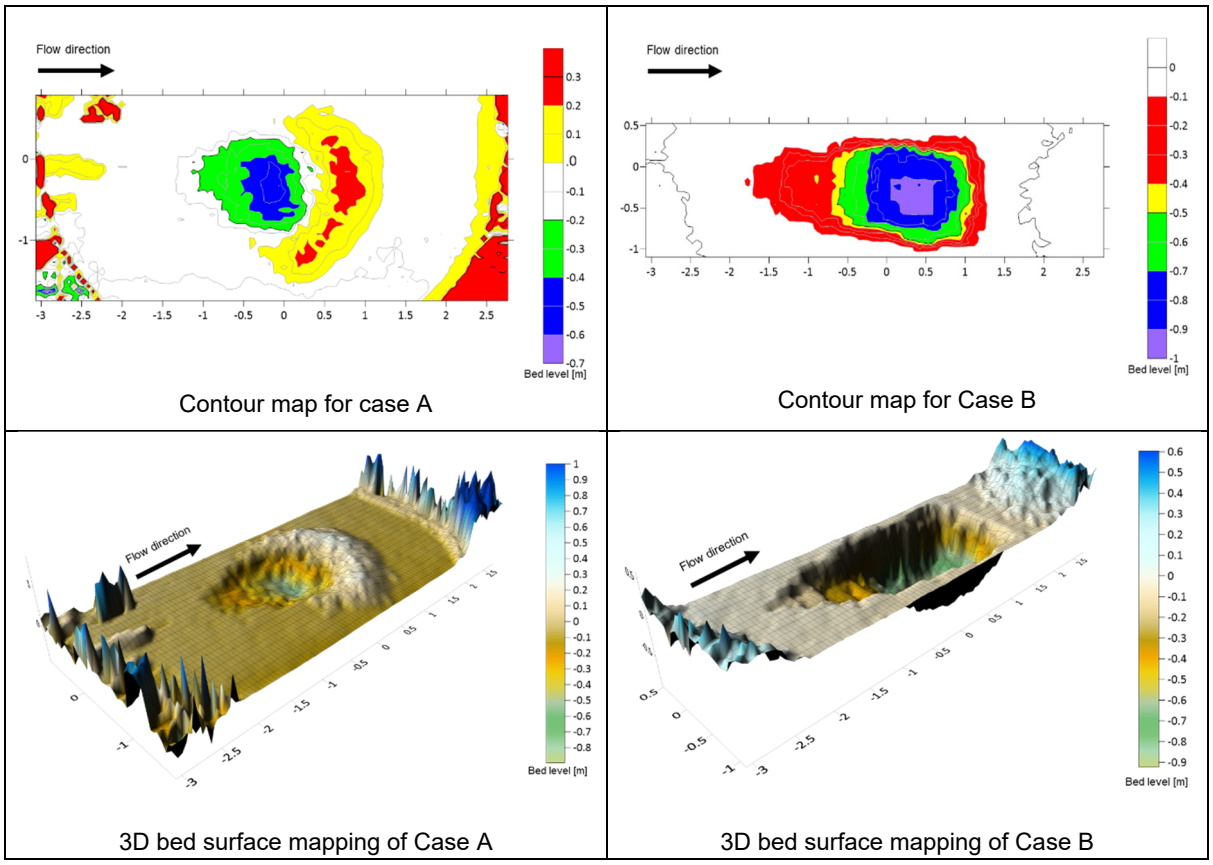

Figure G.12: Equilibrium bed levels for Test6.1A (Q_{max}, H_{med}, TWD_{min}) for Case A (scour and deposition) and B (scour with deposited rocks removed)

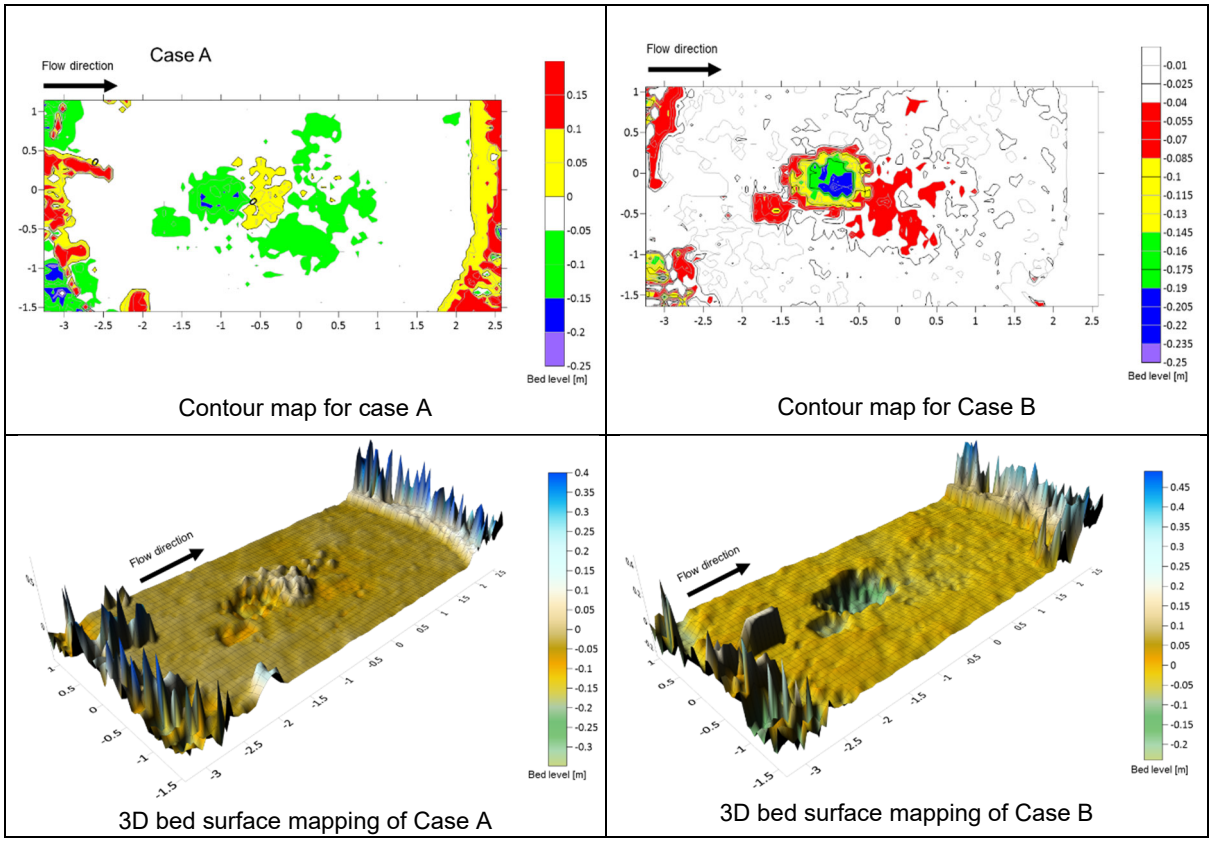

Figure G.13: Equilibrium bed levels for Test7A (Q_{min}, H_{max}, TWD_{max}) for Case A (scour and deposition) and B (scour with deposited rocks removed)

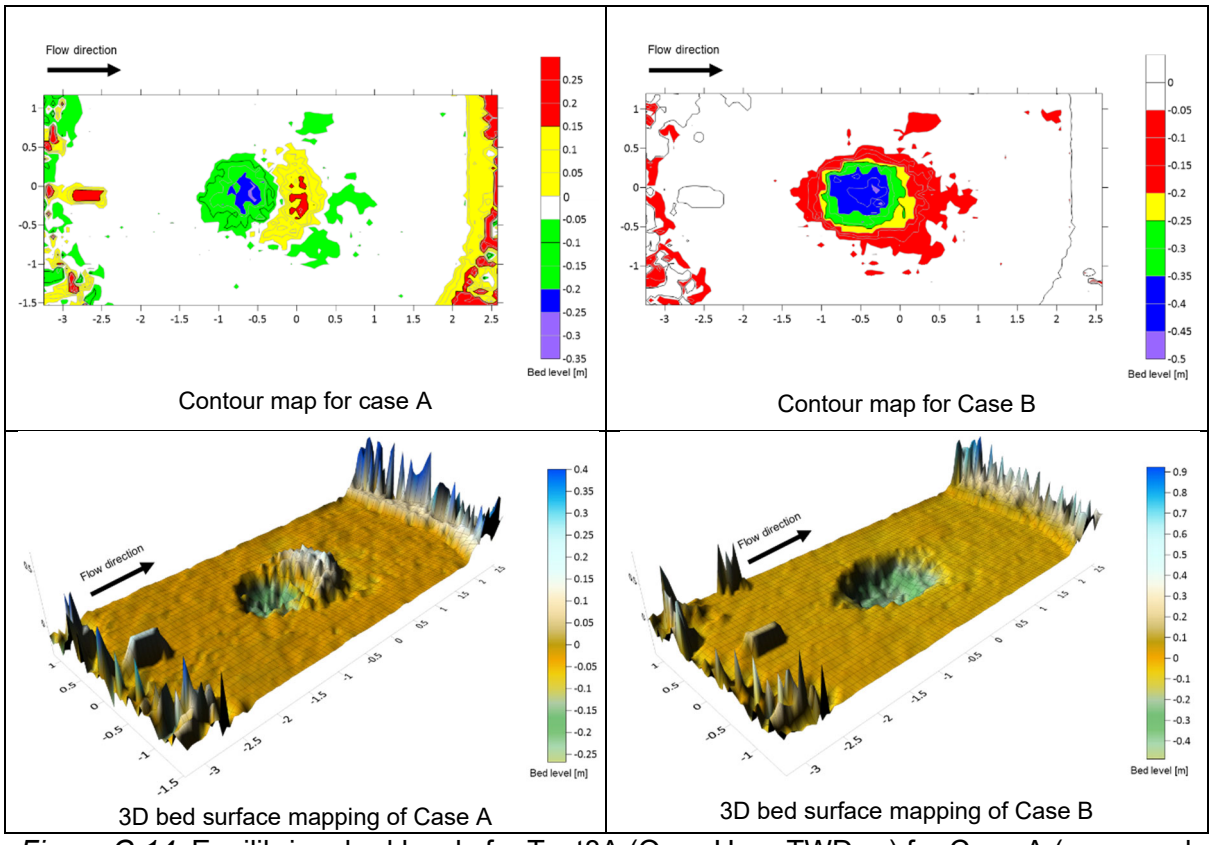

Figure G.14: Equilibrium bed levels for Test8A (Q_{med}, H_{max}, TWD_{max}) for Case A (scour and deposition) and B (scour with deposited rocks removed)

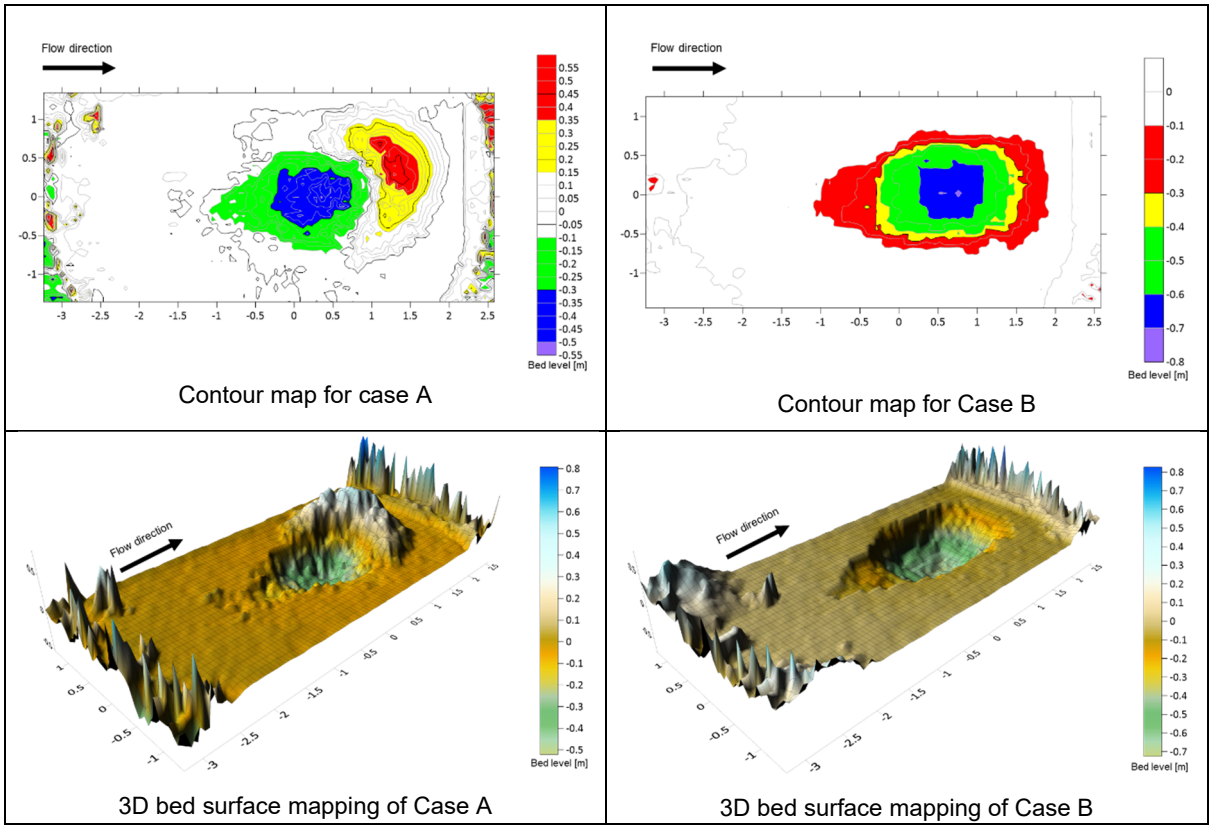

Figure G.15: Equilibrium bed levels for Test9A (Q_{max}, H_{max}, TWD_{max}) for Case A (scour and deposition) and B (scour with deposited rocks removed)

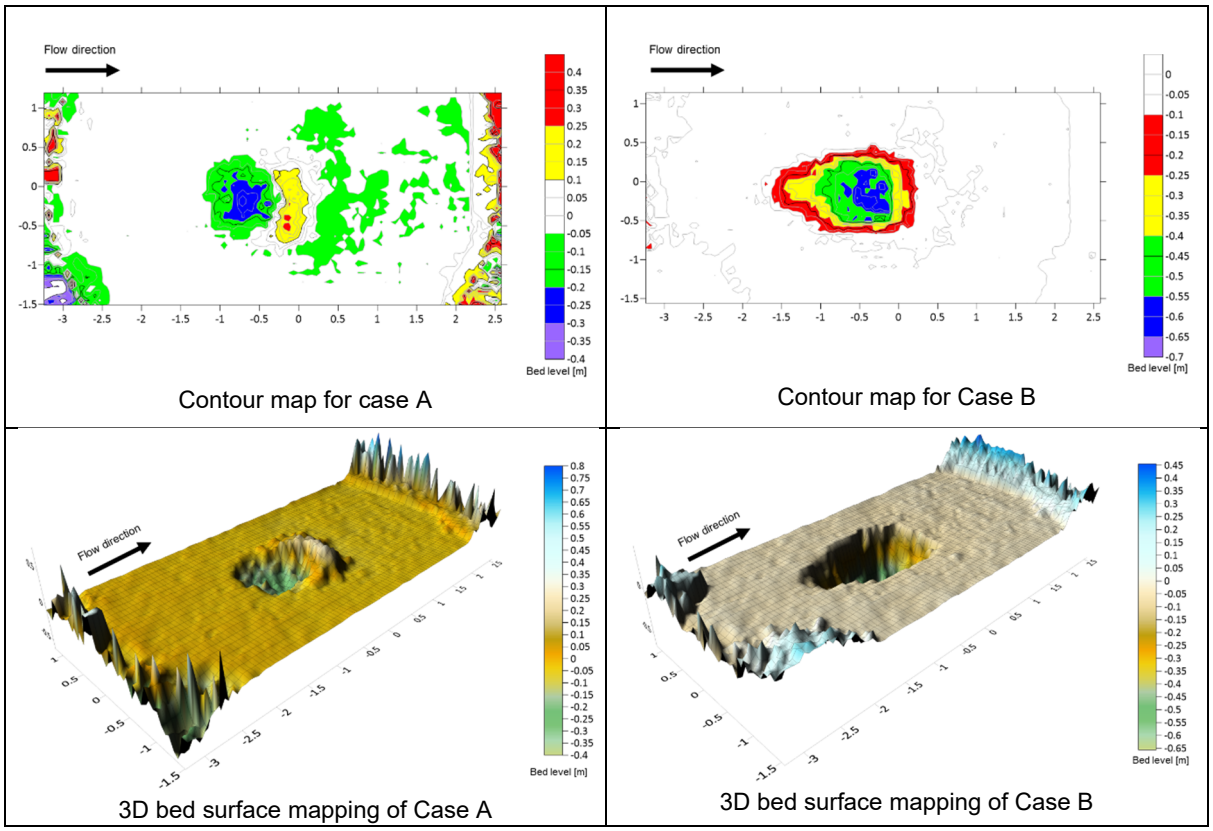

Figure G.16: Equilibrium bed levels for Test7.1A (Q_{min}, H_{max}, TWD_{min}) for Case A (scour and deposition) and B (scour with deposited rocks removed)

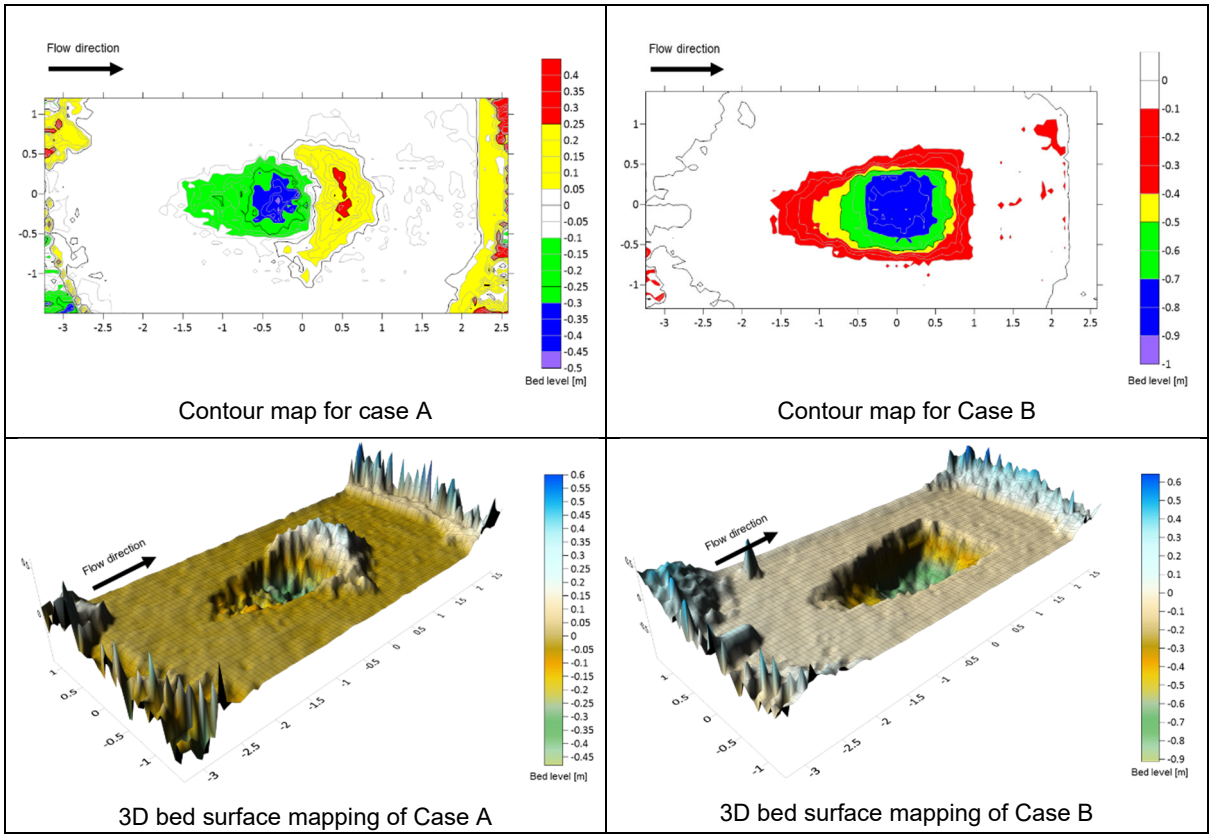

Figure G.17: Equilibrium bed levels for Test8.1A (Q_{med}, H_{max}, TWD_{min}) for Case A (scour and deposition) and B (scour with deposited rocks removed)

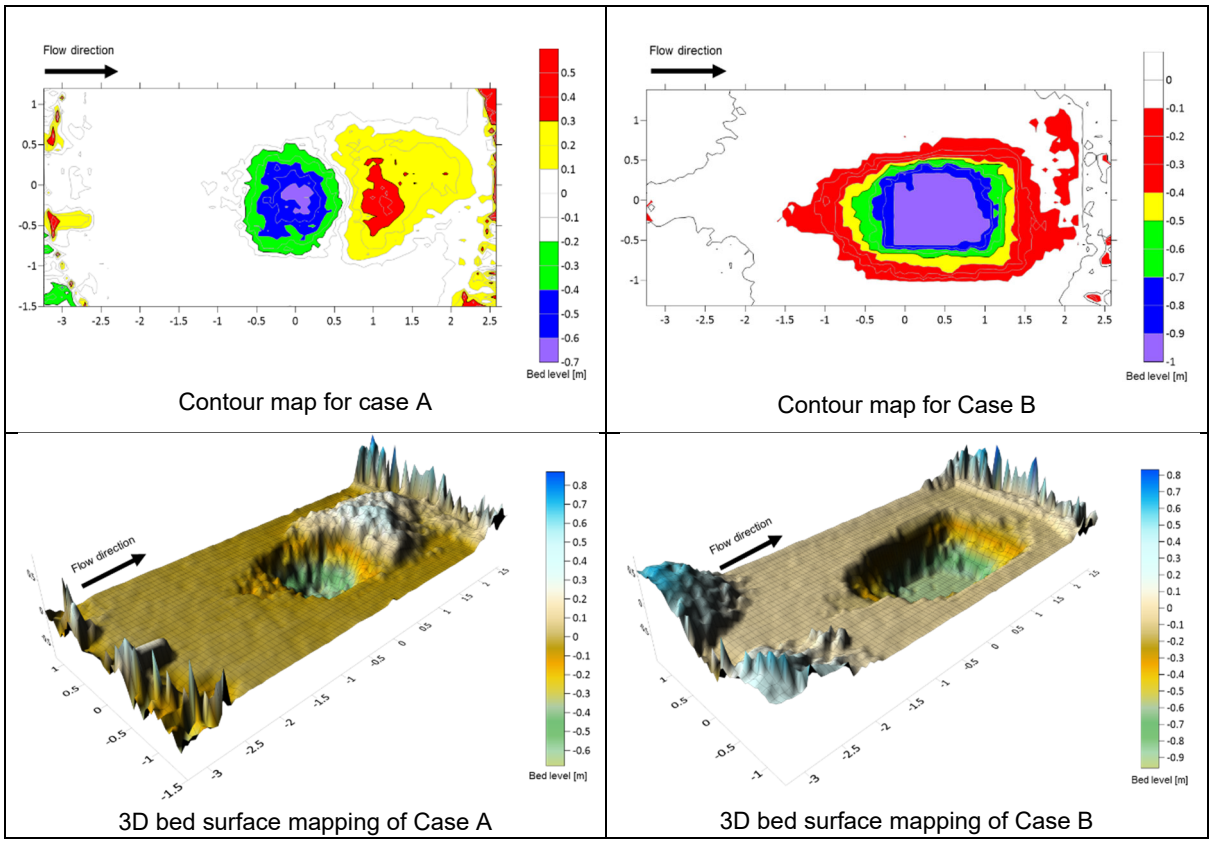

Figure G.18: Equilibrium bed levels for Test9.1A (Q_{max}, H_{max}, TWD_{min}) for Case A (scour and deposition) and B (scour with deposited rocks removed)

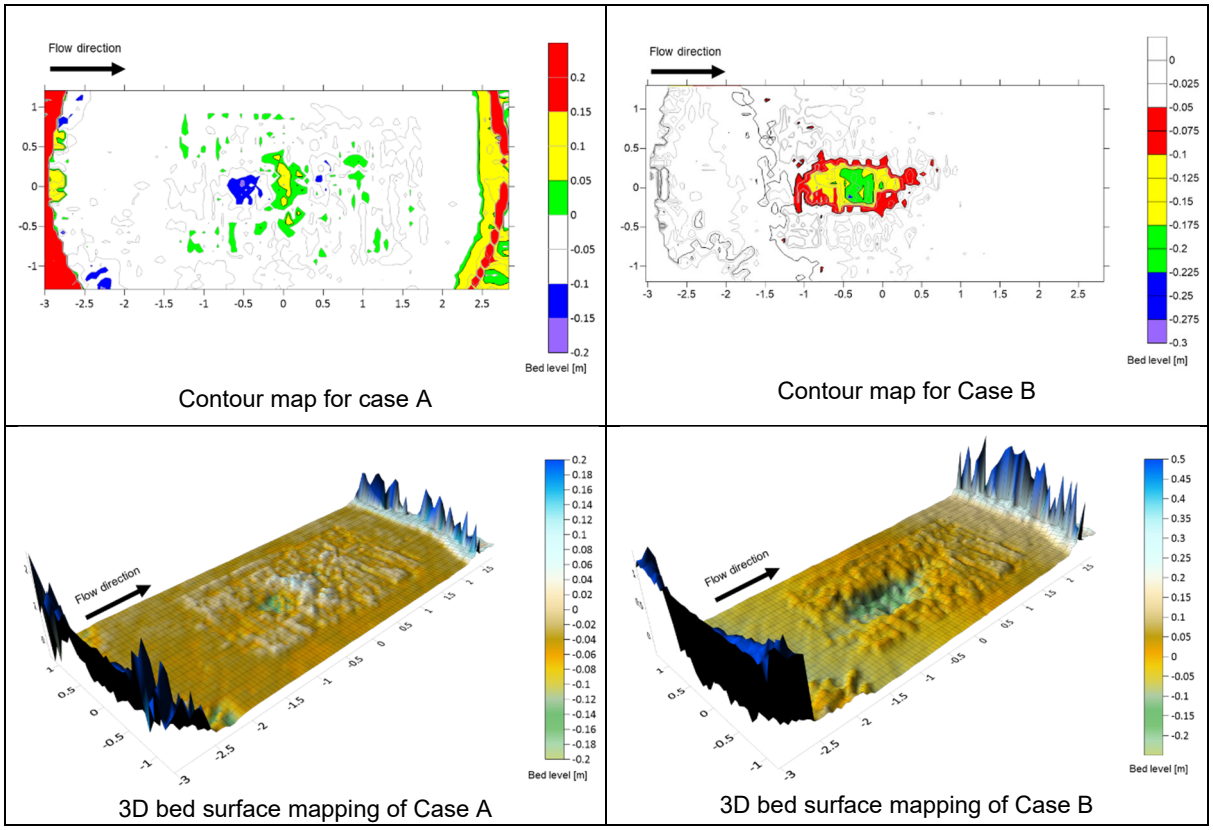

Figure G.19: Equilibrium bed levels for Test10A (Q_{min}, H_{max}, TWD_{max}, joint against flow) for Case A (scour and deposition) and B (scour with deposited rocks removed)

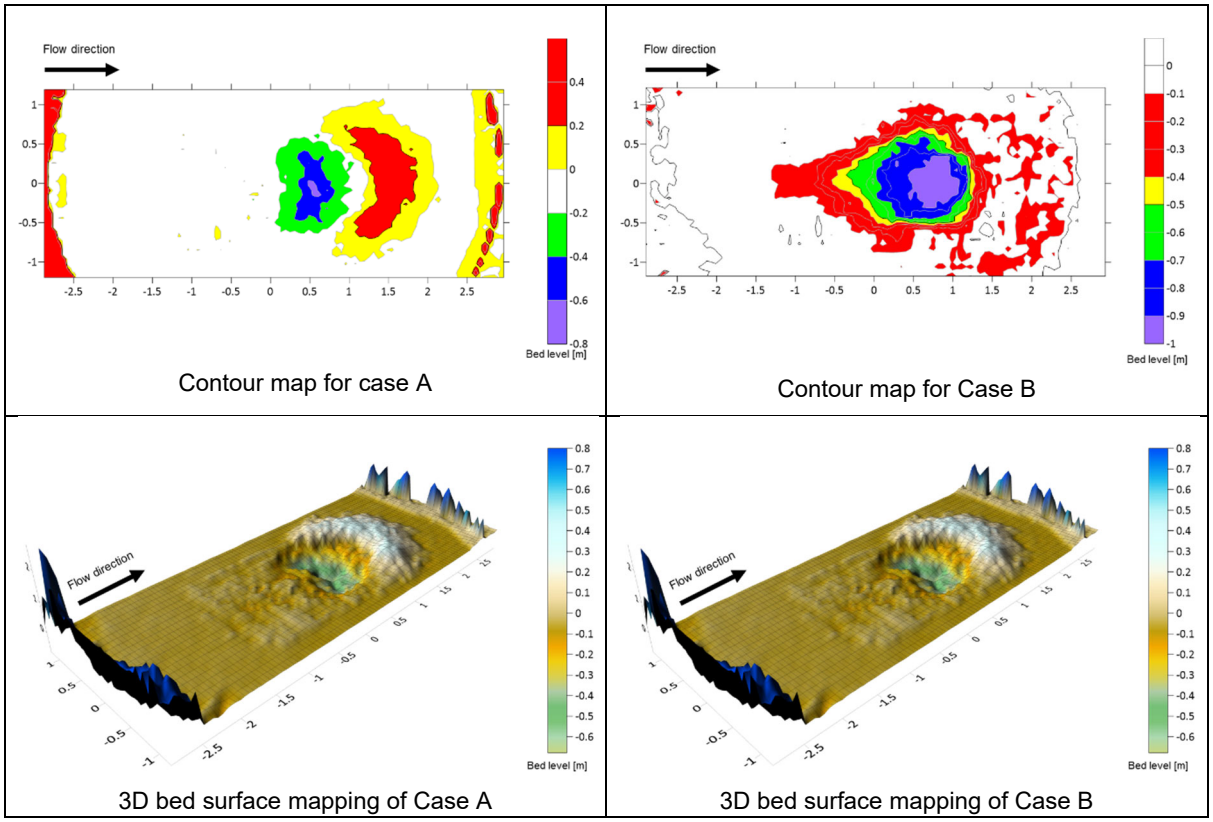

Figure G.20: Equilibrium bed levels for Test10.1A (Q_{min}, H_{max}, TWD_{min}, joint against flow) for Case A (scour and deposition) and B (scour with deposited rocks removed)

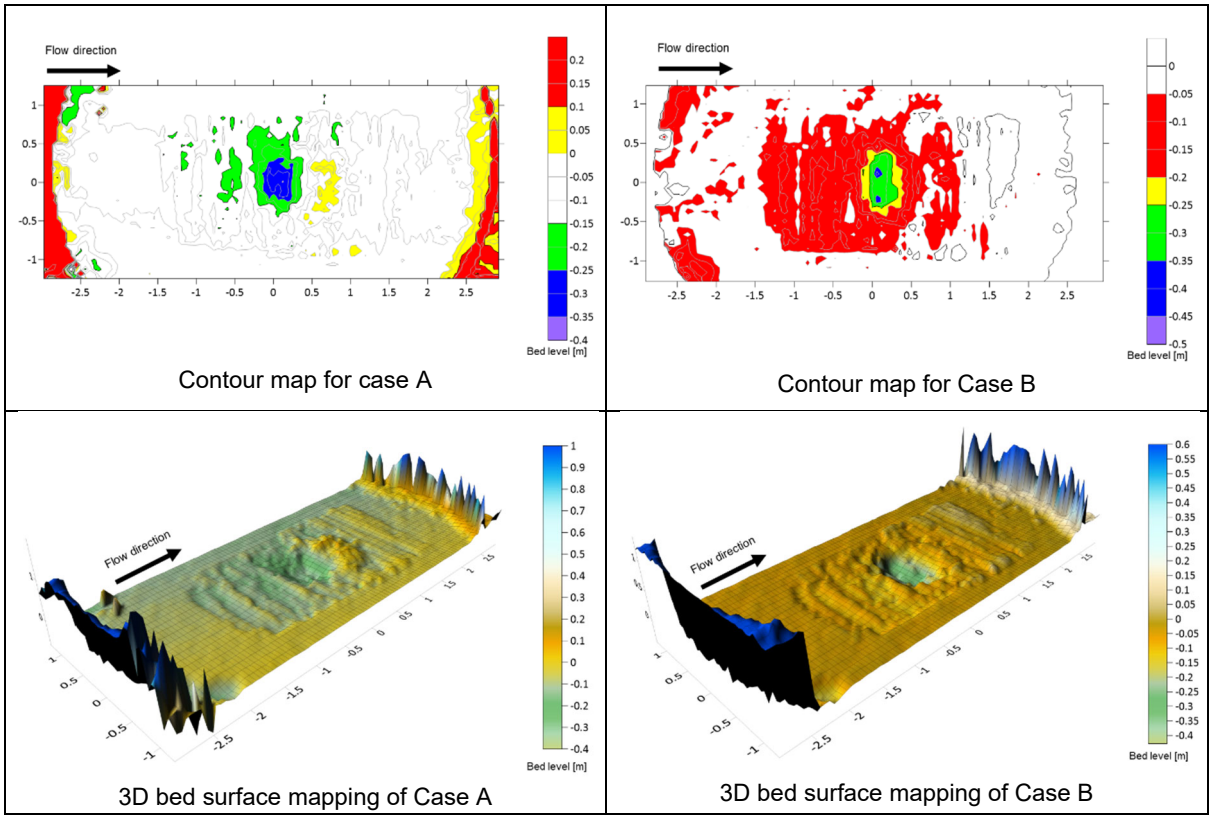

Figure G.21: Equilibrium bed levels for Test11A (Q_{min}, H_{max}, TWD_{max}, joint with flow) for Case A (scour and deposition) and B (scour with deposited rocks removed)

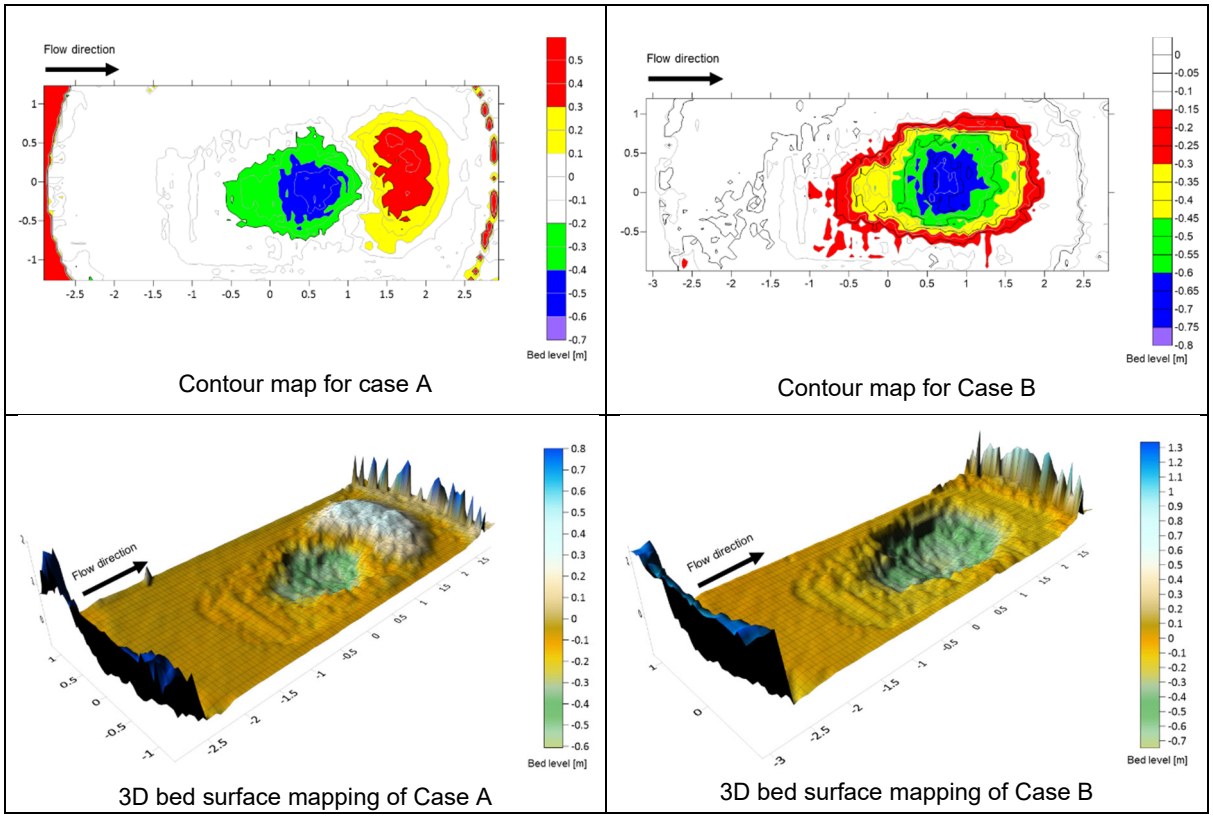

Figure G.22: Equilibrium bed levels for Test12A (Q_{max}, H_{max}, TWD_{max}, joint with flow) for Case A (scour and deposition) and B (scour with deposited rocks removed)

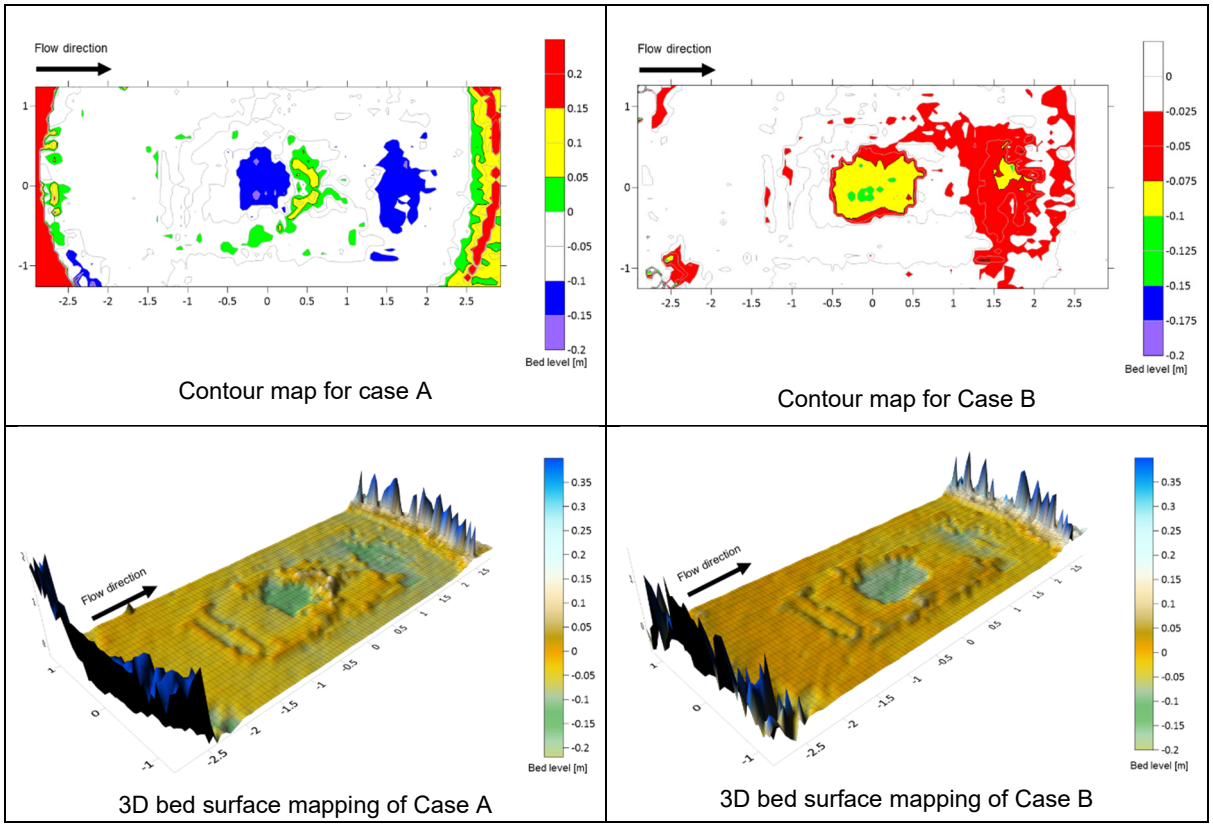

Figure G.23: Equilibrium bed levels for Test13A (Q_{min}, H_{max}, TWD_{max}, large blocks) for Case A (scour and deposition) and B (scour with deposited rocks removed)

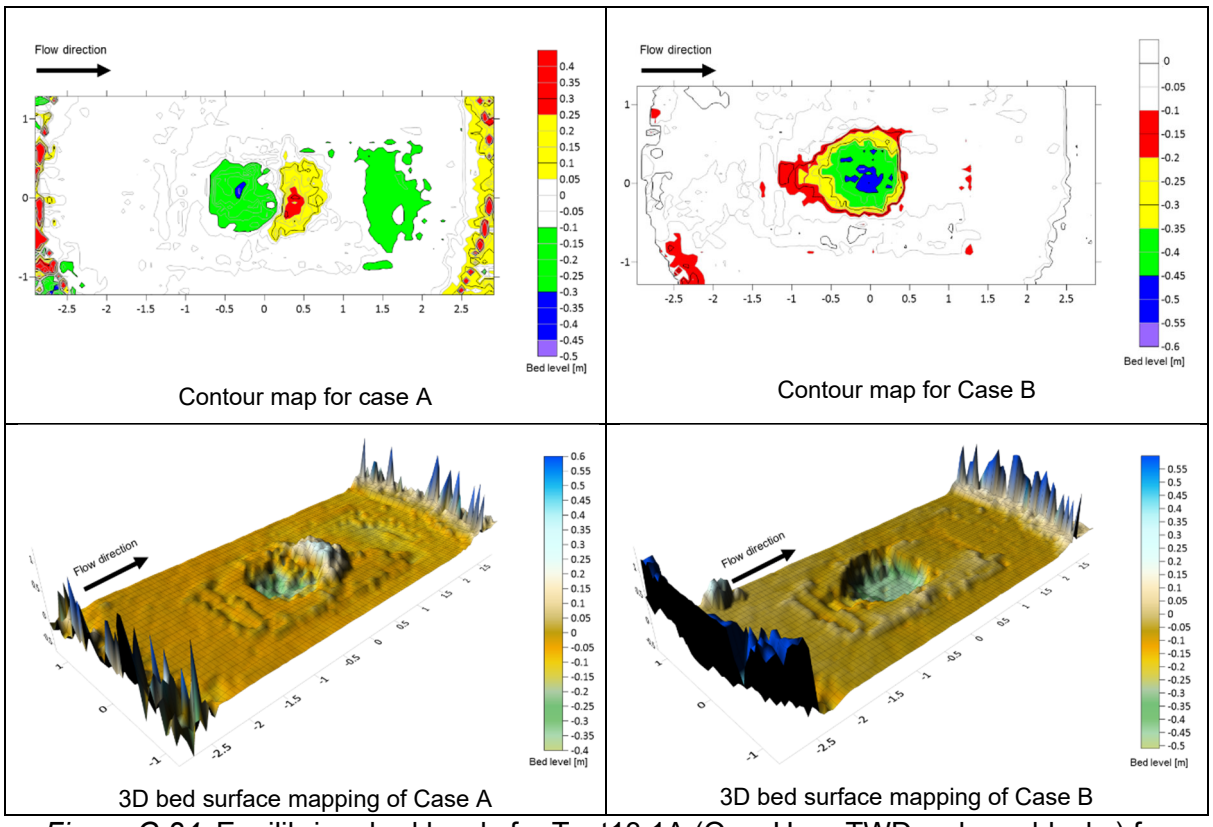

Figure G.24: Equilibrium bed levels for Test13.1A (Q_{min}, H_{max}, TWD_{min}, large blocks) for Case A (scour and deposition) and B (scour with deposited rocks removed)

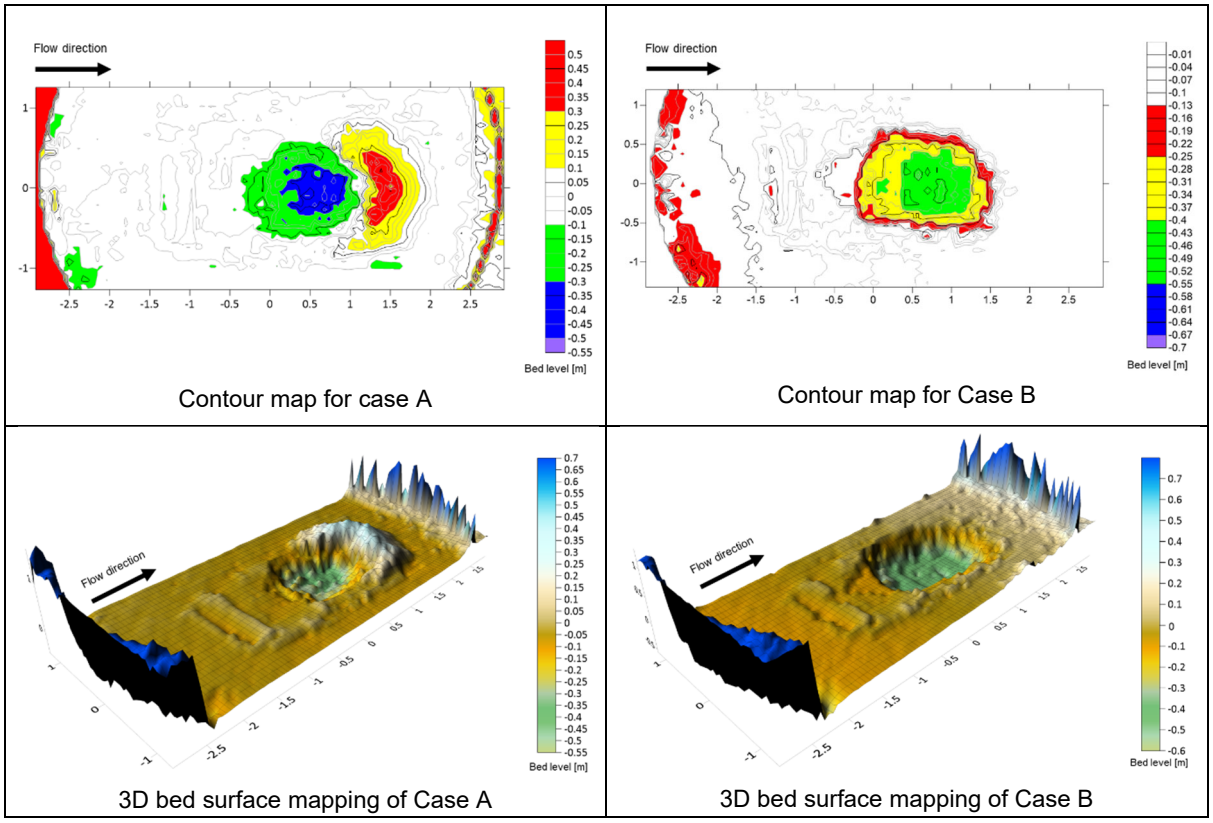

Figure G.25: Equilibrium bed levels for Test14A (Q_{max}, H_{max}, TWD_{max}, large blocks) for Case A (scour and deposition) and B (scour with deposited rocks removed)

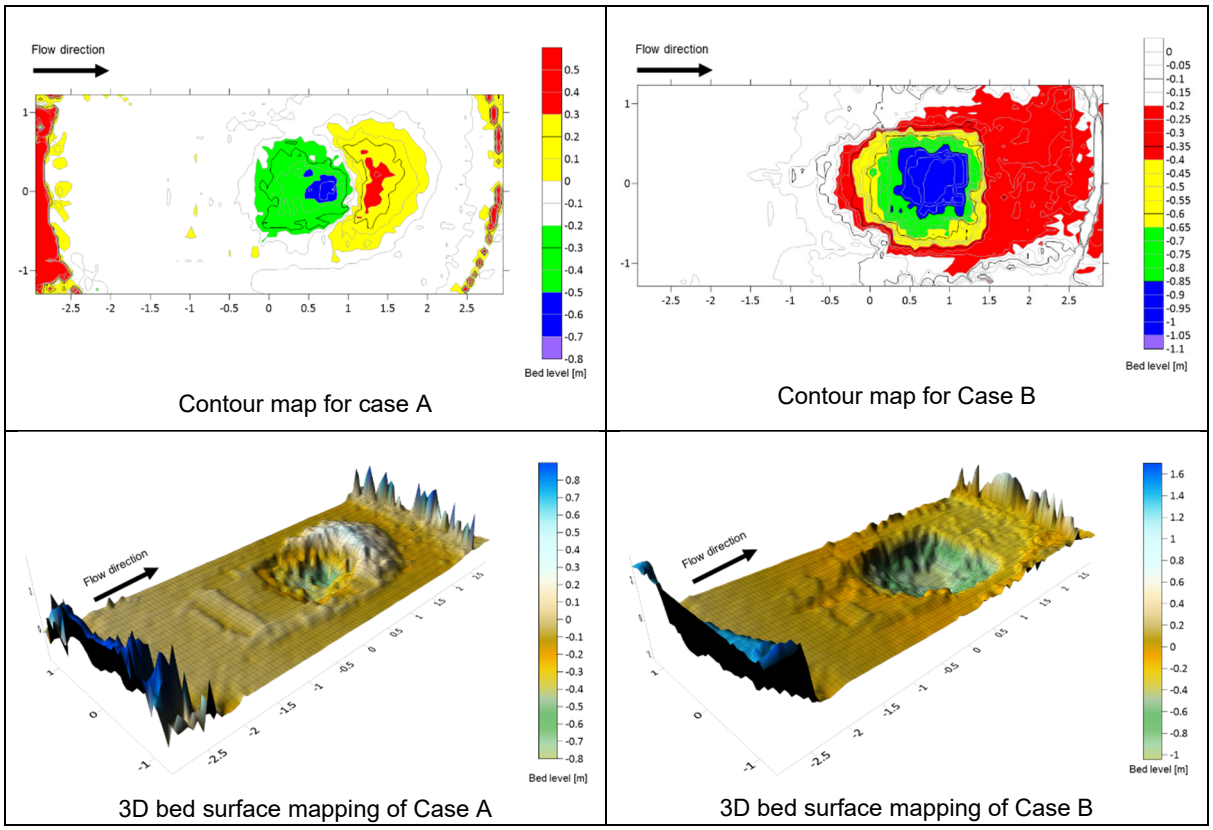

Figure G.26: Equilibrium bed levels for Test14.1A (Q_{max}, H_{max}, TWD_{min}, large blocks) for Case A (scour and deposition) and B (scour with deposited rocks removed)

G.3 Scour depth results for Case A compared to scour prediction methods from literature

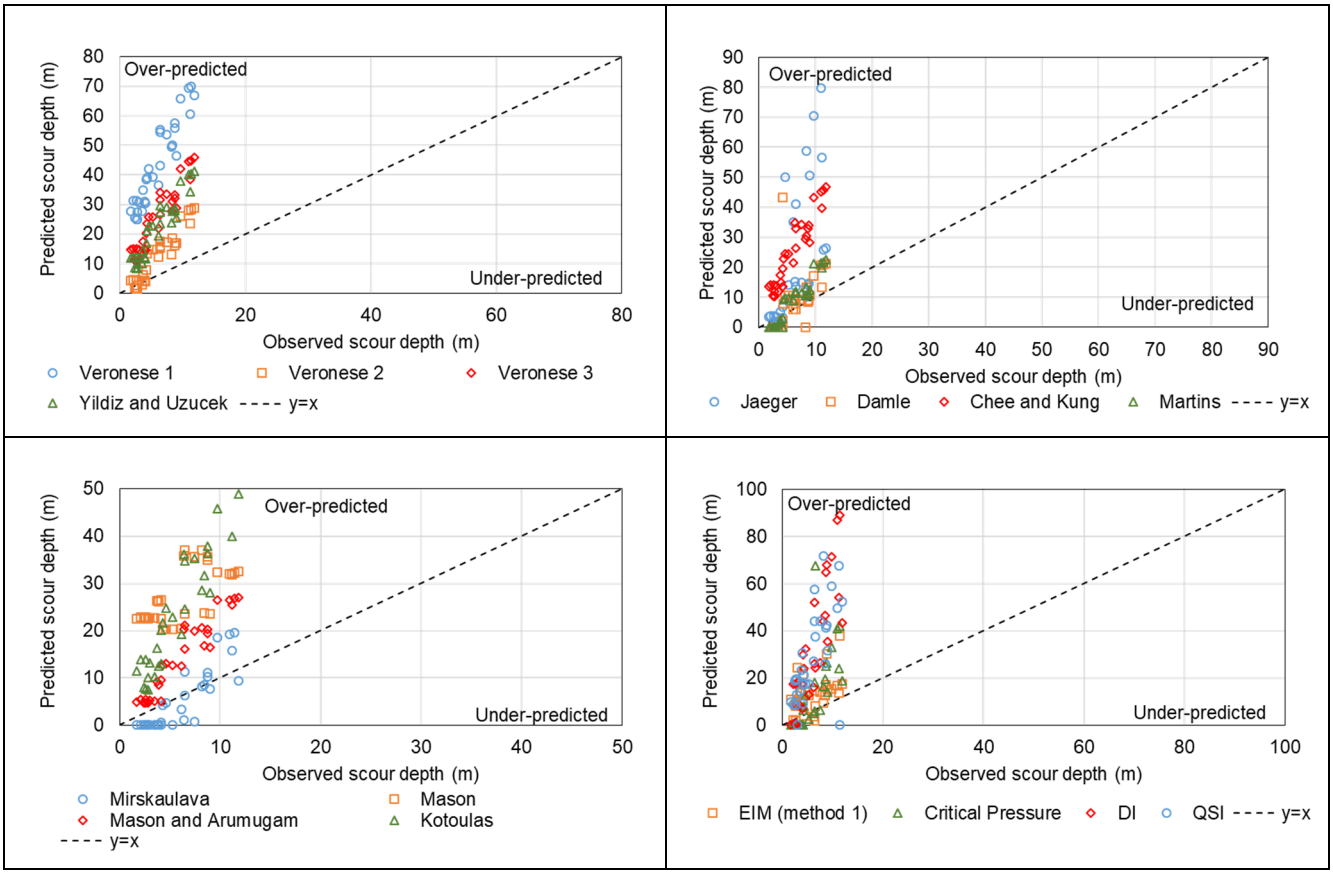

Figure G.27: Comparison of equilibrium scour depths observed from experimental tests and predicted by the different methods for Case A

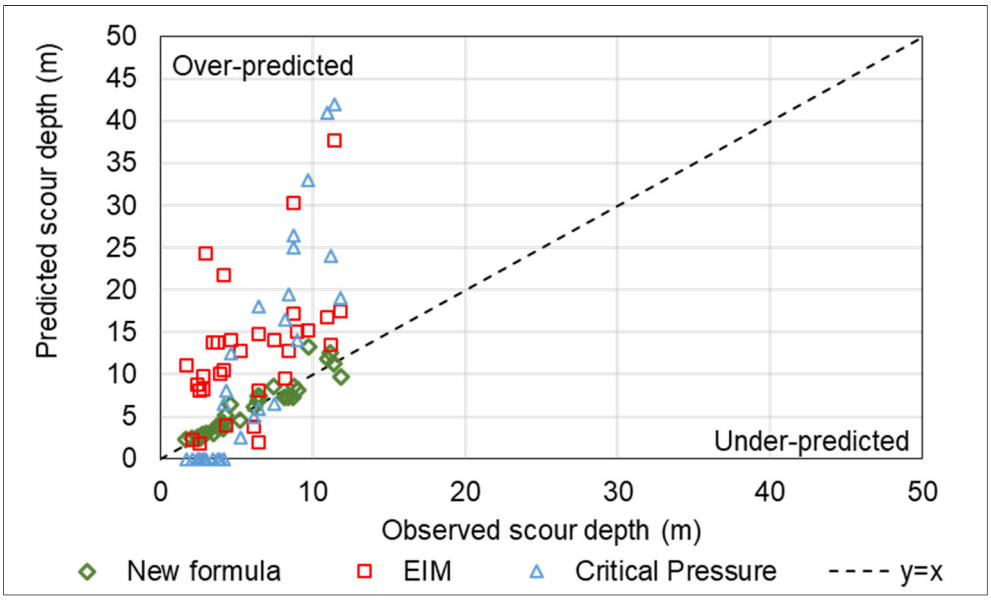

Figure G.28: Scour hole depth comparison between regression formula from this study and EIM and Critical Pressure methods for Case A

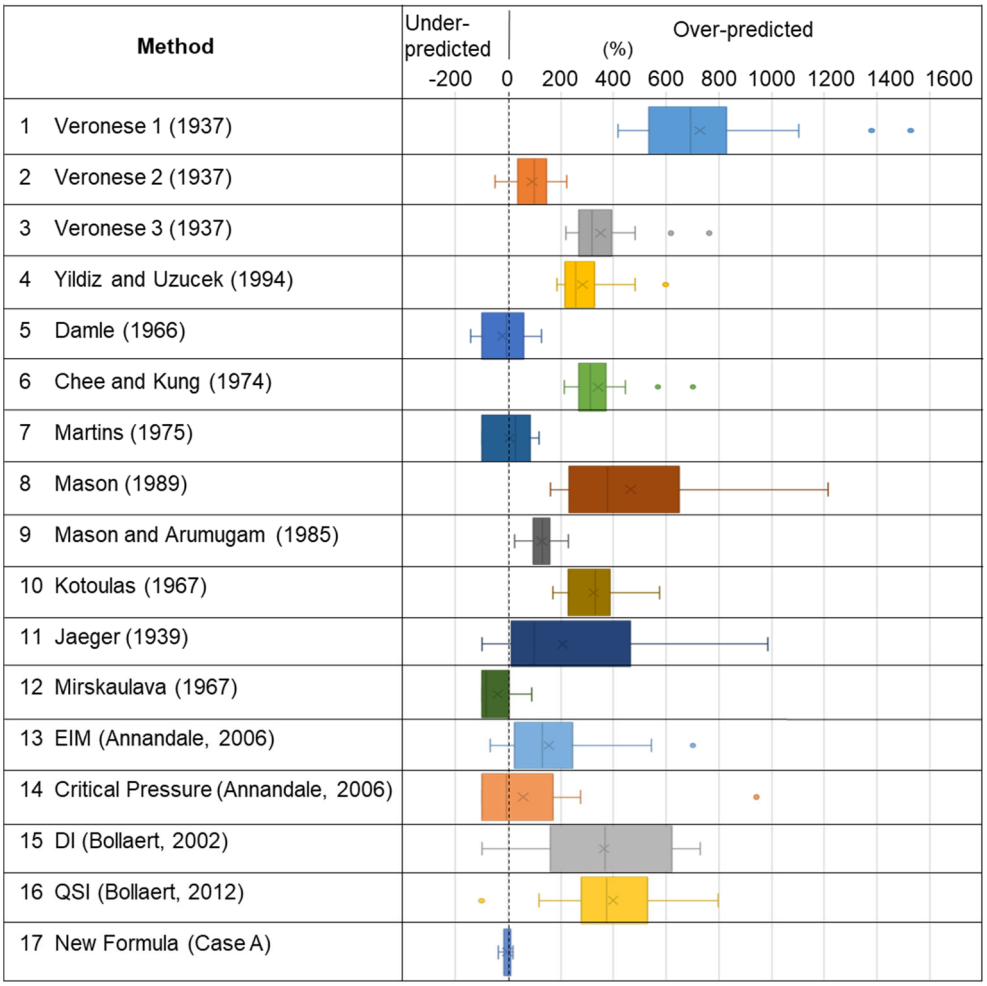

Figure G.29: Scour depth distribution as a percentage difference for the different scour prediction methods from the experimental work for Case A

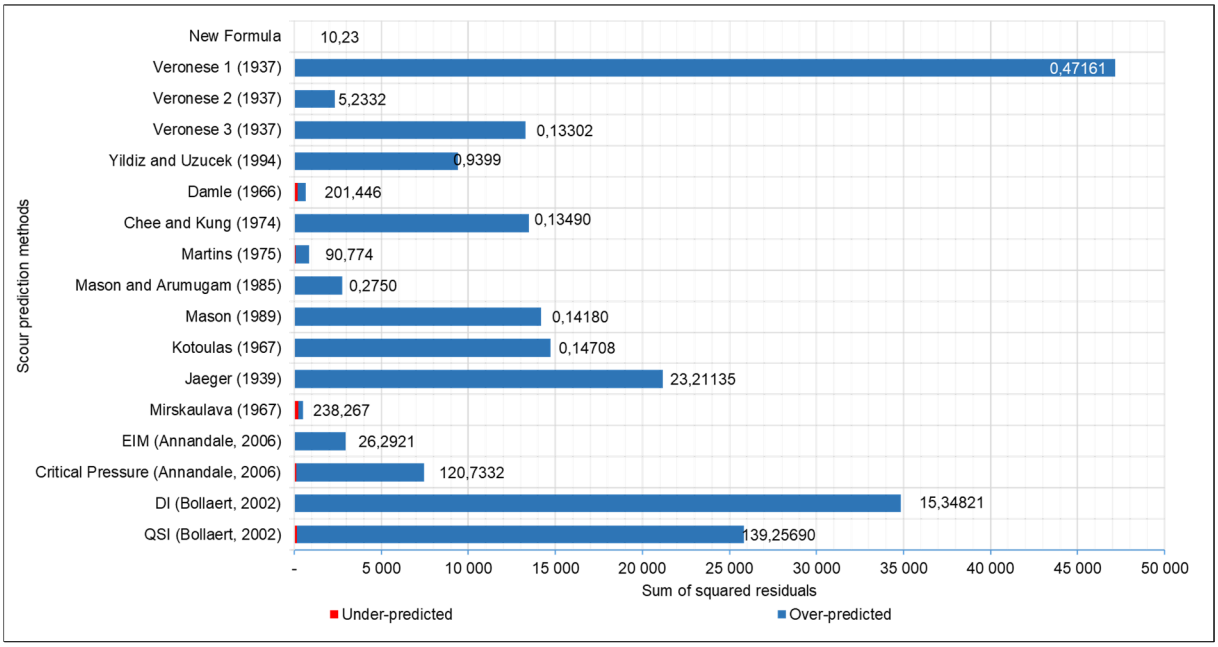

Figure G.30: Comparison of the sum of squared residuals for the various scour prediction methods for Case A

ANNEXURE H: STATISTICAL PARAMETERS REQUIRED FOR REGRESSION ANALYSIS

The coefficient of determination, R^2, is defined as:

$$R^2 = \left[\frac{1}{n} \cdot \frac{\sum(x_i - \bar{x}) \cdot (y_i - \bar{y})}{\sigma_x \cdot \sigma_y}\right]^2 \qquad \textit{Equation H.1}$$

where:

n: total sample size

x_i: x-value for observation i

$\bar{x}$: mean x-value

y_i: y-value for observation i

$\bar{y}$: mean y-value

σ_x: standard deviation of x

σ_y: standard deviation of y

The adjusted R^2 value is calculated by:

$$R^2_{adj} = 1 - \left[\frac{(1 - R^2) \cdot (n - 1)}{n - k - 1}\right] \qquad \textit{Equation H.2}$$

where:

k: number of independent variables in the model, excluding the constant

The mean absolute error (MAE) is defined as:

$$MAE = \frac{1}{n}\sum_{j=1}^{n}|z_j - z| \qquad \textit{Equation H.3}$$

where:

z_j: predicted value

z: observed value

The root mean square error (RMSE) is given by:

$$RMSE = \sqrt{\frac{1}{n}\sum_{j=1}^{n}\left(z_j - z\right)^2} \qquad \textit{Equation H.4}$$

The Akaike Information Criterion (AIC) is determined as follows:

$$AIC = n \cdot ln\left(\frac{SS_{error}}{n}\right) + 2k \qquad \textit{Equation H.5}$$

where

n: number of observations

SS_{error}: log sums of squared error

k: number of parameters of fit +1

The Log-likelihood is calculated as follows:

$$LL = -\frac{n}{2}ln(2\pi) - \frac{n}{2}ln(\sigma^2) - \frac{1}{2\sigma^2}\sum_{i=1}^{n}(x_i - \mu)^2 \qquad \textit{Equation H.6}$$

where

σ^2: variance

μ: mean

ANNEXURE I: NUMERICAL SIMULATION RESULTS

I.1 Hydrodynamic results for the Calibration and Confirmation tests for Case A

The hydrodynamic results for a jet impinging onto a bed emulating the experimental scour hole shape for Case A for the tests used to calibrate the numerical model are shown in Figures I.1 to I.6.

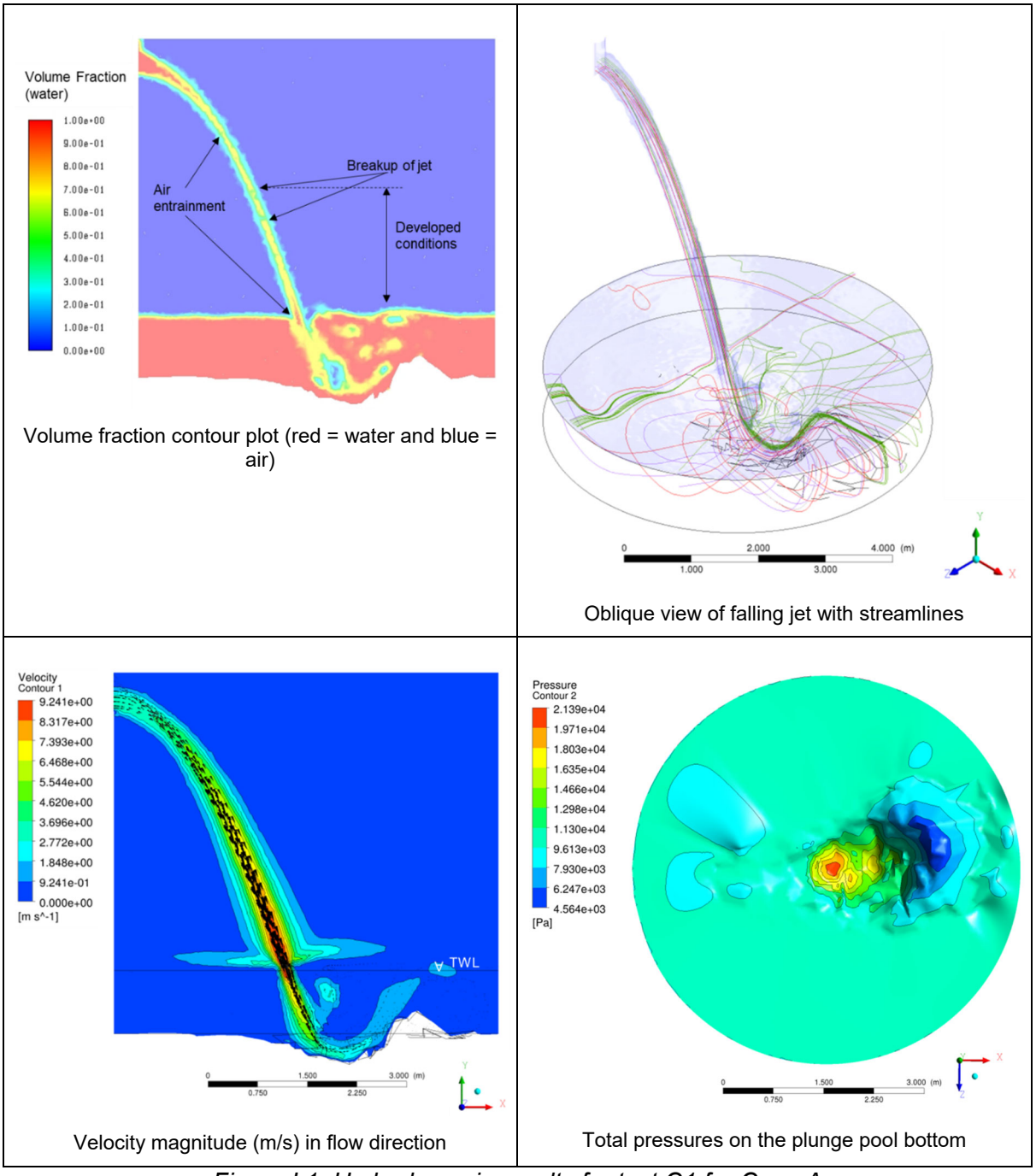

Volume fraction contour plot (red = water and blue = air)

Oblique view of falling jet with streamlines

Velocity magnitude (m/s) in flow direction

Total pressures on the plunge pool bottom

Figure I.1: Hydrodynamic results for test C1 for Case A

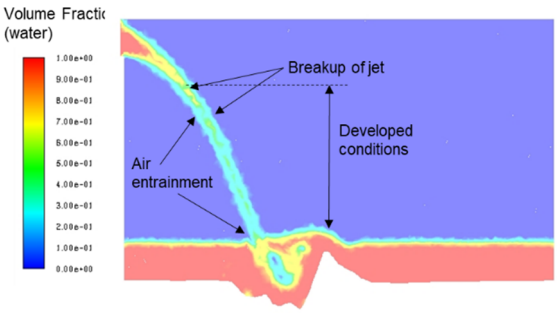

Volume fraction contour plot (red = water and blue = air)

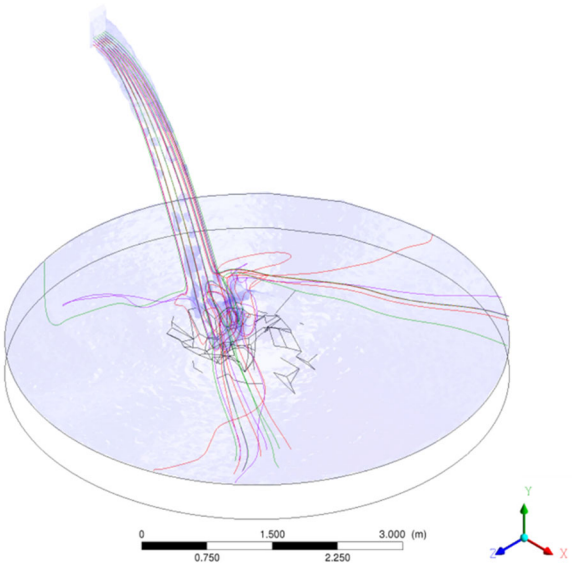

Oblique view of falling jet with streamlines

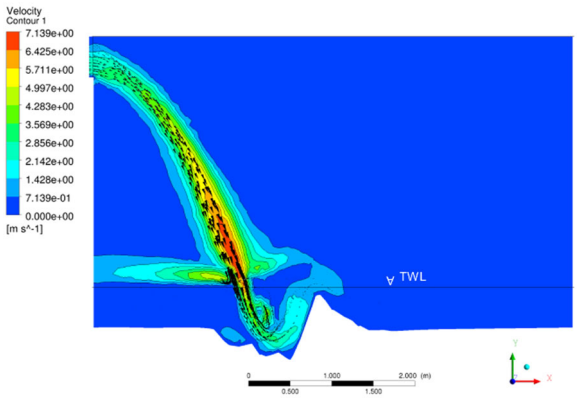

Velocity magnitude (m/s) in flow direction

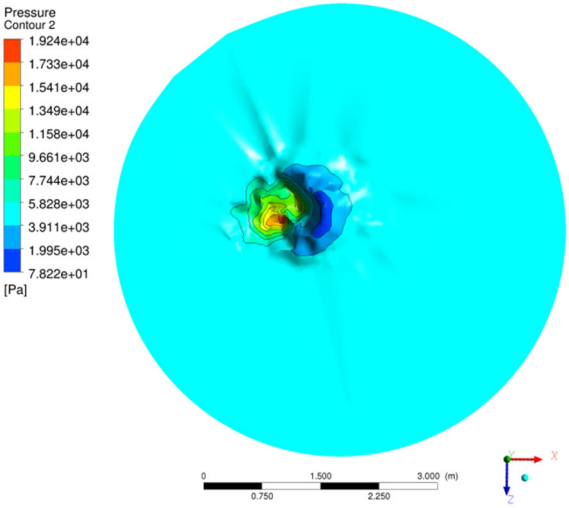

Total pressures on the plunge pool bottom

Figure I.2: Hydrodynamic results for test C2 for Case A

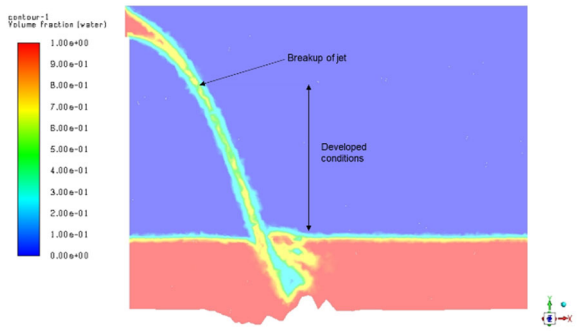

Volume fraction contour plot (red = water and blue = air)

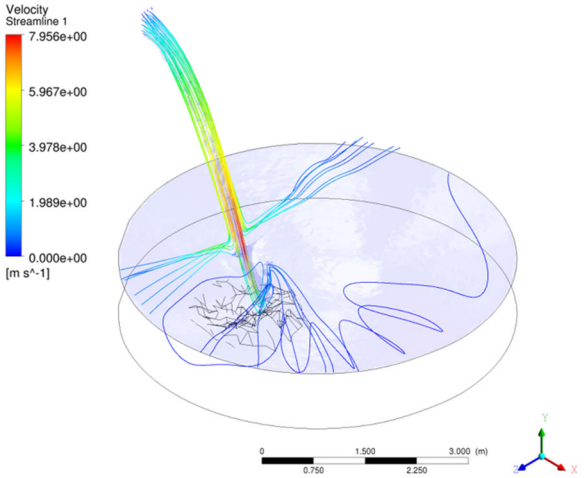

Oblique view of falling jet with streamlines

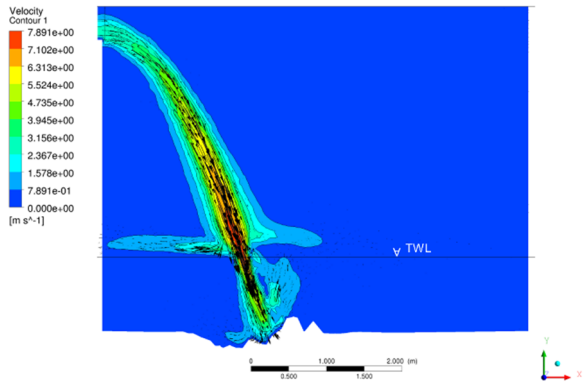

Velocity magnitude (m/s) in flow direction

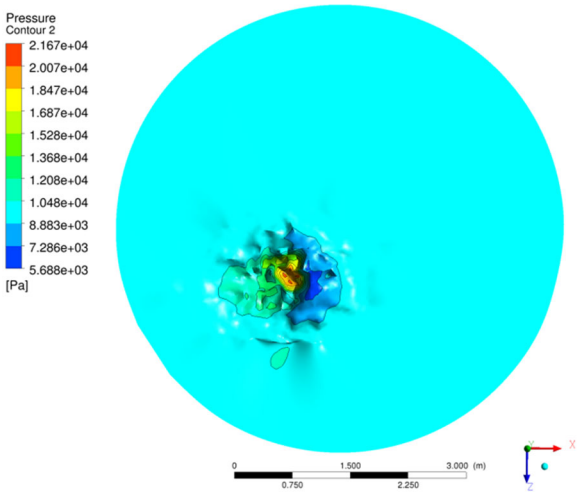

Total pressures on the plunge pool bottom

Figure I.3: Hydrodynamic results for test CF1 for Case A

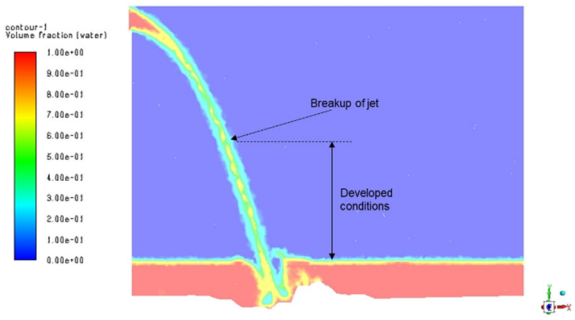

Volume fraction contour plot (red = water and blue = air)

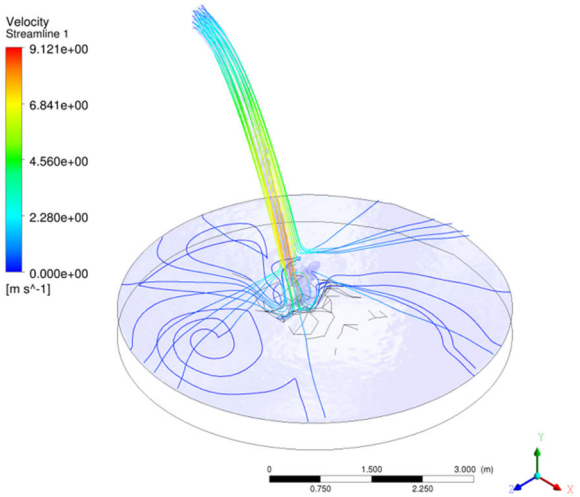

Oblique view of falling jet with streamlines

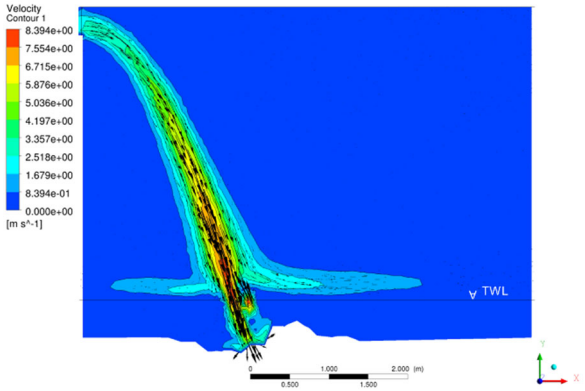

Velocity magnitude (m/s) in flow direction

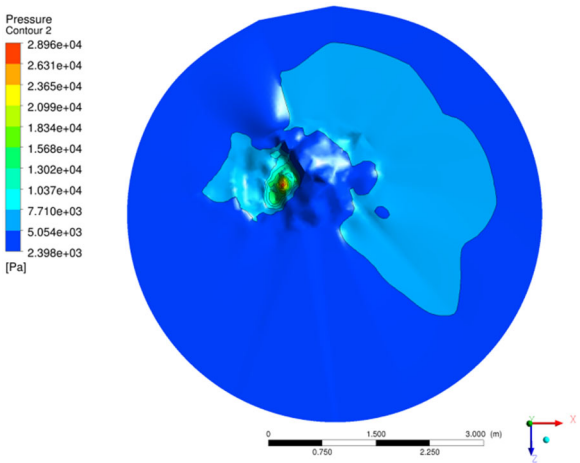

Total pressures on the plunge pool bottom

Figure I.4: Hydrodynamic results for test CF2 for Case A

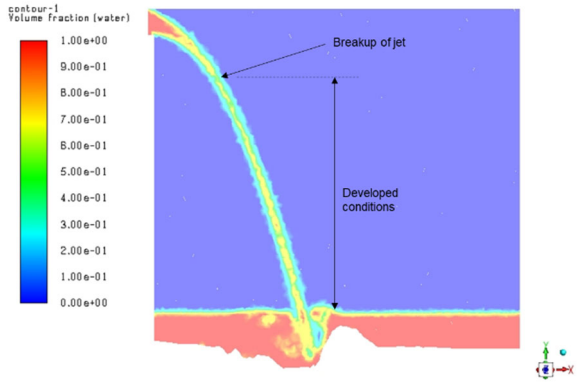

Volume fraction contour plot (red = water and blue = air)

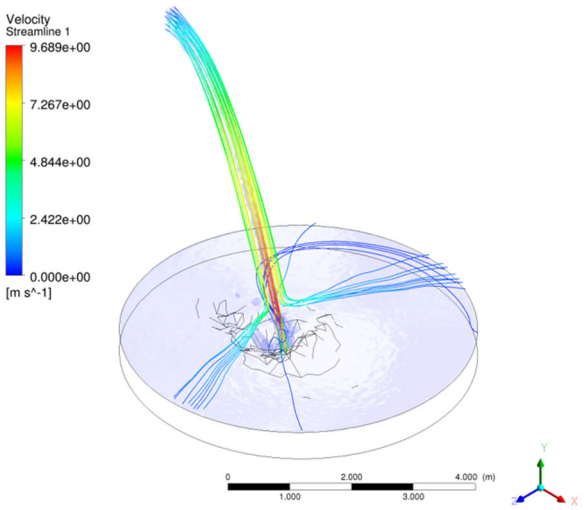

Oblique view of falling jet with streamlines

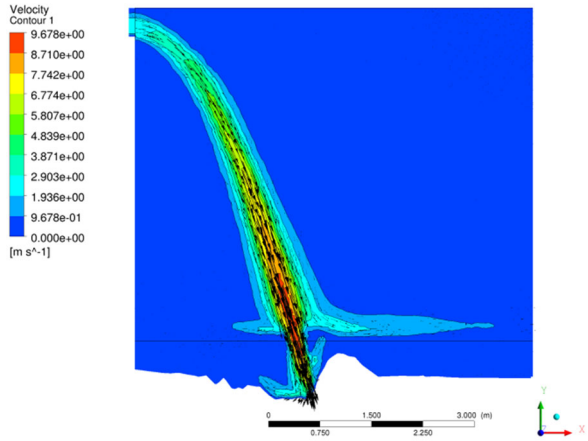

Velocity magnitude (m/s) in flow direction

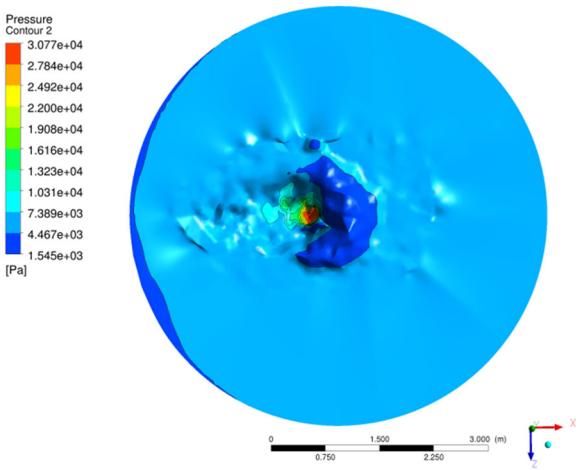

Total pressures on the plunge pool bottom

Figure I.5: Hydrodynamic results for test CF3 for Case A

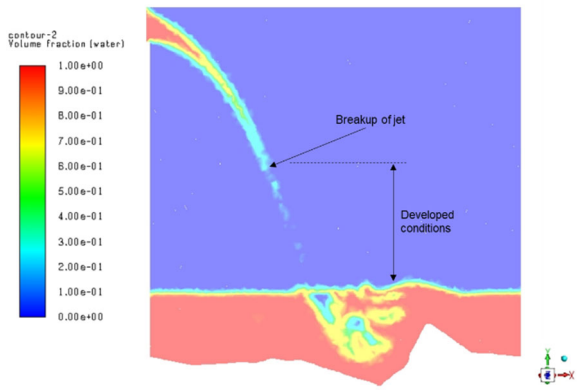

Volume fraction contour plot (red = water and blue = air)

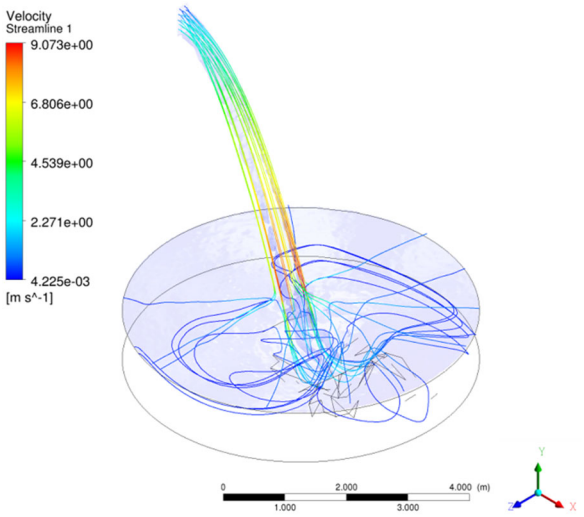

Oblique view of falling jet with streamlines

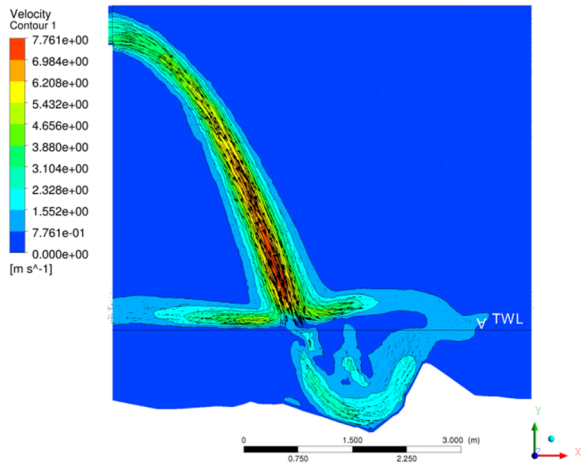

Velocity magnitude (m/s) in flow direction

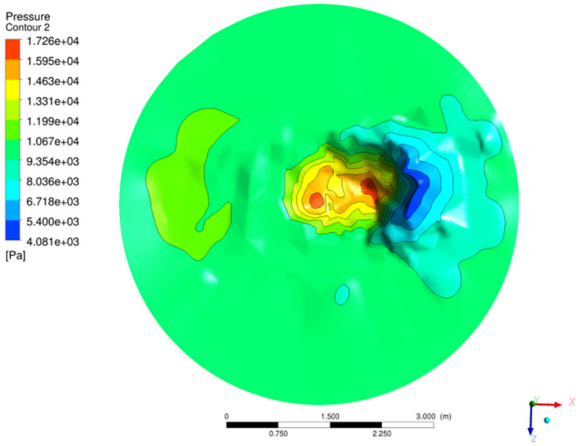

Total pressures on the plunge pool bottom

Figure I.6: Hydrodynamic results for test C3 for Case A

I.2 Hydrodynamic results for the Calibration and Confirmation tests for Case B

The hydrodynamic results for a jet impinging onto an initial flat bed for Case B for the Calibration and Confirmation tests are shown in Figures I.7 to I.15.

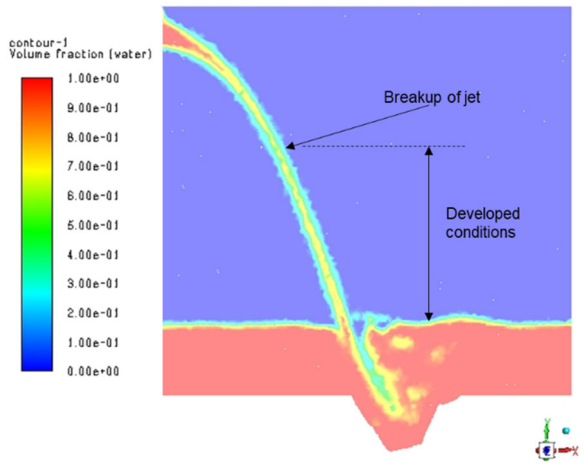

Volume fraction contour plot (red = water and blue = air)

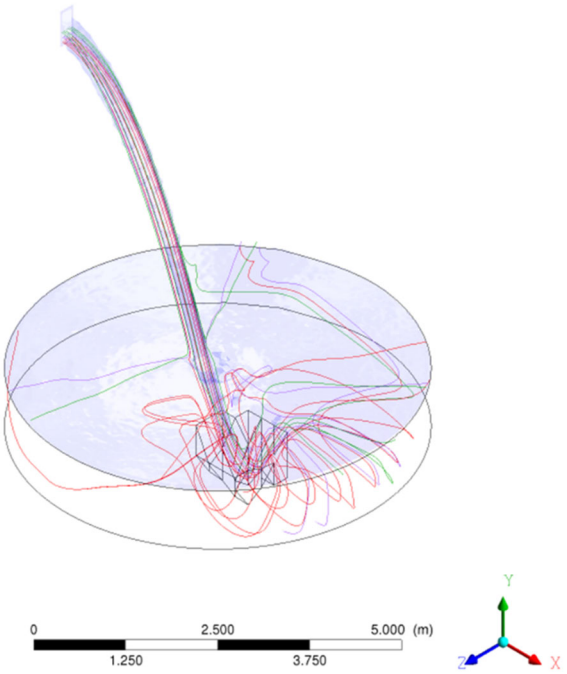

Oblique view of falling jet with streamlines

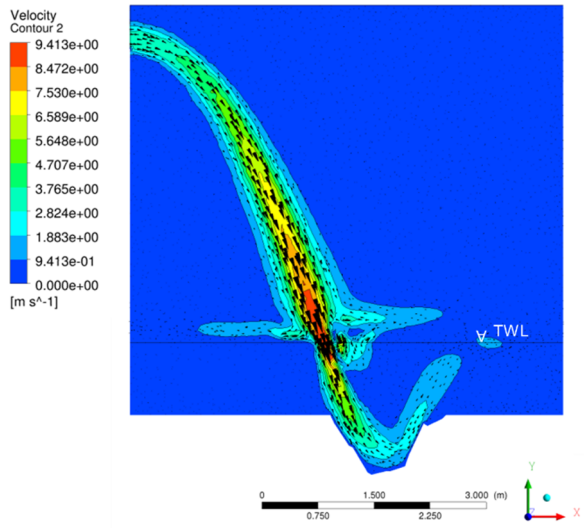

Velocity magnitude (m/s) in flow direction

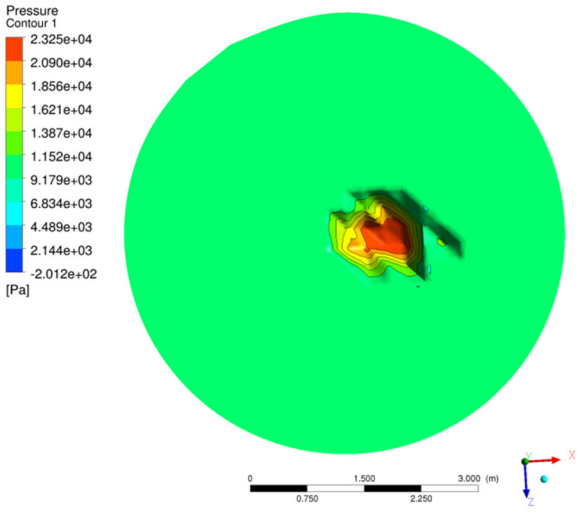

Total pressures on the plunge pool bottom

Figure I.7: Hydrodynamic results for test C1 for Case B

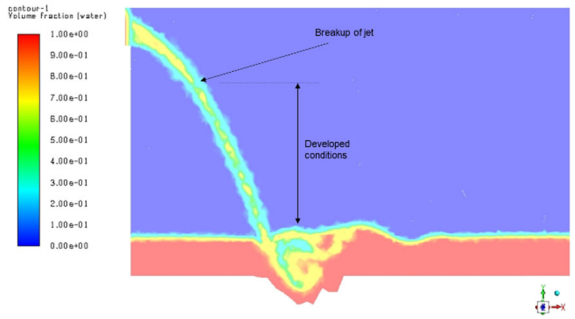

Volume fraction contour plot (red = water and blue = air)

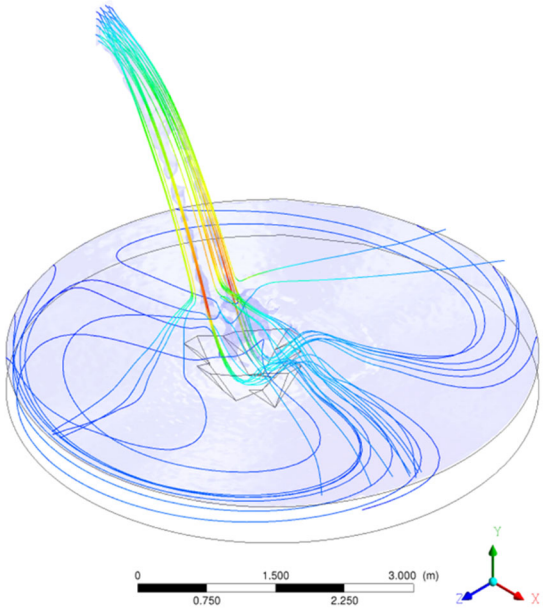

Oblique view of falling jet with streamlines

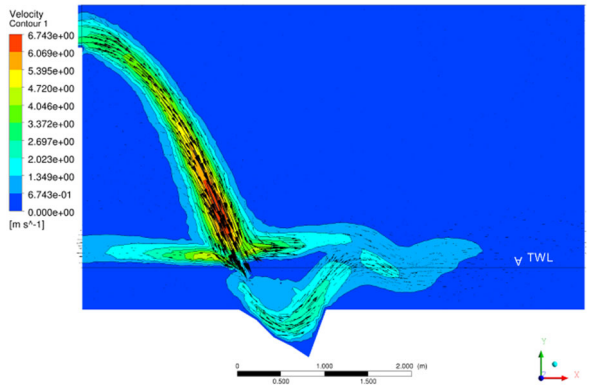

Velocity magnitude (m/s) in flow direction

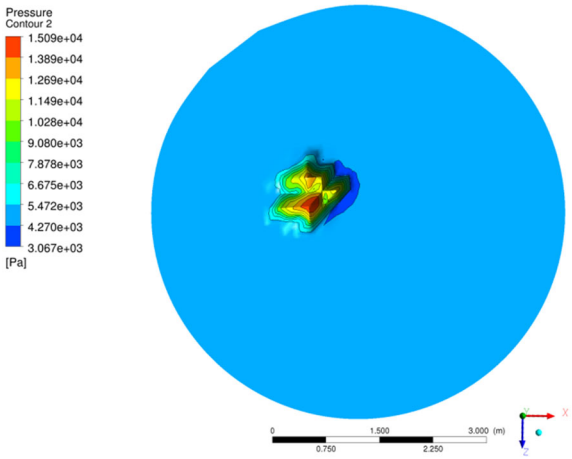

Total pressures on the plunge pool bottom

Figure I.8: Hydrodynamic results for test C2 for Case B

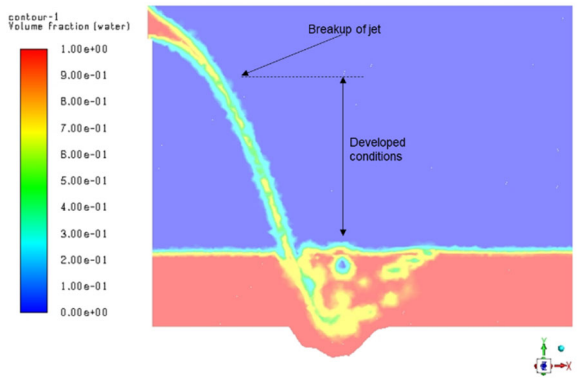

Volume fraction contour plot (red = water and blue = air)

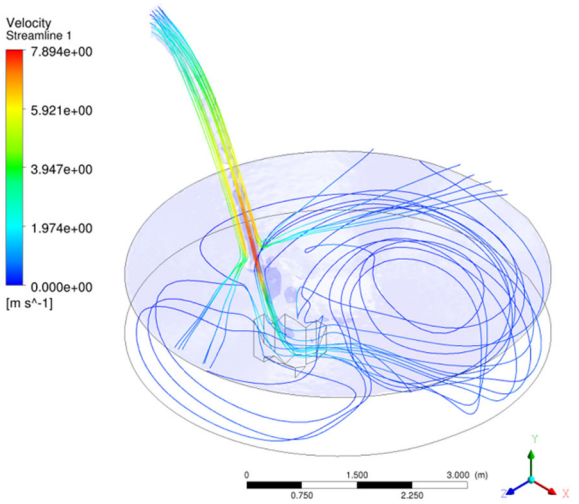

Oblique view of falling jet with streamlines

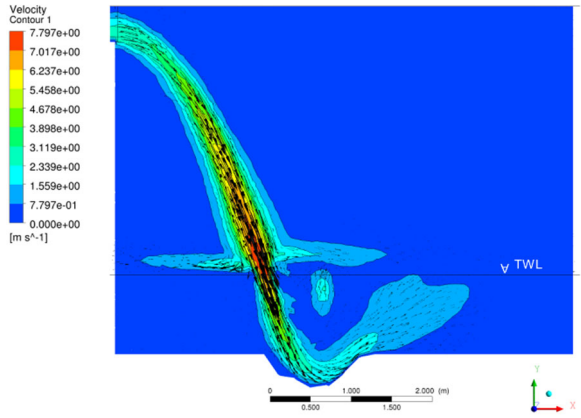

Velocity magnitude (m/s) in flow direction

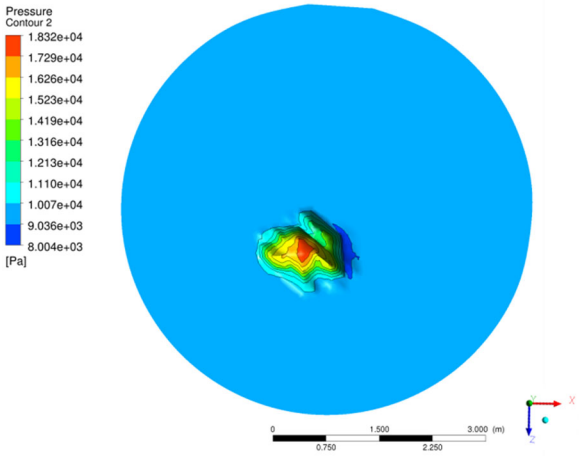

Total pressures on the plunge pool bottom

Figure I.9: Hydrodynamic results for test CF1 for Case B

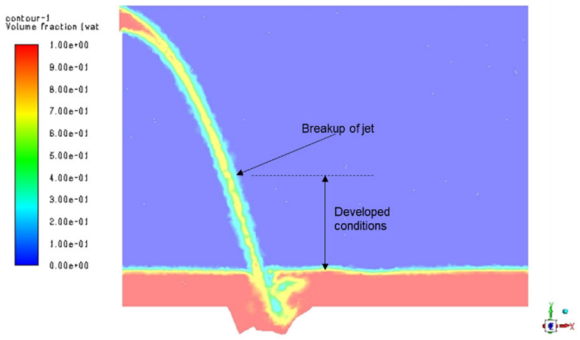

Volume fraction contour plot (red = water and blue = air)

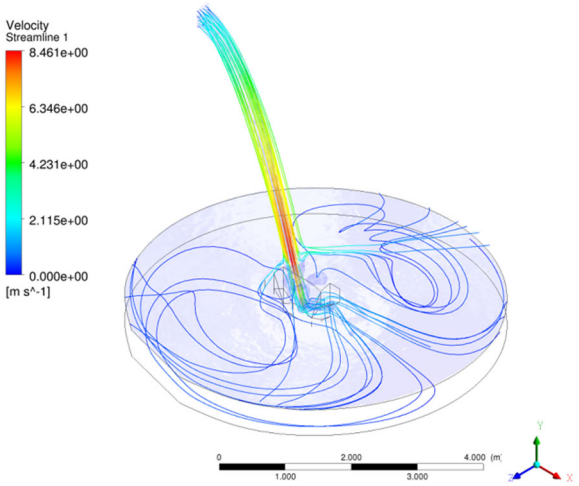

Oblique view of falling jet with streamlines

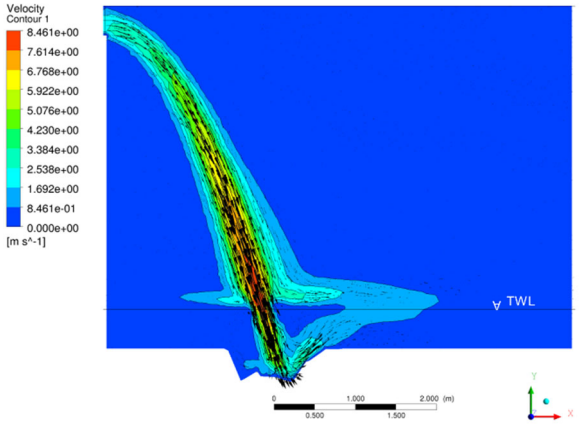

Velocity magnitude (m/s) in flow direction

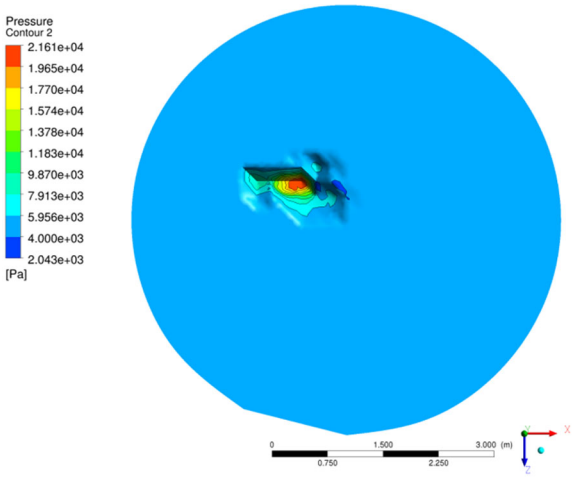

Total pressures on the plunge pool bottom

Figure I.10: Hydrodynamic results for test CF2 for Case B

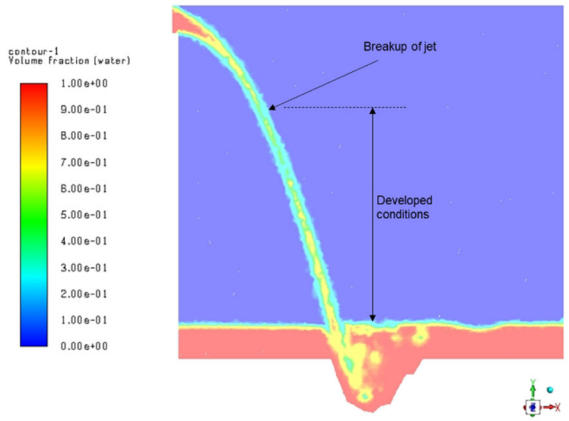

Volume fraction contour plot (red = water and blue = air)

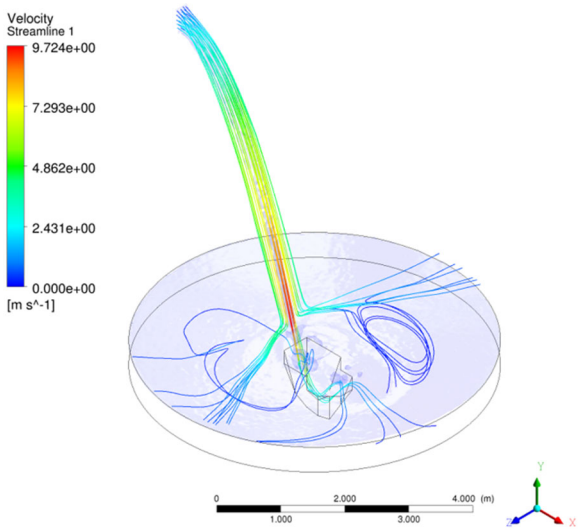

Oblique view of falling jet with streamlines

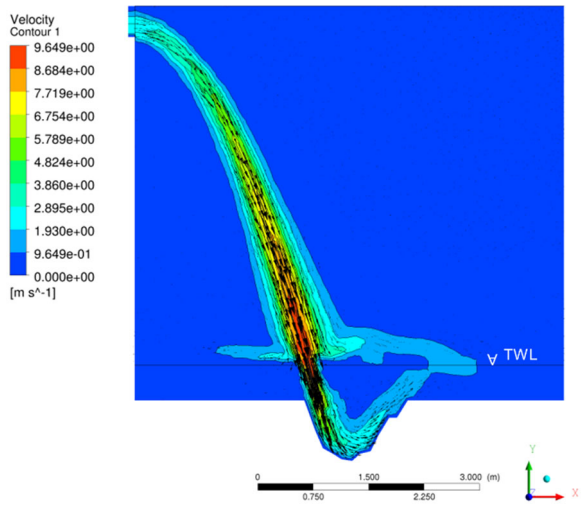

Velocity magnitude (m/s) in flow direction

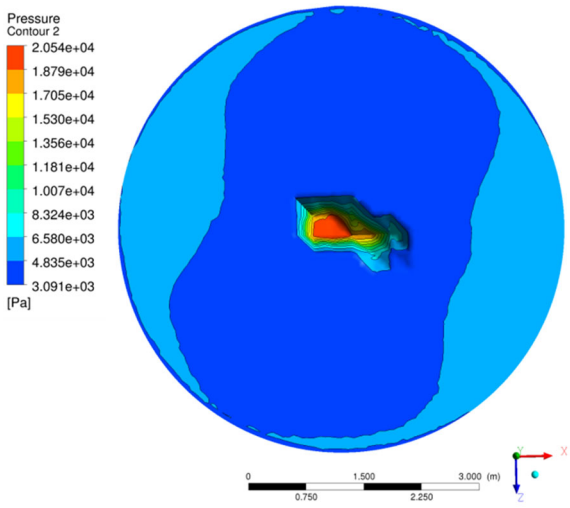

Total pressures on the plunge pool bottom

Figure I.11: Hydrodynamic results for test CF3 for Case B

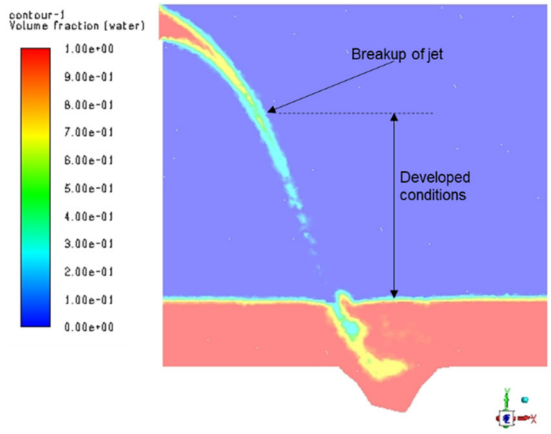

Volume fraction contour plot (red = water and blue = air)

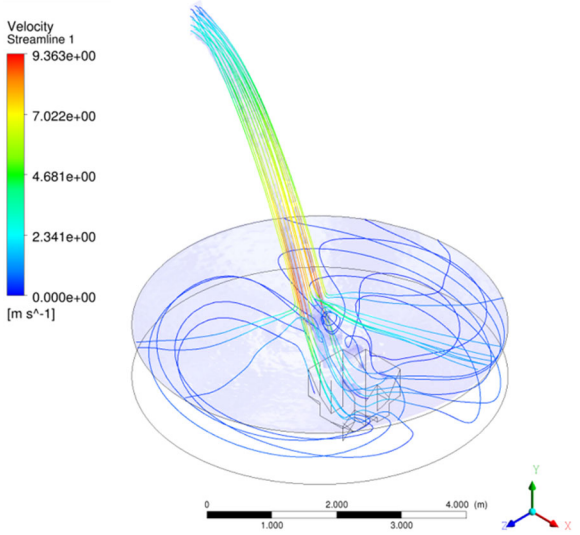

Oblique view of falling jet with streamlines

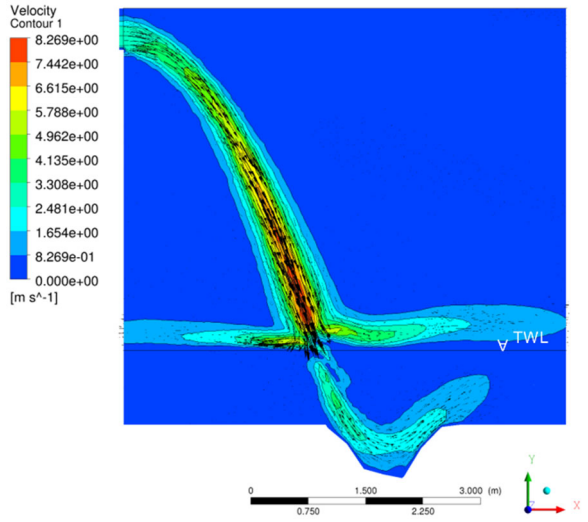

Velocity magnitude (m/s) in flow direction

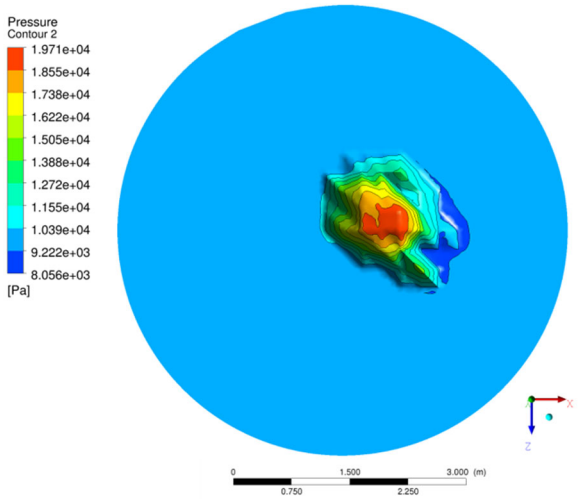

Total pressures on the plunge pool bottom

Figure I.12: Hydrodynamic results for test C3 for Case B

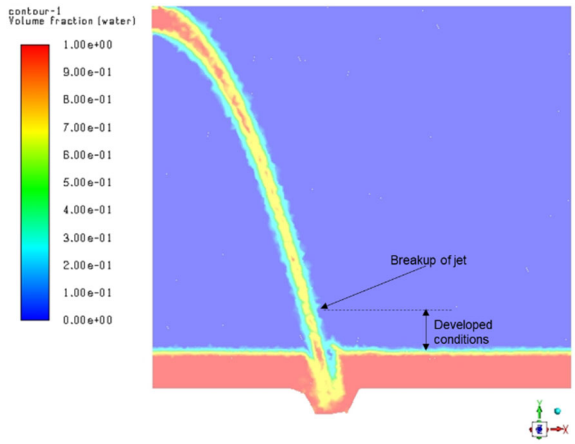

Volume fraction contour plot (red = water and blue = air)

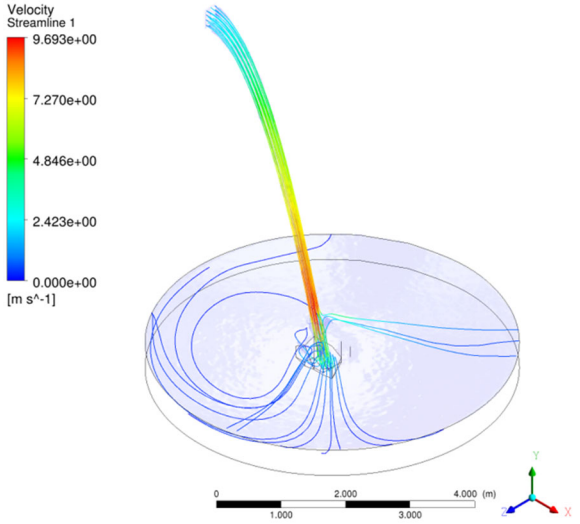

Oblique view of falling jet with streamlines

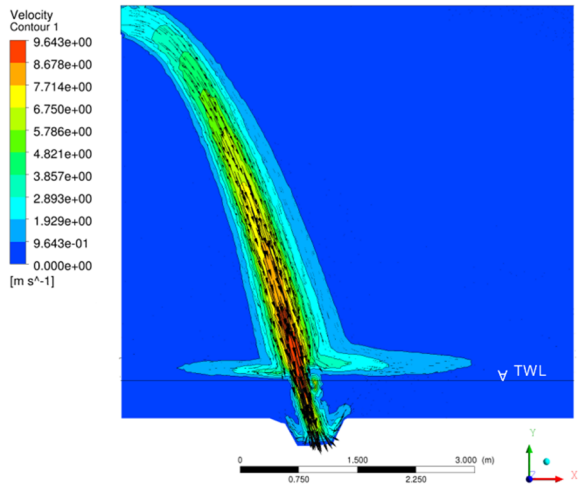

Velocity magnitude (m/s) in flow direction

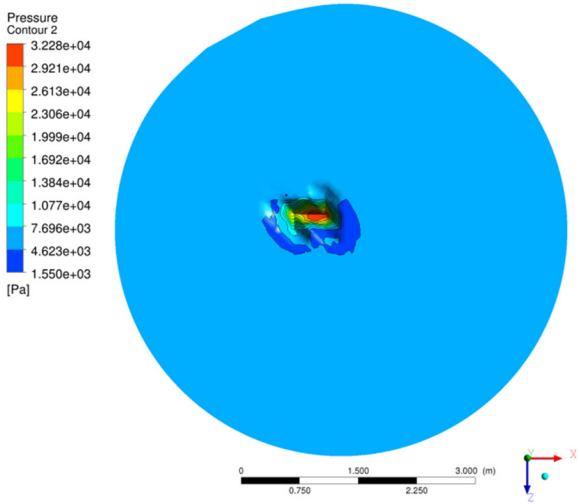

Total pressures on the plunge pool bottom

Figure I.13: Hydrodynamic results for test CF4 for Case B

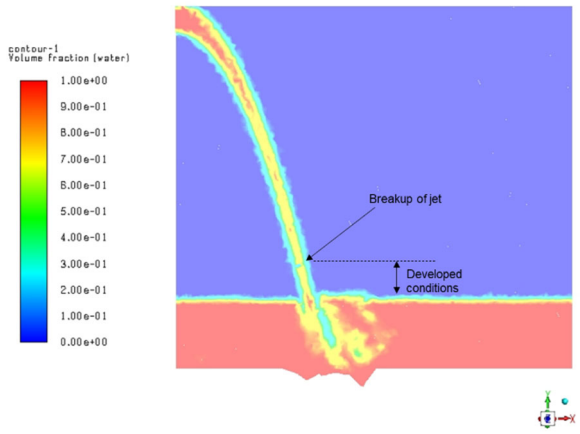

Volume fraction contour plot (red = water and blue = air)

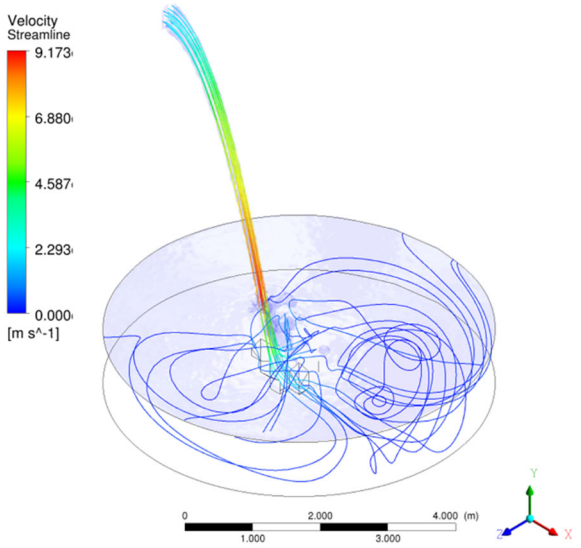

Oblique view of falling jet with streamlines

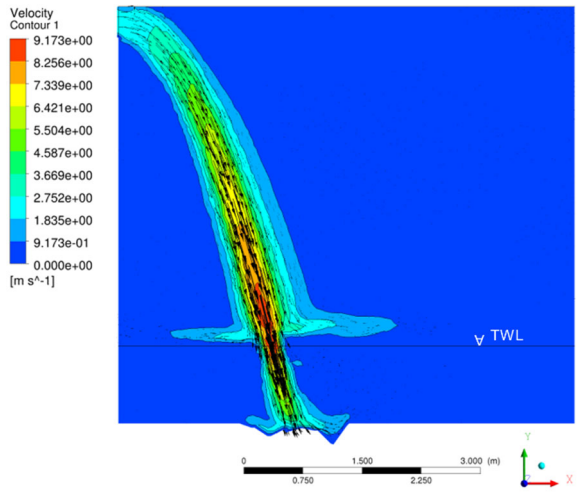

Velocity magnitude (m/s) in flow direction

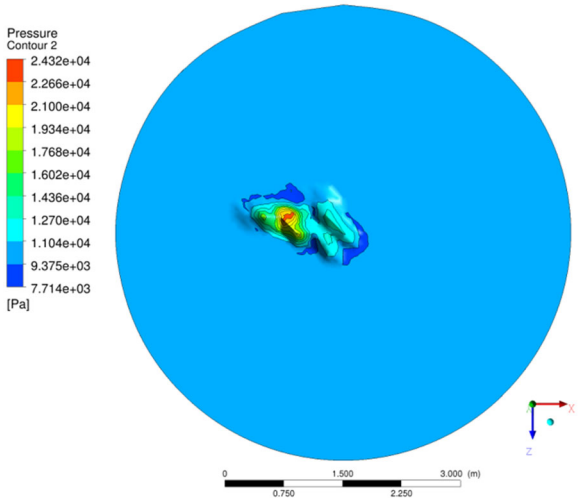

Total pressures on the plunge pool bottom

Figure I.14: Hydrodynamic results for test with joint structure dip against flow direction for Case B

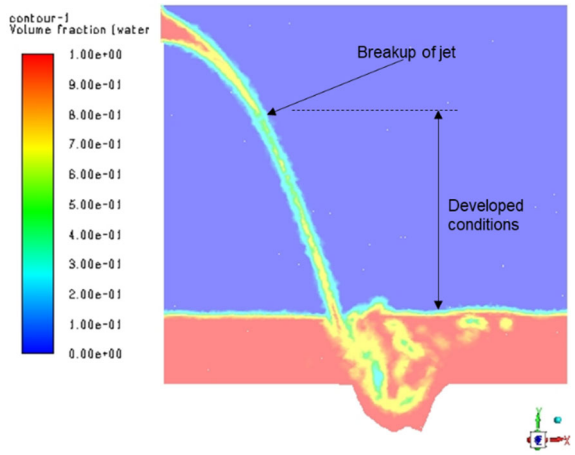

Volume fraction contour plot (red = water and blue = air)

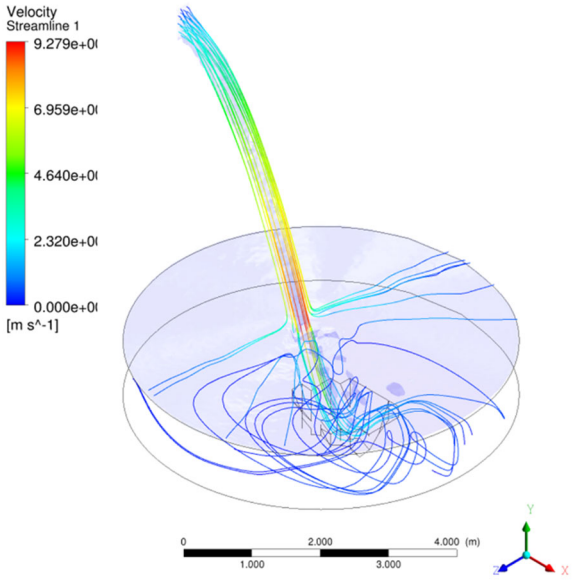

Oblique view of falling jet with streamlines

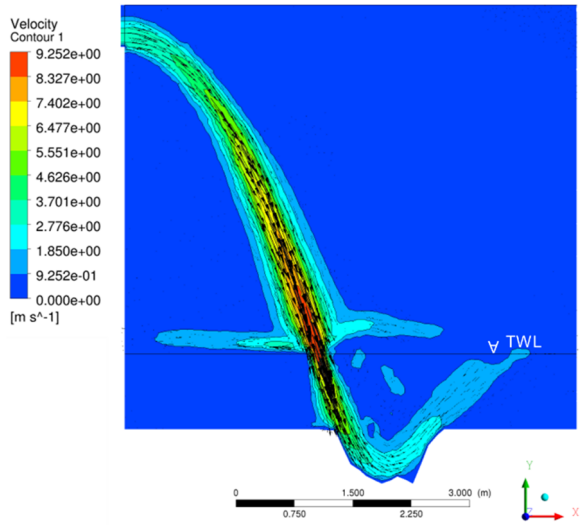

Velocity magnitude (m/s) in flow direction

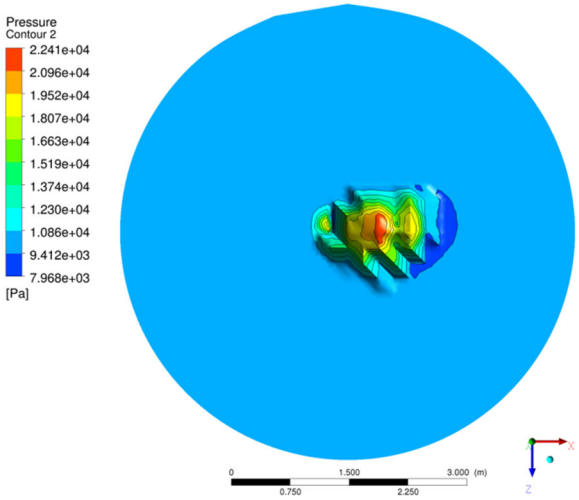

Total pressures on the plunge pool bottom

Figure I.15: Hydrodynamic results for test with joint structure dip in flow direction for Case B